University of Southampton

Pulsed laser deposition of thin-film oxides for waveguide lasers

by

Jake Jonathan Prentice

A thesis submitted for the degree of Doctor of Philosophy

In the Faculty of Engineering and Physical Sciences

Optoelectronics Research Centre

March 2020

University of Southampton

Abstract

Faculty of Engineering and Physical Sciences

Doctor of Philosophy

by Jake Jonathan Prentice

Pulsed laser deposition (PLD) is a technique for depositing materials and PLD displays versatility and high growth rates. It can be used to grow active single-crystal materials, which can be used as planar waveguide lasers. During PLD, particulates can be embedded into the growing film, which can reduce the planar waveguide lasers optical-to-optical efficiency and degrade the physical characteristics of a grown film. The experiments presented in this thesis focus on reducing the density of particulates in PLD-grown films and using this knowledge to grow high quality, novel materials.

Three particulate reduction techniques were investigated including a shadow-mask, segmented targets and bi-directional ablation. All of these techniques reduced the particulate density and bi-directional ablation was implemented as the new standard ablation regime. This novel technique increased target utilisation by 50%, target lifetime by 100% and demonstrated an average particulate density reduction of 80%. As a direct result of bi-directional ablation, films with losses down to 0.12 dB/cm were realised.

The versatility of PLD was exploited to tune the lattice constant of a mixed-sesquioxide film to demonstrate a <0.1% lattice mismatch with sapphire. Waveguiding was realised for the first time in a 3% Yb-doped sapphire waveguide, a material that is impossible to grow via traditional crystal growth methods.

A Yb:LuAG laser with cladding layers was demonstrated, for the first time with PLD, with output powers of 3.3 W. Using bi-directional ablation, an Er:YGG film was grown and 3.46 dB of gain was realised in a channel waveguide geometry. Previous attempts had not achieved any such gain due to high losses.

The particulate reduction technique demonstrated in this thesis and the subsequent exploitation, pave the way for PLD as a commercially viable technique for waveguide fabrication. Without the drawback of high particulate densities, high quality optical devices can be fabricated via PLD that would compete with other growth techniques.

“I hear the jury’s still out on science”

George Oscar Bluth Jr

Table of Contents

Table of Tables

Table of Figures

Research Thesis: Declaration of Authorship

Print name:	Jake Prentice

Title of thesis:	Pulsed laser deposition of thin-film oxides for waveguide lasers

I declare that this thesis and the work presented in it are my own and has been generated by me as the result of my own original research.

I confirm that:

1. This work was done wholly or mainly while in candidature for a research degree at this University;
2. Where any part of this thesis has previously been submitted for a degree or any other qualification at this University or any other institution, this has been clearly stated;
3. Where I have consulted the published work of others, this is always clearly attributed;
4. Where I have quoted from the work of others, the source is always given. With the exception of such quotations, this thesis is entirely my own work;
5. I have acknowledged all main sources of help;
6. Where the thesis is based on work done by myself jointly with others, I have made clear exactly what was done by others and what I have contributed myself;
7. Parts of this work have been published as:

Prentice, J.J., Grant-Jacob, J.A., Kurilchik, S.V., Mackenzie, J.I. and Eason, R.W., 2019. Particulate reduction in PLD-grown crystalline films via bi-directional target irradiation. Applied Physics A, 125(2), p.152.

Prentice, J.J., Grant-Jacob, J.A., Shepherd, D.P., Eason, R.W. and Mackenzie, J.I., 2018. Yb-doped mixed-sesquioxide films grown by pulsed laser deposition. Journal of Crystal Growth, 491, pp.51-56.

Signature:		Date:	

Acknowledgements

The work detailed in this thesis was primarily funded by EPSRC grant number EP/N018281/1 and my stipend funded through EPSRC grant number EP/M50662X/1, I offer my thanks for these. I'd also like to thank my examiners, Judith and Ioannis for my viva, although it was virtual you made it enjoyable and getting 3 hours to talk only about my work is a privilege that I doubt I'll have again.

I am incredibly grateful to Jacob, my primary supervisor throughout this PhD. Your attention to detail in both research and written endeavours has made me a far superior scientist than I otherwise would be. All the 5-minute pop ins turned 2-hour meetings were awfully helpful for applying context to my research and finding the best way forward. I know you are frequently busy, but the fact that you always found time for me when I needed it made my PhD just that bit easier and I've eternally grateful.

James GJ, who basically taught me all I know experimentally, you have always been a pleasure, swapping all the juicy gos. Thank you for bearing with me through my younger, more naïve first year days, your down to earth attitude helped me navigate the ORC which I feel is a huge part of how well a PhD goes. Without you this thesis would not be half as brilliant.

There is also Rob Eason to whom I owe much, your unfiltered enthusiasm and depth of knowledge has kept me on my toes. It's always a great relief when you say you tried something 20 years ago, since then I didn't have to do it, and could move on to something else. Your open-door policy is a credit to high flying professors, and I am extremely grateful.

I would also like to thank my family and I hope this thesis proves that I've actually been doing something for the last few years. All of my family have supported me and helped me to get where I am now, and I could not be more indebted. My Mum and Dad have supported me so much more than just financially, your seemingly genuine excitement when I tell you what I've been doing helped me carry on. Harriet, Neil and Ariana, you are all so generous and visiting all of you gives me something to strive for in the future. James, my best of men, I'm writing this the day after I saw you with a partial haircut, and I'd like to record that here as one of the best things I've ever seen. Friend, confidant, brother, pick a word and it probably describes you.

I also appreciate that all of my friends and colleagues at the ORC, everyone is so friendly and try to make people feel at home. There are some unbelievably gifted technicians in the university, without the guidance and raw talent of Glenn Topley, Neil Sessions and countless others this thesis would not be what it is.

Finally, Julia, my long-term fiancé (COVID pending), I must thank you the most. I can’t really believe that you stood by me through this PhD. You have made my life through this PhD incalculably easier, knowing I could come back home to you is exactly what I needed. You were and still are my rock and I couldn’t be happier that we have forged ourselves a life.

Definitions and Abbreviations

AF	Ablation fluence
BDA	Bi-directional ablation
BSE	Backscattered electron
CAD	Computer aided design
CVD	Chemical vapour deposition
CW	Continuous wave
DF	Dark-field
EDX	Electron dispersive x-ray analysis
FWHM	Full width half maximum
GGG	Gadolinium gallium garnet
GIXRD	Grazing incidence x-ray diffraction
HIP	Hot isotropic press
HR	High reflectivity
HT	High transmissivity
LACVD	Laser-assisted chemical vapour deposition
LIPSS	Laser induced periodic surface structure
LPE	Liquid phase epitaxy
LuAG	Lutetium aluminium garnet
MBE	Molecular beam epitaxy
MOCVD	Metal-organic chemical vapour deposition
NA	Numerical aperture
OSA	Optical spectrum analyser
PECVD	Plasma-enhanced chemical vapour deposition
PLD	Pulsed Laser Deposition
RC	Rocking curve

RE	Rare-earth
SEM	Scanning electron microscope
SHP	Substrate heating power
SM	Shadow mask
SPIP	Scanning probe image processor
TIR	Total internal reflection
UDA	Uni-directional ablation
UV	Ultraviolet
XRD	X-ray diffraction
YAG	Yttrium aluminium garnet
YG	Y_2O_3 and Ga_2O_3
YGG	Yttrium gallium garnet
YIG	Yttrium iron garnet

Chapter 1 Introduction

1.1 Solid-state lasers

Solid state lasers are becoming increasingly important in laser manufacturing (Kannatey-Asibu Jr, 2009), medical procedures such as eye surgery (Lubatchowski, 2007), laser printers (Hu *et al.*, 2008) and environmental instrumentation (Hering *et al.*, 2013) to name but a few. Single crystal materials are historically used as the gain medium, with the first laser demonstrated in 1960 with ruby (Cr^{3+}:Al_2O_3) (Maiman, 1960). Since this achievement, countless numbers of single-crystal gain media have been created, with Nd-doped YAG finding particular success, demonstrating the first room temperature, continuous wave laser operation in 1964 (Geusic *et al.*, 1964). Garnets and sesquioxides generally have an intrinsic mechanical and chemical stability that enables them to handle high thermal loads, essential for a high-power gain media. However, the growth of garnets and sesquioxides is difficult via traditional melt techniques due to their high melting point, and it can take several weeks to grow. The volume of material with a uniform concentration of dopant can also be low (Lupei *et al.*, 2004).

Techniques that avoid having to heat bulk material to the melting point are ceramic materials and deposition growth techniques such as molecular beam epitaxy and pulsed laser deposition (PLD). Ceramic laser materials consist of tightly packed, randomly orientated crystallites and are generally fabricated by pressing at high pressures and sintering at high temperatures. The quality of these materials has dramatically increased in recent years and can be used to tailor the size, shape and dopant distribution of the ceramic (Ikesue and Aung, 2008). An example of this is a Yb:YAG ceramic laser system, DiPOLE, which is capable of 10 J of pulse energy with pulse width from 2 ns to 10 ns (Banerjee *et al.*, 2015).

Deposition techniques can grow garnets and sesquioxides to be single-crystal and with an extremely high dopant concentration. In this case, single crystal is taken to mean only one orientation of a specific crystal phase is observed. However, it is noted that no crystal will ever be perfectly single crystal, with even the most perfect crystals containing defects (Prokopenko *et al.*, 2000). Deposition techniques create films on substrates that can be used as a planar waveguide. This architecture, unlike bulk crystal, confines the propagating light in one dimension and can be designed to have diffraction limited outputs.

The physical requirements of the deposition material, doping concentration, dimensions and film thickness will all depend on the desired application. For example, the doping concentration will depend on the dopant properties and the desired gain needed from the device. However, the thickness will need to be larger than the minimum spot size of the pump radiation. In this thesis, lasing waveguides need to be at least 8 µm.

The single largest challenge with deposition techniques for planar waveguide fabrication is achieving a high quality, low propagation loss crystals. This is the focus of this thesis, which explores several ways in which the PLD technique could be improved to provide higher quality, lower defect films. A novel technique is presented which provides a relatively simple, cheap to implement technique to improve film quality. This technique will now be utilised in the PLD technique at the university of Southampton for the foreseeable future.

1.2 Creation of solid-state devices with pulsed laser deposition

Pulsed laser deposition is a versatile epitaxial growth method used for depositing thin films onto a surface. Pulses of laser light, predominantly in the UV range, are focussed onto a target consisting of the material to be deposited. The irradiated target material is rapidly heated, leading to ablation and the ejection of material. This material forms a plume which expands away from the target and is deposited onto a substrate. Over numerous iterations a film is formed which can be as thin as a single unit cell. The crystallinity and orientation of the film will depend on the substrate and whether it is heated. PLD can produce single-crystal epitaxial films assuming the correct growth parameters.

PLD compares favourably to other techniques, with a fast growth rate (up to 25 µm/hr) and the ability to grow complex compositions. The setup of a PLD system is relatively simple and inexpensive, and with a high number of controllable growth parameters, precise control over the films properties is possible. PLD does however have drawbacks, in particular, the creation and subsequent deposition of particulates, which can drastically reduce the quality of the films grown by PLD.

The first basic deposition of films using a setup akin to PLD was reported in 1965 (Smith and Turner, 1965). However, in the 1970s there was a significant step forward in the field of lasers with relatively low cost Q-switching and second harmonic generation available. This allowed easy access to nanosecond pulses at short wavelengths and was exploited in the 1980s, with PLD-grown high temperature superconducting films (Chiba *et al.*, 1991). This breakthrough and more affordable laser systems led to a surge in PLD research.

In the late 1980s, the first garnet type material grown by PLD was demonstrated with YIG (yttrium iron garnet) (Kidoh *et al.*, 1991) followed by the first PLD-grown laser (Gill *et al.*, 1996). Subsequently, various materials have been demonstrated with a wide range of applications, including photonics (Chapter 2). Currently, PLD is an established technique for the growth of materials for novel devices. However, it has not managed to find significant commercial success despite a few companies making superconductive tape. In the case of optical waveguides, this is most likely due to the prevalence of particulates in the deposited film, cost related difficulties and struggles in scale-up to commercial outputs.

Within the PLD group at Southampton, the benefits of the PLD have been thoroughly explored for waveguides, with examples of controlling the stoichiometry (Darby *et al.*, 2008), refractive index (Gazia *et al.*, 2008) and strain (May-Smith *et al.*, 2011). These techniques, along with the development of a multi-target PLD system (Eason *et al.*, 2009), have demonstrated the promise of the PLD technique with the growth of clad waveguides (May-Smith *et al.*, 2007) and superlattices for use as crystal mirrors (Sloyan *et al.*, 2010).

All these aforementioned applications would be vastly improved if the particulate density was decreased, increasing efficiencies and output power in laser devices and increasing reflectivity and damage thresholds in crystal mirrors. The experiments in this thesis were designed to reduce the particulate density to enable the growth of high-quality thick films. The films described in this thesis were explored as potential laser devices, however the methods developed here will have a large impact on other applications explored in the future.

1.3 Structure of this thesis

In Chapter 2, details of the theory used in this project are presented, with PLD, waveguide and lasing theory presented. The materials and architectures of interest in this project will be described in Chapter 3, along with the crystal films grown using PLD in this project. Alternative deposition techniques and their relative advantages and disadvantages will be compared to PLD, providing some context to the results detailed in this thesis. Chapter 4 will explore the methodology of this project, including the PLD schematics and the characterisation techniques. Chapter 5 describes the attempts at resolving the particulate issue in the PLD method and chapters 6-8 detail the growth of different materials and their applications. Chapter 9 summarises the thesis and discusses the possible future directions for this research.

1.4 Summary of achievements

- Design and implementation of bi-directional ablation (BDA) as a particulate reduction technique, realising an 80% reduction in the density of scattering points in the film.
- Demonstrating control of the lattice constant by creating a lutetium scandium oxide film lattice matched to sapphire with a mismatch of <0.1%.
- Achieving internal gain for the first time to our knowledge in a PLD-grown Er:YGG (Er-doped yttrium gallium garnet) planar waveguide amplifier with 3.46 dB gain.
- Realising losses down to 0.12 dB/cm with YGG channel waveguides
- Demonstration of lasing in a Yb-doped lutetium aluminium garnet (Yb:LuAG) multilayer waveguide with 3.3 W output power and 20% efficiency, the first demonstration of lasing in a PLD-grown LuAG waveguide.
- First demonstration of waveguiding in a Yb-doped sapphire film

1.5 List of publications

The listed publications describe the experimental results resulting directly from experiments described in this thesis:

1.5.1 Journal Articles

- **Prentice, J.J.**, Grant-Jacob, J.A., Kurilchik, S.V., Mackenzie, J.I. and Eason, R.W., 2019. Particulate reduction in PLD-grown crystalline films via bi-directional target irradiation. Applied Physics A, 125(2), p.152.
- **Prentice, J.J.**, Grant-Jacob, J.A., Shepherd, D.P., Eason, R.W. and Mackenzie, J.I., 2018. Yb-doped mixed-sesquioxide films grown by pulsed laser deposition. Journal of Crystal Growth, 491, pp.51-56.
- Grant-Jacob, J.A., Beecher, S.J., **Prentice, J.J.**, Shepherd, D.P., Mackenzie, J.I. and Eason, R.W., 2018. Pulsed laser deposition of crystalline garnet waveguides at a growth rate of 20 μm per hour. Surface and Coatings Technology, 343, pp.7-10.
- Grant-Jacob, J.A., **Prentice, J.J.**, Beecher, S.J., Shepherd, D.P., Eason, R.W. and Mackenzie, J.I., 2018. Particulate reduction in ternary-compound film growth via pulsed laser deposition from segmented binary-targets. Materials Research Express, 5(3), p.036402.

- Kurilchik, S.V., **Prentice, J.J.**, Eason, R.W. and Mackenzie, J.I., 2019. Characterisation and laser performance of a Yb: LuAG double-clad planar waveguide grown by pulsed laser deposition. Applied Physics B, 125(11), p.201.
- Beecher, S.J., Grant-Jacob, J.A., Hua, P., **Prentice, J.J.**, Eason, R.W., Shepherd, D.P. and Mackenzie, J.I., 2017. Ytterbium-doped-garnet crystal waveguide lasers grown by pulsed laser deposition. Optical Materials Express, 7(5), pp.1628-1633.

1.5.2 Conference submissions

- **Prentice, J.J.**, Grant-Jacob, J.A., Beecher, S.J., Shepherd, D.P., Eason, R.W. and Mackenzie, J.I., 2017, June. Ytterbium-doped mixed sesquioxides grown by pulsed laser deposition. In The European Conference on Lasers and Electro-Optics (p. CM_1_3). Optical Society of America.
- **Prentice, J.J.**, Kurilchik, S.V., Grant-Jacob, J.A., Eason, R.W. and Mackenzie, J.I., 2018. Rare-earth doped, ternary garnets waveguides grown via pulsed laser deposition. ECCG6 - Sixth European Conference on Crystal Growth, Varna, Bulgaria. 16 - 20 Sep
- **Prentice, J.J.**, Grant-Jacob, J.I., Kurilchik, S.V., Eason, R.W. and Mackenzie, J.I., 2019. Quantitative analysis of bi-directional ablation in pulsed laser deposition. IOP Plasma Surfaces and Thin Films 2019, London, United Kingdom. 12 Jun.
- Mackenzie, J.I., Kurilchik, S.V., **Prentice, J.J.**, Grant-Jacob, J.A., Carpenter, L.G., Gates, J.C., Smith, P.G.R., Gawith, C.B.E., Riris, H., Yu, A.W. and Eason, R.W., 2019, March. 1.6-µm Er: YGG waveguide amplifiers. In Solid State Lasers XXVIII: Technology and Devices (Vol. 10896, p. 1089604). International Society for Optics and Photonics.
- Mackenzie, J.I., Grant-Jacob, J.A., Beecher, S.J., **Prentice, J.J.**, Hua, P., Shepherd, D.P. and Eason, R.W., 2017. Planar waveguides grown by pulsed laser deposition for power amplifiers.
- Stirling, C.J., Donko, A.L., Baktash, N., Grabska, K., Rosales, A.L.C., Clarke, D.T., **Prentice, J.J.** and Posner, M.T., 2018, September. Student-led outreach and public engagement activities at the University of Southampton to celebrate the inaugural International Day of Light. In Optics Education and Outreach V (Vol. 10741, p. 107410B). International Society for Optics and Photonics.

- Kurilchik, S.V., Grant-Jacob, J.A., **Prentice, J.J.**, Hua, P., Eason, R.W. and Mackenzie, J.I., 2018. Pulsed-laser-deposited Yb: YAG planar-waveguide amplifier. 8th EPS-QEOD Europhoton Conference, Barcelona, Spain. 02 - 07 Sep
- Mackenzie, J.I, **Prentice, J.J.**, Grant-Jacob, J.A., Kurilchik, S.V., Shepherd, D.P. and Eason, R.W., 2018. Functional crystal films fabricated by pulsed laser deposition. Pacific Rim Laser Damage 2018: Optical Materials for High-Power Lasers: PHOTONICS International Congress 2018, Yokohama, Japan. 25 - 27 Apr
- Eason, R.W, Prentice J.J. Kurilchik, S.V, Grant-Jacob, J.A, Mackenzie, J.I. 2019. A novel particulate reduction protocol for PLD-growth of low loss planar waveguide lasers. Conference of Laser Ablation, Maui, Hawaii 8-13 Sep

1.5.3 Awards

- Winner of “Ion and plasma surface interactions group best poster prize” 2019 at IOP Plasma Surfaces and Thin Films 2019, London, United Kingdom. 12 Jun.

1.6 References

Banerjee, S., Ertel, K., Mason, P. D., Phillips, P. J., De Vido, M., Smith, J. M., Butcher, T. J., Hernandez-Gomez, C., Greenhalgh, R. J. S. and Collier, J. L. (2015) 'DiPOLE: a 10 J, 10 Hz cryogenic gas cooled multi-slab nanosecond Yb: YAG laser. ', *Optics Express,* 23(15), pp. 19542-19551.

Chiba, H., Murakami, K., Eryu, O., Shihoyama, K., Mochizuki, T. and Masuda, K. (1991) 'Laser excitation effects on laser ablated particles in fabrication of high T_c superconducting thin films', *Japanese journal of applied physics,* 30(4B), pp. L732.

Darby, M. S. B., May-Smith, T. C. and Eason, R. W. (2008) 'Deposition and stoichiometry control of Nd-doped gadolinium gallium garnet thin films by combinatorial pulsed laser deposition using two targets of Nd:Gd3Ga5O12 and Ga2O3', *Applied Physics A,* 93(2), pp. 477-481.

Eason, R. W., May-Smith, T. C., Grivas, C., Darby, M. S. B., Shepherd, D. P. and Gazia, R. (2009) 'Current state-of-the-art of pulsed laser deposition of optical waveguide structures: Existing capabilities and future trends', *Applied Surface Science,* 255(10), pp. 5199-5205.

Gazia, R., May-Smith, T. C. and Eason, R. W. (2008) 'Growth of a hybrid garnet crystal multilayer structure by combinatorial pulsed laser deposition', *Journal of Crystal Growth,* 310(16), pp. 3848-3853.

Geusic, J. E., Marcos, H. M. and Van Uitert, L. (1964) 'Laser oscillations in Nd-doped yttrium aluminum, yttrium gallium and gadolinium garnets.', *Applied Physics Letters,* 4(10), pp. 182-184.

Gill, D. S., Anderson, A. A., Eason, R. W., Warburton, T. J. and Shepherd, D. P. (1996) 'Laser operation of an Nd:Gd3Ga5O12 thin-film optical waveguide fabricated by pulsed laser deposition', *Applied Physics Letters,* 69(1), pp. 10-12.

Hering, P., Lay, J. P. and Stry, S. e. (2013) *Laser in environmental and life sciences: modern analytical methods.* . Springer Science & Business Media.

Hu, X. P., Zhao, G., Yan, Z., Wang, X., Gao, Z. D., Liu, H., He, J. L. and Zhu, S. N. (2008) 'High-power red-green-blue laser light source based on intermittent oscillating dual-wavelength Nd: YAG laser with a cascaded $LiTaO_3$ superlattice.', *Optics Letters,* 33(4), pp. 408-410.

Ikesue, A. and Aung, Y. L. (2008) 'Ceramic laser materials', *Nature photonics,* 2(12), pp. 721.

Kannatey-Asibu Jr, E. (2009) *Principles of laser materials processing.* John Wiley & Sons.

Kidoh, H., Morimoto, A. and Shimizu, T. (1991) 'Synthesis of ferromagnetic Bi-substituted yttrium iron garnet films by laser ablation', *Applied Physics Letters,* 59(2), pp. 237-239.

Lubatchowski, H. (2007) *Lasers in Medicine: Laser-Tissue Interactions and Applications.*: Wiley.

Lupei, V., Lupei, A. and Ikesue, A. (2004) 'Single crystal and transparent ceramic Nd-doped oxide laser materials: a comparative spectroscopic investigation', *Journal of Alloys and Compounds,* 380(1-2), pp. 61-70.

Maiman, T. H. (1960) 'Stimulated optical radiation in ruby', *Nature,* 187(4736), pp. 493-494.

May-Smith, T. C., Shepherd, D. P. and Eason, R. W. (2007) 'Growth of a multilayer garnet crystal double-clad waveguide structure by pulsed laser deposition', *Thin Solid Films,* 515(20-21), pp. 7971-7975.

May-Smith, T. C., Sloyan, K. A., Gazia, R. and Eason, R. W. (2011) 'Stress Engineering and Optimization of Thick Garnet Crystal Films Grown by Pulsed Laser Deposition', *Crystal Growth & Design,* 11(4), pp. 1098-1108.

Prokopenko, I. V., Kislovskii, E. N., Olikhovskii, S. I., Tkach, V. M., Lytvyn, P. M. and Vladimirova, T. P. (2000) 'Comprehensive investigation of defects in highly perfect silicon single crystals.', *Semiconductor Physics Quantum Electronics & Optoelectronics.,* 3, pp. 275-281.

Sloyan, K. A., May-Smith, T. C., Zervas, M., Eason, R. W., Huband, S., Walker, D. and Thomas, P. A. (2010) 'Growth of crystalline garnet mixed films, superlattices and multilayers for optical applications via shuttered Combinatorial Pulsed Laser Deposition.', *Optics Express,* 18(24), pp. 24679-24687.

Smith, H. M. and Turner, A. F. (1965) 'Vacuum deposited thin films using a ruby laser.', *Applied Optics,* 4(1), pp. 147-148.

Chapter 2 Theory

2.1 Introduction

In this chapter, the theoretical concepts behind PLD and planar waveguides are introduced. Much of the theory behind PLD is qualitative, however experimental values are included when helpful. Initially, the processes involved in PLD are presented, including ablation, plume formation and propagation and crystal growth. Following this, theory about planar waveguides and their lasing applications are described. This chapter should provide context for understanding the background, experimental setup and the results chapters.

2.2 PLD theory

PLD has proven challenging in terms of developing a theoretical model of the entire process due to the high number of interdependent variables. Attempts have been made to look at specific parts of the process, for example the ablation process (Zhigilei *et al.*, 1997), but no complete qualitative model has yet been published. This section provides an overview of each of the mechanisms involved in successful pulsed laser deposition and bring them into context with the growth of single-crystal, defect free films.

2.2.1 Ablation

A basic schematic of how a laser pulse can ablate a surface and form a plume of material is demonstrated in Figure 2.1. There are several processes that contribute to varying degrees to ablation and these are categorised as follows:

2.2.1.1 Electronic induced ablation

This ablation process is dominant at pulse lengths of around 10^{-15} s (Perrière *et al.*, 2002) (e.g. femtosecond PLD). In this process, simultaneous absorption of multiple photons causes atoms to be ionised directly from the laser beam, and therefore there is no energy transfer to the lattice. The free electron can then ionise other atoms by interacting with bound electrons, causing an exponential increase in ionisation or “avalanche ionisation” (Murray *et al.*, 2013) a non-linear absorption process. The removal of material occurs by Coulomb explosion: as electrons escape, positive charge builds up on the surface resulting in a release of energetic ions.

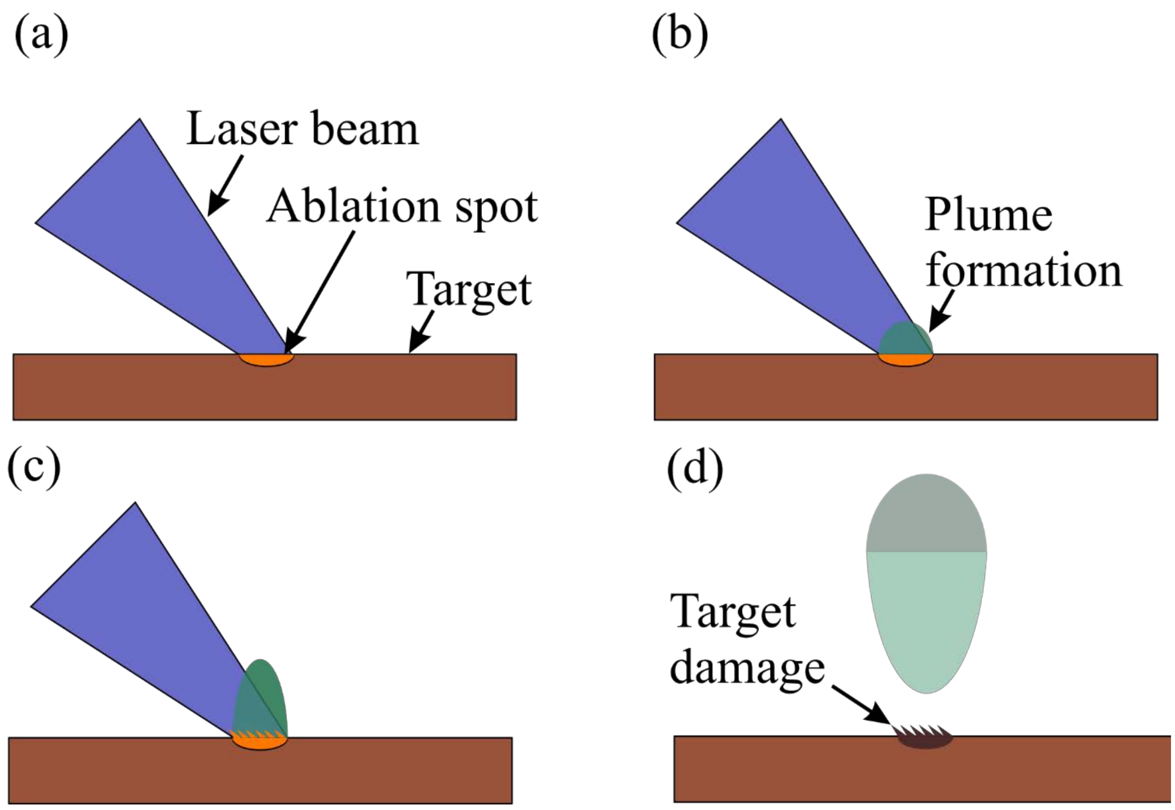

Figure 2.1. Diagram of ablation process. (a) the laser pulse is absorbed by the target, (b) the target melts and evaporates creating a plume, (c) the plume is dense enough to absorb some of the laser light and the constituents ionise, (d) laser pulse has ended, the plume expands and cools, the target re-solidifies with an irregular/damaged surface profile.

2.2.1.2 Thermally induced ablation

Thermally induced ablation generally occurs when the length of the ablation laser pulse is on the order of nanoseconds. Electronic ablation does occur but is not significant in terms of the whole pulse (Ashfold *et al.*, 2004). Free electrons, initially generated by multi-photon absorption, are accelerated by the ongoing laser pulse. The target material is then heated by electron-phonon interactions that cause melting and then evaporation, forming a plume of material. In some cases, such as binary ceramic targets, it is the melting and solidifying that causes a relief structure to be formed on the target's surface. For thermally induced ablation to occur, heat must not be transferred away from the target's surface quicker than it is absorbed. This means the thermal diffusion length must be shorter than the absorption length. This is illustrated in equation 3.1 and 3.2 (Cheung, 1993). In equation 3.1, L_d is the diffusion length, D and τ are the thermal diffusivity and pulse duration. In equation 3.2, L_α is the absorption length and α is the absorption coefficient.

$$L_d = 2\sqrt{D.\tau} \qquad (3.1)$$

$$L_a = \frac{1}{\alpha} \qquad (3.2)$$

From these equations, to achieve $L_d < L_\alpha$, short pulse widths and materials with low thermal diffusivity are ideal. In most materials, short wavelengths of light have short absorption depths. Consequently, frequently in PLD UV lasers with ns pulse width are used for the ablation of materials.

2.2.1.3 Collisional ablation

Inside the plume created by ablation, there are numerous collisions expanding the plume and creating segregated plume dynamics for the constituent elements (discussed further in 2.2.2) (Harilal *et al.*, 2014). As a consequence, ejected ions can be scattered back towards the target with high energy. This can cause sputtering of the target surface over areas that are larger than the ablation spot (Ashfold *et al.*, 2004), however the sputtered elements are likely to be a small contribution when compared to elements ablated directly from the ablation beam.

2.2.2 Plume dynamics and propagation

2.2.2.1 Plume ionisation

The Saha equation (equation 3.3) (Eason, 2007) can be used to estimate the ratio between charged ions and neutral atoms in a gas at thermal equilibrium. Although there will be temperature gradients in the plume, for this purpose, however, it can be assumed it is in thermal equilibrium. The symbols and their definition in equation 3.3 are presented in Table 2.1. From this equation, it can be seen that the fraction of ions in the plume will not reach a significant level until U_i is much larger than kT. However, the fraction of ions will increase exponentially after this condition is met and a plasma plume will be formed. The temperature of the plume will increase until the laser pulse stops as it absorbs the pulse via inverse bremsstrahlung absorption (Lenk *et al.*, 1997). The value of the first ionisation potential are typically ~10 eV, which means ionisation densities of $>10^{18}$ cm^{-3} or temperatures of 6000 K are needed for a 10% ionisation fraction (Geohegan, 1994). This is considered unreasonable for typical ablation fluence values of <10 Jcm^{-2} (Willmott and Huber, 2000) and when only considering thermal effects. However, other processes such as laser hotspots, impurities and the plume absorbing the ablation beam will result in higher ionisation densities (Willmott and Huber, 2000).

$$\frac{n_i}{n_n} = 2.4 \times 10^{15} \frac{T^{\frac{3}{2}}}{n_i} e^{-\frac{U_i}{kT}} \tag{3.3}$$

Table 2.1. Definitions of the symbols used in equation 3.3.

Symbol	Definition
n_i	Ion density (cm^{-3})
n_n	Neutral density (cm^{-3})
T	Temperature (K)
U_i	First ionisation potential (eV)
k	Boltzmann’s constant

2.2.2.2 Plume expansion

The plume will expand away from the target and the manner in which it will expand depends on the background pressure, the size of the constituent ions and the size of the ablation spot. All of these conditions are interdependent, for example, the size of the ablation spot will be less significant at high background pressures (Ojeda *et al.*, 2015).

As the background pressure is increased the mean free path of the plume constituents will decrease, consequently, the ability of the plume to expand into this space is negated (Figure 2.2 (a) and (b)). This will confine the plume and decrease the velocity of the plume constituents. The effect of this when depositing onto a central 10x10 mm substrate is that, at high pressures (10^{-2} – 10^{-1} mbar), there is more material deposition.

The expansion is also affected by the size of the constituent ions and atoms (Figure 2.2 (c) and (d)). Ablated elements that have a smaller mass number (Z) will create a larger plume than that created by an element with a larger mass number. The distribution of plume constituents will follow a $\cos^n \theta$ distribution with $7 < n < 20$, where the value of n will depend on the ablation fluence and background pressure. The distribution of particulates is more directional (due to particulates being ballistic). This is particularly relevant when growing complex materials with more than one element with the resulting deposited film not being the same stoichiometry as the target. When growing a binary oxide, oxygen can be used as a background gas to compensate for any potential oxygen loss. However, ternary oxides, such as YAG, will lose more aluminium in the transfer from target to substrate than yttrium. This can be compensated for by deliberately creating targets with more aluminium than stoichiometric YAG. The same principle can be used for other materials grown via PLD.

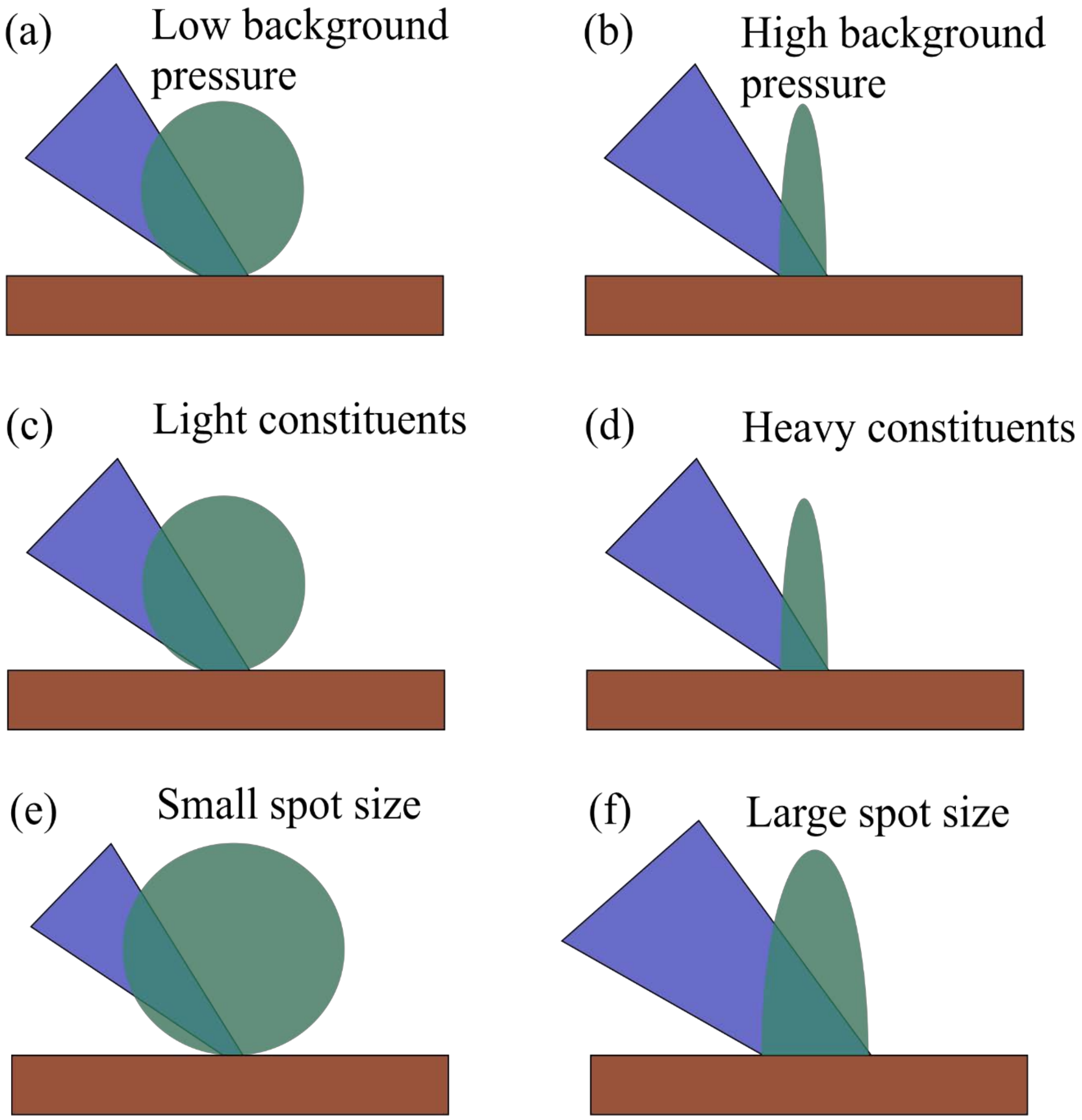

Figure 2.2. Diagram depicting the effect on the plume expansion for (a) and (b) background pressure, (c) and (d) constituent size (e) and (f) spot size.

Depending on the background pressure, the ablation spot will also have an impact on the size and shape of the plume (Figure 2.2 (e) and (f)). In this thesis, the ablation spot is rectangular, creating an elliptical shaped plume. The change in plume dynamics due to the spot size is called the "flip over effect", so called since a small ablation spot will result in a larger plume than a large ablation spot. This is due to a small spot creating a plume with higher pressure gradients, increasing the velocity of the plume constituents in the directions perpendicular to the target face (Ojeda *et al.*, 2015). Thus a large spot size is preferable for creating a less expansive plume and hence increase the growth rate. However, this needs to be balanced with the available pulse energy, since a larger spot size will require more energy to create the same ablation fluence.

All these effects are interconnected and will have an impact on the plume expansion and the deposited film characteristics. Consequently, the optimisation of the growth parameters is of critical importance for each individual material.

2.2.2.3 Velocity of the plume

A typical PLD-induced plasma plume will consist of electrons, ions, atoms and particles, which will all have different masses and therefore, given the same energy, different velocities. Electrons will have the highest velocities, but cannot escape the plasma due to the space-charge field generated by their movement away from the ions (Sloyan, 2012). The ions and atoms will have an average velocity of $\sim 1 \times 10^4\ ms^{-1}$ (Chiba *et al.*, 1991) and the particulates will have a velocity distribution of $\sim 1 - 2\ \times 10^2\ ms^{-1}$ (Dupendant *et al.*, 1990). These velocities will be similar regardless of material and laser fluence. However, the background pressure will have an impact, with the mean free path of atoms decreasing with increase background pressures. Therefore, as the pressure is increased the number of ablated atoms reaching the substrate will decrease, balanced by the flip over effect discussed in the previous section.

The velocity contrast between particulate and non-particulate species has been exploited by introducing a velocity filter between the target and substrate and this will be discussed further in section 2.2.5.

2.2.3 Crystal growth

2.2.3.1 Growth mechanisms

The growth of crystalline materials has been widely researched with the mechanisms involved of growth via melt and deposition being established. The mechanisms of growth via PLD can be altered by changing the growth parameters such as heating the substrate and changing the ablation fluence. By increasing the substrate heating power, the adatoms (surface atoms) can have the energy to move around the surface to find the most energetically favourable position, whereas not heating the substrate will generally result in the growth of an amorphous film (Kumar *et al.*, 2008). However, heating can result in the desorption of more volatile materials, such as lithium (Kim *et al.*, 2013), changing the stoichiometry of the growing film.

The deposition of materials can result in three basic modes of growth (Aziz, 2008; Venables and Spiller, 1983):

- Two-dimensional monolayers (Frank-van der Merwe) growth in which the adatoms are more strongly attracted to the surface material than other adatoms.
- Growth as islands or clusters (Volmer-Weber) where the adatoms are more strongly attracted to each other than the surface.
- A mix of island growth and monolayer growth (Stranski-Krastinov) where the adatoms will bond with other adatoms or the surface.

These mechanisms of growth are a basic model and reports are prevalent of growths that will switch modes of growths part way through the deposition (Sun *et al.*, 1996). This can occur as the physical properties of the surface change during the growth process.

2.2.3.2 Defects

All crystals will have defects in the lattice regardless of the growth technique. Below is a list of common defects that can be found in crystalline materials:

- Point defects – individual atoms missing or in the wrong position in the lattice, for example, vacancies, substitutions or interstitials (an atom where no atom would usually be found). Indiffusion techniques would not be functional without vacancies in the crystal lattice (Tan *et al.*, 1991).
- Line defects – groups of atoms in the incorrect position.
- Planar defects – regions of different materials, forming an interface between the two.

Defects will change the film's physical characteristics, such as the thermal conductivity (Li *et al.*, 1998) and refractive index (Kostritskii and Sevostyanov, 1997).

2.2.3.3 Lattice mismatch

The most energetically favourable growth for deposited material to grow is epitaxial. This can be achieved through various mechanisms, shown in Figure 2.3. An example of quasi-lattice matching (Figure 2.3 (b)) is the growth of cubic sesquioxides onto hexagonal sapphire (Bär *et al.*, 2003). It is not always possible to get a perfect lattice match through these mechanisms however, and a lattice mismatch of up to 9% (depending on growth process) can be accommodated through a combination of film stresses (Figure 2.4 (a)) and edge dislocations (Figure 2.4 (b)) (Ohring, 2001).

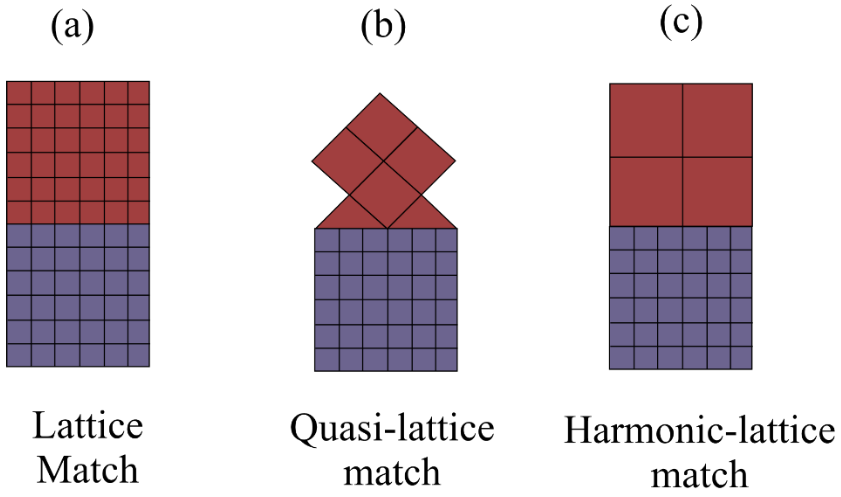

Figure 2.3. Lattice matching mechanisms with (a) a perfect lattice match, (b) quasi-lattice match and (c) harmonic lattice match

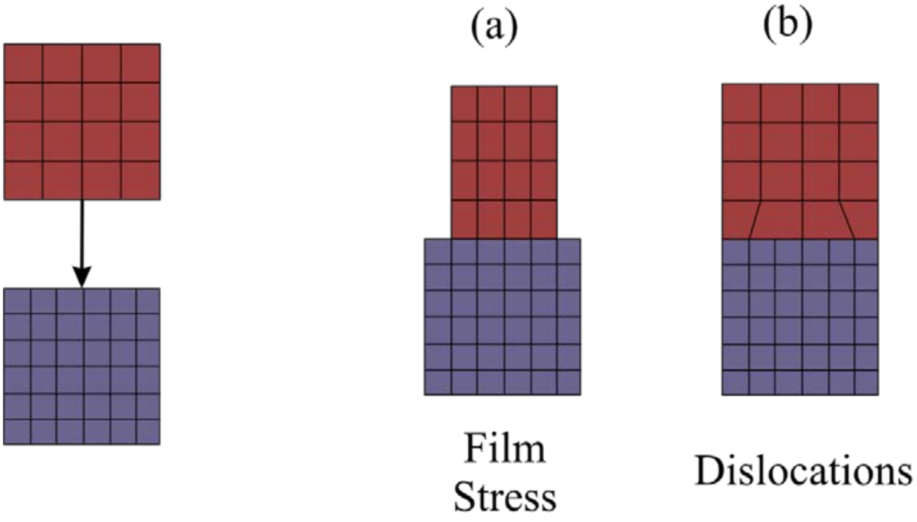

Figure 2.4. Effects of lattice mismatch on films creating (a) stress in the film and/or (b) dislocations in the lattice

Although lattice mismatch at room temperature is important, the thermal expansion contrast between the substrate and deposited material must be considered. If a material is deposited onto a substrate that is heated, the film may grow epitaxially. However, when the substrate is subsequently cooled, the film and substrate may contract at different rates, resulting in different room-temperature lattice constants, causing stress and potentially cracking.

With PLD, it has been shown that the ablation fluence can be used to control the stress of the film, purposely putting the growing film under stress so that when it is cooled, stress is negated (May-Smith *et al.*, 2011).

2.2.4 Target damage

As already mentioned, when a material is ablated the surface of the material is modified both in surface topography and stoichiometry. Depending on the structure of the target, the structure can be left as cones or waves commonly labelled as LIPSS (laser induced periodic surface structure). The structural change will alter the effective ablation fluence, by increasing the surface area of the target and relative angle of incidence between the ablation laser and the surface. These structural changes will be noticeable in bulk crystal as well as ceramic targets (targets created by mixing µm-sized powders and pressing them into a ceramic disk, will be discussed in section 4.2.4). In this thesis, only ablation using ceramic targets is discussed.

The creation of a wave-like structure is suggested to form due to the Kelvin-Helmholtz instability (Ang *et al.*, 1998) and Marangoni flow (Lippert *et al.*, 1993). Kelvin-Helmholtz instability occurs due to a velocity difference between two fluids. In this case, the fluids would be the molten target surface and the plasma plume, functioning in the same way as the wind creates waves in the ocean. Marangoni flow occurs when there is difference in surface tension between two liquids, causing a surface tension gradient where a liquid will naturally flow towards the area of high surface tension. In our experience the creation of wave-like structures occurs exclusively on binary targets, i.e. targets created with one material. This is demonstrated in Figure 2.5 (a) with an SEM image of an Al_2O_3 target after 600,000 pulses and wave-like structures with a period of ~2 µm can be seen on the surface.

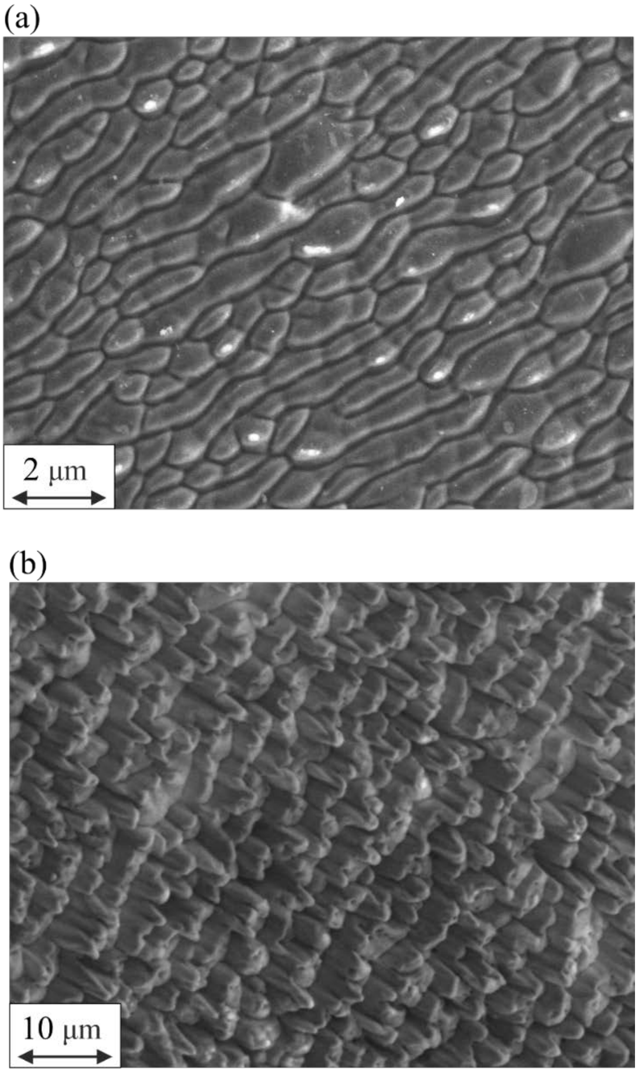

Figure 2.5. SEM images of an (a) Al2O3 target ablated by 600,000 pulses and (b) a mixed Y2O3 + Ga2O3 target ablated by 72,000 pulses

Cone-like structures form when different regions of the target surface have different ablation thresholds. Consequently, the material with a higher ablation threshold is removed at a slower rate, forming differential heights, and eventually forming cones, that point towards the laser beam (Ashfold *et al.*, 2004). These cones will become progressively larger with increasing numbers of laser pulses, leading to an increase in the effective surface area and a lower ablation fluence. The change in fluence will affect the ablation characteristics and consequently the growth rate and stoichiometry of the film. Potential exfoliation of the cones from the target's surface and subsequent deposition into the film is one mechanism for particulate generation.

The different ablation thresholds required for cone growth can be due to irregularities or impurities in the target but is more commonly due to the use of a ternary ceramic target. Since the ceramic targets are created through a mix of powders of finite size, the resulting target will not be atomically mixed. Therefore, there will be regions of each separate material on the target’s surface, creating the conditions for cone formation, as seen with a YGG target in Figure 2.5 (b).

In this thesis, I explore the formations of cones and hypothesise whether preventing the cones from forming will result in grown films having a lower particulate density.

2.2.5 Particulates

Particulate formation and subsequent deposition into a growing film is a common feature of PLD-grown films. A high density of particulates in films has been shown to reduce the thermal conductivity, alter the local refractive index and seed polycrystalline growth (Eason, 2007). When using a PLD-grown film as a planar waveguide, particulates will also increase the scattering of propagating light, consequently increasing the loss of the waveguide (Barrington *et al.*, 2000). As this is such a crucial factor in PLD-grown films, many attempts have been made to define how particulates are created and methods to prevent their creation. The state-of-the-art research in this area will be discussed in the next two sub-sections.

2.2.5.1 Particulate formation

There are three main mechanisms that have been suggested as potential formation mechanisms for particulates in the PLD-process (Gorbunoff, 2002):

- Splashing – a molten surface material is ablated, causing liquid material to be ejected and deposited
- Condensation of material in the plume
- Exfoliation of material directly from the target’s surface

Of these, for ns ablation pulses, condensation and exfoliation are considered as the main particulate mechanisms. Splashing is considered a mechanism for high repetition rate ablation (kHz) in which the surface has no time to cool between subsequent pulses.

Condensation can be controlled by optimisation of the growth parameters, i.e. moving the substrate closer to the target to reduce the possibility of condensation (although any change in growth parameters will have a knock-on effect). However, exfoliation cannot necessarily be controlled by growth parameters, especially if it is a target surface structure issue.

2.2.5.2 Particulate reduction techniques

Numerous particulate reduction techniques have been explored for application in the PLD process. The methods can be split into two categories, either an active technique, stopping the particulates from being deposited or passive, preventing particulates from being formed. Many of the active techniques exploit the size difference of the particulates and desirable atoms/ions, meaning, a plume of atoms/ions will expand to fill space behind an obstacle whereas particulates can be assumed to be ballistic. As discussed above, there will also be a substantial velocity difference between the atoms/ions and particulates. A selection of particulate reduction techniques is listed and briefly described in Table 2.2. In this thesis, the particulate reduction techniques of a shadow-mask, growth optimisation, uni-directional ablation (UDA) and target reconditioning are used and the new particulate reduction techniques, segmented targets and bi-directional ablation (BDA), are introduced.

Table 2.2. Examples of particulate reduction techniques via PLD with a categorisation and description

Technique	**Category**	**Description**
Velocity Filter	Active	A time delayed jet of gas or spinning blade exploits the velocity difference between the atoms/ions and the particulates and alters their trajectory, preventing their deposition onto the growing film (Barrington *et al.*, 2000).
Cross beam	Active	Two or more ablation plumes are directed across one another, so they miss the substrate. Collisions in the plume will divert the atoms and ions onto the substrate whereas the less dense ballistic particulates will not (Strikovsky *et al.*, 1993).
Flux screening	Active	A stainless-steel mesh with µm sized grid spacing is placed between the target and substrate. The atoms and ions will be able to pass but the particulates will be blocked (Chen *et al.*, 2006).
Shadow mask	Active	A small slab of material is placed directly in the centre of the plume, blocking particulates and ions/atoms (Fominski *et al.*, 2012). The atom/ion plume that misses the shadow mask will expand into the space created behind the shadow mask and deposit onto the substrate (discussed further in 5.2)
Inverse PLD	Active	The film is grown on the side of the substrate facing away from the target and the plume (Szörényi *et al.*, 2004). Particulates will not be diverted onto the back surface, but atoms and ions will be. Growths detailed in this thesis typically had 40 nm of growth on the back surface for every 1 µm of growth on the front surface.
Double slit	Active	Two misaligned slits are placed between the target and the substrate meaning particulates are blocked by either the first barrier or the second. However, some of the atoms and ions in the plume will make it through both slits onto the substrate (Hino *et al.*, 2003).
Growth optimisation	Passive	By altering the ablation fluence, substrate temperature, background gas pressure and species, target-substrate distance and ablation laser repetition rate the particulate density in the film can be reduced (Kilburger *et al.*, 2007).
Uni-directional ablation	Passive	Moving a disc target in epitrochoidal motion, more of the face is utilised, reducing the speed of formation of target surface-structure (Darby, 2009). This reduces the density of particulates in the film and will be discussed further in section 5.4.
Target reconditioning	Passive	A technique in which the face of a disc target is lapped and re-polished after a certain number of ablation pulses to remove any surface structure that has formed (Sloyan, 2012).

2.2.6 Thick film growth

The growth of thick films (> 10 µm) is required for the utilisation of the films as planar waveguide lasers. However, thick film growth has several challenges that are not encountered with thin film growth (< 2 µm). One issue that has been touched on in previous sections is the higher density of particulates that comes with the extended use of one target. The growth of 10 µm-thick films takes hundreds of thousands of ablation pulses and depends on the growth material and ablation fluence. This number of pulses will create significant target surface-structure, which, as described in section 2.2.4, will increase the density of particulates in the growing film. To counteract this issue, the formation of target surface-structure will need to be mitigated, or the ablation pulse density per unit area of the target be reduced (i.e. increase the area of target utilised for ablation).

Another issue observed in this project is that when growing thick films there can change from growing epitaxially to growing textured. In some cases, the film will initially grow epitaxially and then as it is grown thicker, it will grow polycrystalline. It has been suggested that this is due to the change in interaction energy between the surface and the adatoms (Kaiser, 2002). Initially, the films are grown onto a polished substrate surface, however subsequently to this, material is deposited onto a rougher surface of different material (Kaiser, 2002). Microscopic impurities will also aid in the growth of polycrystalline films (Granasy *et al.*, 2004). This suggests that cleanliness of the growth environment, substrate and deposition material is key for the removal of impurities. Also, the optimisation of thick-film growths is key, to find the substrate temperature that encourages epitaxial growth on the proceeding layers of deposited crystal.

2.3 Waveguide theory

A waveguide confines light in one or more spatial dimensions while light can propagate in another dimension. This will generally consist of a region of high refractive index surrounded by a low refractive index material. A common example of this is an optical fibre, however in this thesis the symmetrical and asymmetric planar waveguide and the channel waveguide geometry is used, with diagrams of each shown in Figure 2.6. The basic theory of these geometries is detailed in this section.

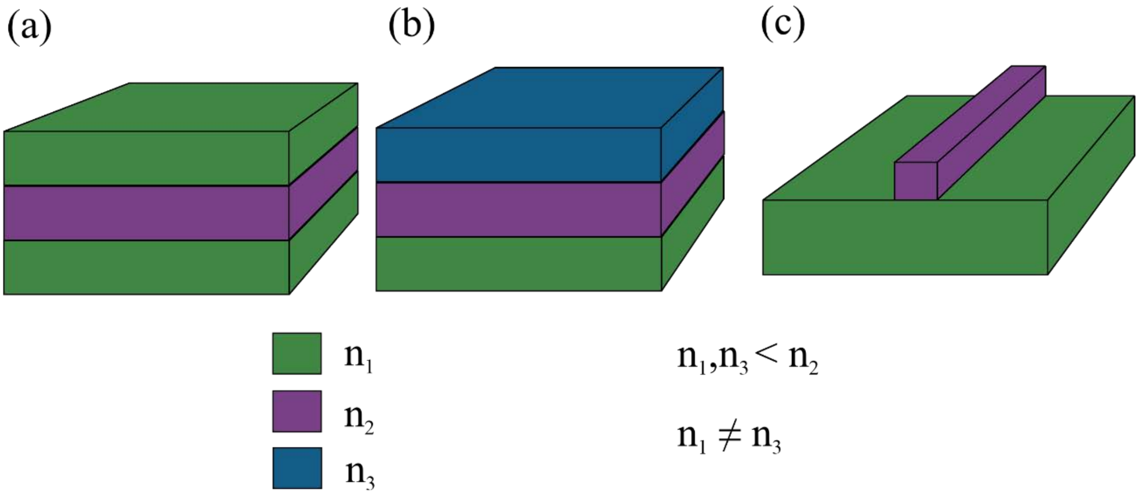

Figure 2.6. Diagrams of different waveguide geometries with (a) symmetrical planar waveguide, (b) asymmetric planar waveguide and (c) ridge channel waveguide.

If the refractive index of the core in the geometries shown in Figure 2.6 is higher than the outer layers, the light will be guided due to TIR (total internal reflection). Snell's law provides the critical angle (θ_c) for waveguiding to occur (equation 3.4) and the maximum acceptance angle (θ_{max}) is given in equation 3.5. In equation 3.4 and 3.5, n_1 and n_2 is the cladding refractive index and core refractive index respectively. n_0 is the refractive index of the surrounding medium and NA is the numerical aperture (Snyder and Love, 2012).

$$\theta_c = \sin^{-1}\left(\frac{n_1}{n_2}\right) \tag{3.4}$$

$$n_0 sin\theta_{max} = \sqrt{n_2^2 - n_1^2} = NA \tag{3.5}$$

The propagation of light in a waveguide can create a set of spatially stable electromagnetic fields known as modes which vary only by a phase factor. Modes are predicted through solutions in the wave equation (equation 3.6). For symmetric waveguides, the number of modes can be predicted using equation 3.7, where M is the number of modes, d is the thickness of the waveguide and λ is the wavelength of light propagating in the medium.

$$\nabla^2\boldsymbol{E} - \mu\epsilon\left(\frac{\delta\boldsymbol{E}}{\delta t}\right) = 0 \tag{3.6}$$

$$M = \frac{2d}{\lambda}NA \tag{3.7}$$

From equation 3.7, the number of modes increases directly with an increase in thickness and numerical aperture (refractive index contrast). This makes thick-films with a high index contrast films multimode in laser operation. A fundamental mode is highly desirable for high-power laser applications, as this represents a diffraction limited beam. Therefore, multimode operation is avoided by careful choice of the core thickness, the numerical aperture and the overall waveguide dimensions (Mackenzie, 2007).

2.3.1 Fresnel reflection

When light interacts with the facet of a waveguide, whether entering or leaving, a proportion of that light will be reflected. This can be detrimental to the waveguide lasers performance by reducing the proportion of pump power entering the waveguide, and it can be useful providing feedback by reflecting unabsorbed pump light back into the waveguide or acting as a cavity mirror for a laser.

In the case where the pump light is coupled in normal to the waveguide, which will be in most cases, the proportion of power reflected (R) is defined in equation 3.8. Here, n_1 and n_2 are the refractive index values for the initial material and the subsequent material respectively.

$$R = \left|\frac{n_1 - n_2}{n_1 + n_2}\right|^2 \tag{3.8}$$

2.4 Lasing waveguides

The word “laser” is an acronym for light amplification by stimulated emission of radiation. The process of a laser involves pumping a material, called the gain medium, with either electricity of light from either another laser, or a flashlight. The energy from this pump source is absorbed into the material causing electrons to increase in energy to a discrete upper energy level. If more than half of these electrons are in the upper energy level compared to the lower energy level, this is called population inversion, and is required for lasing. The electrons will eventually fall back to the lower energy level through spontaneous emission, however, if a photon passes with the right energy, the electron will fall back to the lower energy level while emitting a photon with the same energy (wavelength) and coherent to the passing photon. Therefore, there are two coherent photons creating amplification. These two photons can then stimulate other electrons, creating more photons. This is how a laser is created and how it emits a coherent beam of light.

The exact properties of the laser will depend on the pump radiation, the gain material and the surrounding environment. In this section, the theory of three-level, four-level and planar waveguide lasers is discussed. The material variations is discussed in Chapter 3.

2.4.1 Three-level lasers

Three-levels lasers consist of the most basic laser geometry with two possible energy level schemes seen in Figure 2.7.

Figure 2.7 (a) shows a three-level laser using the ground level as the lower lasing level. In this scheme the pump radiation is absorbed by electrons in the ground level and excited to the pump level. The electrons then undertake rapid non-radiative decay to a metastable upper laser level. If this level has a long lifetime, population inversion compared to the lower laser level can occur. This scheme of three-level laser requires high pump powers since the lower lasing level is the ground state and therefore highly populated, meaning population inversion between the upper and lower lasing levels is difficult to achieve. As the population of the upper lasing level is increased to above 50%, lasing will begin, rapidly refilling the ground level with electrons and therefore stopping population inversion, creating a short laser pulse. This can lend itself to pulsed lasers since continuous population inversion is challenging.

Figure 2.7 (b) shows an energy diagram of a three-level laser system that uses the pump level as the upper laser level. In this scheme, the pump radiation is absorbed when electrons are promoted into a metastable energy level. Radiative decay into the lower laser level can occur due to spontaneous or stimulated emission. The lower laser level will generally have a short lifetime, allowing rapid non-radiative decay into the ground level. Population inversion in this scheme is easier than that seen in Figure 2.7 (a) since, at room temperature, the lower laser level has a relatively low population.

Quasi-three level lasers exploit Stark splitting of energy levels. This means that either the pump level and the upper lasing level or the lower laser level and ground level are in the same manifold (group of sub-levels). In the latter case, reabsorption of the laser wavelength becomes a saturable loss, since the population of the lower lasing level is likely to be significant, becoming more significant with rising temperatures. This can be compensated for with efficient cooling of the lasing device.

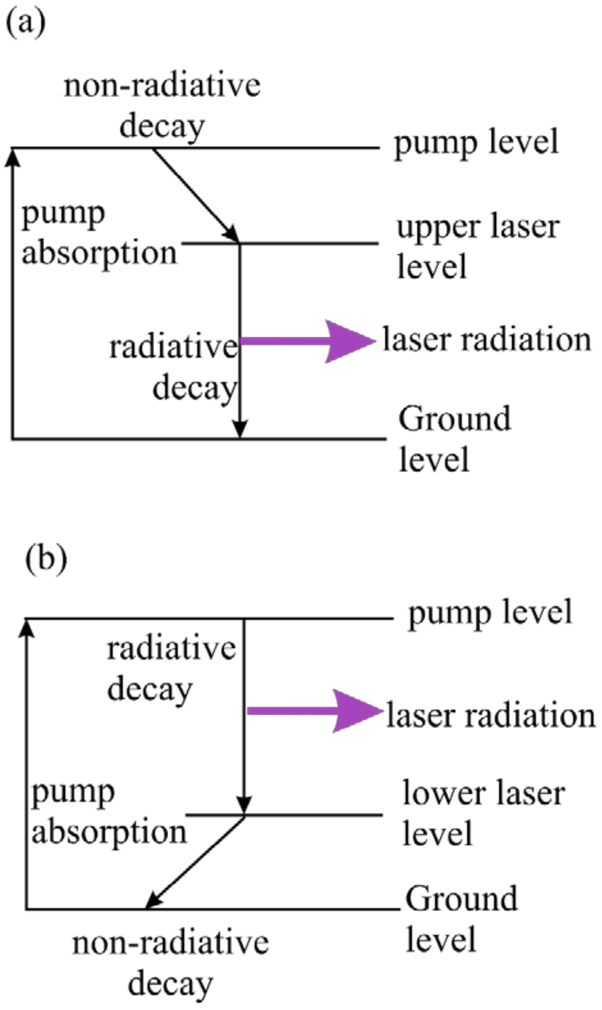

Figure 2.7. Energy level diagrams of two different schemes available for a three-level laser with (a) showing the ground state also being the ground level and (b) the pump level also being the upper laser level.

2.4.2 Four-level lasers

An energy level diagram of a four-level laser is presented in Figure 2.8 (a). In this scheme, the pump radiation is absorbed by electrons, transitioning them into the pump level. From here, they undergo a rapid non-radiative decay to the upper laser level. The electrons then transition to the lower laser level from spontaneous or stimulated emission. Then through another rapid non-radiative decay they transition back to the ground level.

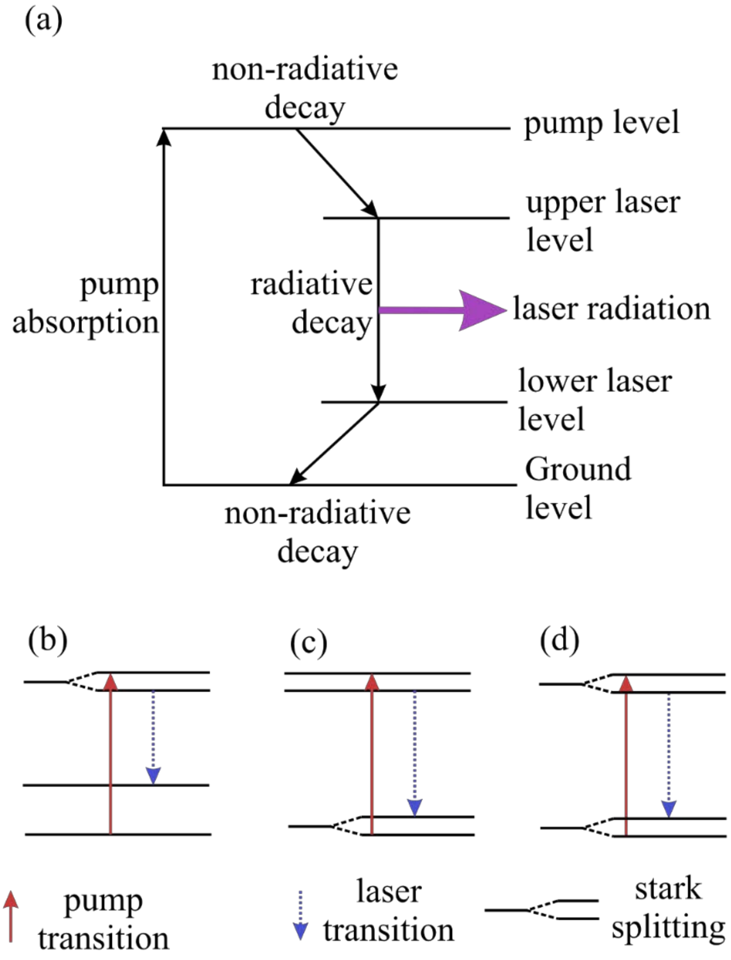

Figure 2.8. (a) Energy level diagram of a four-level laser system and (b) (c) (d) schematic of possible quasi-four level systems.

Four-level laser schemes generally have low population levels in the lower laser energy level. This means population inversion is relatively easily achieved assuming the lifetime of the upper laser level is higher than the lower laser level. Energy diagrams of quasi-four level lasers are presented in Figure 2.8 (b) (c) and (d). The same disadvantages of having multiple lasing levels in the same manifold apply to quasi four level lasers as they do for quasi-three level lasers. Ytterbium-doped gain media, discussed in section 3.2.1.1, is an example of a quasi-four level laser.

2.4.3 Waveguide lasers

Lasers in a planar waveguide geometry have several advantages over their bulk crystal counterparts. The advantages are as follows (Snyder and Love, 2012; Shepherd *et al.*, 2001):

- **Lower lasing thresholds –** due to the spatial overlap between the pump and laser beams, the theoretical lasing thresholds of waveguides are lower than bulk. This effect becomes more significant the more confined the light is, i.e. channel waveguides have much lower thresholds. This advantage can only be exploited with low-loss waveguides.
- **Potential higher slope efficiencies –** there is greater spatial overlap between the pump and the laser beams due to the dimensional confinement allowing higher gain values in comparison to overall losses.
- **Efficient cooling –** due to the higher surface area to volume ratio, cooling in a waveguide geometry can be achieved with greater efficiency. Consequently, higher pump powers can be used without significant thermal effects allowing power-scalable compact devices to be created.
- **Single-mode output –** clad waveguides can produce lasing in the fundamental mode with careful selection of the core and cladding layers thicknesses.
- **Integrated optics –** there is potential to integrate waveguides in an on-chip optical circuit.

To exploit these advantages for low threshold, high-power waveguides the propagation loss needs to be small in comparison to the potential gain. Planar waveguides grown via PLD have typically demonstrated significant scattering losses reducing the efficiencies of these lasers, making it imperative to improve the crystal quality if the commercial application of PLD for waveguide lasers is to become feasible.

2.5 Conclusions

In this chapter an overview of the theory behind PLD and the effect of the different process parameters on the growing film was described. The problems with the formation of particulates with focus on the exfoliation from the target surface structure was explored with a description of previous methods of reducing the particulate density in the growing film. Finally, details of waveguide and laser theory were given. This chapter gives context to the experiments described in this thesis and the theoretical basis from which decisions about experimental directions were made.

2.6 References

Ang, L. K., Lau, Y. Y., Gilgenbach, R. M., Spindler, H. L., Lash, J. S. and Kovaleski, S. D. (1998) 'Surface instability of multipulse laser ablation on a metallic target', *Journal of Applied Physics,* 83(8), pp. 4466-4471.

Ashfold, M. N., Claeyssens, F., Fuge, G. M. and Henley, S. J. (2004) 'Pulsed laser ablation and deposition of thin films', *Chem Soc Rev,* 33(1), pp. 23-31.

Aziz, M. J. (2008) 'Film growth mechanisms in pulsed laser deposition', *Applied Physics A,* 93(3), pp. 579-587.

Bär, S., Huber, G., Gonzalo, J., Perea, A., Climent, A. and Paszti, F. (2003) 'Europium-doped sesquioxide thin films grown on sapphire by PLD', *Materials Science and Engineering: B,* 105(1-3), pp. 30-33.

Barrington, S. J., Bhutta, T., Shepherd, D. P. and Eason, R. W. (2000) 'The effect of particulate density on performance of Nd:$Gd_3Ga_5O_{12}$ waveguide lasers grown by pulsed laser deposition', *Optics Communications,* 185(1-3), pp. 145-152.

Chen, Y., Lu, T., Zhang, X., Vittoria, C. and Harris, V. G. (2006) 'A Flux Screening Technique for Growth of High-Quality Ferrite Films by Pulsed Laser Deposition', *IEEE Transactions on Magnetics,* 42(10), pp. 2888-2890.

Cheung, J. T. (1993) 'History and fundamental of pulsed laser deposition', *Pulsed laser deposition of thin films*.

Chiba, H., Murakami, K., Eryu, O., Shihoyama, K., Mochizuki, T. and Masuda, K. (1991) 'Laser excitation effects on laser ablated particles in fabrication of high T_c superconducting thin films', *Japanese journal of applied physics,* 30(4B), pp. L732.

Darby, M. S. B. (2009) *Femtosecond pulsed laser deposition.* PhD, University of Southampton.

Dupendant, H., Gavigan, J. P., Givord, D., Lienard, A. and Rebouillat, J. P. (1990) 'Velocity distribution of micron-size particles in thin film laser ablation deposition (LAD) of metals and oxide superconductors', *Beam Processing and Laser Chemistry,* 43(1), pp. 369-376.

Eason, R. W. e. (2007) *Pulsed Laser Deposition of Thin Films: Applications-Led Growth of Functional Materials.* John Wiley and Sons.

Fominski, V. Y., Grigoriev, S. N., Gnedovets, A. G. and Romanov, R. I. (2012) 'Pulsed laser deposition of composite Mo–Se–Ni–C coatings using standard and shadow mask configuration', *Surface and Coatings Technology,* 206(24), pp. 5046-5054.

Geohegan, D. B. (1994) *Diagnostic and characteristics of pulsed laser deposition laser plasmas from pulsed laser deposition of thin films.*: Wiley, New York, p. 115.

Gorbunoff, A. (2002) *Laser-assisted synthesis of nanostructured materials.*: VDI-Verlag, Duesseldorf.

Granasy, L., Pusztai, T., Borzsonyi, T., Warren, J. A. and Douglas, J. F. (2004) 'A general mechanism of polycrystalline growth', *Nat Mater,* 3(9), pp. 645-50.

Harilal, S. S., Farid, N., Freeman, J. R., Diwakar, P. K., LaHaye, N. L. and Hassanein, A. (2014) 'Background gas collisional effects on expanding fs and ns laser ablation plumes', *Applied Physics A,* 117(1), pp. 319-326.

Hino, T., Mustofa, S., Nishida, M. and Araki, T. (2003) 'Reduction of droplet of tantalum oxide using double slit in pulsed laser deposition', *Vacuum,* 70(1), pp. 47-52.

Kaiser, N. (2002) 'Review of the fundamentals of thin-film growth', *Applied Optics,* 41(16), pp. 3053-3060.

Kilburger, S., Chety, R., Millon, E., Di Bin, P., Di Bin, C., Boulle, A. and Guinebretière, R. (2007) 'Growth of $LiNbO_3$ thin films on sapphire by pulsed-laser deposition for electro-optic modulators', *Applied Surface Science,* 253(19), pp. 8263-8267.

Kim, S., Hirayama, M., Taminato, S. and Kanno, R. (2013) 'Epitaxial growth and lithium ion conductivity of lithium-oxide garnet for an all solid-state battery electrolyte', *Dalton Trans,* 42(36), pp. 13112-7.

Kostritskii, S. M. and Sevostyanov, O. G. (1997) 'Influence of intrinsic defects on light-induced changes in the refractive index of lithium niobate crystals.', *Applied physics B,* 65(4), pp. 527-533.

Kumar, N., Prasad, S., Misra, D. S., Venkataramani, N., Bohra, M. and Krishnan, R. (2008) 'The influence of substrate temperature and annealing on the properties of pulsed laser-deposited YIG films on fused quartz substrate', *Journal of Magnetism and Magnetic Materials,* 320(18), pp. 2233-2236.

Lenk, A., Schultrich, B., Witke, T. and Weiß, H. J. (1997) 'Energy and particle fluxes in PLD processes', *Applied Surface Science,* 109(1), pp. 419-423.

Li, J., Porter, L. and Yip, S. (1998) 'Atomistic modeling of finite-temperature properties of crystalline β-SiC: II. Thermal conductivity and effects of point defects', *Journal of Nuclear Materials,* 255(2), pp. 139-152.

Lippert, T., Zimmermann, F. and Wokaun, A. (1993) 'Surface analysis of excimer-laser-treated polyethylene-terephthalate by surface-enhanced Raman scattering and x-ray photoelectron spectroscopy. ', *Applied Spectroscopy,* 47(11), pp. 1931-1942.

Mackenzie, J. I. (2007) 'Dielectric Solid-State Planar Waveguide Lasers: A Review', *IEEE Journal of Selected Topics in Quantum Electronics,* 13(3), pp. 626-637.

May-Smith, T. C., Sloyan, K. A., Gazia, R. and Eason, R. W. (2011) 'Stress Engineering and Optimization of Thick Garnet Crystal Films Grown by Pulsed Laser Deposition', *Crystal Growth & Design,* 11(4), pp. 1098-1108.

Murray, M., Jose, G., Richards, B. and Jha, A. (2013) 'Femtosecond pulsed laser deposition of silicon thin films', *Nanoscale research letters,* 8(2), pp. 1-6.

Ohring, M. (2001) *Materials science of thin films.* . Elsevier.

Ojeda, G. P. A., Schneider, C. W., Döbeli, M., Lippert, T. and Wokaun, A. (2015) 'The flip-over effect in pulsed laser deposition: Is it relevant at high background gas pressures?', *Applied Surface Science,* 357, pp. 2055-2062.

Perrière, J., Millon, E., Seiler, W., Boulmer-Leborgne, C., Craciun, V., Albert, O., Loulergue, J. C. and Etchepare, J. (2002) 'Comparison between ZnO films grown by femtosecond and nanosecond laser ablation', *Journal of Applied Physics,* 91(2), pp. 690-696.

Shepherd, D. P., Hettrick, S. J., Li, C., Mackenzie, J. I., Beach, R. J., Mitchell, S. C. and Meissner, H. E. (2001) 'High-power planar dielectric waveguide lasers.', *Journal of Physics D: Applied Physics*, 34(16), pp. 2420-2425.

Sloyan, K. A. (2012) *Multi-beam pulsed laser deposition for engineered crystal films.* PhD, University of Southampton.

Snyder, A. W. and Love, J. (2012) *Optical waveguide theory.* Springer Science & Business Media.

Strikovsky, M. D., Klyuenkov, E. B., Gaponov, S. V., Schubert, J. and Copetti, C. A. (1993) 'Crossed fluxes technique for pulsed laser deposition of smooth $YBa_2Cu_3O_{7-x}$ films and multilayers', *Applied Physics Letters,* 63(8), pp. 1146-1148.

Sun, X. W., Huang, H. C. and Kwok, H. S. (1996) 'On the initial growth of indium tin oxide on glass', *Applied Physics Letters,* 68(19), pp. 2663-2665.

Szörényi, T., Hopp, B. and Geretovszky, Z. (2004) 'A novel PLD configuration for deposition of films of improved quality: a case study of carbon nitride', *Applied Physics A,* 79(4-6), pp. 1207-1209.

Tan, T. Y., Gösele, U. and Yu, S. (1991) 'Point defects, diffusion mechanisms, and superlattice disordering in gallium arsenide-based materials.', *Critical Reviews in Solid State and Material Sciences*, 17(1), pp. 47-106.

Venables, J. A. and Spiller, G. D. T. (1983) 'Nucleation and Growth of Thin Films', *Binh V.T. (eds) Surface Mobilities on Solid Materials*: Springer, Boston, MA.

Willmott, P. R. and Huber, J. R. (2000) 'Pulsed laser vaporization and deposition', *Reviews of Modern Physics,* 72(1), pp. 315-325.

Zhigilei, L. V., Kodali, P. B. and Garrison, B. J. (1997) 'Molecular dynamics model for laser ablation and desorption of organic solids', *The Journal of Physical Chemistry B,* 101(11), pp. 2028-2037.

Chapter 3 Background

3.1 Introduction

This chapter introduces the materials of interest in this thesis. It aims to provide context and the motivations for the experiments described in the results chapters. The state-of-the-art in PLD is presented for each material and competing deposition techniques described and compared to PLD.

3.2 Materials

In the following sections, the materials utilised in this project is described and put into context with PLD and/or other growth methods. This begins with trivalent rare-earth (RE) dopants and then details the host materials and the effect of doping on the host materials.

3.2.1 Rare-earth dopants

RE-doped laser crystals, ceramics and glasses are a huge commercial success and used in high-power laser and amplifier systems in industry and research marketplaces.

The RE elements include all the lanthanides excluding promethium (which is radioactive) but including scandium and yttrium. The RE ions used for doping are nearly always trivalent (having had three electrons removed), however divalent RE doping has been used in cryogenic operation (Bachmann *et al.*, 2006). The RE-ions generally replace other ions of similar size, for example in Yb:YAG (Yb-doped yttrium aluminium garnet), the ytterbium will replace the yttrium.

The electronic transitions in trivalent RE-ions will occur in the 4f shell, which is shielded by the optically passive outer 6s shell. This mitigates the influence of the host lattice on the bandwidths, wavelengths and cross-sections of the optical transitions. The most frequently used RE ions for laser active materials and their commonly used host material is seen in Table 3.1. Other RE ions, such as yttrium and gadolinium are not commonly used for laser media, but can be used as a co-dopant, for example to quench certain energy levels.

Table 3.1. List of trivalent RE-dopants and their corresponding commonly used host media and important emission wavelengths (Weber, 2018) (Kalisky, 2004)

RE ion (trivalent)	Host media	Emission wavelengths (µm)
Ytterbium	YAG, tungstates, silica	1.0-1.1
Neodymium	YAG, silica, fluorides	1.03-1.1, 0.9-0.95, 1.32-1.35
Erbium	YAG, silica	1.5-1.6, 2.7, 0.55
Holmium	YAG, fluorides, silica	2.1, 2.8-2.9
Cerium	fluorides	0.28-0.33
Thulium	YAG, silica, glasses	1.7-2.1, 1.45-1.53, 0.48, 0.8
Praseodymium	Silica, glasses	1.3, 0.635, 0.6, 0.52, 0.49

RE-doped gain media all operate on pump and laser transitions that are dubbed “weakly allowed transitions”. For this reason, the upper-state lifetimes can be long, reaching milliseconds. This allows large amounts of energy to be stored, making high-energy pulse generation with Q-switching a possibility.

In this thesis, the main RE-ions used are ytterbium, erbium and neodymium. Therefore, the following three sections will focus on these and describe their relative optical characteristics and the benefits/drawbacks this brings.

3.2.1.1 Trivalent ytterbium (Yb^{3+})

Ytterbium is a commonly used dopant material and brings with it a wide range of benefits. The energy level diagram of Yb^{3+} is presented in Figure 3.1 (DeLoach *et al.*, 1993) and the pump and laser transitions for Yb:YAG are labelled. Here, a simple electronic level structure with one excited state manifold and a ground-state manifold is shown. The quantum defect, defined as the difference between the pump wavelength and the lasing wavelength, for ytterbium is particularly small compared to other RE ions. This will allow for high power efficiencies and reduces thermal effects which arise from phonon scattering to the upper laser level. Having a simple electronic structure also prevents excited state absorption and other quenching effects related to other energy manifolds. The gain bandwidth is relatively large, compared to neodymium, allowing a greater degree of wavelength tuning and the generation of ultra-short pulse lasers. The upper-state lifetime of Yb^{3+} is on the order of ms, which is ideal for Q-switching lasers (Fan *et al.*, 1993).

However, issues do arise from having such a small quantum defect, such as the pump and laser wavelength being similar. This means it is difficult to obtain a dichroic mirror that has high reflectivity at the lasing wavelength and low reflectivity at the pump wavelength. It also creates substantial quasi-four-level behaviour, where the lower laser level has some inherent population at room temperature, making population inversion more difficult and hence requires high-pump intensities and has a high lasing threshold (Lacovara *et al.*, 1991).

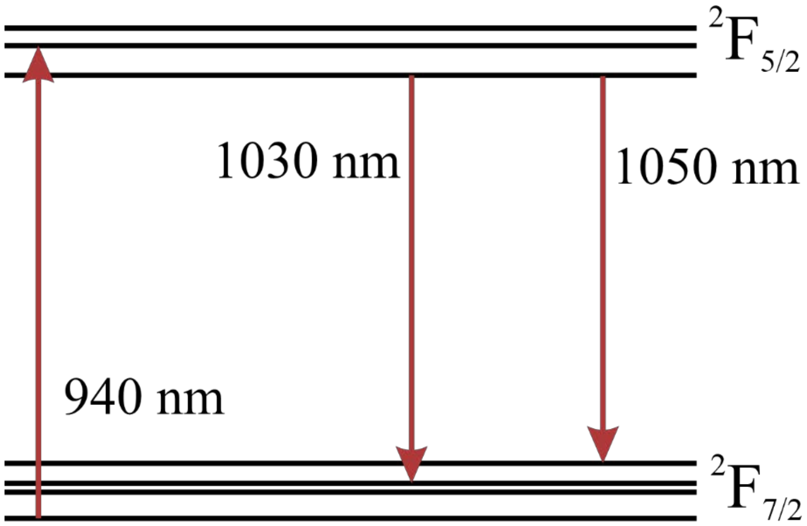

Figure 3.1. Energy levels and usual pump and laser transitions with the corresponding wavelengths for Yb^{3+} doped YAG (DeLoach *et al.*, 1993).

3.2.1.2 Trivalent erbium (Er^{3+})

Er^{3+} is a common dopant ion with various possible emission wavelengths. It is widely used in erbium-doped fibre amplifiers that enable long-range optical fibre communication by amplifying light with a wavelength of ~1500 nm. An energy level diagram with some common transitions is shown in Figure 3.2 (Zharikov *et al.*, 1975). The absorption cross section of the transition from $^4I_{15/2}$ to $^4I_{11/2}$ is low, meaning efficient pump absorption is difficult. This has led to research into co-doped materials with ytterbium and erbium. The ytterbium ions efficiently absorb at a wavelength of ~980 nm and will transfer the absorbed energy to the erbium ions transitioning the ions to the $^4I_{11/2}$ state. The lifetime of this level is on the order of μs so the erbium ions are quickly transferred to the $^4I_{13/2}$ level, suppressing energy transfer back to the ytterbium. From here, lasing can be realised from the $^4I_{13/2}$ to $^4I_{15/2}$ (Fermann *et al.*, 1988).

High-dopant concentrations can cause various energy transfer processes. An example of this is cooperative upconversion, where one erbium ion in $^4I_{13/2}$ transfers energy to a second ion in the same level. The consequence of this is one ion in $^4I_{11/2}$ and one in the ground state. Cooperative upconversion cannot occur in ytterbium due to no available state in the upper energy bands.

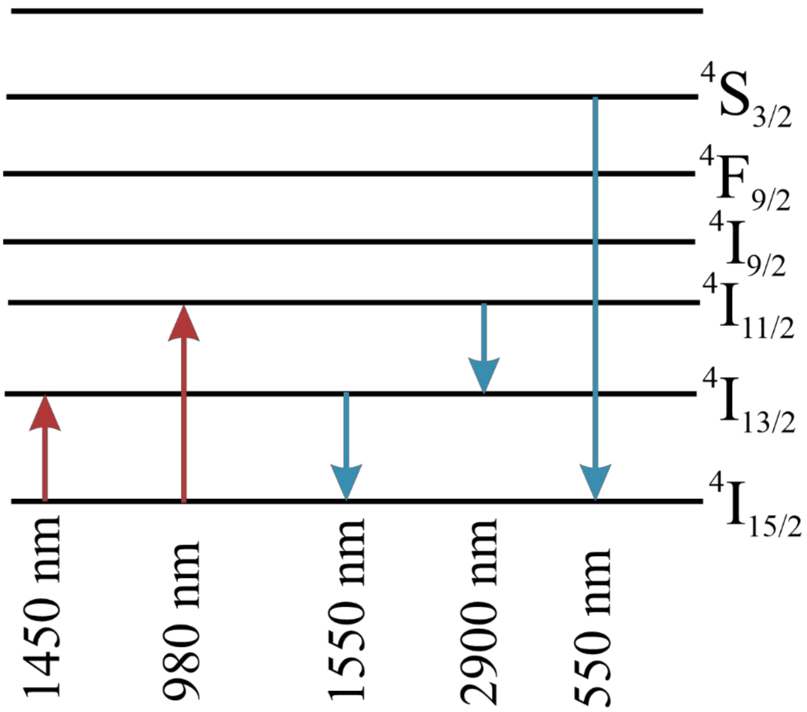

Figure 3.2. Energy levels of a trivalent erbium ion with some common optical transitions labelled with values which will vary depending on the host material.

3.2.1.3 Trivalent neodymium (Nd^{3+})

Nd^{3+} is a common RE-dopant for applications in high-power and Q-switched lasers. The energy diagram and optical absorption and emission for different transitions in Nd:YAG is presented in Figure 3.3 (Kück *et al.*, 1998). The strongest lasing transition is 1064 nm but other lasing wavelengths are possible with appropriate suppression of 1064 nm. The upper state lifetime is longer than the lower state lifetimes, meaning there is generally a negligible population in the terminal level, consequently three of the four transitions are described as a purely four level gain medium. The 946 nm lasing transition instead exhibits quasi-four level laser behaviour. This puts neodymium in contrast to ytterbium-doped gain media which will only operate as a quasi-four level laser, and consequently have a higher lasing threshold. However, ytterbium can be added with higher concentrations without other parasitic effects and has a higher upper state lifetime allowing for more efficient power scaling and Q-switching.

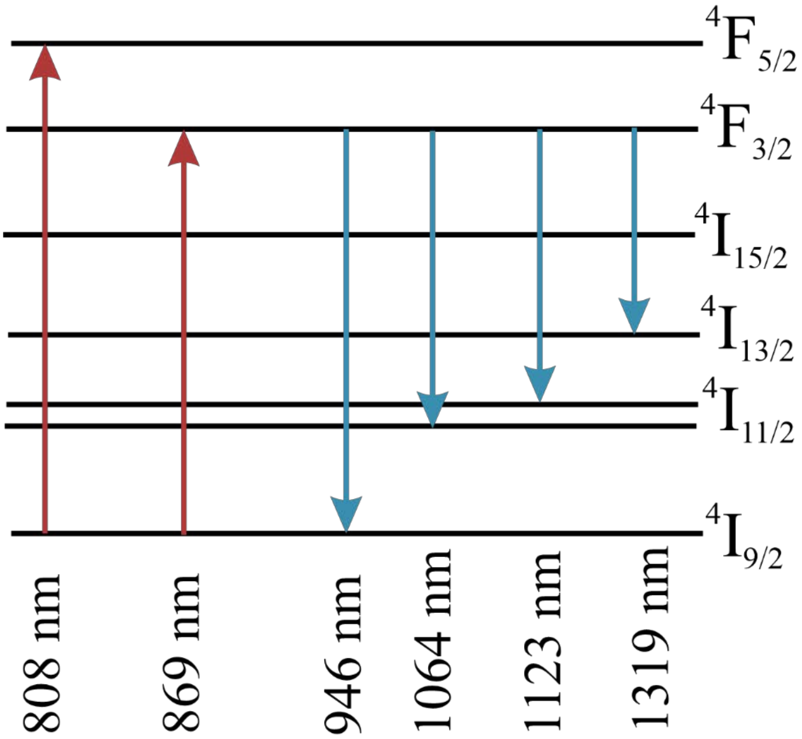

Figure 3.3. The energy levels of Nd^{3+} and optical emission wavelengths of Nd:YAG

3.2.2 Host material choices

3.2.2.1 Garnets

Garnets are commonly used solid state laser hosts, due to their advantageous physical and optical properties, being chemically inert, mechanically hard and having a high thermal conductivity (Kalisky, 2004). They also have a wide optical transparency covering a broad range of pump and emission wavelengths. Their generic composition is $A_3B_2C_3O_{12}$ arranged in a cubic lattice, although B and C are often the same element making $A_3B_5O_{12}$. Garnets have the same crystal structure as well as a wide range of refractive indices (n_{YAG} =1.82 and n_{YIG} = 2.2 at 1060 nm (Weber, 2018)) making them ideal for multilayer films, such as crystal mirrors.

In 1991, the first garnet growth via PLD was achieved (Kidoh *et al.*, 1991) and subsequently a wide range of garnets suited for various applications have been deposited by PLD. A selection of successfully grown garnets is displayed in Table 3.2.

Table 3.2. Examples of PLD-grown garnets

Material	Formula	Example Application	Reference
YAG	$Y_3Al_3O_{12}$	Laser waveguides	(Beecher *et al.*, 2017)
YbAG	$Yb_3Al_3O_{12}$	Laser waveguides	(Gün *et al.*, 2008b)
LGG	$La_3Ga_3O_{12}$	Magneto-optic devices	(Khartsev and Grishin, 2005)
BIG	$Bi_3Fe_5O_{12}$	Magneto-optic devices	(Khartsev and Grishin, 2005)
LLZO	$Li_3La_3Zr_2O_{12}$	Solid state batteries	(Kim *et al.*, 2013)
YGG	$Y_3Ga_3O_{12}$	Laser waveguides	(Beecher *et al.*, 2017)
YIG	$Y_3Fe_3O_{12}$	Magneto-optic devices	(Sposito *et al.*, 2013)
GGG	$Gd_3Ga_3O_{12}$	Q-switch laser	(Vainos *et al.*, 1998)

3.2.2.2 RE-doped garnets grown via PLD

YAG (yttrium aluminium garnet) is a commonly used host material particularly for high-power and Q-switched lasers. It has been shown to lase with a range of RE ions and is commonly used as a high-power laser with neodymium doping.

In the previous section, a selection of garnet films grown via PLD was presented. PLD has grown various RE-doped garnets and demonstrated lasing with the materials shown in Table 3.3. All the results shown in Table 3.3 could be improved with further growth optimisation.

Table 3.3. Re-doped garnets grown via PLD and their lasing output powers and efficiencies

Materials	Output Power	Lasing Efficiency	Reference
Yb:YAG	21 W	70%	(Kurilchik *et al.*, 2018)
Yb:GGG	1.8 W	11%	(Beecher *et al.*, 2017)
Yb:YGG	1.2 W	15%	(Beecher *et al.*, 2017)
Nd:GGG	14 mW	17.5%	(Grivas *et al.*, 2004)

In this thesis, Yb:YAG is explored further with the aim of reducing the particulate density and consequently reducing the propagation loss in Yb:YAG planar waveguides. Ialso experiment with Yb:LuAG (lutetium aluminium garnet), an alternative to Yb:YAG. Yb:LuAG has similar optical properties to Yb:YAG, meaning current Yb:YAG systems could incorporate Yb:LuAG without significant alteration (Beil *et al.*, 2010). When Yb:YAG is highly doped (10%), its thermal conductivity reduces from ~10 W/mK to 6 W/mK, which is in contrast to Yb:LuAG, where the thermal conductivity is lowered by 0.3 W/mK (7.7 W/mK to 7.4 W/mK) (Beil *et al.*, 2010). Having a high thermal conductivity allows for more efficient cooling of the laser crystal, meaning scaling to higher powers can be realised. LuAG also has a smaller lattice constant than YAG (11.91 Å for LuAG and 12.00 Å for YAG (Euler and Bruce, 1965)), which results in narrower linewidths, higher absorption and higher emission bandwidths.

The final garnet that will be explored is YGG. This garnet, when doped with Er^{3+}, has favourable spectroscopic characteristics for the detection of carbon dioxide and methane. This is of interest for understanding the dynamics and distribution of greenhouse gases in the earth’s atmosphere (Mackenzie *et al.*, 2017). The lattice constant mismatch of YGG and YAG is 2.2%, which is low enough for YGG to be grown onto YAG substrates.

3.2.2.3 Sesquioxides

Sesquioxides are simple, binary oxides with the chemical formula of A_2O_3 where A can be one or a mixture of elements and O is oxygen. In their crystalline form, these materials are mechanically strong, have low thermal expansion, high thermal conductivity and a wide transparency range. Cubic rare earth sesquioxides are generally formed by Lu, Er, Y and Sc, the smallest of the rare earth elements. Ho and Sm can also be found in cubic form under certain growth conditions (Zinkevich, 2007). However, aside from Lu^{3+}, Y^{3+} and Sc^{3+}, all other RE^{3+} are optically active. Attempts have been made to use gadolinium as a sesquioxide laser host since UV light is required for optical excitation. However, the cubic phase of Gd_2O_3 is thermodynamically unstable, making high quality growth difficult (Druon *et al.*, 2013). In this section, only RE sesquioxides are introduced, with sapphire (Al_2O_3) introduced in section 3.2.2.5.

All RE sesquioxides in this thesis are cubic bixbyite and have lattice constants of ~10 Å (Pauling and Shappell, 1930). The RE cation densities are around twice as high as YAG, meaning a 1% doping in a sesquioxide crystal approximately corresponds to a 2% doping in a YAG crystal. The melting point of RE sesquioxides exceeds 2400 ^{o}C, meaning in Czochralski-growth it is difficult to maintain stable thermal gradients that are required for high quality single-crystal growth (Fornasiero *et al.*, 1999). PLD however, does not require temperatures exceeding the melting point, making it a suitable growth technique for RE sesquioxides.

In general, it is possible to dope in high concentrations all RE sesquioxides with RE ions. The crystal field in these materials is stronger compared to, for example, RE:YAG, leading to longer emission wavelengths and broader emission bandwidths (Krankel, 2015). The broad emission bandwidths make these materials suitable for ultra-short pulse lasers. The thermal conductivity of these materials when doped with RE ions is not as adversely affected as RE-doped YAG, with $Yb:Lu_2O_3$ being the exemplar instance. This is due to Yb and Lu being very similar sizes, meaning doping of up to 100% is possible without significant degradation of the thermal conductivity (Gaumé *et al.*, 2003). The emission wavelength, bandwidth and the thermal conductivity of 1% Yb-doped YAG and sesquioxides is displayed in Table 3.4.

Table 3.4. Optical emission and thermal conductivity values of 1% Yb-doped sesquioxides and YAG (Klopp *et al.*, 2004; Peters *et al.*, 2009)

Property	**YAG**	**Y_2O3**	**Sc_2O_3**	**Lu_2O_3**	**$LuScO_3$**
Emission wavelength (nm)	1030	1031	1041	1032	1038
Emission bandwidth (nm)	8.5	14.5	11.6	13	22
Thermal Conductivity (W/mK)	11	13.6	12.5	16.5	4

Mixed sesquioxides have also been used to realise even broader emission bandwidths of ~22 nm (Peters *et al.,* 2009), presenting the opportunity for mode-locked lasers. The wide bandwidths in mixed sesquioxides are due to the Yb^{3+} being sited in different positions in the lattice, creating distortion with respect to the other cations. However, as presented in Table 3.4, the thermal conductivity is reduced from >10 W/mK to 4 W/mK, making power scaling difficult.

Lasing has been demonstrated in RE-doped sesquioxides, with focus being placed on the research of sesquioxide based thin-disc lasers. Yb^{3+}-doped lutetia and scandia have both reached in excess of 100 W of output power with optical-to-optical efficiencies reaching 85% (Peters *et al.*, 2011). Scattering effects in Yb-doped Y_2O_3 due to bulk fabrication issues have hampered efforts for lasing with this material in the thin-disc lasing architecture (Krankel, 2015).

These results show great promise for the utilisation of sesquioxides as a laser host and illustrate the research space for PLD as the growth mechanism.

3.2.2.4 Sesquioxides grown via PLD

The PLD technique can grow high-melting point materials without having to heat bulk material to such a high temperature. Consequently, PLD is a good candidate for the growth of high-quality sesquioxides. Various RE sesquioxides have been grown via PLD with a selection shown in Table 3.5. This shows the host and dopant material separately.

The first lasing of a sesquioxide grown by PLD was demonstrated with Yb^{3+} :$(Gd,Lu)_2O_3$ by (Kühn *et al.*, 2009) in a rib waveguide. Since then, lasing has been observed in Tm:Y_2O_3 (Szela *et al.*, 2013), Yb:Y_2O_3 (Beecher *et al.*, 2014) and Yb:Lu_2O_3 (Parsonage *et al.*, 2015), with the maximum slope efficiency being 38%. These results show the promise of PLD as a growth technique for RE-doped sesquioxides. However, more research to optimise for single-crystal, defect free growths is needed for higher output powers and efficiencies.

Table 3.5. List of sesquioxides grown via PLD and the respective dopant materials.

Host Material	**Dopant Material**	**References**
Lu_2O_3	Yb, Eu	(Parsonage *et al.*, 2015; Bär *et al.*, 2003)
Sc_2O_3	Eu, Er	(Bär *et al.*, 2003; Gün *et al.*, 2007)
Y_2O_3	Yb, Tm, Eu, Nd	(Szela *et al.*, 2013; Beecher *et al.*, 2014; Bär *et al.*, 2003; Burmester *et al.*, 2005)
$(Gd,Lu)_2O_3$	Yb, Nd	(Kühn *et al.*, 2009) (Gün *et al.*, 2008a)
Gd_2O_3	Eu	(Smith *et al.*, 2010)

3.2.2.5 Sapphire

Although corundum is a sesquioxide, it will be dealt with separately due to its importance later in this thesis. Sapphire is the alpha-phase of alumina (α-Al_2O_3) with 7 other commonly described phases. Alpha-alumina is the only thermodynamically stable phase, if the temperature passes 1100 ^oC no other phase can exist at atmospheric pressure (Łodziana and Parliński, 2003). An example of another phase is the κ-phase, which has a coexisting octahedral and tetrahedral lattice (Ollivier *et al.*, 1997) and is stable up to 970 ^oC (Brindley and Choe, 1961).

Sapphire has a hexagonal lattice and displays high thermal conductivity, moderate thermal expansion, high mechanical strength and wide transparency range. For these reasons it is considered to be an excellent laser host, and has found commercial success in the Ti:sapphire laser. In this thesis, all sapphire substrates used were c-cut (Figure 3.4).

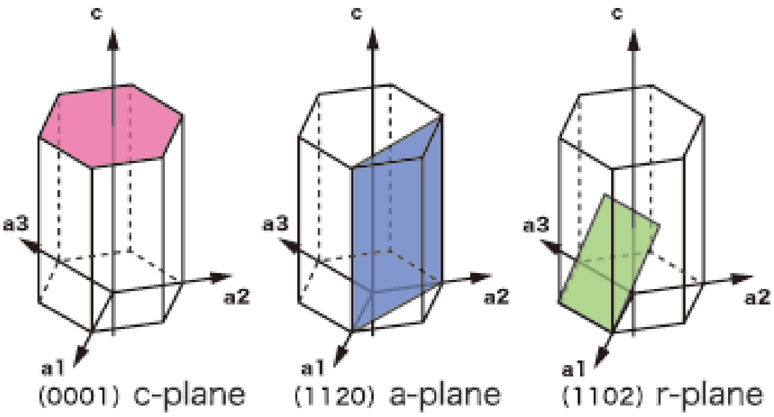

Figure 3.4. Diagram of the key planes in the hexagonal crystal lattice of sapphire. Taken from www.ad-na.com.

3.2.2.6 PLD-grown sapphire

Titanium-doped sapphire found in commercial laser systems will generally have a low dopant concentration of <0.15% (Mak *et al.*, 1994). This is because the titanium ion is much larger than the aluminium ions, therefore if grown from a melt, the titanium will segregate, degrading the crystal quality (Roth *et al.*, 2009). For the same reason, RE ions have not been incorporated into the sapphire lattice using a melt growth process. Ytterbium, for example, is almost twice the radius of aluminium (1.0 Å compared to 0.53 Å respectively) (Dobrovinskaya *et al.*, 2009; Waeselmann *et al.*, 2016). However, PLD does not rely on thermodynamic equilibrium growth processes (Heinrich *et al.*, 2012), and can therefore incorporate higher dopant concentrations than traditional methods.

Initial PLD-grown sapphire was doped with titanium and first grown by (Anderson *et al.*, 1997). Lasing was then achieved in a planar waveguide architecture with 350 mW of output power with a 26 % slope efficiency (Vainos *et al.*, 1998). Subsequently, lasing of PLD-grown Ti:sapphire was also demonstrated in a rib waveguide (Grivas *et al.*, 2005). RE-doped sapphire growth has been demonstrated with neodymium (Waeselmann *et al.*, 2016), ytterbium (Heinrich *et al.*, 2012) and erbium (Serna and Afonso, 1996). The only lasing result to date has been demonstrated with Nd:sapphire in planar and rib waveguide architectures. As a planar waveguide, 137 mW of output power was demonstrated with 7.5% slope efficiency (Waeselmann *et al.*, 2016) and with a rib waveguide, 322 mW of output power and 12% slope efficiency (Waeselmann *et al.*, 2017). These results were achieved with relatively thin samples (2 µm) that limits the achievable coupling efficiency due to the mismatch between waveguide and free space numerical aperture.

These results show the promise of PLD-grown RE-doped sapphire, but also have room for improvement. The demonstration of thick-film RE-doped sapphire would be a major milestone and to do this, the crystal quality needs to be greatly improved.

3.3 Structures of interest

3.3.1 Planar waveguides

A planar waveguide consists of a layer of material sandwiched between two layers of material with a lower refractive index (Figure 3.5). The material, and hence the refractive index, of the outer layers do not necessarily need to be the same, and one of the layers can be air. The width of a planar waveguide is much larger than the thickness, meaning the light is confined in one dimension via total internal reflection. The core can be doped with an active material creating a lasing device. Heat generated by this process can be removed through the outer layers, where there is a large surface area to volume ratio, making this process more efficient than bulk lasers. Consequently, planar waveguides do not suffer as greatly from thermal lensing effects.

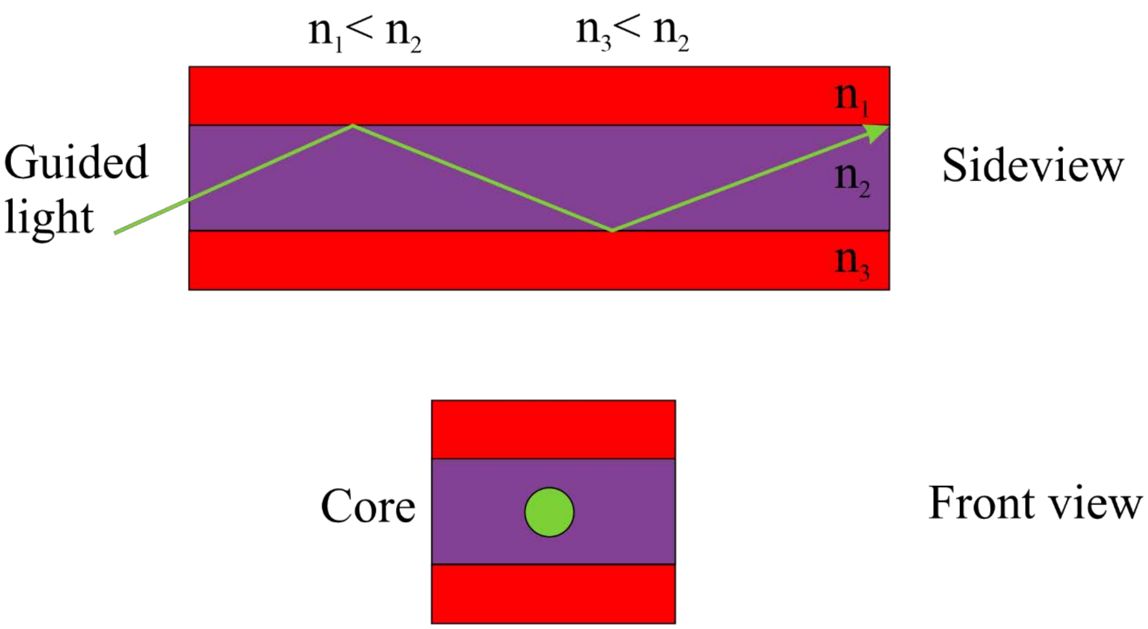

Figure 3.5. Diagram of a typical planar waveguide structure

Due to their compact size and guided wave geometry, the overlap between pump and lasing beams is very good, meaning high efficiencies can be realised. However, coupling efficiently into a thin planar waveguide (10 µm thick) can be difficult with diode stacks and bars. For example, if the minimum pump beam diameter is larger than the waveguide thickness only a fraction of pump power will be coupled into the core. This can be avoided by simply having thicker waveguides, which can in turn lead to multi-mode operation. A technique that increases coupling efficiency while having single mode operation is to have cladding layers of smaller, but similar refractive index to the core. This allows for pump coupling and guiding in the clad waveguide but absorption only in the core. Single mode output depends on the ratio of thickness between the core and the cladding layers (Bhutta *et al.*, 2002). Single-mode operation can be realised with this architecture assuming index contrast between the cladding layers and capping layers is significantly higher than the contrast between the cladding and core.

Planar waveguides can be fabricated with numerous different techniques and will be further discussed in section 3.4. PLD, as discussed in previous sections (3.2.2.2, 3.2.2.4, 3.2.2.6) has been used to grow planar waveguides and successfully demonstrated as the gain element of lasers.

3.3.2 Channel waveguides

In contrast to planar waveguides which confine light in one dimension, channel waveguides confine light in two dimensions. Structurally, channel waveguides are strips of material either free standing on a substrate or buried within it. Confining the light in two dimensions allows for greater cooling efficiency, with a larger surface area to volume ratio than planar waveguides. However, having surfaces in two directions increases the importance of flat, non-scattering surfaces with channel waveguides being prone to scattering losses from the interfaces.

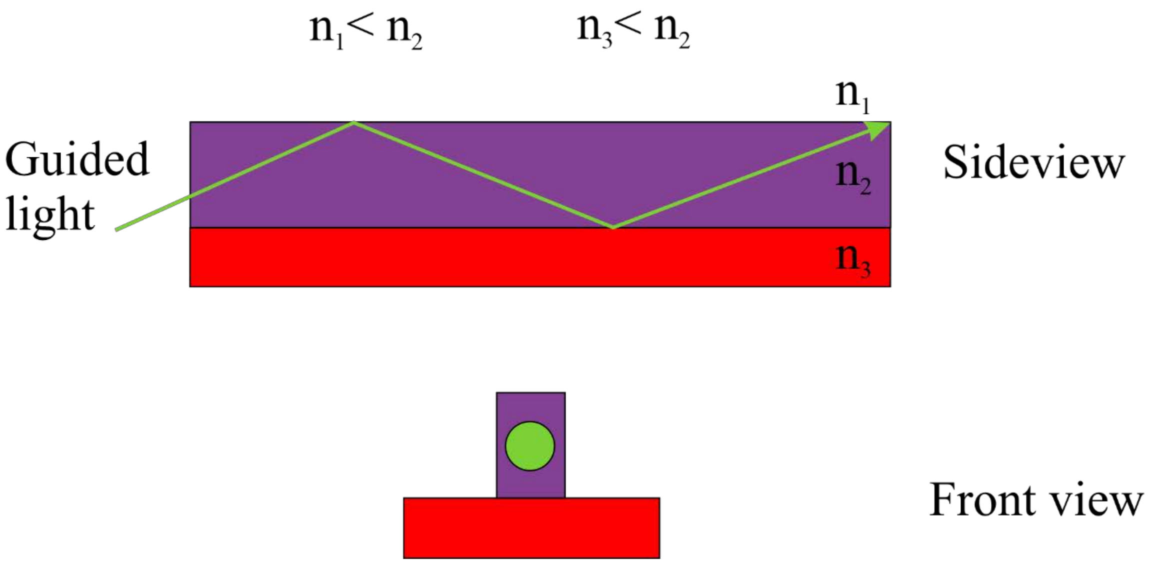

Figure 3.6. Diagram of a typical ridge channel waveguide structure.

Channel waveguides can be fabricated through various approaches. Bulk material may have channels fabricated in them by altering the refractive index. This can be achieved via indiffusion (Cantelar *et al.*, 2003), ion beam implantion (Chen, 2008), laser writing (Zoubir *et al.*, 2004), reactive ion etching (Crunteanu *et al.*, 2002) and ion exchange (Johansson *et al.*, 1992). It is also possible to dice channels into a material using a diamond dicing saw. This method has been shown to produce optical quality facets with minimal scattering losses from the edges of the channel (Loiko *et al.*, 2018).

PLD-grown materials have been subsequently processed to produce channel waveguides. Lasing has been demonstrated in Nd:GGG (Gottmann *et al.*, 2007), Ti:Al_2O_3 (Grivas *et al.*, 2005) and Nd:Al_2O_3 (Waeselmann *et al.*, 2017). The output powers have been confined to mW (with the maximum of 322 mW from Nd:Al_2O_3) due to poor film quality and lossy channel fabrication, with scattering from interfaces of the channel. Nevertheless, PLD is a quick and simple deposition technique for the base material of channel waveguides and can grow structures with a high numerical aperture. With further improvements in crystal quality and channel fabrication the potential output powers for PLD-grown channel waveguides will be increased.

3.4 Candidate deposition techniques for waveguide coatings

In this series of subsections, alternative film deposition techniques for waveguide applications and their relative advantages and disadvantages compared to PLD will be discussed, putting PLD into context with current state-of-the-art methods.

3.4.1 Flame hydrolysis deposition

In this technique, a substrate has a hydrogen-oxygen flame pointed towards it. Precursors are put into the flame where they react, forming particulates that are subsequently deposited onto the substrate. The substrate is then annealed creating films of glass. The growth rate for flame hydrolysis deposition can be up to 10 µm/hr (Ruano *et al.*, 2000) and dopants can be incorporated into the material to tune the refractive index, melting point or photosensitivity. Generally, this technique is used for the growth of silica onto silicon, and loss values of 0.01 dB/cm have been achieved using this method (Kominato *et al.*, 1990). However, the choice of materials is limited by the chemical reactions needed for this technique, meaning materials such as garnets and sesquioxides cannot be grown with this technique and the materials that are grown are not crystalline.

3.4.2 Molecular beam epitaxy

Molecular beam epitaxy (MBE) takes place in a high vacuum where materials are held in separate cells. These cells are heated until they sublime (transition directly from a solid phase to a gaseous phase) and the cells can be opened simultaneously or consecutively. This means MBE has control over the stoichiometry and can easily create complex structures with precise control over the thickness of layers. The substrate can be heated to aid in the growth of crystalline films with typical growth rates of 1 µm/hr (Capper *et al.*, 2017). MBE, like PLD, is not a thermal equilibrium growth and therefore can grow materials not possible through traditional methods. The first demonstration of RE-doped sapphire was fabricated via MBE (Kumaran *et al.*, 2009), however MBE is typically used to grow semiconductor materials. The slow growth rates coupled with an expensive setup means high-volume production using the MBE technique is difficult.

3.4.3 Chemical vapour deposition

The chemical vapour deposition (CVD) technique has many variants. The fundamentals of CVD involve the use of precursor gases that are passed along a vacuum chamber and past a substrate. The gases contain diluted material to be deposited as a film. As the gases pass, they react with the substrate, causing deposition and some by-product gases. The precursor and by-product gases can be toxic, increasing the risk and environmental impact of this technique. The stoichiometry of the material deposited depends directly on the temperature of the substrate.

The most common forms of CVD are metalorganic (MOCVD), laser assisted (LACVD) and plasma enhanced (PECVD). MOCVD an organic precursor with the metal embedded, allowing deposition of complex stoichiometries (Bai *et al.*, 1994). LACVD uses a laser to provide extra energy at certain points on the substrate, accelerating the reactions and hence increasing the deposition rate. PECVD introduces a precursor in a plasma state, which can change the reaction dynamics, increasing the deposition rate.

CVD can be used to grow garnet crystals, with garnet type solid electrolytes commonly grown for solid-state batteries (Loho *et al.*, 2016). Examples of single-crystal YIG (Okada *et al.*, 1991) and YAG (Bai *et al.*, 1994) have also been demonstrated. However, CVD of garnets generally suffers with low growth rates of around 0.5 µm/hr. This growth rate can be increased with the use of, for example, LACVD but even this doesn’t reach the speeds that PLD can produce. CVD also has the disadvantage of only being able to grow materials with a suitable precursor.

3.4.4 Sputtering

Sputtering is a vacuum technique where ions are accelerated by an electric field and hit a target of the desired material. The high energy ions, usually Ar^+, cause material to be ejected from the target and deposited as a thin film onto a substrate. In sputtering, the material ejected from the target is widely distributed meaning that large area depositions are possible but with the drawback of slow growth rates (~1 µm/hr). Efforts have been made to increase this with magnetron sputtering (~3.5 µm/hr) (Hanby *et al.*, 2018) and can be significantly increased with multiple targets and substrates at close proximity to the targets. Growth of crystalline films can be formed by heating the substrate however, post-annealing can also achieve crystallinity. In general, sputtering is suited to simple stoichiometries such as metals and binary oxides, but attempts have been made to grow YAG (Deng *et al.*, 2005) and YIG (Cuomo *et al.*, 1972) using multi-target sputtering systems. These films were polycrystalline after annealing and had stoichiometry variations across the film, however, there is potential to avoid these stoichiometry variations by using composite targets.

3.4.5 Cathodic arc physical vapour deposition

In this technique, an electric arc is formed at the surface of a target of desired material. This causes extreme local heating and vaporises the targets surface, causing a plume of high energy ions to be ejected and deposit onto a substrate. This technique is used for the growth of hard, high-melting point materials such as diamond-like materials. The main disadvantage of this technique is the formation of macro-particles that will embed in the growing film (Mubarak *et al.*, 2005). The extremely high energies of the ions reaching the substrate can cause surface etching, causing excess stress on the substrate, however, this can be avoided by increasing the distance between the substrate and target.

3.4.6 Thermal evaporation

Thermal evaporation is a basic vacuum technique in which a substrate is placed above a crucible filled with the desired material. This material is then heated, forming a low-energy vapour which deposits onto the substrate. This technique is suited to materials with a low boiling point and high vapour pressures. Generally, it is only used for simple metals since the stoichiometry of multi-component materials is difficult to control. The growth rate is slow with typical growth rates of 100 nm/hr (Abegunde *et al.*, 2019) however, large areas can be covered with this technique. To date, crystalline waveguides have not been grown using this technique.

3.4.7 Electron-beam physical vapour deposition

Electron-beam physical vapour deposition (EBPVD) is similar to thermal evaporation, however instead of conventional heating of a target material, the material is bombarded with a beam of electrons, causing atoms to transform into a gaseous state. The target is usually in the form of an ingot or a rod. These gaseous atoms will then deposit onto a substrate forming a film of material. EBPVD is predominantly used to create thermal barrier coatings for applications in, for example, jet engines. The deposition rate can be rapid, ranging from 0.1 µm-100 µm, however, single-crystalline growth can be difficult with EBPVD, with research focussing more on metals and ceramics (Singh and Wolfe, 2005).

3.4.8 Liquid phase epitaxy

Liquid phase epitaxy (LPE) is a crystal growth technique that can result in high crystal qualities and fast growth rates (typical growth rates of 60 µm/hr (Lu *et al.*, 2019)). In this technique, a material is dissolved into a liquid melt and the substrate is dipped in the solution and cooled. The material then condenses onto the substrate and forms a film. Once perfected, LPE offers good control over the stoichiometry and fast growth rates. However, LPE can be time-consuming to find the correct growth parameters, and, unlike PLD, materials are limited to those with suitable solvents and these solvents can be corrosive and therefore difficult to handle and dispose of. There are also problems controlling the orientation of the grown crystal and difficulties with dopant homogeneity which is crucial for lasing applications.

The growth of active materials using garnet crystals with LPE epitaxy is well established. Nd:YAG has been grown by LPE (Pelenc *et al.*, 1991) and lasing realised (Bonner *et al.*, 1998). Yb:YAG has also been grown for thin-disc applications (Ubizskii *et al.*, 2004).

3.5 Alternative waveguide fabrication techniques

The fabrication of channel waveguides was briefly discussed in section 3.3.2, in the following sections, direct bonding is discussed as an alternative planar waveguide fabrication technique, and precision dicing is explored in more detail for the fabrication of channel waveguides.

3.5.1 Direct bonding

Direct bonding involves polishing two bulk pieces of material to a near-atomically flat finish. These materials can be bought together and, if free of any surface contaminants (e.g. dust or grease), will bond via Van der Waals forces. Post-annealing can strengthen the bond between the two materials, preventing delamination, assuming the two materials have similar thermal expansion coefficients. Direct bonding of thin materials can be difficult and is prone to cracking of the sample, so in general, thicker materials are bonded and polished back. This technique does not require similar lattice constants, increasing the choices available for materials.

Direct bonding has successfully created planar waveguide lasers with materials including Tm:YAG (Mackenzie *et al.*, 2001), Nd:YAG (Shepherd *et al.*, 1999), Ti:sapphire (Sugiyama *et al.*, 1998) and various others (Mackenzie, 2007).

3.5.2 Precision dicing

Precision dicing uses a circular saw and was originally developed for the removal of integrated circuits from a wafer. It has evolved to enable rapid processing of optically flat facets for waveguide structures. The saw generally consists of a nickel core, with small diamonds sintered into the nickel. Important process conditions including the blade composition, rotation speed, depth of cut and sample translation speed. Using this process, channel waveguide lasers have been demonstrated in Nd:YAG (Jia *et al.*, 2013) and surface roughness values of 0.29 nm have been realised (Carpenter *et al.*, 2017).

Precision dicing is a useful post-processing tool for the fabrication of channel waveguides from samples grown by PLD and for facet preparation.

3.6 Conclusions

In this chapter, various materials were introduced and discussed. They were put into context with the current state-of-the-art in PLD. The ability of PLD to grow novel materials, including RE-doped sapphire, was presented along with the potential of improvement in crystal quality for these materials. Alternative deposition and waveguide fabrication techniques were presented, and their relative advantages and disadvantages compared with PLD discussed. PLD has the growth rate and material flexibility to compete in a crowded market of deposition techniques, however, in order to exploit these advantages, more needs to be done to increase the achievable crystal quality.

3.7 References

Abegunde, O. O., Akinlabi, E. T., Oladijo, O. P., Akinlabi, S. and Ude, A. U. (2019) 'Overview of thin film deposition techniques', *AIMS Materials Science,* 6(2), pp. 174-180.

Anderson, A. A., Eason, R. W., Jelinek, M., Grivas, C., Lane, D., Rogers, K., Hickey, L. M. B. and Fotakis, C. (1997) 'Growth of Ti: sapphire single crystal thin films by pulsed laser deposition', *Thin Solid Films,* 300(1), pp. 68-71.

Bachmann, V., Jüstel, T., Meijerink, A., Ronda, C. and Schmidt, P. J. (2006) 'Luminescence properties of $SrSi_2O_2N_2$ doped with divalent rare earth ions', *Journal of Luminescence,* 121(2), pp. 441-449.

Bai, G. R., Chang, H. L. M. and Foster, C. M. (1994) 'Preparation of single-crystal $Y_3Al_5O_{12}$ thin film by metalorganic chemical vapor deposition', *Applied Physics Letters,* 64(14), pp. 1777-1779.

Bär, S., Huber, G., Gonzalo, J., Perea, A., Climent, A. and Paszti, F. (2003) 'Europium-doped sesquioxide thin films grown on sapphire by PLD', *Materials Science and Engineering: B,* 105(1-3), pp. 30-33.

Beecher, S. J., Grant-Jacob, J. A., Hua, P., Prentice, J. J., Eason, R. W., Shepherd, D. P. and Mackenzie, J. I. (2017) 'Ytterbium-doped-garnet crystal waveguide lasers grown by pulsed laser deposition', *Optical Materials Express,* 7(5), pp. 1628.

Beecher, S. J., Parsonage, T. L., Mackenzie, J. I., Sloyan, K. A., Grant-Jacob, J. A. and Eason, R. W. (2014) '1.2 W Yb:Y_2O_3 Planar Waveguide Laser', *Advanced Solid State Lasers,* 22(18), pp. 22056-22061.

Beil, K., Fredrich-Thornton, S. T., Tellkamp, F., Peters, R., Kränkel, C., Petermann, K. and Huber, G. (2010) 'Thermal and laser properties of Yb:LuAG for kW thin disk lasers', *Optics express,* 18(20), pp. 20712-20722.

Bhutta, T., Mackenzie, J. I., Shepherd, D. P. and Beach, R. J. (2002) 'Spatial dopant profiles for transverse-mode selection in multimode waveguides', *JOSA B,* 19(7), pp. 1539-1543.

Bonner, C. L., Brown, C. T. A., Shepherd, D. P., Clarkson, W. A., Tropper, A. C., Hanna, D. C. and Ferrand, B. (1998) 'Diode-bar end-pumped high-power Nd:$Y_3Al_5O_{12}$ planar waveguide laser. ', *Optics Letters,* 23(12), pp. 942-944.

Brindley, G. W. and Choe, J. O. (1961) 'The reaction series, gibbsite→ chi alumina→ kappa alumina→ corundum ', *American Mineralogist: Journal of Earth and Planetary Materials,* 46(7), pp. 771-785.

Burmester, P. B. W., Huber, G., Kurfiss, M. and Schilling, M. (2005) 'Crystalline growth of cubic (Eu, Nd):Y2O3 thin films on α -Al2O3 by pulsed laser deposition', *Applied Physics A,* 80(3), pp. 627-630.

Cantelar, E., Torchia, G. A., Sanz-García, J. A., Pernas, P. L., Lifante, G. and Cussó, F. (2003) 'Red, green, and blue simultaneous generation in aperiodically poled Zn-diffused

LiNbO3:Er3+/Yb3+ nonlinear channel waveguides', *Applied Physics Letters,* 83(15), pp. 2991-2993.

Capper, P., Irvine, S. and Joyce, T. (2017) 'Epitaxial Crystal Growth: Methods and Materials', *Springer Handbook of Electronic and Photonic Materials*. Springer Handbooks: Springer.

Carpenter, L. G., Berry, S. A. and Gawith, C. B. E. (2017) 'Ductile dicing of $LiNbO_3$ ridge waveguide facets to achieve 0.29 nm surface roughness in single process step', *Electronics Letters,* 53(25), pp. 1672-1674.

Chen, F. (2008) 'Construction of Two-Dimensional Waveguides in Insulating Optical Materials by Means of Ion Beam Implantation for Photonic Applications: Fabrication Methods and Research Progress', *Critical Reviews in Solid State and Materials Sciences,* 33(3-4), pp. 165-182.

Crunteanu, A., Pollnau, M., Jänchen, G., Hibert, C., Hoffmann, P., Salathé, R. P., Eason, R. W., Grivas, C. and Shepherd, D. P. (2002) 'Ti:sapphire rib channel waveguide fabricated by reactive ion etching of a planar waveguide', *Applied Physics B,* 75(1), pp. 15-17.

Cuomo, J. J., Sadagopan, V., DeLuca, J., Chaudhari, P. and Rosenberg, R. (1972) 'Growth of uniaxial magnetic garnet films by rf sputtering', *Applied Physics Letters,* 21(12), pp. 581-584.

DeLoach, L. D., Payne, S. A., Chase, L. L., Smith, L. K., Kway, W. L. and Krupke, W. F. (1993) 'Evaluation of absorption and emission properties of Yb^{3+} doped crystals for laser applications. ', *IEEE Journal of Quantum Electronics,* 29(4), pp. 1179-1191.

Deng, Y., Fowlkes, J. D., Fitz-Gerald, J. M. and Rack, P. D. (2005) 'Combinatorial thin film synthesis of Gd-doped Y3Al5O12 ultraviolet emitting materials', *Applied Physics A,* 80(4), pp. 787-789.

Dobrovinskaya, E. R., Lytvynov, L. A. and Pishchik, V. (2009) *Sapphire: material, manufacturing, applications.*: Springer Science & Business Media.

Druon, F., Velazquez, M., Veber, P., Janicot, S., Viraphong, O., Buse, G., Ahmed, M. A., Graf, T., Rytz, D. and Georges, P. (2013) 'Laser demonstration with highly doped Yb:Gd2O3 and Yb:Y2O3 crystals grown by an original flux method', *Opt Lett,* 38(20), pp. 4146-9.

Euler, F. and Bruce, J. A. (1965) 'Oxygen coordinates of compounds with garnet structure. ', *Acta Crystallographica,* 19(6), pp. 971-978.

Fan, T. Y., Klunk, S. and Henein, G. (1993) 'Diode-pumped Q-switched Yb: YAG laser.', *Optics Letters,* 18(6), pp. 423-425.

Fermann, M. E., Hanna, D. C., Shepherd, D. P., Suni, P. J. and Townsend, J. E. (1988) ' Efficient operation of an Yb-sensitised Er fibre laser at 1.56 µm', *Electronics Letters,* 24(18), pp. 1135-1136.

Fornasiero, L., Mix, E., Peters, V., Petermann, K. and Huber, G. (1999) 'New oxide crystals for solid state lasers', *Crystal Research and Technology: Journal of Experimental and Industrial Crystallography,* 34(2), pp. 255-260.

Gaumé, R., Viana, B., Vivien, D., Roger, J.-P. and Fournier, D. (2003) 'A simple model for the prediction of thermal conductivity in pure and doped insulating crystals', *Applied Physics Letters,* 83(7), pp. 1355-1357.

Gottmann, J., Wortmann, D., Vasilief, I., Moiseev, L. and Ganser, D. (2007) 'Manufacturing of Nd:$Gd_3Ga_5O_{12}$ ridge waveguide lasers by pulsed laser deposition and ultrafast laser micromachining', *Applied Surface Science,* 254(4), pp. 1105-1110.

Grivas, C., May-Smith, T. C., Shepherd, D. P. and Eason, R. W. (2004) 'Laser operation of a low loss (0.1 dB/cm) Nd:Gd3Ga5O12 thick (40 µm) planar waveguide grown by pulsed laser deposition', *Optics Communications,* 229(1-6), pp. 355-361.

Grivas, C., Shepherd, D. P., May-Smith, T. C., Eason, R. W. and Pollnau, M. (2005) 'Single-transverse-mode Ti: sapphire rib waveguide laser.', *Optics Express,* 13(1), pp. 210-215.

Gün, T., Kahn, A., İleri, B., Petermann, K. and Huber, G. (2008a) 'Two-dimensional growth of lattice matched Nd-doped (Gd,Lu)2O3 films on Y2O3 by pulsed laser deposition', *Applied Physics Letters,* 93(5).

Gün, T., Kuzminykh, Y., Petermann, K., Scheife, H. and Huber, G. (2007) 'Epitaxial growth by pulsed laser deposition of Er-doped Sc2O3 films on sesquioxides monitored in situ by reflection high energy electron diffraction', *Applied Physics Letters,* 91(8).

Gün, T., Kuzminykh, Y., Tellkamp, F., Petermann, K. and Huber, G. (2008b) 'Epitaxial layer-by-layer growth of Yb:YAG and YbAG PLD-films', *Applied Physics A,* 93(2).

Hanby, B. V. T., Stuart, B. W., Grant, C., Moffat, J., Blissett, J., Gerada, C., Gimeno-Fabra, M. and Grant, D. M. (2018) 'Dielectric breakdown of alumina thin films produced by pulsed direct current magnetron sputtering', *Thin Solid Films,* 662, pp. 145-154.

Heinrich, S., Gün, T. and Huber, G. 'Neodymium and ytterbium doped sapphire films grown by pulsed laser deposition.', *In Advances in Optical Materials,* San Diego, California United States: Optical Society of America, IF2A-5.

Jia, Y., Rüter, C. E., Akhmadaliev, S., Zhou, S., Chen, F. and Kip, D. (2013) 'Ridge waveguide lasers in Nd: YAG crystals produced by combining swift heavy ion irradiation and precise diamond blade dicing', *Optical Materials Express,* 3(4), pp. 433-438.

Johansson, J., Djanta, G. and Coutaz, J. L. (1992) 'Optical waveguides fabricated by ion exchange in high-index commercial glasses', *Applied Optics,* 31(15), pp. 2796-2799.

Kalisky, Y. Y. (2004) 'Garnet Crystals as Laser Hosts', *The Physics and Engineering of Solid State Lasers.*

Khartsev, S. I. and Grishin, A. M. (2005) 'Heteroepitaxial Bi3Fe5O12⁄La3Ga5O12 films for magneto-optical photonic crystals', *Applied Physics Letters,* 86(14).

Kidoh, H., Morimoto, A. and Shimizu, T. (1991) 'Synthesis of ferromagnetic Bi-substituted yttrium iron garnet films by laser ablation', *Applied Physics Letters,* 59(2), pp. 237-239.

Kim, S., Hirayama, M., Taminato, S. and Kanno, R. (2013) 'Epitaxial growth and lithium ion conductivity of lithium-oxide garnet for an all solid-state battery electrolyte', *Dalton Trans,* 42(36), pp. 13112-7.

Klopp, P., Petrov, V., Griebner, U., Petermann, K., Peters, V. and Erbert, G. (2004) 'Highly efficient mode-locked Yb: Sc_2O_3 laser', *Optics Letters,* 29(4), pp. 391-393.

Kominato, T., Ohmori, Y., Okazaki, H. and Yasu, M. (1990) 'Very low-loss GeO_2-doped silica waveguides fabricated by flame hydrolysis deposition method', *Electronics Letters,* 26(5), pp. 327-329.

Krankel, C. (2015) 'Rare-Earth-Doped Sesquioxides for Diode-Pumped High-Power Lasers in the 1-, 2-, and 3-μm Spectral Range', *IEEE Journal of Selected Topics in Quantum Electronics,* 21(1), pp. 250-262.

Kück, S., Fornasiero, L., Mix, E. and Huber, G. (1998) 'Excited state absorption and stimulated emission of Nd^{3+} in crystals. Part I: $Y_3Al_5O_{12}$, $YAlO_3$, and Y_2O_3. ', *Applied Physics B,* 67(2), pp. 151-156.

Kühn, H., Heinrich, S., Kahn, A., Petermann, K., Bradley, J. D., Wörhoff, K., Pollnau, M. and Huber, G. (2009) 'Monocrystalline Yb^{3+}:(Gd, Lu)$_2O_3$ channel waveguide laser at 976.8 nm', *Optics Letters,* 34(18), pp. 2718-2720.

Kumaran, R., Webster, S. E., Penson, S., Li, W., Tiedje, T., Wei, P. and Schiettekatte, F. (2009) 'Epitaxial neodymium-doped sapphire films, a new active medium for waveguide lasers', *Optics Letters,* 34(21), pp. 3358-3360.

Kurilchik, S. V., Grant-Jacob, J. A., Prentice, J. J., Hua, P., Eason, R. W. and Mackenzie, J. I. 'Pulsed-laser-deposited Yb:YAG planar-waveguide amplifier', *8th EPS-QEOD Europhoton,* Barcelona, Spain, 02-07 September.

Lacovara, P., Choi, H. K., Wang, C. A., Aggarwal, R. L. and Fan, T. Y. (1991) 'Room-temperature diode-pumped Yb: YAG laser', *Optics Letters,* 16(14), pp. 1089-1091.

Łodziana, Z. and Parliński, K. (2003) 'Dynamical stability of the α and θ phases of alumina', *Physical Review B,* 67(17).

Loho, C., Djenadic, R., Bruns, M., Clemens, O. and Hahn, H. (2016) 'Garnet-Type $Li_7La_3Zr_2O_{12}$ Solid Electrolyte Thin Films Grown by CO_2-Laser Assisted CVD for All-Solid-State Batteries', *Journal of The Electrochemical Society,* 164(1), pp. A6131-A6139.

Loiko, P., Soulard, R., Brasse, G., Doualan, J. L., Guichardaz, B., Braud, A., Tyazhev, A., Hideur, A. and Camy, P. (2018) 'Watt-level Tm:$LiYF_4$ channel waveguide laser produced by diamond saw dicing', *Opt Express,* 26(19), pp. 24653-24662.

Lu, Y., Dekker, P. and Dawes, J. M. (2019) 'Liquid-Phase Epitaxial Growth and Characterization of Nd:YAl3(BO3)4 Optical Waveguides', *Crystals,* 9(2).

Mackenzie, J. I. (2007) 'Dielectric Solid-State Planar Waveguide Lasers: A Review', *IEEE Journal of Selected Topics in Quantum Electronics,* 13(3), pp. 626-637.

Mackenzie, J. I., Grant-Jacob, J. A., Beecher, S., Riris, H., Yu, A. W., Shepherd, D. P. and Eason, R. W. 'Er:YGG planar waveguides grown by pulsed laser deposition for LIDAR applications', *Solid State Lasers XXVI: Technology and Devices.*

Mackenzie, J. I., Mitchell, S. C., Beach, R. J., Meissner, H. E. and Shepherd, D. P. (2001) '15 W diode-side-pumped Tm:YAG waveguide laser at 2 µm', *Electronics Letters,* 37(14).

Mak, A. A., Gulevich, E., Dvornikov, S. S., Kachinsky, A., Kalitukho, I., Protasenya, A. L. and Tugbayev, V. A. 'Current state and prospects for tunable titanium-sapphire lasers', *Laser Physics*, 102-104.

Mubarak, A. M. A., Hamzah, E. H. E. and Tofr, M. T. M. (2005) 'Review of physical vapour deposition (PVD) techniques for hard coating', *Jurnal Mekanikal,* 20(2), pp. 42-51.

Okada, M., Katayama, S. and Tominaga, K. (1991) 'Preparation and magneto-optic properties of Bi-substituted yttrium iron garnet thin films by metalorganic chemical vapor deposition', *Journal of Applied Physics,* 69(6), pp. 3566-3570.

Ollivier, B., Retoux, R., Lacorre, P., Massiot, D. and Férey, G. (1997) 'Crystal structure of κ-alumina: an X-ray powder diffraction, TEM and NMR study.', *Journal of Materials Chemistry,* 7(6), pp. 1049-1056.

Parsonage, T. L., Beecher, S. J., Choudhary, A., Grant-Jacob, J. A., Hua, P., Mackenzie, J. I., Shepherd, D. P. and Eason, R. W. (2015) 'Pulsed laser deposited diode-pumped 7.4 W Yb:Lu_2O_3 planar waveguide laser', *Opt Express,* 23(25), pp. 31691-31697.

Pauling, L. and Shappell, M. D. (1930) 'The Crystal Structure of Bixbyite and the C-Modification of the Sesquioxides', *Zeitschrift für Kristallographie-Crystalline Materials,* 75(1), pp. 128-142.

Pelenc, D., Chambaz, B., Chartier, I., Ferrand, B. and Vial, J. C. (1991) 'Epitaxial Growth of Garnets for Thin Film Lasers', *Le Journal de Physique IV,* 01(C7), pp. C7-311-C7-314.

Peters, R., Kränkel, C., Fredrich-Thornton, S. T., Beil, K., Petermann, K., Huber, G., Heckl, O. H., Baer, C. R. E., Saraceno, C. J., Südmeyer, T. and Keller, U. (2011) 'Thermal analysis and efficient high power continuous-wave and mode-locked thin disk laser operation of Yb-doped sesquioxides', *Applied Physics B,* 102(3), pp. 509-514.

Peters, R., Petermann, K. and Huber, G. 'A new mixed sesquioxide Yb: $LuScO_3$: spectroscopic properties and highly efficient thin-disk laser operation.', *Advanced Solid-State Photonics,* Denver, Colorado, United States: Optical Society of America.

Roth, P. W., Maclean, A. J., Burns, D. and Kemp, A. J. (2009) 'Directly diode-laser-pumped Ti: sapphire laser', *Optics Letters,* 34(21), pp. 3334-3336.

Ruano, J. M., Benoit, V., Aitchison, J. S. and Cooper, J. M. (2000) 'Flame hydrolysis deposition of glass on silicon for the integration of optical and microfluidic devices', *Analytical Chemistry,* 72(5), pp. 1093-1097.

Serna, R. and Afonso, C. N. (1996) 'In situ growth of optically active erbium doped Al2O3 thin films by pulsed laser deposition', *Applied Physics Letters,* 69(11), pp. 1541-1543.

Shepherd, D. P., Bonner, C. L., Brown, C. T. A., Clarkson, W. A., Tropper, A. C., Hanna, D. C. and Meissner, H. E. (1999) 'High-numerical-aperture, contact-bonded, planar waveguides for diode-bar-pumped lasers', *Optics Communications,* 160(1), pp. 47-50.

Singh, J. and Wolfe, D. E. (2005) 'Nano and macro-structured component fabrication by electron beam-physical vapor deposition (EB-PVD)', *Journal of materials Science,* 40(1), pp. 1-26.

Smith, E. R., Gruber, J. B., Wellenius, P., Muth, J. F. and Everitt, H. O. (2010) 'Spectra and energy levels of Eu^{3+} in cubic phase Gd_2O_3', *physica status solidi (b),* 247(7), pp. 1807-1813.

Sposito, A., May-Smith, T. C., Stenning, G. B. G., de Groot, P. A. J. and Eason, R. W. (2013) 'Pulsed laser deposition of high-quality µm-thick YIG films on YAG', *Optical Materials Express,* 3(5).

Sugiyama, A., Fukuyama, H., Sasuga, T., Arisawa, T. and Takuma, H. (1998) 'Direct bonding of Ti: sapphire laser crystals.', *Applied Optics,* 37(12), pp. 2407-2410.

Szela, J. W., Sloyan, K. A., Parsonage, T. L., Mackenzie, J. I. and Eason, R. W. (2013) 'Laser operation of a Tm:Y2O3 planar waveguide', *Opt Express,* 21(10), pp. 12460-8.

Ubizskii, S. B., Matkovskii, A. O., Melnyk, S. S., Syvorotka, I. M., Muller, V., Peters, V., Petermann, K., Beyertt, A. and Giesen, A. (2004) 'Optical properties of epitaxial YAG:Yb films', *physica status solidi (a),* 201(4), pp. 791-797.

Vainos, N. A., Grivas, C., Fotakis, C., Eason, R. W., Anderson, A. A., Gill, D. S., Shepherd, D. P., Jelinek, M., Lancok, J. and Sonsky, J. (1998) 'Planar laser waveguides of Ti: sapphire, Nd: GGG and Nd: YAG grown by pulsed laser deposition.', *Applied Surface Science,* 127, pp. 514-519.

Waeselmann, S. H., Heinrich, S., Kränkel, C. and Huber, G. (2016) 'Lasing of Nd^{3+}in sapphire', *Laser & Photonics Reviews,* 10(3), pp. 510-516.

Waeselmann, S. H., Rüter, C. E., Kip, D., Kränkel, C. and Huber, G. (2017) 'Nd:sapphire channel waveguide laser', *Optical Materials Express,* 7(7).

Weber, M. J. (2018) *Handbook of optical materials.* CRC press.

Zharikov, E. V., Zhekov, V. I., Kulevskii, L. A., Murina, T. M., Osiko, V. V., Prokhorov, A. M., Savel'ev, A. D., Smirnov, V. V., Starikov, B. P. and Timoshechkin, M. I. (1975) 'Stimulated emission from Er^{3+} ions in yttrium aluminum garnet crystals at λ= 2.94 µm.', *Soviet Journal of Quantum Electronics,* 4(8), pp. 1049-1050.

Zinkevich, M. (2007) 'Thermodynamics of rare earth sesquioxides', *Progress in Materials Science,* 52(4), pp. 597-647.

Zoubir, A., Richardson, M., Rivero, C., Schulte, A., Lopez, C., Richardson, K., Hô, N. and Vallée, R. (2004) 'Direct femtosecond laser writing of waveguides in As_2S_3 thin films', *Optics Letters,* 29(7), pp. 748-750.

Chapter 4 PLD setup and characterisation methods

4.1 Introduction

In this chapter the PLD setup and improvements made to this setup throughout this project will be detailed. The fabrication methods used in the target fabrication will be explained with details of the experimental techniques used for target reconditioning and sample polishing. The equipment and techniques used to characterise the physical and optical properties of the grown films will be described.

4.2 Pulsed laser deposition setup

4.2.1 Chamber schematics

The apparatus used for the deposition of all the materials described in this thesis is illustrated in Figure 4.1. Features of this setup and how it has been used in the experiments in this thesis are as follows:

- Stainless steel vacuum chamber that is evacuated to 10^{-4} mbar before being refilled with a background gas. In this project, 0.02 mbar of backfilled oxygen was used for all samples described to compensate for the loss of oxygen when material is transferred from the target to the substrate.
- A UV laser beam is focussed onto a target, causing ablation and a plume to propagate in the chamber. The laser used was a Coherent Compex Pro 110 at 248 nm wavelength with 20 ns pulse width at 100 Hz. This relatively high repetition rate is used to increase the deposition rate, other PLD systems generally used repetition rates of 1-20 Hz.
- The target is rotated and translated via an offset cam mechanism, creating epitrochoidal motion which will be discussed at length in section 5.5.
- The substrate is heated from behind with a CO_2 laser (10.6 µm) which has been reshaped by a tetraprism (May-Smith *et al.*, 2008) (discussed further in section 4.2.3).
- The substrate is held in position by alumina rods (discussed further in section 4.2.5), in these experiments, the substrate sizes were 10x10x1 mm.

- The plume can be blocked by a retractable plume blocker (aluminium sheet) that will prevent deposition and allow "pre-ablation" of the target. Pre-ablation removes potential contamination on the target surface before subsequent film growth.
- Laser spot size can be altered by moving the position of the focussing lens, which can be used to control the fluence and hence plume size.
- The substrate-target distance can be changed but for the experiments described in this thesis, is set at 6 cm, which from previous experiments from this group, was found to be optimum.

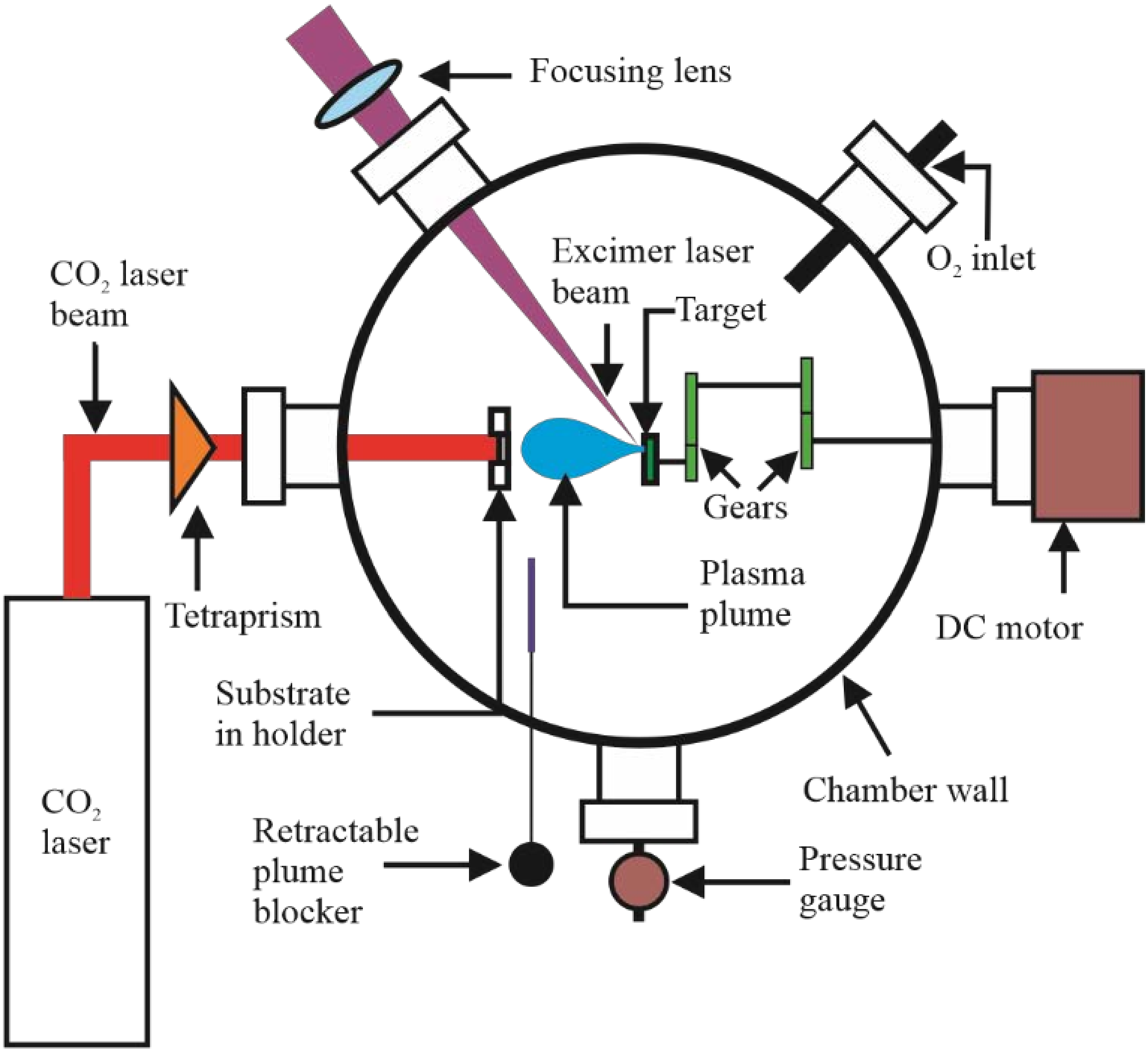

Figure 4.1. Diagram of the setup of the PLD system

4.2.2 CO_2 laser control

The substrate is heated via the beam from a CO_2 laser, either a Synrad UC-2000 with a maximum output power of 40 W, or a Rofin OEM10IX with a maximum output power of 170 W with an output wavelength of 10.6 µm. The Rofin CO_2 was installed in this project and is controlled via MATLAB. To have an adjustable output power, the laser is pulse-frequency modulated, then pulse-width modulated, which involves rapid switching of the laser from on to off. At low frequencies this can cause significant power fluctuations at the substrate, and as a result, can cause significant temperature fluctuations. To avoid this, MATLAB controls a waveform generator which uses a 5 µs pulse width and increases the frequency of pulses up to maximum allowed in the laser, 120 kHz. From here, to increase the power, the pulse width is gradually increased at a constant frequency of 120 kHz.

By using pulse width modulation with the maximum possible frequency and smallest possible pulse width, the temperature of the substrate will be as stable as possible. In the initial development stage of driving the CO_2 laser, significant temperature fluctuations were seen when using a 500 Hz frequency, realised due to a sapphire substrate warping due to the power fluctuations.

4.2.3 CO_2 laser beam reshaping

For the samples detailed in this thesis, the substrate size is a square faced crystal with dimensions 10x10x1 mm. Therefore, to ensure uniform heating the CO_2 laser beam needs to be reshaped from a Gaussian profile to a square top-hat intensity profile. This is achieved using a ZnSe tetraprism with 1^o angled faces (Figure 4.2 (a)). The tetraprism splits the gaussian beam into four quadrants and superimposes them onto one another, forming a quasi-top hat profile (Figure 4.2 (b)). The overlap of the beams does cause interference effects; however, these do not significantly affect the uniformity of heating on the front surface of the substrate. Any non-uniformities of the beam on the back surface of the substrate are smoothed as the heat propagates through to the front surface (May-Smith *et al.*, 2008).

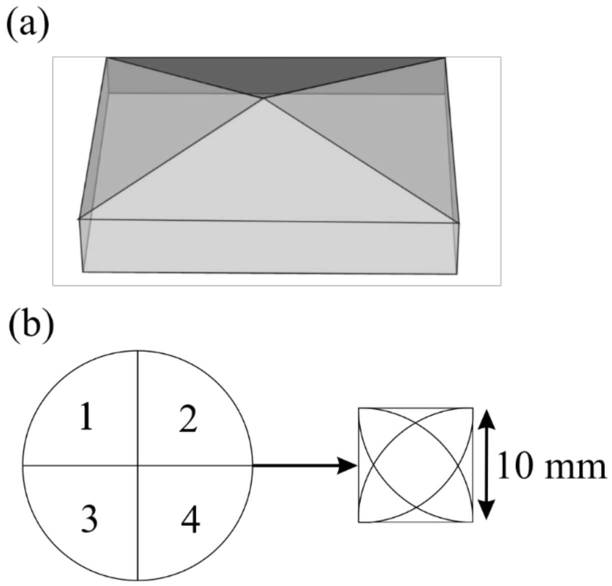

Figure 4.2. (a) diagram of a tetraprism and (b) transformation of gaussian beam to a quasi-top hat beam (Sloyan, 2012).

The 1^{o} angles of the tetraprism is determined by the working distance between the tetraprism and the substrate, and the size of the substrate. Theoretically, a perfectly aligned tetraprism setup would provide a standard deviation in temperature across the substrate of 2.2 ^{o}C, significantly smaller than a gaussian beam or square tapered beam (43 ^{o}C and 7 ^{o}C respectively (Darby, 2009))

4.2.4 Target fabrication

The targets were acquired from external companies such as Testbourne, Scotech and Sindelhauser. They consist of mixing specified weights of µm-sized oxide powders and pressing them into a dense ceramic. This is then either annealed at temperatures in excess of 1000 ^{o}C or put through a hot isotropic press (HIP). In the HIP process, the target material is put into an atmosphere of inert gas (usually argon) and put under extreme pressures and temperatures in order to increase the density of the target material. The target material is then cut to size, which in this case is a 50 mm diameter, 5 mm thick disc.

I specified a goal to create targets of greater than 85% of the theoretical constituent density (this value appeared to allow the fabrication of films with low particulate densities), however this was not always possible for the suppliers. Low-density targets appear to be more susceptible to exfoliation of particles due to the prevalence of pores. Densities of targets used in experiments in this thesis are mostly >75% dense, it was generally found that targets could not be consistently fabricated with density levels above our set goal. This is assumed to be due to the lack of optimisation in the fabrication process, with a commonly used and therefore optimised ceramic target consisting only of Al_2O_3 reaching densities of over 95% the theoretical value.

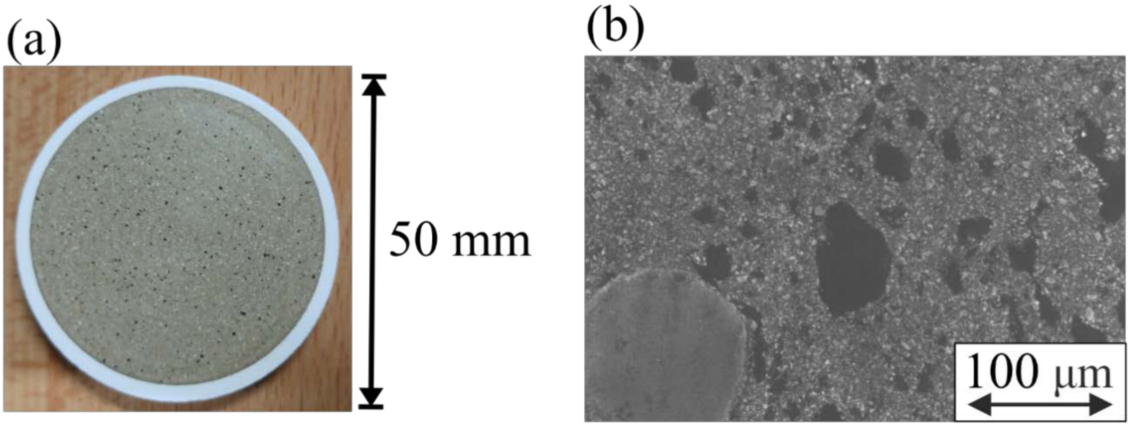

Figure 4.3. (a) photograph of a YAG target (fabricated with yttria and alumina powder) after 72,000 ablation pulses with domains of material and (b) SEM image of the same target.

Careful optimisation of the target fabrication parameters is required for each different mixture of materials. Poor optimisation can lead to regions of different materials in the target (Figure 4.3), which will lead to inconsistent ablation and an increase in particulate formation.

4.2.5 Substrate holder

The substrate needs to be held in place for deposition in the centre of the plume while ensuring it is as isolated from the exterior environment as possible. Any material in contact with the substrate will serve as a heat sink and create temperature differentials across the substrates surface. In order to facilitate this, the substrate holder was redesigned, as seen in Figure 4.4. Originally, the alumina posts held the substrate in a slit cut into the post (Figure 4.4 (a)) and encroached onto the substrate surface by 2 mm in three places. This meant that there is an area of the sample that is not useable as a planar waveguide. A new holder (Figure 4.4 (b)) encroaches by 0.2 mm on the top two corners and does not encroach on the bottom two corners, only being in contact with the side. This means that the area not deposited on can be removed during the facet polishing process, meaning practically the entire sample can be used for waveguide experiments.

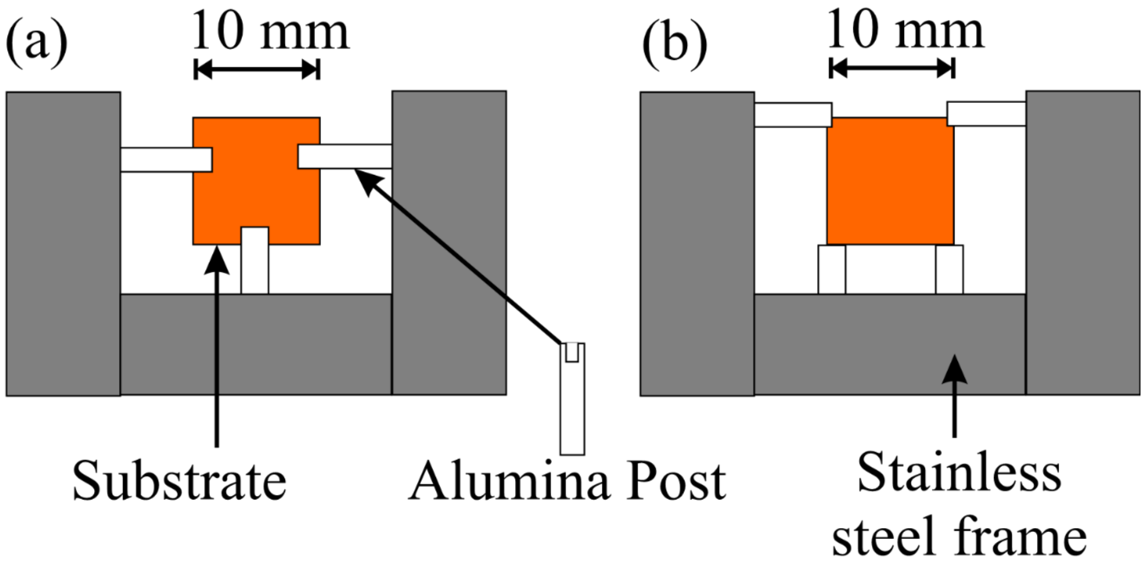

Figure 4.4. (a) original substrate holder and (b) newly designed substrate holder.

4.2.6 Shadow-mask setup

In section 5.1, experiments using a shadow mask as a method of particulate reduction are presented. This involves inserting a piece of material between the substrate and the target to block the particulates and this can be seen in Figure 4.5.

To be an effective shadow mask, the material must be able to resist the temperature fluctuations from the plume and not eject material as it is bombarded with high energy atoms and ions. Initially, a lutetia substrate was suspended in position using tungsten wire, however the substrate cracked and split in two by the intense heat variations. It was then decided that aluminium would hold up to the thermal pressures more effectively despite a lower melting point. On all subsequent growths, squares of aluminium sheet were suspended using tungsten wire from two directions.

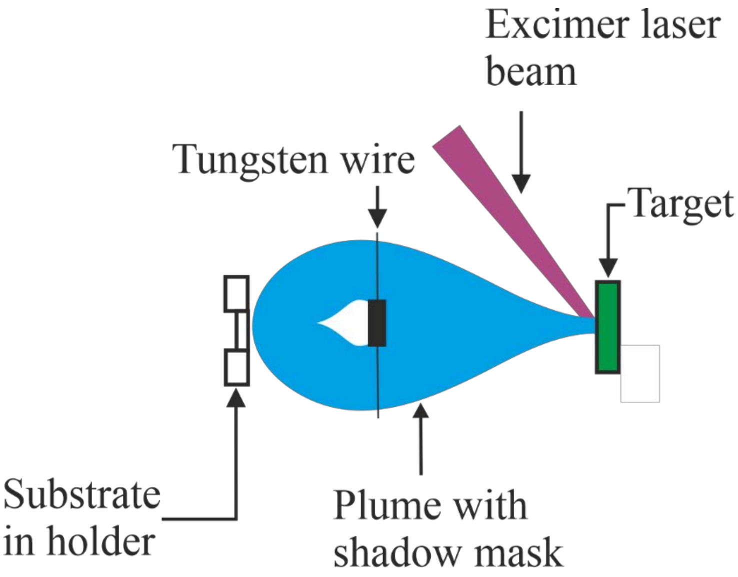

Figure 4.5. Diagram of PLD setup with a shadow mask between the target and substrate.

4.3 Other experimental techniques

4.3.1 Target reconditioning

After the target has been extensively used in the ablation process (the number of ablation pulses depends on material and density of the target, as well as the ablation technique) there is a substantial increase in the density of particulates deposited into the growing film. The target can be reused if the surface-structure formed during ablation is removed. This was initially achieved via lapping of the target surface with 9 µm alumina slurry. In this process, the target was attached with wax to a parallel plate with a mirrored back surface and aligned using a back-surface reflection when attached to a polishing jig. The alignment process can be seen in Figure 4.6. The length of time to remove the surface structure on a target would range from twenty minutes to two hours, depending on the density and constituent material of the target.

Alumina targets, which were used frequently in the work presented in this thesis, generally took two hours to lap one face. Due to the time-consuming nature of this process, an alternative was sought, and a diamond-based polishing system was found. This reduced the lapping time by a factor of 10 and was subsequently used for all target reconditioning.

Post-lapping, the targets are cleaned in an ultra-sonic bath with distilled water to remove any contaminants and placed in a 120 ^{o}C oven for 24 hours to evaporate any water residue.

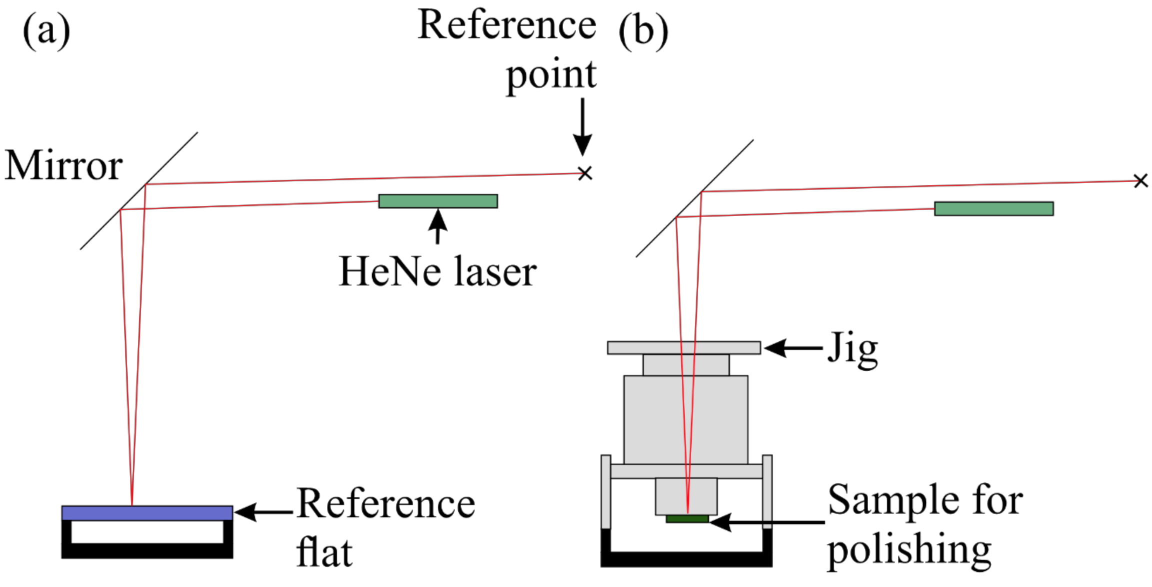

Figure 4.6. Setup for alignment of the lapping targets and polishing samples. The steps are: (a) mark position of laser with a known flat material and (b) adjust the sample positioning until the laser position matches that seen in (a). This can be used for lapping/polishing of targets.

4.3.2 Surface and facet polishing

Multiple samples described later in this thesis have undergone surface and facet polishing processes. For surface polishing, the procedure is identical to that described in the first paragraph of section 4.3.1. Facet polishing is required for films that will be coupled into with laser light. This also follows similar steps, however, instead of attaching the samples to a parallel plate, the samples themselves are used as a reflective surface to ensure parallel facets.

Six samples can be polished at once by stacking and sticking together with wax. The reference laser is then reflected off of the opposite side to the side to be polished, to ensure a parallel finish. To achieve an approximate flat surface, 16 µm (average particle size) grit is used for films grown onto a sapphire substrate, or 9 µm alumina powder for films grown onto a YAG substrate. Once a flat surface is achieved, further lapping stages with 9 µm, 3 µm and 1 µm alumina slurry is used to remove scratches caused by the previous sized grit. To achieve an optical finish, alkaline colloidal silica polishing fluid (Syton) is used on a polyethylene polishing plate. This fluid combines mechanical and chemical processes to polish the samples.

4.4 Physical characterisation

4.4.1 Reflective dark field microscopy

Films that are amorphous or have a high density of particulates may appear translucent or even opaque by eye. Dark field (DF) microscopy can give an insight into the particulate density of the grown film. In the work described in this thesis, only reflective DF microscopy is used, and a diagram of the functionality is provided in Figure 4.7. This technique shines light in a cone shape that focusses at the samples surface. If the sample is transparent, the light will pass through the sample, however, a defect or particulate in the film will scatter light, and some of this light will be collected by the microscope objective, allowing defects in the film to be observed clearly against an otherwise black background.

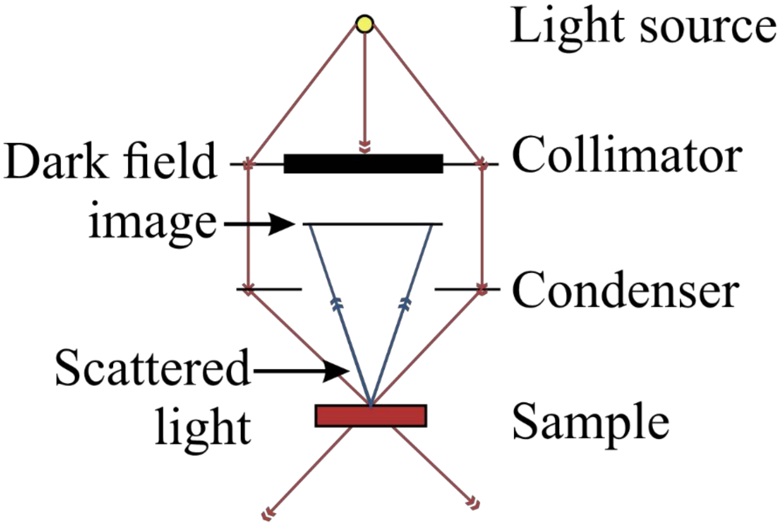

Figure 4.7. Schematics of reflective dark field microscopy.

To extract quantitative information from the DF images a routine was written in python to read a DF image and turn all the pixels above a certain threshold intensity to 1 and all pixels below the threshold to 0. As presented in Figure 4.8, this routine will approximate the DF image satisfactorily. From this, the percentage number of pixels above this threshold (20% in Figure 4.8) can be calculated and will be proportional to the number of scattering points in the film. Comparisons can then be made, quantitatively, between different films providing the DF images were captured with the same intensity of light from the microscope, the same camera settings, and the intensity threshold is set at the same level. Optical microscopy is limited by the Abbé diffraction limit, which, for visible light is limited to resolutions of

~290 nm (for 550 nm wavelength of light (Born and Wolf, 1999)). However, in this setup, the pixel size will be larger than 290 nm decreasing the achievable resolution.

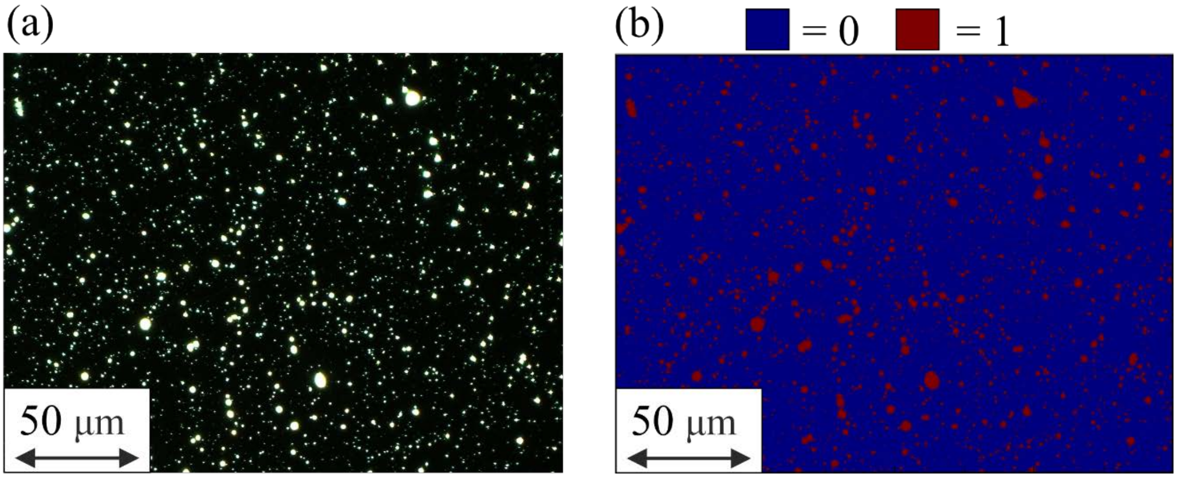

Figure 4.8. (a) DF microscopy image of a YGG film and (b) a computer-generated approximation of the DF image, setting all the pixels above 20% of the maximum intensity to 1.

4.4.2 Surface profiling

Surface profiling can give information about the film's surface roughness, curvature and the number of surface particulates protruding from the surface. In this thesis, surface profilometry is performed using a stylus profiler and a white light interferometric profiler.

4.4.2.1 Stylus profilometry

A stylus profiler offers a two-dimensional measurement technique that uses a stylus on the end of a cantilever to obtain information from the surface of the sample. As the stylus is moved across the surface of the sample, the cantilever will be moved in a vertical direction dependant on the topology of the sample. This application can be extremely accurate with theoretical resolution of less than 1 nm in the vertical axis. The resolution is limited on the horizontal axis by the radius of the stylus tip and vibrational noise in the instrument. The stylus used for the work described in this thesis is a KLA Tencor P6 with 2 μm radius tip, limiting the horizontal resolution to 2 μm. This was initially used for the measurement of thickness by measuring between the areas shielded from deposition by the alumina substrate holder rods (Figure 4.4 (a)) but is also used for roughness measurements.

4.4.2.2 Optical profilometry

The optical profiler used for the work in this thesis was a Zemetrics Zescope. This system has three microscope objective interferometers that work in two geometries, presented in

Figure 4.9. For greater magnifications, a smaller working distance is required and therefore is not compatible with a beam splitter. Since the Mirau interferometer does not require a beamsplitter, it is used for 10x and 50x magnification and also offers greater stability of measurement compared to a Michelson interferometer. The sample or interferometer is moved vertically, measuring the intensities of interference fringes of the reflected and reference light. Signal processing algorithms then process the data and create a three-dimensional map of the sample's surface. 0.1 nm resolution is possible in theory, but vibrational noise will reduce this, however, < 1 nm resolution is still observed. By using the software package SPIP (scanning probe image processor) a roughness value of the film can be calculated, and the number and size of surface particles/pores can be counted.

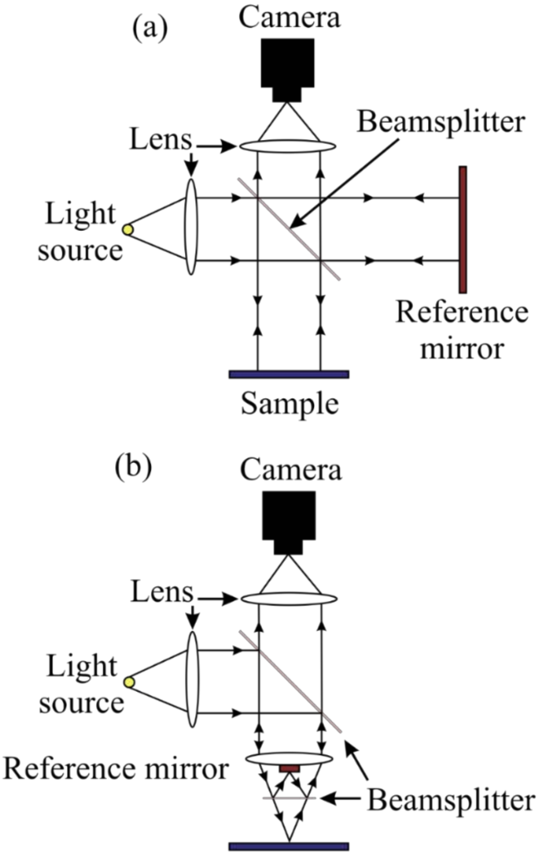

Figure 4.9. Diagrams of white light interferometer used in the Zemetrics Zescope with (a) a Michelson interferometer (used in 5x magnification) and (b) a Mirau interferometer (used for 10x and 50x magnification).

4.4.3 M-line prism coupling

M-line prism coupling can be used to measure material refractive index, optical loss, film-thickness and anisotropy (Monneret *et al.*, 2000). The relationship between the refractive index and the wavelength or the temperature of the sample can also be studied. The equipment used for the measurements presented in this thesis is the Metricon Model 2010/M.

The basic principle of measurement is displayed in Figure 4.10. For a bulk material, a prism with a known, higher refractive index than the bulk, is brought into contact with the material via a pneumatically operated coupling head. Although a perfect contact will not be achieved, an airgap less than half the wavelength of the coupling light is acceptable (Monneret *et al.*, 2000). The angle (θ) of the incident light on the material is changed while the intensity reflected onto the photodetector is measured. At some critical angle, the light will be able to couple into the material and so the intensity of light measured will decrease suddenly, causing a “knee”. The location of this knee will allow calculation of the refractive index of the material.

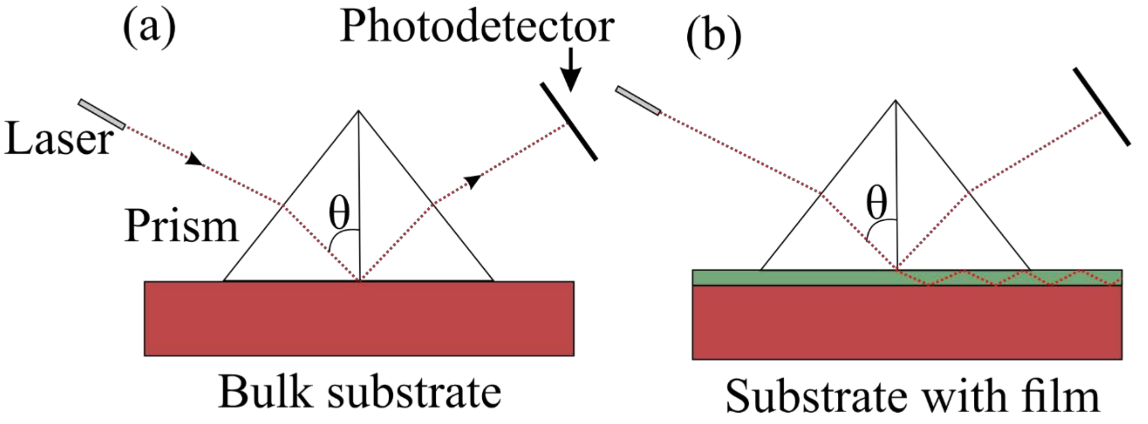

Figure 4.10. Schematics for a m-line prism coupler measuring (a) bulk material and (b) bulk material with a thin-film for measuring refractive indices of materials.

For a substrate with a thin film, the same measurement will couple to modes of the waveguide. Modes are discrete values where the photons can tunnel across the airgap and couple into the film (Figure 4.10 (b)) and consequently decrease the intensity of reflected light measured by the photodetector. The location of the first mode will approximately determine the refractive index, whereas the angular difference between the modes can be used to calculate the thickness of the film. These values are calculated by the software provided using the methodology described by (Monneret *et al.*, 2000).

Thickness measurements can be performed with samples of thicknesses of ~100-15000 nm (depending on material and wavelength of light). A 100 nm film is required to support a mode, however, if only one mode is supported then either the refractive index or the thickness must be known in order to calculate the other. At thicknesses over 15 μm, the refractive index can be measured using the bulk measurement method.

For measurements using m-line coupling described in this thesis, there can be considerable challenges achieving a contact closer than half of the wavelength of light (less than a 316.5 nm air gap required for 633 nm HeNe laser). Surface particles on the PLD-grown films can protrude greater than 1 µm, making close contact difficult. The substrates used are small and mechanically hard (YAG and sapphire) so the samples cannot flex to provide a close contact as with large samples of silica. This has meant that face polishing of the samples is sometimes required to produce a reliable refractive index measurement using this method.

4.4.4 X-ray diffraction

X-ray diffraction (XRD) is a rapid, non-destructive method for measuring crystal structure of bulk material or films. A standard XRD setup is presented in Figure 4.11, where the x-ray beam is incident on a sample and the resultant scattered light is detected by the x-ray detector. An XRD spectrum is obtained by changing the 2θ and or θ. All the XRD spectra presented in this thesis were measured using a Rigaku Smartlab, which uses a copper filament for the generation of x-rays with the $K_{\alpha1}$ emission emitted at a wavelength of 1.54059 Å. A secondary emission, $K_{\alpha2}$, at a wavelength of 1.5411 Å is also emitted, which will create secondary peaks in the XRD spectrum. This can confuse interpretations of the measurements, however the $K_{\alpha2}$ emission can be filtered out using a monochromator.

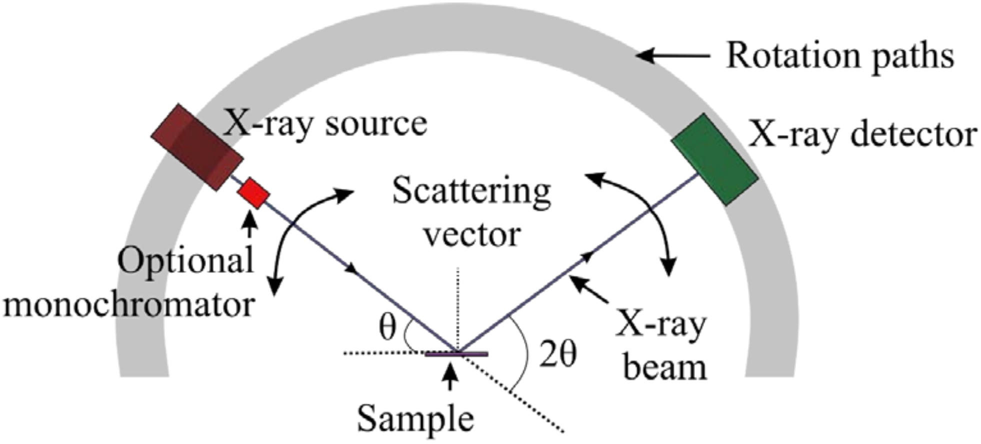

Figure 4.11. Diagram of a simple XRD setup.

4.4.4.1 θ/2θ XRD

The standard XRD measurement technique is a θ/2θ measurement, which measures periodicities parallel to the sample's surface. This is a symmetrical measurement where the θ angle (Figure 4.11) is changed at the same rate as 2θ. This method of measurement can be understood by the stacked planes model, where the sample can be thought of as a series of planes. If these planes are separated by a distance (d), then the scattered x-rays will constructively interfere when the Bragg condition is met, which is shown in equation 4.1. Here, d is the distance between planes, θ is the angle of incident light (Figure 4.12), m is the order of the diffraction peak (an integer) and λ is the wavelength of light.

$$2d\sin\theta = m\lambda \tag{4.1}$$

Constructive interference will create a peak in intensity incident on the detector. This peak will have a finite width due to phonons in the sample creating lattice constant disturbances. Defects and inhomogeneous strain in the measured sample will also have an impact on the lattice constant, causing broadening of XRD peaks. Therefore, the FWHM (full width half maximum) of the peaks can be a useful comparison between samples as a perfect, defect free crystal will have a lower FWHM than a sample with a high defect density.

The position of the XRD peak can be a useful indicator of the stoichiometry of the film. Comparing the peak value with literature values can indicate whether the material has grown in the correct orientation and with the correct stoichiometry. This will be discussed further in section 6.2.1, where the position of the YAG peak is shifted due to a non-stoichiometric transfer of aluminium from target to sample.

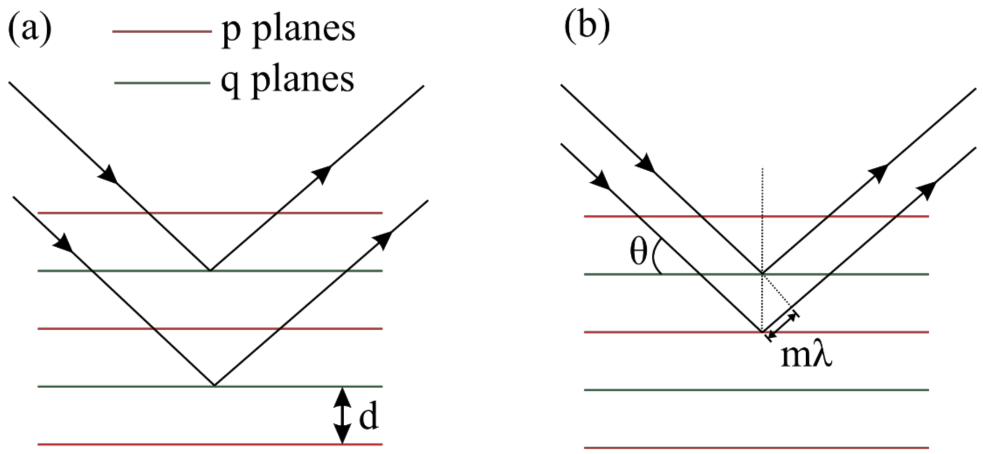

Figure 4.12. Diagram of diffraction between (a) p and p/ q and q planes and (b) p and q planes.

For a cubic garnet crystal, such as YAG, the unit cell can be described as 8 planes, alternating in composition. The two types of plane are called p plane and q plane (Figure 4.12). If the crystal orientation is (100), then the XRD spectra measured in a θ/2θ setup will produce two peaks, at (400) and (800) planes. These two peaks arise from constructive interference between the planes, with p/p and q/q interference causing the (400) peak and p/q interference causing the (800) interference. The p/q plane interference is more sensitive to stoichiometry changes, and hence the (800) peak will generally be shorter and broader than (400) peak.

4.4.4.2 Grazing incidence XRD

Grazing incidence XRD (GIXRD) can be used to determine the phase crystallinity, thickness and depth crystallinity profile of a thin film. With θ/2θ XRD, the substrate will be visible in the spectra for films < 30 µm thick, which for epitaxial growths, can obscure the peak from the film. GIXRD instead will provide information about the top layers (thickness of the top layers will depend on the incident angle and material’s linear absorption coefficient) that may not be visible in an θ/2θ XRD measurement due to the dominance of the substrate.

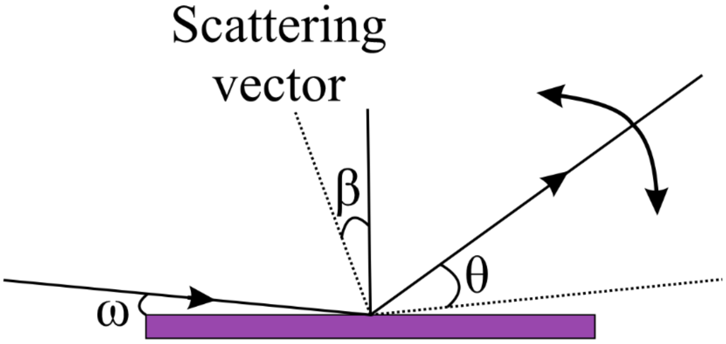

Figure 4.13. Schematics of grazing incidence XRD with small, fixed incidence angle and a variable detection angle

The incident angle, ω, is set at a constant angle of 1^o or less and the detection angle, θ, is changed (Figure 4.13). By setting the incident angle to a low value, the penetration depth of the light is reduced, meaning the influence of the substrate is removed in sufficiently thick films. This technique cannot be used as a replacement for θ/2θ XRD since with an increasing θ angle, the scattering vector angle, β, will increase. A larger β angle will increase the tilt of the measured planes compared to the sample’s surface, which will be significantly different compared to a θ/2θ measurement where the scattering vector angle will remain at 0^o and hence the measured planes will be parallel to the sample’s surface. However, it will provide an indication of other, undesirable orientations that are growing in the top layers of the sample. In the GIXRD measurements discussed in this thesis, the incident angle is set at 1^o.

4.4.4.3 Rocking curve XRD

Rocking curve (RC) XRD is used to analyse the level of crystallite preferred alignment in the sample. This technique generally follows an θ/2θ XRD measurement where the peak positions are noted. The θ position is fixed on the peak of interest. and the ω angle is varied (Figure 4.14). This will indicate whether the planes in the sample are parallel, with perfectly parallel planes producing a peak with FWHM determined by the resolution of the equipment. However, samples with defects, stresses or numerous orientations will have planes that are not parallel, which will broaden the peak seen in the RC measurement. This is useful for comparing the quality of single-crystal films where comparing θ/2θ XRD measurements provide no quantitative data.

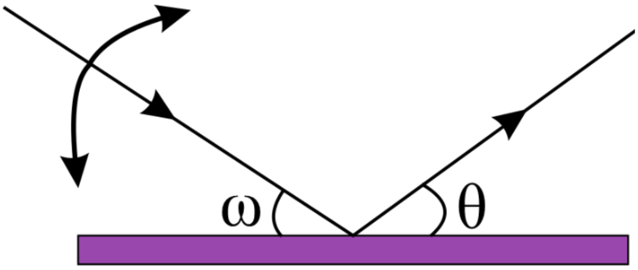

Figure 4.14. Schematics of rocking curve XRD with a fixed θ angle and a varying ω angle.

4.4.5 Scanning electron microscope

A scanning electron microscope (SEM) uses a focussed beam of electrons to produce a variety of emissions from a sample's surface in a vacuum. Since electrons will have a shorter wavelength than the visible light used in optical microscopy (for electrons accelerated at 10 keV, λ= 10pm (Sposito, 2014)), the achievable spatial resolutions will be higher. In practise, the resolution is ~1 nm, due to the size of the electron beam and interaction volume (seen in Figure 4.15). The electron beam penetration depth will be determined by the energy of incident electrons and the density of the material, with a larger penetration depth causing a larger teardrop shape (Figure 4.15) and therefore decreasing the resolution. For example, for YAG, the bulk density is 4.53 gcm^{-3}, so for electron energies of 20 keV (the energy used for measurements described in this thesis) the penetration depth is ~2 µm.

The absorption of electrons will create an electric field which, for an electrically conductive sample, will be removed. However, for non-conductive samples the build-up of charge will create excess heat, which will change the emission characteristics of the sample. A thin coating of gold can be used to remove excess electrons; however, this can hide small surface features. The measurements can also be performed in a partial vacuum, which will help to remove the electrons, but will reduce the achievable resolution due to scattering of the electron beam in the partial atmosphere.

The SEM used in the work described in this thesis is a Zeiss Evo 50. There are several modes of emission that can be detected while using an SEM, including secondary electrons, backscattered electron (BSE) and characteristic x-rays. These different emissions are described in the following three subsections.

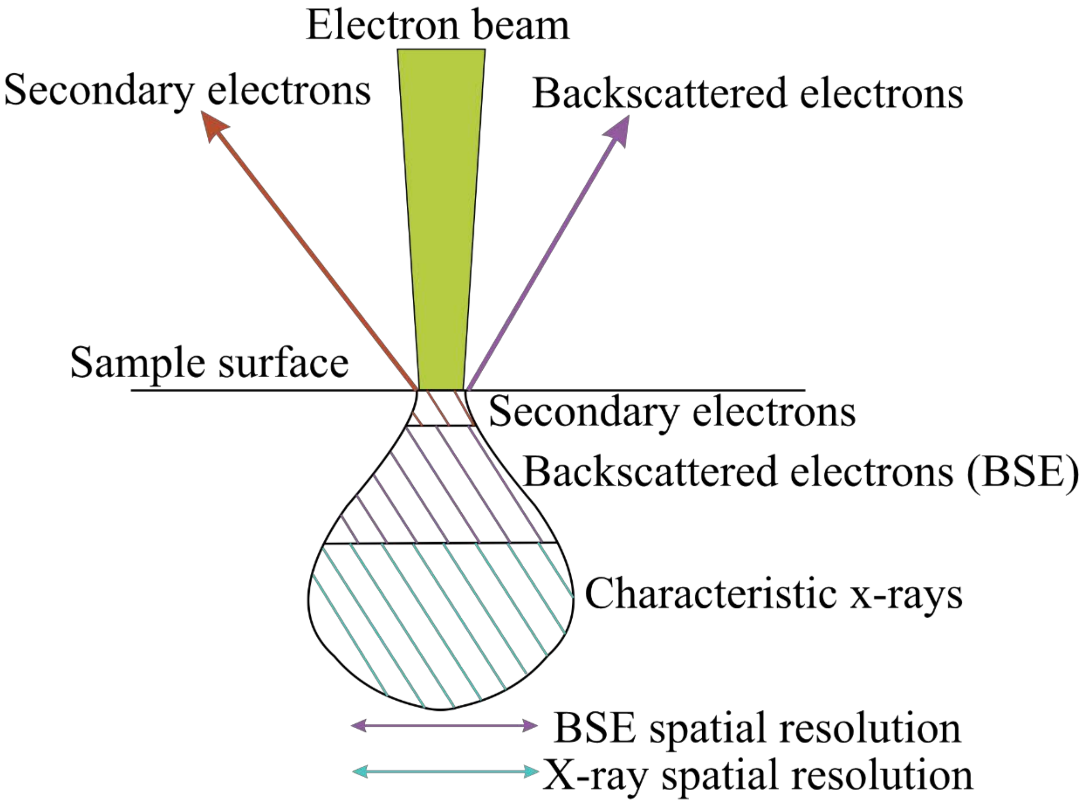

Figure 4.15. Schematic of interactions and subsequent emissions of an electron beam incident on a surface of material.

4.4.5.1 Secondary electron detection

An image of the surface of a material can be taken by raster scanning the electron beam and detecting the secondary electron (SE) emission. The SEs are generated through inelastic scattering of the electrons at the top surface of the material (Figure 4.15), meaning higher resolutions compared to BSE and EDX (energy-dispersive x-ray). Since the SEs are emitted at the top surface of the electron interaction teardrop, it is commonly used to observe the surface of a sample, with topological features down to nm scale able to be observed.

4.4.5.2 Backscattered electron detection

The BSE are generated via elastic scattering of high-energy electrons. This technique has a lower resolution than detection of SE since they are generated by a larger interaction volume

(Figure 4.15). However, heavier elements will backscatter a larger proportion of electrons than lighter elements, meaning the measurement can differentiate between areas of different chemical compositions. This is used in this thesis to differentiate between layers of material with and without RE-doping.

4.4.5.3 Energy dispersive X-ray analysis

X-rays are emitted during the electron's interaction with the material in the form of bremsstrahlung and characteristic X-rays. Bremsstrahlung x-rays are generated through the rapid change in electron velocity when it passes near the nucleus of an atom. Characteristic x-rays are generated when electrons in the inner shell of an atom are ejected through an interaction with a high-energy electron. Subsequently, electrons from the outer shells can lose energy in the form of an x-ray photon via filling a vacancy in the inner shell. When an electron falls from the L shell or the M shell the emission is called the K_α and K_β respectively. The energy of these x-rays will be directly related to the element that created the emission. By detecting these x-rays, the relative composition of elements can be measured and a map of elements in the surface material can be created.

However, when measuring materials with multiple peaks, or a small concentration of one element (<1%) there is a risk of misidentification of elements (Newbury and Ritchie, 2013). This means a prior knowledge of the sample to be measured is essential to ensure reliable EDX measurements. In the work described in this thesis, the EDX measurements were taken using a Oxford Inca PentaFet-x3 EDX analyser attached to the SEM.

4.5 Optical characterisation

Characterization of a sample's optical properties can provide invaluable information about the quality of the sample. The active element, in this case, trivalent RE ions, will have optical properties that will be altered by the surrounding environment. This means, for example, if in a Yb:YAG sample, the ytterbium is incorporated into an aluminium lattice site rather than a yttrium lattice site, the optical properties such as the fluorescence spectrum and lifetime will be affected. This is particularly important in PLD-grown samples, since, due to the non-thermodynamic growth process, the large ytterbium ions can take the place of the small aluminium ions (Heinrich *et al.*, 2012). In this section, the techniques involved in the characterisation of a sample's fluorescence spectrum, fluorescence lifetime and lasing experiments will be presented.

4.5.1 Fluorescence spectrum measurements

These measurements were performed with different setups that will be described in the relevant sections in the results chapters. The basic principle, however, is to either couple pump light into the waveguide, or “face pump” where the pump light with a large (~3 mm) spot size is directly onto the sample’s face. The resultant fluorescence is then collected by a series of lenses or with a proximity-coupled fibre and the light analysed by an optical spectrum analyser (OSA). If the pump light is near any emission features, it can be useful to attenuate the pump light with a long pass filter.

4.5.2 Fluorescence lifetime measurements

The fluorescence lifetime measures the time it takes for ~70% of the electrons in the upper laser levels to spontaneously transition to the lower laser levels. This measurement can be performed with the same basic setup as the fluorescence spectrum measurements. Instead, the pump light is pulsed and the OSA is replaced with a photodiode with a fast rise and fall time. The photodiode will measure the exponential decay in fluorescence intensity as a function of time. Using this measurement and equation 4.2, the lifetime (τ) can be calculated by means of a linear fit with $\ln(\mathrm{I}(\mathrm{t})$ and t. In equation 4.2, I(t) is the intensity as a function of time (t), I_0 is the intensity at t=0 and τ is the fluorescence lifetime.

$$I(t) = I_0 e^{-\frac{t}{\tau}} \tag{4.2}$$

In this experiment, it is important to filter any collected pump light that can contaminate the lifetime signal. The lifetime of samples can be compared to literature values to give an indication of the quality of the film. Smaller lifetimes than expected can indicate the presence of quenching effects, such as multi-phonon transitions or energy transfers (between laser ions, to impurities or to defects in the crystal structure). Therefore, the fluorescence lifetime is a good indicator of the quality of an active material.

4.5.3 Laser experiments

The specific setup for each laser experiment detailed in this thesis will be presented in the appropriate results section. However, as an introduction, a basic waveguide laser experiment will involve coupling pump light into the waveguide which will be absorbed by the active ions. A cavity will be created around the waveguide that is highly reflective (HR) for laser light at the input, and HR for pump light at the output. This can be achieved mirrors or alternatively, the Fresnel reflections of the waveguides can be used as a cavity. The reflection of pump and laser light will provide optical feedback to achieve population inversion of the upper laser level compared to the lower laser level. The output beam is then filtered of any remaining pump light before the output power is measured.

The measured output power compared to the pump power (pump power at the input facet of the sample) can be used to calculate the threshold laser power (minimum pump power in which lasing is achieved) and the slope efficiency (the calculated slope value from a linear fit between pump and output power).

4.5.4 Calculation of loss from slope efficiencies

The propagation loss of a sample can be calculated from the slope efficiencies from measurements with different output mirror reflectivities. This technique assumes the spatial overlap between pump and laser light is the same for each of the output mirrors, as well as the quantum efficiency. Equation 4.3 shows the calculation needed for the propagation loss (May-Smith, 2005) with the symbol definitions shown in Table 4.1.

$$Propagation\ loss = \frac{\eta_A \ln(R_{2B}) \ln(R_1 R_{2A}) - \eta_B \ln(R_{2A}) \ln(R_1 R_{2B})}{\eta_A \ln(R_{2B}) - \eta_B \ln(R_{2A})} \tag{4.3}$$

Table 4.1. Definitions of symbols in equation 4.3

Symbol	**Definition**
$\boldsymbol{\eta_A}$	Slope efficiency with output mirror “A”
$\boldsymbol{\eta_B}$	Slope efficiency with output mirror “B”
$\boldsymbol{R_1}$	Reflectivity of input mirror
$\boldsymbol{R_{2A}}$	Reflectivity of output mirror “A”
$\boldsymbol{R_{2B}}$	Reflectivity of output mirror “B"

4.6 Conclusions and next steps

In this chapter, the PLD setup used in the experiments described in this thesis was presented along with other experimental techniques such as optical polishing. Some of the alterations to the setup were described, including a redesign of the substrate holder and the setup used for the shadow mask experiments. The tools and methodologies for characterisation of the samples were also described.

Other alterations, including designing a new and improved target movement cam and changing beamlines to permanently increase the fluence energy capability will be discussed in sections 5.5 and 8.2.1 respectively. Other experimental techniques such as polishing, were also described. Characterization techniques were detailed with the theoretical concepts and the application to the work in this thesis.

The next four chapters will detail experimental work using the techniques described in this chapter.

4.7 References

Born, M. and Wolf, E. (1999) *Principles of Optics.* Cambridge: Cambridge Univ. Press.

Darby, M. S. B. (2009) *Femtosecond pulsed laser deposition.* PhD, University of Southampton.

Heinrich, S., Gün, T. and Huber, G. 'Neodymium and ytterbium doped sapphire films grown by pulsed laser deposition.', *In Advances in Optical Materials*, San Diego, California United States: Optical Society of America, IF2A-5.

May-Smith, T. C. (2005) *Pulsed laser deposition of thick multilayer garnet crystal films for waveguide laser devices.* PhD, University of Southampton.

May-Smith, T. C., Muir, A. C., Darby, M. S. B. and Eason, R. W. (2008) 'Design and performance of a ZnSe tetra-prism for homogeneous substrate heating using a CO_2 laser for pulsed laser deposition experiments.', *Applied Optics*, 47(11), pp. 1767-1780.

Monneret, S., Huguet-Chantome, P. and Flory, F. (2000) 'm-Lines technique: Prism coupling measurement and discussion of accuracy for homogeneous waveguides.', *Journal of Optics A: Pure and Applied Optics*, 2(3), pp. 188-193.

Newbury, D. E. and Ritchie, N. W. (2013) 'Is scanning electron microscopy/energy dispersive X-ray spectrometry (SEM/EDS) quantitative?', *Scanning*, 35(3), pp. 141-68.

Sposito, A. (2014) *Pulsed laser deposition of thin film magneto-optic materials and lasing waveguides.* PhD, University of Southampton.

Chapter 5 Particulate reduction techniques

5.1 Introduction

Particulates are a critical challenge for the growth of laser waveguide material via the PLD technique (discussed in section 2.2.5). They are detrimental to high-quality epitaxial growth and, via an increased propagation loss and hence decreased slope efficiency, hinder the lasing performance of the resulting waveguides (Barrington *et al.*, 2000).

Two basic methodologies, active and passive, can be used to reduce particulate density. Active methods, for example, the use of velocity filtering, stop the particulates from reaching the substrate. Passive methods, for example, prevent the formation of particulates. The most basic passive technique is the optimisation of growth parameters, which is required to be implemented for each different material. As such, this technique will not be presented in this chapter but in the relevant materials chapter. This chapter will outline my other attempts, using passive and active techniques, to reduce the density of particulates embedded into films during the PLD process.

In this chapter, I will present the use of three methods to reduce particulate density, a shadow mask, segmented targets and bi-directional ablation. With each of these techniques, significant particulate reduction is achieved. The advantages and disadvantages of each technique will be discussed as well as the future directions to exploit these particulate reducing methodologies further.

5.2 Shadow Masks

An active approach to remove the number of particulates is to physically block them from reaching the sample. This takes advantage of the fact that the plume of ions and atoms expand to a greater degree than particulates (Ojeda *et al.*, 2015). The basic theory of this approach is shown in Figure 5.1. Here, the plume, consisting of ions and atoms, expands around the shadow mask (SM) and can be deposited onto the surface of the substrate. However, particulates can be assumed to be ballistic, hence, the particulates will travel in straight lines, meaning an object between them and the substrate will prevent them from reaching the substrate.

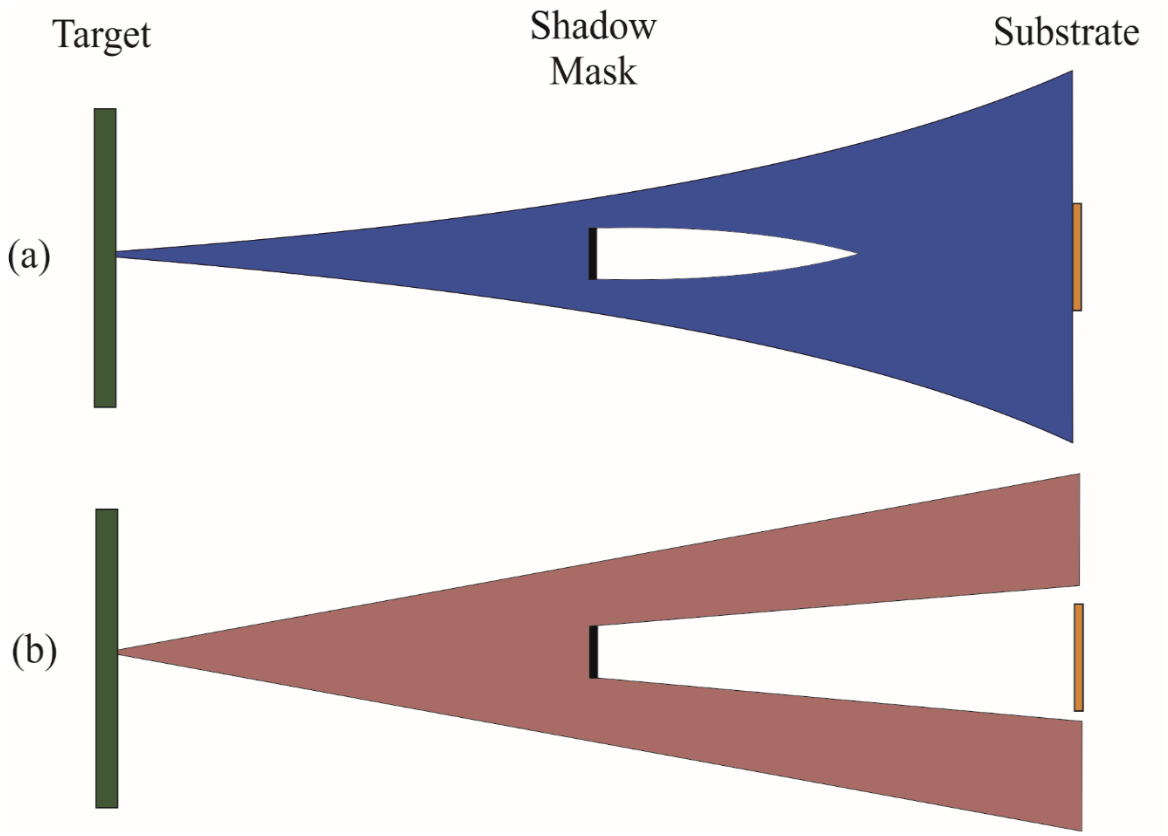

Figure 5.1. Diagram of the plume reacting to a shadow mask for (a) ions and atoms and (b) particulates

5.2.1 Methodology

As seen in Figure 4.5, a SM consists of a sheet of material blocking the central region of the plume that would be directly depositing onto the substrate. The SM, a 10x10x0.5 mm plate of aluminium (material choice was discussed in section 4.2.6), was suspended between the target and the substrate using an aluminium rod. This size was chosen to match the substrate size. A photograph of this setup is shown in Figure 5.2. After initial experiments with this setup, it was found that the deposition was non-uniform with the outer regions of the substrate having a substantially higher deposition rate. Further experiments found that smaller shadow masks of 6x6x0.5 mm suspended by tungsten wire provided a uniform growth across the substrate. The optimum size of shadow mask will vary depending on the spot size, background pressure, target-substrate distance and shadow mask position.

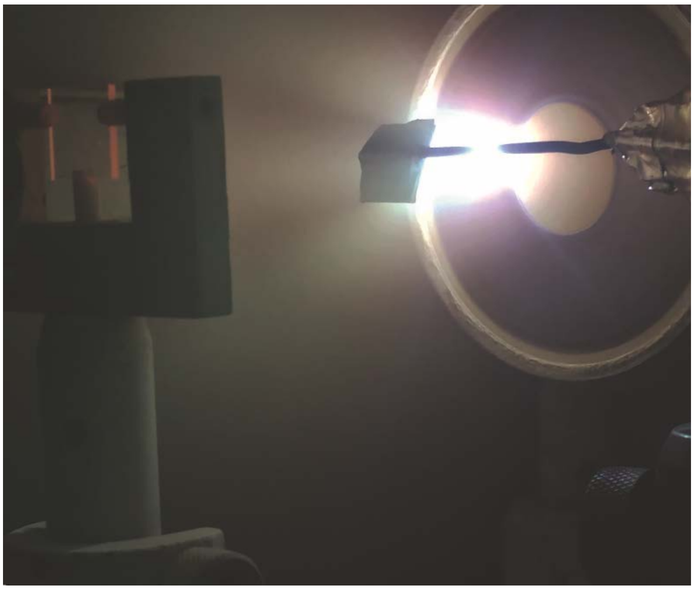

Figure 5.2. Photograph of SM with a 10x10x0.5 mm aluminium plate suspended with an aluminium rod.

5.2.2 Scattering point density

Using this SM setup, a $LuScO_3$ film was grown with 36000 shots at an ablation fluence of 1.05 Jcm^{-2}. The resultant growth was wedged with the film being 300-nm-thick film on one side, and 100 nm on the other. This means that the shadow mask was too large to allow a significant number of atoms and ions to deposit onto the substrate and was positioned non-centrally with respect to the ablation-spot on the target and substrate.

Growths using an ytterbium-doped mixed Lu_2O_3 and Sc_2O_3 target were performed with and without the shadow mask with 1.05 Jcm^{-2} ablation fluence and 25 W of substrate heating power. The growth rate was reduced from 10 µm/hr to 3 µm/hr when using a SM. Figure 5.3 shows dark field images for the resulting deposited films with and without a shadow mask grown under comparable conditions. The scattering-point density (as discussed in section 4.4.1) measures the observable defect density via dark-field microscopy and for these images is 38.5 % without a SM and 0.49 % with. This demonstrates a 78-fold reduction in particulate density.

Table 5.1 displays the samples grown with a SM compared to a typical growth without a SM. The growth rate of JP55 is significantly smaller than JP54 due to target degradation when a target is used for a substantial period of time. The particulate density of JP8 is much greater than any sample which used a shadow mask, but also has a larger growth rate of

10 µm/hr, showing the trade off with growth rate and particulate density with the SM technique.

Table 5.1. Growth parameters of films grown with different types of shadow mask grown at 100 Hz, 1.05 Jcm^{-2} ablation fluence and 25 W substrate heating power.

Sample number	**Material**	**Number of shots**	**Shadow mask size (mm)**	**Growth rate (µm/hr)**	**Particulate density (%)**
JP47	$LuScO_3$	36000	10x10	1-3	0.53
JP54	$LuScO_3$	36000	6x6	3	0.49
JP55	$LuScO_3$	540000	6x6	1.3	1.05
JP8	$LuScO_3$	36000	None	10	38.5

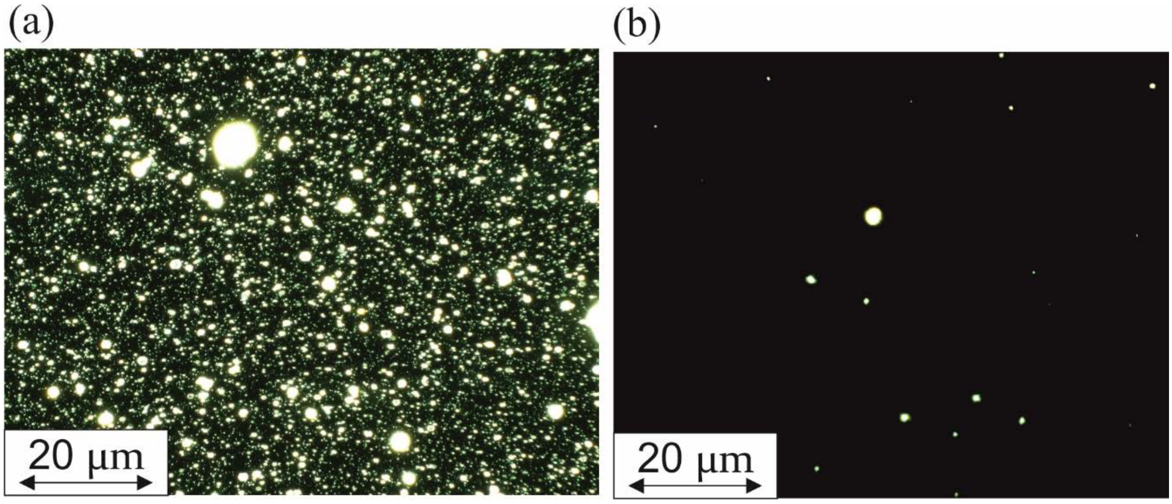

Figure 5.3. Dark field microscopy optical images of films grown from a ytterbium-doped mixed-sesquioxide target (a) without a SM (JP8) and (b) with a 6x6 mm SM (JP54).

5.2.3 XRD measurements

When using a SM to grow materials with multiple constituents, the stoichiometry of the growth will likely be different compared to a growth without a SM. This can be explained with the different rates of plume expansion depending on material (detailed in section 2.2.2.2). To test this, XRD measurements were taken of a film grown with a SM (JP54) and without a SM (JP8).

Figure 5.4 (a) shows the (222) XRD peak for the film grown with (blue line) and without (green line) the SM along with the database locations of scandia and lutetia (222). There is a shift of ~0.5° in the 2θ peak position towards the Sc_2O_3 peak when using the SM, implying that the ratio of scandia to lutetia is increasing. This is due to the size difference between scandium and lutetium; a plume consisting of lighter elements expands to a greater degree than heavier elements so a larger proportion of scandium will reach the substrate. The FWHM also increases from 0.03 to 0.05 ^{o} when using a shadow mask; this can be explained by the presence of a lutetia (622) peak as seen in Figure 5.4 (b). Domains of different orientations of the crystal will disturb the lattice causing stress at the boundaries of the different orientations. The stress can cause the broadening of the peaks as seen in Figure 5.4 (a).

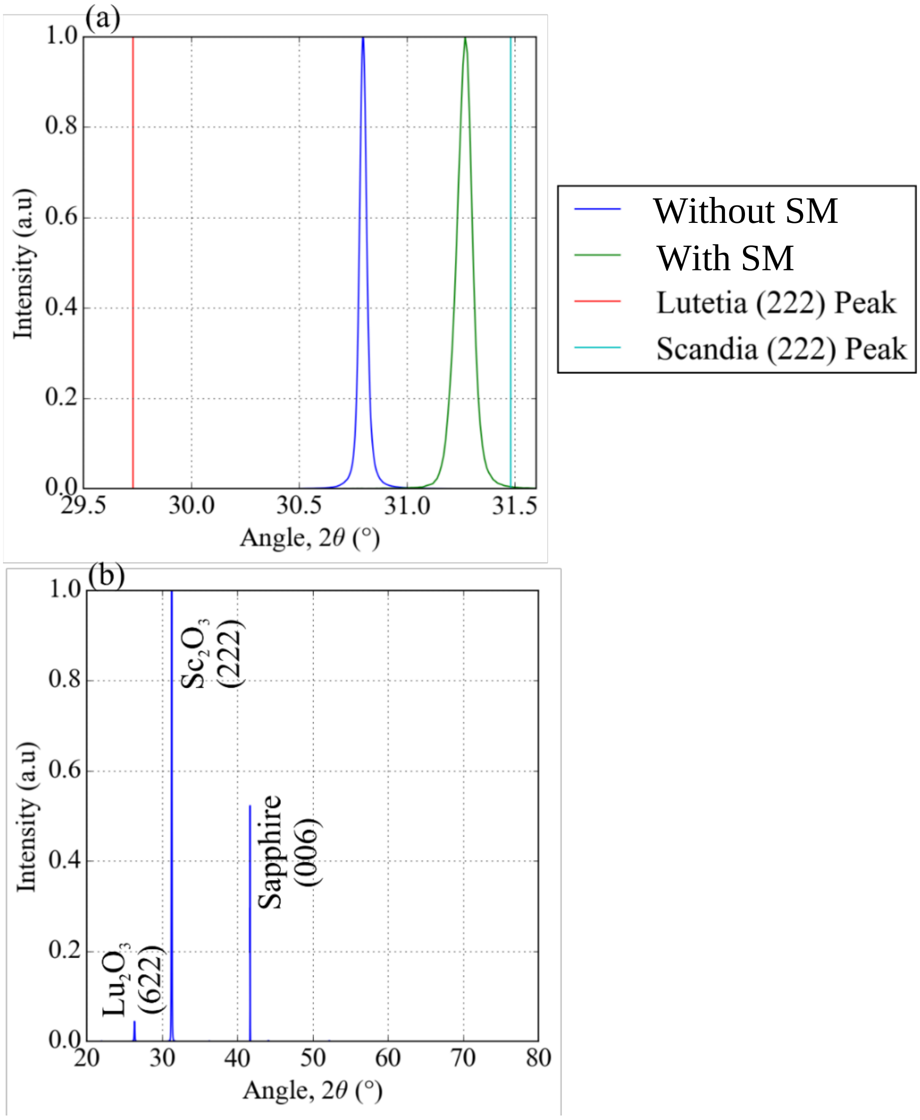

Figure 5.4. (a) XRD spectrum of sample number JP54 grown from mixed sesquioxide target with a SM (green line) and a comparison of the (222) peak of sample number JP8 grown from the same target without a SM (dark blue line). The locations the lutetia and scandia (222) peaks are indicated by the red and light blue line respectively. (b) XRD spectrum from 20^{o} to 80^{o} of JP54 with the peaks labelled with material and orientation.

5.2.4 Limitations and Future Improvement

I have shown that the SM technique can be used to reduce the particulate density by nearly 78x. With the mixed-sesquioxides, the expected amount of the heavier element is reduced in the final composition of the film. This will also be true when growing with RE-materials, making growing active waveguides with this technique challenging. One potential solution would be a velocity selective gas jet to increase the diversion of the plume around the substrate. This would create a more stoichiometric transfer of materials from target to substrate and it would likely increase the growth rate.

Attempts to grow Yb:Lu_2O_3 to a viable thickness (>10 µm) to use as a waveguide and with a growth rate of just 3 um/hr would exceed the typical life span of the ceramic targets by requiring over 3 hours of growth, or over 1 million pulses. This would significantly degrade the target's surface and would require growths of Yb:Lu_2O_3 with a SM to determine how significant this would be to the quality of the growth.

Despite having advantages of reducing the density of particulates embedded into the growing film, a major drawback is the limited growth rate and altered stoichiometry of ternary films. However, the growth of Yb:Lu_2O_3 would not suffer the same stoichiometry alteration since ytterbium and lutetium are similar masses. This avenue was not explored any further due to time constraints and the adoption of the bi-directional ablation technique mentioned earlier.

5.3 Segmented targets

In chapter 2, I discussed the manufacturing process of the targets used in our PLD system. These targets are formed from a mix of binary oxide powders, which are pressed and sintered into a ceramic disc. During the fabrication process, clustering of materials can occur causing domains. Typically, these domain sizes will be on the order of microns to millimetres and will each have different ablation thresholds and material ejection rates. As a consequence of the clustering and different ablation thresholds across the target surface, LIPSS (laser induced periodic surface structure) appears during target ablation, manifesting as cones facing towards the ablation laser beam (Ashfold *et al.*, 2004). As the surface structure develops, the tips of the cones exfoliate, embedding themselves into the growing film. Observations in this work showed that LIPSS do not appear in binary targets since any domains will have the same ablation characteristics, as shown Figure 5.5. This shows SEM images of ablated gallia and yttria targets ((a) and (b)) and a ternary YG (Y_2O_3 + Ga_2O_3) target (c).

In this section, the fabrication of a target made of sections of binary targets is presented. Using a segmented target, I grew a YGG film and compared this with a similar growth using a ternary mixed target. DF microscopy images were used to compare the scattering point density and XRD measurements to compare the crystallinity and stoichiometry.

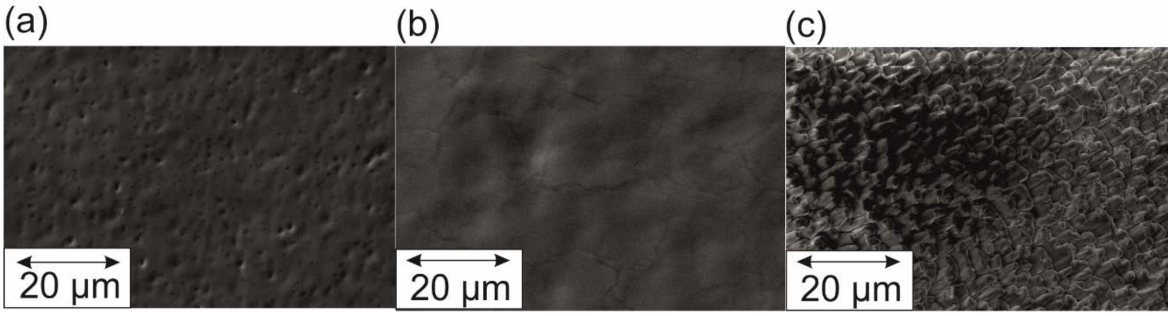

Figure 5.5. SEM images of targets after 180,000 shots for (a) Ga_2O_3, (b) Y_2O_3 and (c) YG

5.3.1 Comparison of segmented targets and mixed targets

(Sloyan *et al.*, 2009) demonstrated that by using multiple binary targets and ablating each target with alternate ablation pulses, a single crystal, ternary film can be grown. This was shown to be effective, however an alternative method using just one laser and one target is to use a segmented target. To demonstrate this, a gallia and a yttria target were diced into two segments using a diamond cutting disc attached to a rotary cutting tool as seen in Figure 5.6. The segmented target pictured, is $\frac{3}{8}$ Y_2O_3 and $\frac{5}{8}$ Ga_2O_3, so when mixed via ablation, the aim is to create crystalline $Y_3Ga_5O_{12}$, or stoichiometric cubic YGG. This target ratio assumes an equal deposition rate when ablating the yttria and gallia segments.

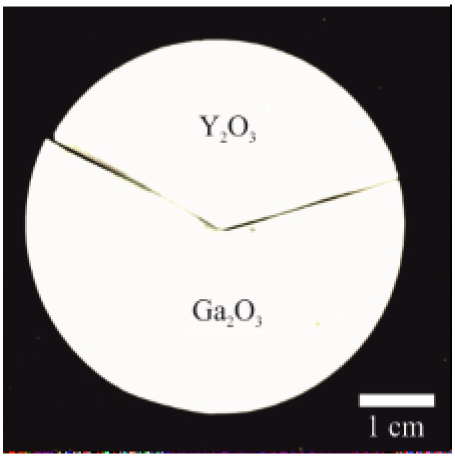

Figure 5.6. Photograph of a segmented target with $\frac{3}{8}$ Y_2O_3 and $\frac{5}{8}$ Ga_2O_3.

Dark-field images were taken of films grown with a mixed YG target (Figure 5.7 (a), J94) and a segmented yttria and gallia target (Figure 5.7 (b), J127) using the same conditions. The scattering point density for the J94 was 5.3 % and for J127 was 0.02 %, demonstrating a ~250-fold decrease in scattering point density when grown with the segmented target.

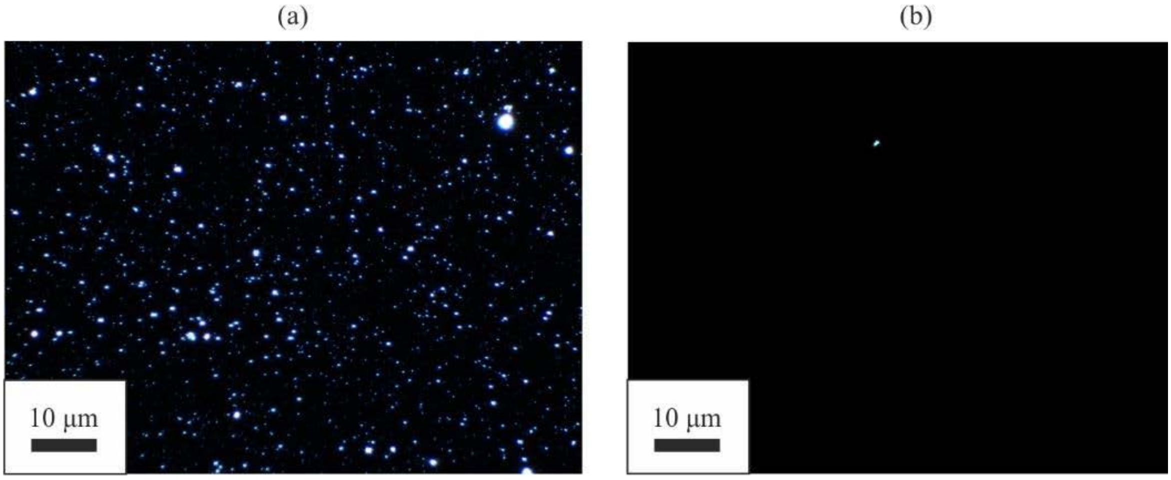

Figure 5.7. Dark-field images of films grown with (a) a mixed YG target (J94) and (b) a segmented YG target (J127) taken from (Grant-Jacob *et al.*, 2018)

Figure 5.8 (a) shows the XRD spectra of J94 (green dotted-line), along with the XRD spectra for J127 (green solid-line). Crystalline YGG has been grown using the segmented target, and the film has the correct phase of $Y_3Ga_5O_{12}$ since the (400) YGG peak position (2θ) from the film is an exact match to the value found in literature (29.06° (Grant-Jacob *et al.*, 2017)). The film grown from the mixed YG target, has a (400) peak position of 28.86°, 0.1° lower than that of the database value (or 0.02 nm larger lattice constant than stoichiometric YGG), indicating a non-stoichiometric growth, having relatively less gallium content than stoichiometric YGG (Mackenzie *et al.*, 2017).

The YGG (400) peak of J127 has a broader FWHM (0.11°) than the (400) peak of J94 (0.03°). This can be explained by the mechanism of deposition, which uses a segmented target that leads to sequential deposition of Y_2O_3 and Ga_2O_3, unlike growth from a mixed target, where Y and Ga will be deposited simultaneously. As discussed in Chapter 2, sequential deposition with a dual target system can be used to grow single crystals, or layers of material depending on how many pulses are used in the sequential ablation. If a film is grown with 5 pulses of one material, and 5 pulses of another, a mix of the materials will be grown since it takes multiple pulses to grow a monolayer. However, if 50 alternate pulses are used, layers of binary material will be grown. For the segmented target growth (J127), on average, 12.5 sequential pulses ablate the Ga_2O_3 section of the target, per rotation. Using preliminary tests, this could grow a 0.625 nm layer of Ga_2O_3. Similarly, the Y_2O_3 segment is ablated by an average of 7.5 pulses per rotation, potentially growing ~ 0.375 nm. This means sublayers of Ga_2O_3 and Y_2O_3 could be grown in addition to the observed $Y_3Ga_5O_{12}$ and is confirmed in Figure 5.8 (b). Here, small peaks of (202) Ga_2O_3 and (721) Y_2O_3 (0.3% and 0.1% of the (400) YGG peak respectively) can be seen. It is out postulate that these integrated layers of gallia and yttria are the source of the broadening of the YGG (400) peak.

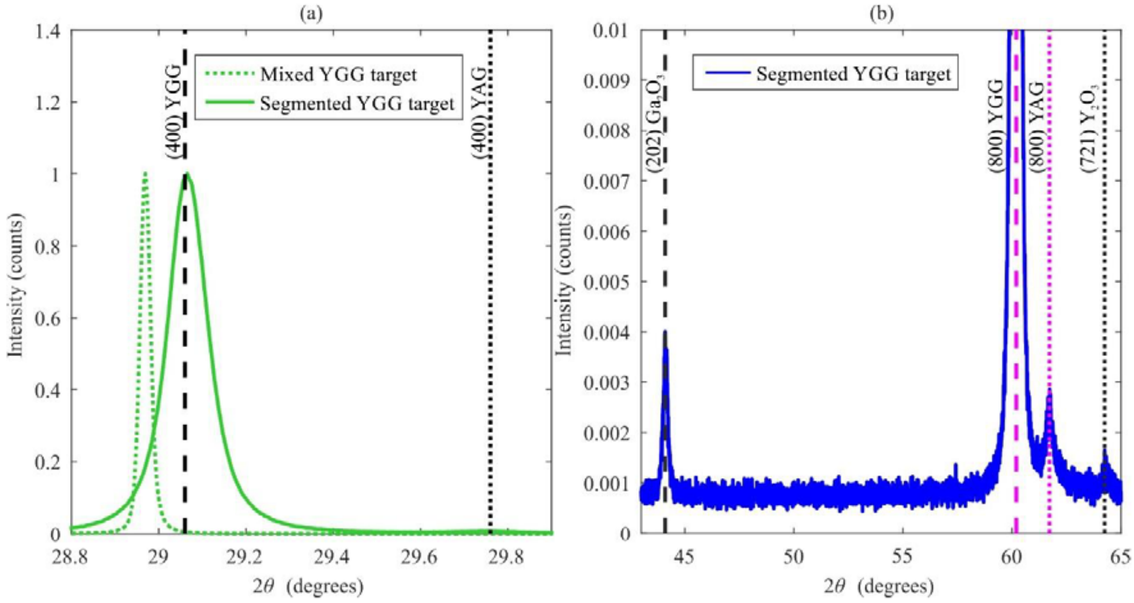

Figure 5.8. XRD spectra showing the (400) peak of YGG films grown via a mixed and segmented YG target (a) and an XRD spectra of a YGG film grown from a segmented target showing the (202), (800) and (721) peak (b). The dotted and dashed lines indicate the labelled database values. This figure was taken from (Grant-Jacob *et al.*, 2018).

These layers of different material could potentially increase the propagation loss in these samples, through scattering at the interfaces between each material. However, previous research into sequential ablation of different materials shows that if the number of shots per binary section of the target is decreased, the prevalence of binary crystal structures in the sample is also decreased (Sloyan *et al.*, 2010).

5.3.2 Limitations and Future Improvement

Segmented targets require circular discs to be cut into the required segment dimensions. Even if these are perfectly cut, there will still be an interface between each segment which, when ablated, could change the angles of the plume and the energy striking each segment. This could be avoided by not ablating these interfaces, via linking the movement of the target and the ablation pulses. This could also be utilised to control the number of shots per segment in each rotation, such that the ratio of pulses per segment is constant. The ratio of pulses per segment could then be optimised to provide a growth without binary layers of materials. This technique has similar advantages to a multi-beam, multi-target setup, which has been previously researched (Sloyan *et al.*, 2012). In the multi-beam technique, binary targets are ablated simultaneously at an angle to the substrate, meaning the plume would be arriving at at an angle. This requires the substrate to be continuously rotated to achieve a uniform growth on the substrate. The advantage of segmented targets over this system is that the plume is still perpendicular to the substrate, allowing for a more uniform growth on the small 10x10 mm substrates used in our PLD setup with rotation of the substrate.

5.4 Uni-directional Ablation

Ablating one point on a target will remove material and effectively drill down into the target. This will alter the plume dynamics and change the stoichiometry of the growing film. A simple method of reducing the particulate density in grown films is to change the location of ablation on the target. This reduces the prevalence of LIPSS and, if ablated uniformly across the surface, reduces the roughness (Sa) of a post-ablated target. It is important to ablate from a flat surface since the plume will travel away from it along the surface normal. In this section, I briefly discuss uni-directional ablation (UDA) as a technique of increasing the target utilisation and particulate reduction. UDA involves the rotation and translation of the target, whilst maintain a unique angle of incidence to the surface.

At the beginning of this PhD project, the PLD chamber had been configured with a cam designed to move the target in an epitrochoidal motion to utilise more of the target’s surface. This can be seen in Figure 5.9, where simulations of this motion are displayed after numerous pulses (100-1000), along with a photograph of a target after 36,000 ablation pulses. Using this motion, approximately 50% of the target’s available surface is utilised.

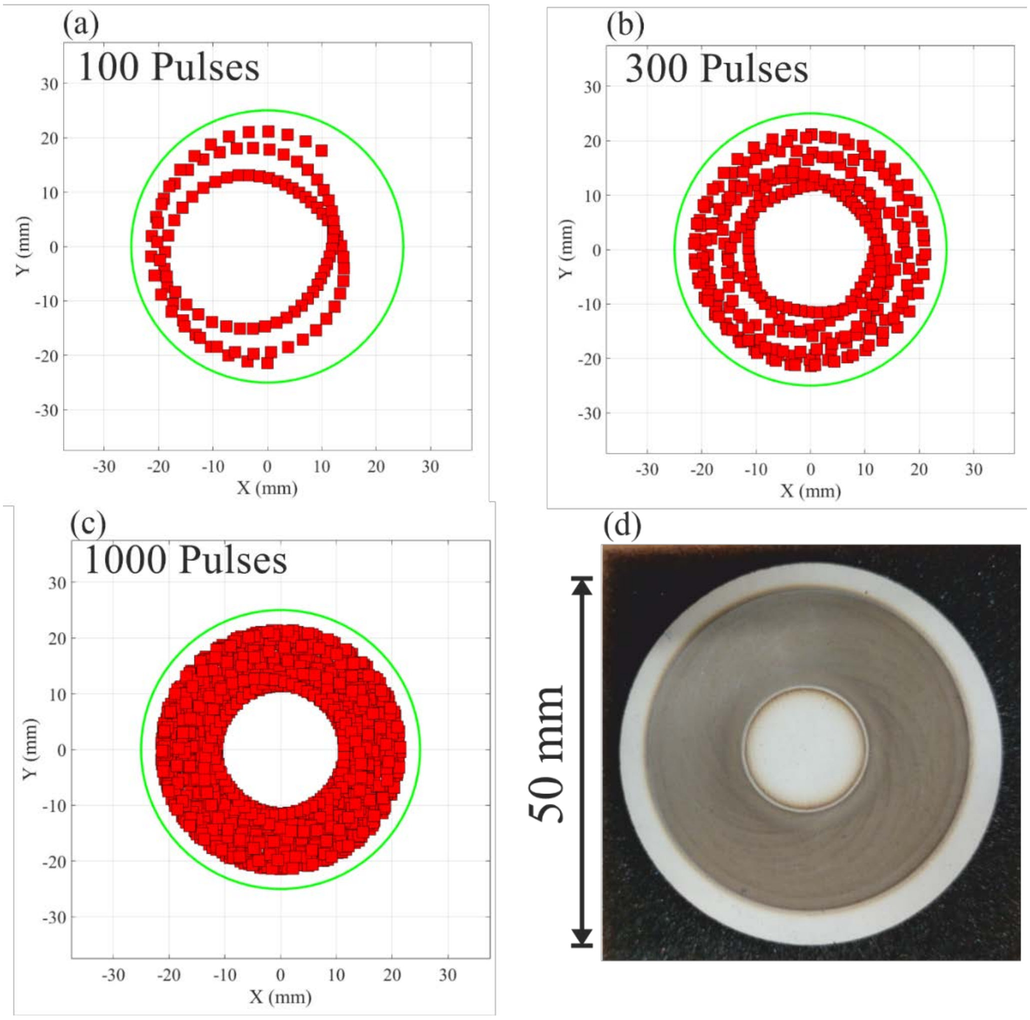

Figure 5.9. (a) (b) and (c) Sequential progression of the ablation spot position on a 25-mm radius target undergoing epitrochoidal motion, with a cam radius and offset of 15 mm and 12.5 mm, respectively. (b) A photograph shows an ablated YG target after 36,000 pulses for the same configuration.

In our PLD process, targets are sourced from three companies Testbourne Ltd, Scotech Ltd and Sindlhauser GmbH. By using pressed ceramic discs instead of using single-crystals, targets can be created with the exact composition required. However, using powders means there can be phases of binary material of micron sizes in the resultant target. I observed that the surface structure of such targets became altered due to the different ablation thresholds of each component. As the laser ablates from one distinct angle and direction, cone-like structures were noted to point back along the direction of incidence of the ablation laser beam (Ashfold *et al.*, 2004). Exfoliation of the cone-tips during ablation and thereby become deposited onto the growing film. This is shown in Figure 5.10, which shows an SEM image of a YG target ablated via UDA with 10,000 shots/cm^2.

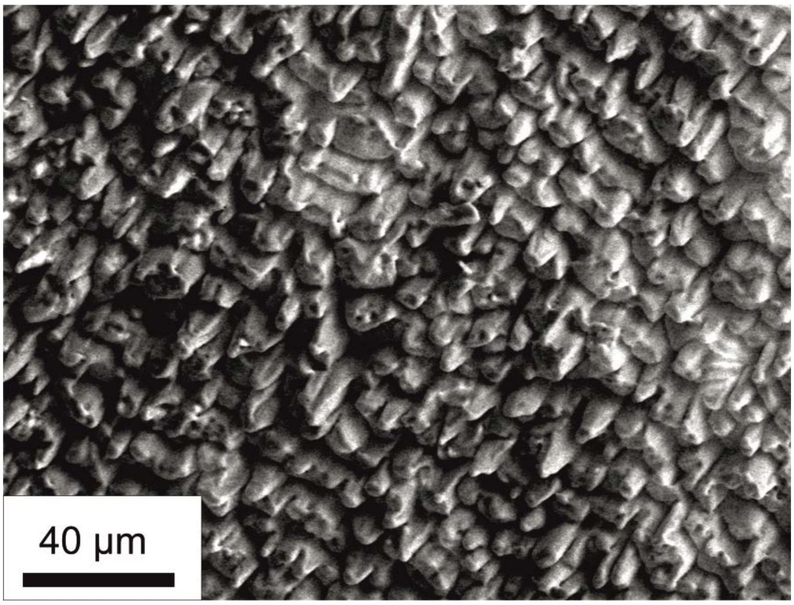

Figure 5.10. SEM image at 750x magnification of a YG target after ~10,000 shots/cm^2.

5.5 Bi-directional Ablation

In order to mitigate the directional surface structuring discussed in the previous section, one solution can be to alter the angle of ablation during the ablation process. The hypothesis underlying this idea is displayed in Figure 5.11, where ablation from one angle ((a) and (b), UDA) cause LIPPS, whereas ablation from two angles cancels out the effects of the other ((c), bi-directional ablation (BDA)), ideally leaving a flat surface on the target.

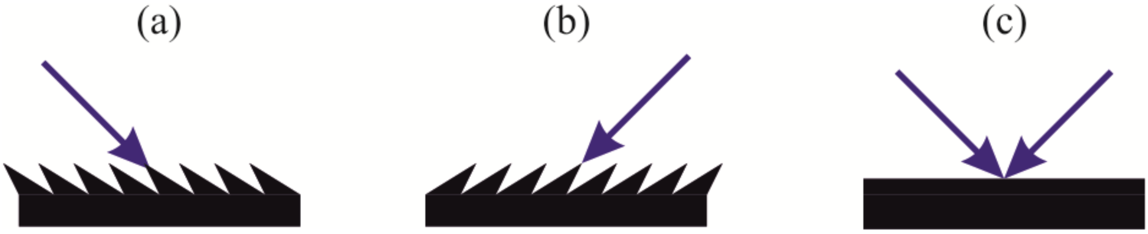

Figure 5.11. (a) Cone production from pulses incident at one unique angle, (b) from an equal and opposite angle, and (c) the resulting ideal situation corresponding to the combination of (a) and (b) either simultaneously, or sequentially as in the case discussed in this work.

The BDA technique does not involve adding another ablation laser. Instead, I devised a method to move the target in such a way to achieve BDA by ablating from opposite angles sequentially instead of simultaneously. In fact, a simple device is achieved by extending the concept of epitrochoidal motion and displacing the target fully across its central axis while maintaining target rotation. This will continue the inherent epitrochoidal motion, but also means a laser pulse hits the target at the same point but when the target is displaced at extreme and the other extreme (an exception is the target's rotational centre, which will be discussed in section 5.5.4). Ablating each area of the target when it is at two different locations, from the target's frame of reference, means the incident laser appears to be coming from two equal and opposite directions. Epitrochoidal motion was also used in UDA, but the displacement was only 12.5 mm and did not cross the central axis of the target.

An offset-cam was designed to provide BDA by increasing the displacement of the target to 45 mm, 5 mm less than the diameter of the target. An additional advantage is that the position of the plume is stationary, which, for small substrates, is required to ensure the film stoichiometry is consistent throughout the growth. The schematic and CAD design of the cam is presented in Figure 5.12.

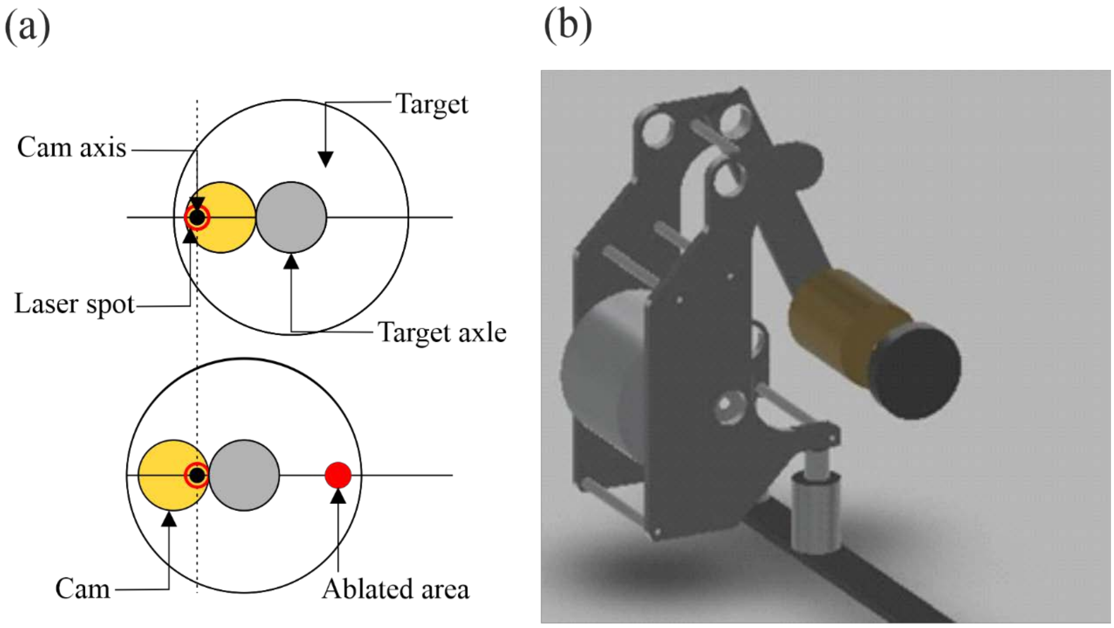

Figure 5.12. (a) Schematic of the rotational geometries of the BDA cam and (b) CAD (computer aided design) image of the BDA cam setup.

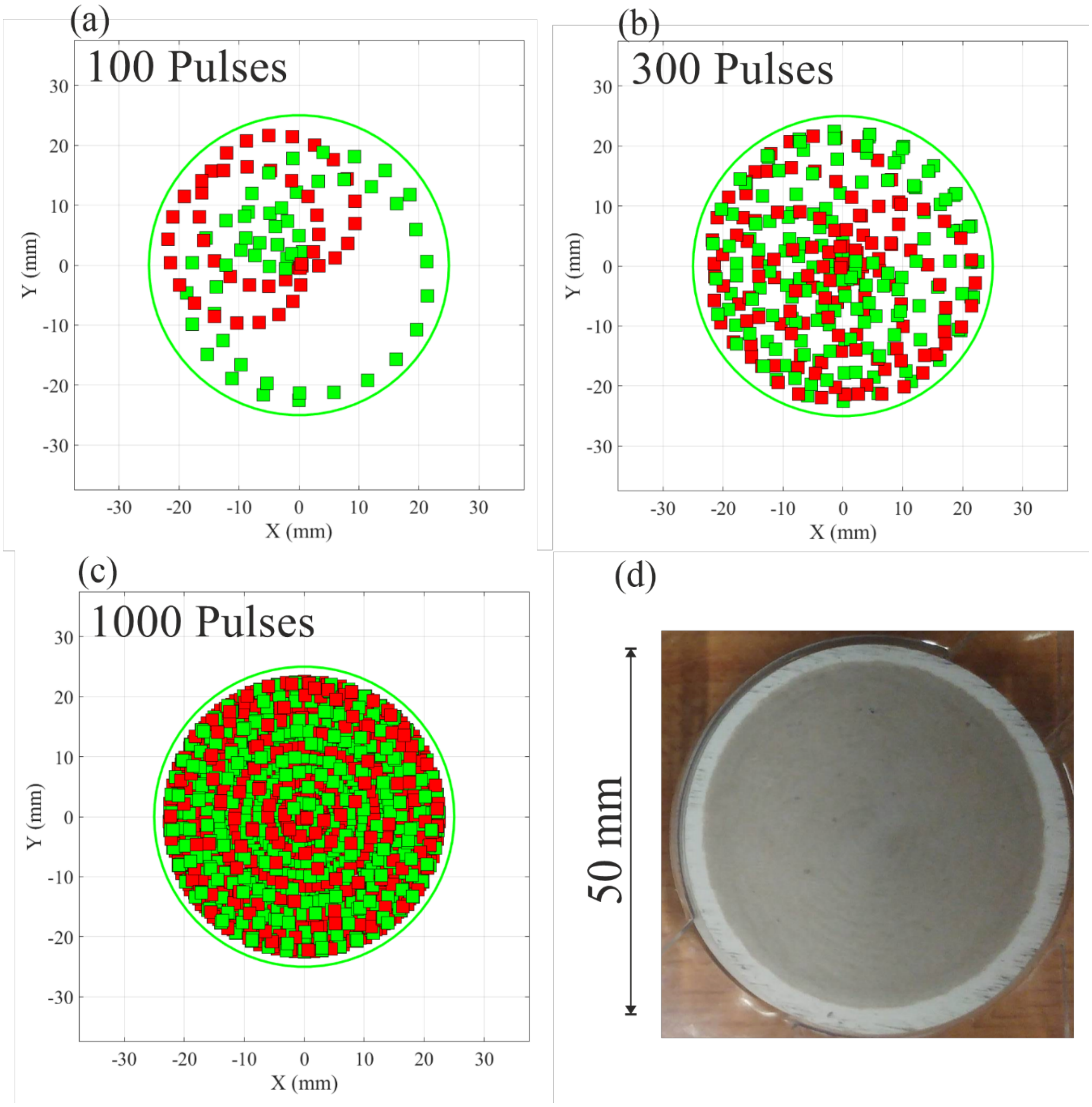

Figure 5.13. (a) (b) and (c) show a model of the ablation pattern with the BDA arrangement after 100, 300 and 1000 pulses. Red and green squares indicate opposing angles of incidence between the laser beam and target normal. The green circle indicates the perimeter of the target. (d) A photograph of a target that has undergone 36,000 ablation pulses is also shown

An offset-cam was built with two gears with one gear spinning off-centre. The critical parameters, to ensure maximum target utilisation and that all areas of the target are ablated equally from both directions, are the radii of both gears and the magnitude of the offset. Simulations were created in MATLAB to find the optimum values for these parameters using equations for epitrochoidal motion. 22.5 mm offset and 80 mm diameter on one gear was chosen to ensure a 45 mm displacement and the diameter of the other gear was varied. Figure 5.13 shows the results of simulations of the progression of the ablation spot on a target for a cam comprising of gears with a 22.5 mm offset and 80 mm diameter, and 0 mm offset and 47 mm diameter. The green/red spots in Figure 5.13 signify the ablation angle from opposing directions, respectively. This setup was shown to be the optimum and Figure 5.14 shows photographs of the targets after 36000 shots when using gears of different sizes, showing the dramatic difference the radii of the gears make.

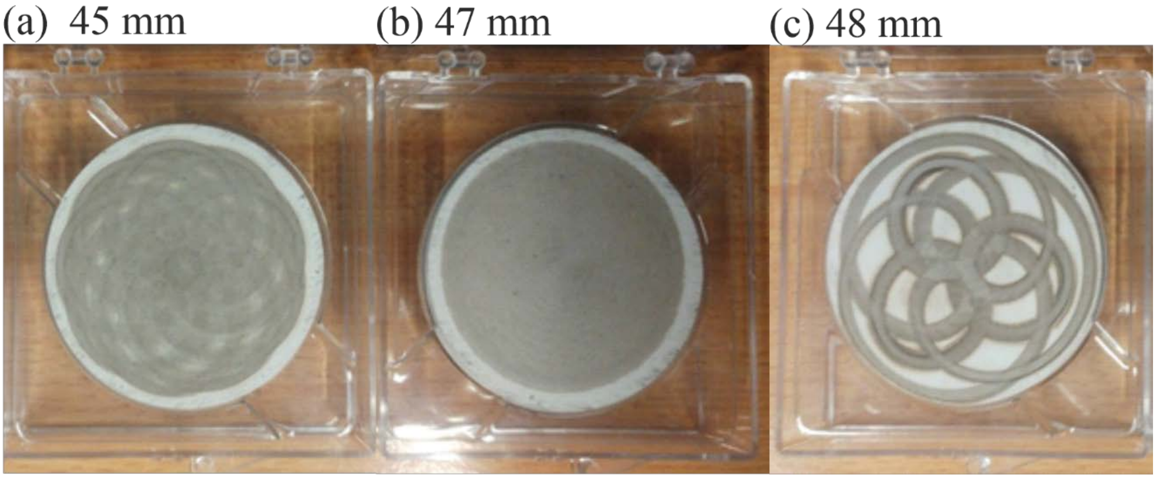
(a) 45 mm (b) 47 mm (c) 48 mm

Figure 5.14. Photographs of targets after 36,000 ablation pulses with the 0 mm offset gear diameter of (a) 45 mm, (b) 47 mm and (c) 48 mm.

5.5.1 Effect of Bi-directional Ablation on Target Morphology

Previously, in section 5.4, I demonstrated that the surface of a ternary target when ablated via UDA develops cone like structures, directly related to the direction of the incoming laser beam. BDA has been designed to ablate the targets from two different directions that will in theory, prevent directional surface features from forming. In this section, the morphology of targets exposed to UDA and BDA are compared. SEM images and stylus profiler measurements of ablated target surfaces provide quantitative metrics to determine the surface roughness and morphology.

YG targets were ablated with UDA on one face and BDA on the other face. However, the BDA setup utilises more of the target, meaning the number of pulses per area for BDA is ~2x less than UDA assuming the same number of net pulses.

Figure 5.15 shows SEM images of the same target, ablated using the same density of irradiation pulses using UDA (a) and BDA (b). Directional cones are observed on the target under UDA, but not with BDA, although, micron-sized surface structure is still present. The inset in Figure 5.15 (a) shows the presence of smaller particles that do not seem to be securely attached to the target. There is also evidence of cracking forming on the UDA target, as seen in the inset, whereas the inset for the BDA shows no sign of small particles or cracking.

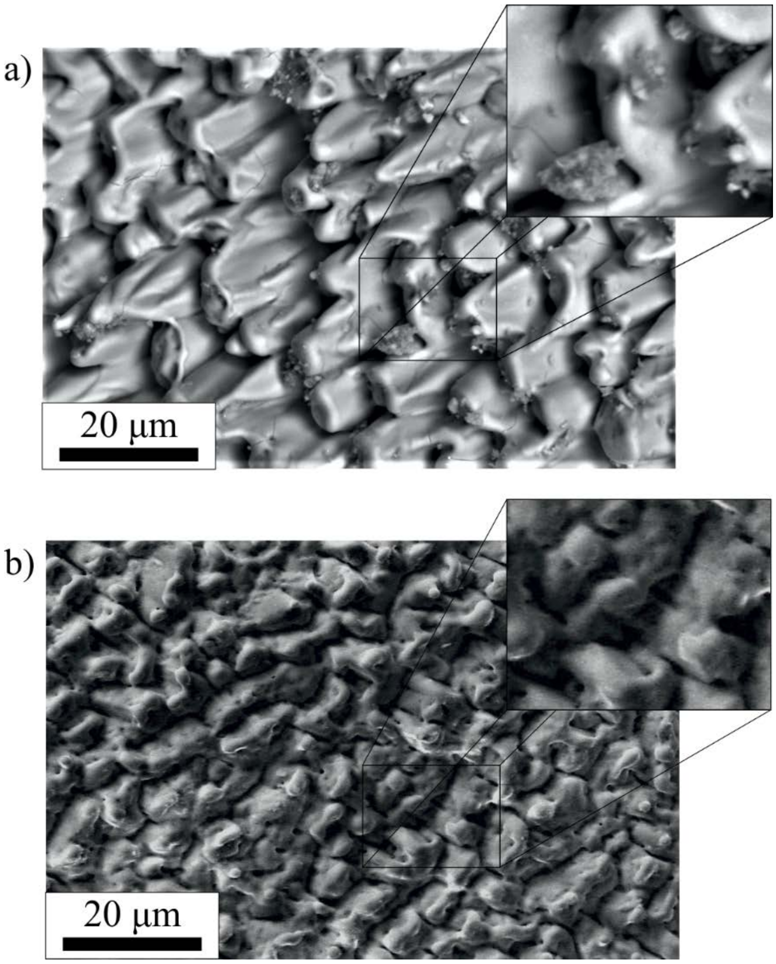

Figure 5.15. SEM images of surface of an ablated YG target after irradiation with ~ 36,000 pulses/cm^2 using the (a) UDA and (b) BDA protocols. The insets highlight small particles and evidence of a "crack" in (a), which could be dislodged and deposited onto the growing film and were only observed for UDA runs, i.e. no small particles can be found in (b).

Figure 5.16 shows stylus profiler measurements of a section of the surface of the ablated YG targets presented in Figure 5.15, and the target where it had not undergone ablation. The peak-to-valley range shows a ~50% reduction for BDA as compared to UDA. The post-ablation structure when using BDA is also only a factor of two larger than a new and unused target. These results are promising, with an additional advantage that it also implies slower target degradation, meaning the target can be used for extended periods before the need for reconditioning to remove significant structure that may affect deposition efficiency and quality.

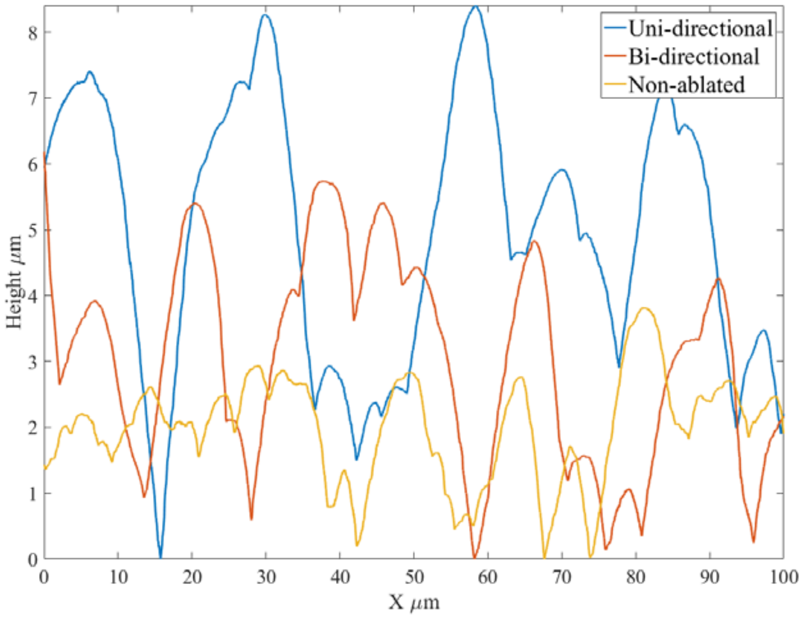

Figure 5.16. Stylus profiler measurements of YG targets prior to use (yellow), after UDA (blue), and BDA (orange).

Although the surface roughness has been reduced, and highly directional cone formation stopped, there is still surface structure being formed. This is considered to be because the target has domains of different material with different ablation thresholds.

The cones formed from ablation have been observed before by (Ashfold *et al.*, 2004), who commented that the most likely explanation was the different ablation thresholds of constituent parts, noting further that they have not been observed when binary/pure elemental materials are ablated. In this section, I have shown how to avoid these cone-like structures using bi-directional ablation, reducing the post-ablated peak to trough value compared to UDA by 50%.

5.5.2 Effect of Bi-directional Ablation on Film Quality

The previous section reported the improvements in the target surface quality of BDA compared to UDA. In this section, I will present the effect on the quality of the resultant films when using BDA, including a decrease in particulate density and surface roughness.

Two films (samples JP65 and JP87) were grown from the same target, albeit from the opposite faces, with an ablation fluence of 1.3 Jcm^{-2} and a substrate temperature of ~700 ^{o}C (using BDA and UDA). These films were then measured with DF microscopy and analysis of these was performed using the pixel intensity method as described in Chapter 2. To demonstrate the repeatability of the BDA technique, 19 other YGG films were grown via BDA with various growth conditions. These samples were also characterised using the pixel-intensity method and white light interferometery to measure the surface topology, from which the number of surface particulates could be determined using the automated function in SPIP. These growths were compared to 28 YGG samples grown via UDA.

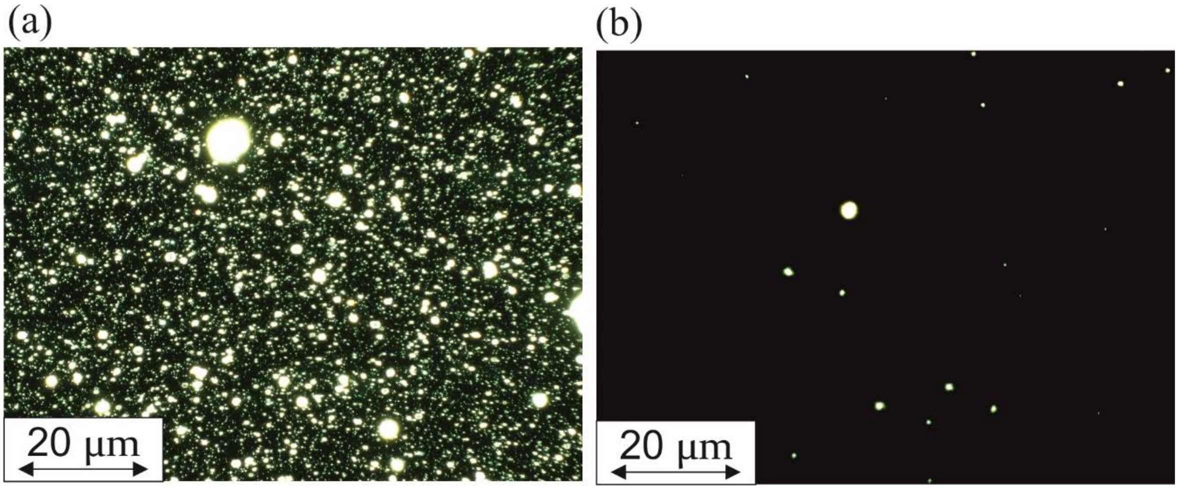

Figure 5.17. Dark-field microscopy images, at 100x magnification, of films grown under the same growth conditions, via UDA (a) and BDA (b).

DF images of samples JP65 and JP87 are shown in Figure 5.17. There is a significant decrease in the density and size of particulates when using BDA. The percentage area of the images that is scattering light, using a threshold of 10% of the maximum intensity, is 3.25 % and 0.27 % for UDA and BDA growths respectively, a greater than 10-fold reduction.

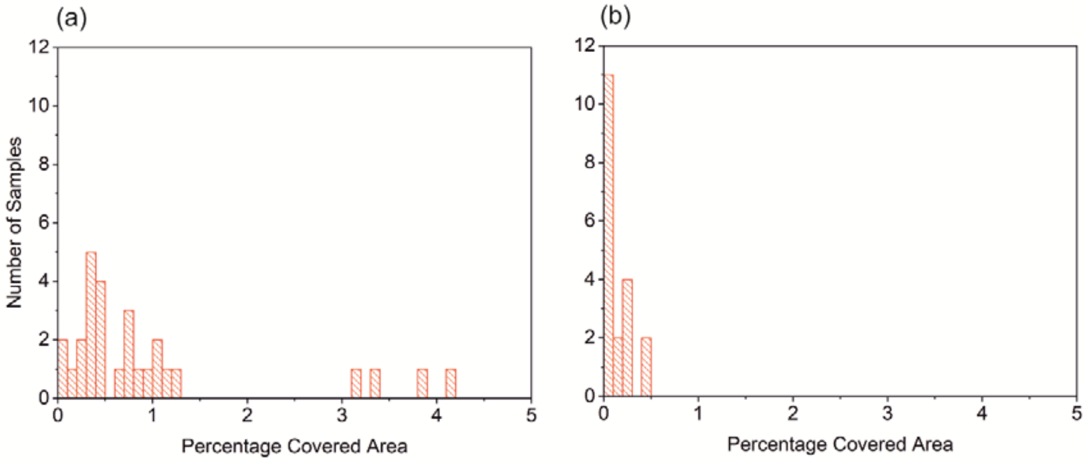

Figure 5.18. Histogram of the percentage of area covered by scattering points in dark field images, at ×100 magnification, when grown via UDA (a) and BDA (b).

Figure 5.18 displays a histogram of the measurements made of the DF images of films grown via UDA (a) and BDA (b). For the films grown with UDA, the average scattering density is

(1.0 ± 0.22) % based on 28 samples and for BDA (0.17 ± 0.03) % based on 19 samples. The uncertainties were calculated using the standard error. This demonstrates an average factor of 5 decrease in scattering sites when using BDA compared to UDA.

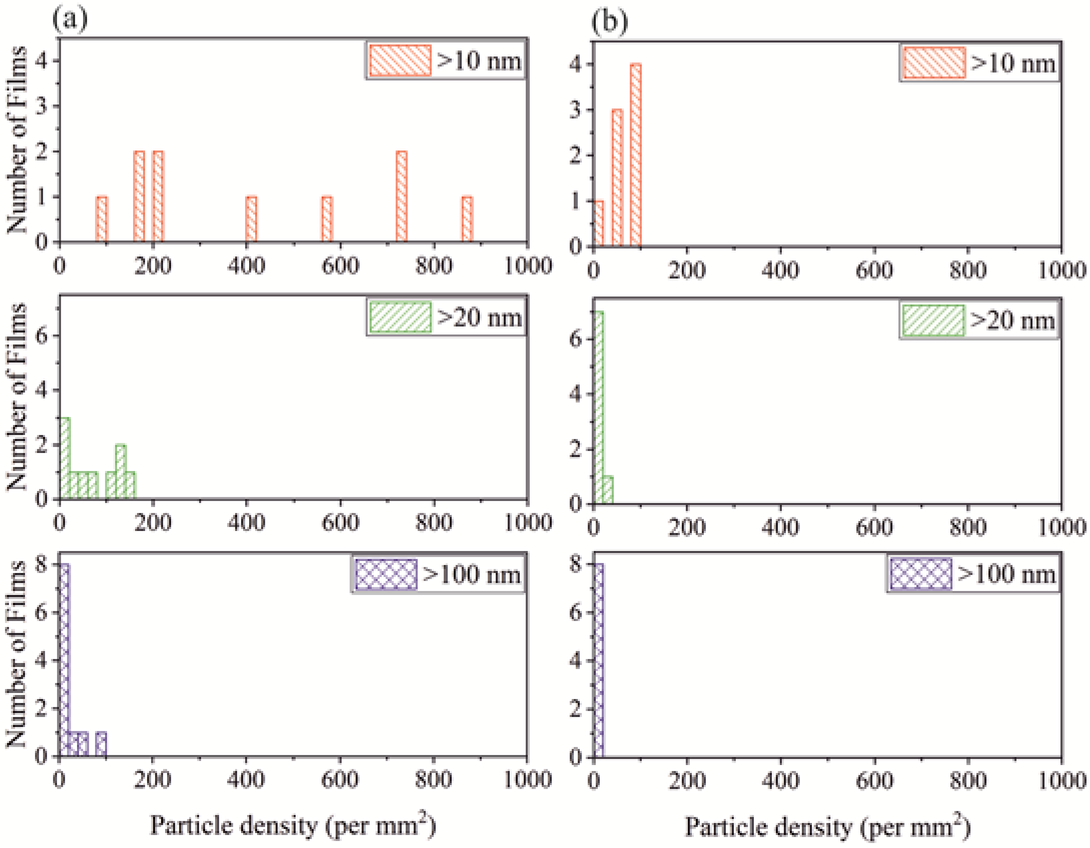

Figure 5.19. Histograms (bin size of 20) of the surface particulate density (particles/mm^2), when counting particles with heights greater than: 10 nm (▨), 20 nm (▨), and 100 nm (▨); on films grown via UDA (a) or BDA (b).

A particle embedded near the surface of the film will change the local height of the film. The change in surface topology can be quantified using a white light interferometer (as discussed in Chapter 2). From these measurements it is possible to find the surface-particle density and surface roughness (S_a). Figure 5.19 displays histograms of the density of particulates, with threshold heights of >10, 20 and 100 nm, for UDA (a) and BDA (b) respectively, based on 11 films grown via UDA and 8 films grown with BDA. Collectively, for all particle sizes, these plots demonstrate an almost two-fold reduction in surface particulates with the BDA approach. The average film S_a (roughness) values were (2.14 ± 0.14) nm and (1.13 ± 0.04) nm for UDA and BDA respectively, a clear demonstration of the improvements in film-surface quality.

5.5.3 Bi-directional ablation effect on waveguide performance

As discussed in Chapter 2, particulates embedded into PLD-grown waveguide films have been shown to increase propagation loss. In this section, I examine the effect that reducing the particulate density has on the resulting waveguide performance.

Three Er:YGG films were grown with BDA and one with UDA with the growth parameters presented in Table 5.2 onto a YAG (100) substrate. Channels were cut into them by Lewis Carpenter with a Disco DAD3430 dicing saw using a nickel-bonded blade (Z09, Disco) with a small grit size (SD5000). Light from a diode laser operating at a wavelength of 1480 nm was launched into the facets of the ridge waveguides and the transmitted power measured. Accounting for the Fresnel reflection at the facets (calculated from equation 3.8 to be -0.85 dB), coupling (assumption based on the symmetry of the channel waveguide) and absorption losses (based on the absorption of Er^{3+} and the dopant concentration), a value for the propagation loss could be determined.

Table 5.2. Growth conditions for Er:YGG grown via UDA and BDA.

Sample number	Ablation regime	Thickness (μm)	Fluence (Jcm^{-2})	Heating power (W)
JP108	BDA	20	1.6	15
JP112	BDA	10	1.6	12
J148	BDA	22	1.9	11.5
J109	UDA	6	1.1	10.5

Table 5.3 shows the losses measured from films grown via BDA and UDA compared with the particulate density range measured from DF images. The best BDA-grown film (JP148) has a propagation loss approaching 0.1 dB/cm, which is more than 50-times lower (in a linear scale) than that of the UDA-grown film (J109) with a 3.5 dB/cm propagation loss, demonstrating the clear relationship between a film's propagation loss and its particulate density. This represents a major improvement compared to previous PLD and UDA-grown waveguides, such as (Beecher *et al.*, 2014; Parsonage *et al.*, 2015), where both reported waveguides with propagation losses of greater than 1 dB/cm, albeit with different materials.

Table 5.3. Particulate density and losses associated with Er:YGG films.

Sample number	Particulate density (%)	Coupling loss (dB)	Absorption loss (dB)	Propergation loss (dB/cm)
JP108	0.15	-0.1	-0.04	0.7
JP112	0.22	-0.2	-0.09	0.6
J148	0.17	-0.2	-0.25	0.12
J109	12.5	-0.4	-0.05	3.5

5.5.4 Optimisation of bi-directional ablation

After the initial studies with BDA, it became clear that the central region of the target was being ablated at a much greater rate than the rest of the surface. This leads to a “dip” forming at the centre of the target’s face as material is being removed at a faster rate than the surrounding areas. Faster degradation of the target’s surface at its centre, potentially leads to a greater number of particulates being ejected. It will also reduce the usable lifetime of the target, as reconditioning will need to remove a larger amount of material to achieve a suitable flatness. This can be seen in Fig 3.4 where the simulations of BDA show the UV laser beam track crossing the target’s centre during each full displacement of the target.

To find a solution to this problem, simulations were performed to find the target’s displacement path and a 2-D histogram of the ablation pulse count per area of target. In this section, I present these simulations and compare stylus measurements of targets using BDA and using UDA.

In Figure 5.20 (a), the displacement path of the target is shown; the target is suspended on a swinging arm with a pivot point 125 mm away from the centre of the target. On each revolution of the cam, at the desired repetition rate, the target will be displaced back and forth along this path. Even when the target is rotated about an axis marked with an “x”, the displacement path will still pass through the centre. To avoid this, it is possible to change the vertical position of the ablation beam as seen in Figure 5.20 (b). In this scenario, the beam has been moved, for practical reasons, upwards by 2 mm so that the centre of the target will not be ablated. It is important to note that for UDA, the beam did not pass through the central axis of the target, as seen in Figure 5.20 (c), so this problem did not need to be considered.

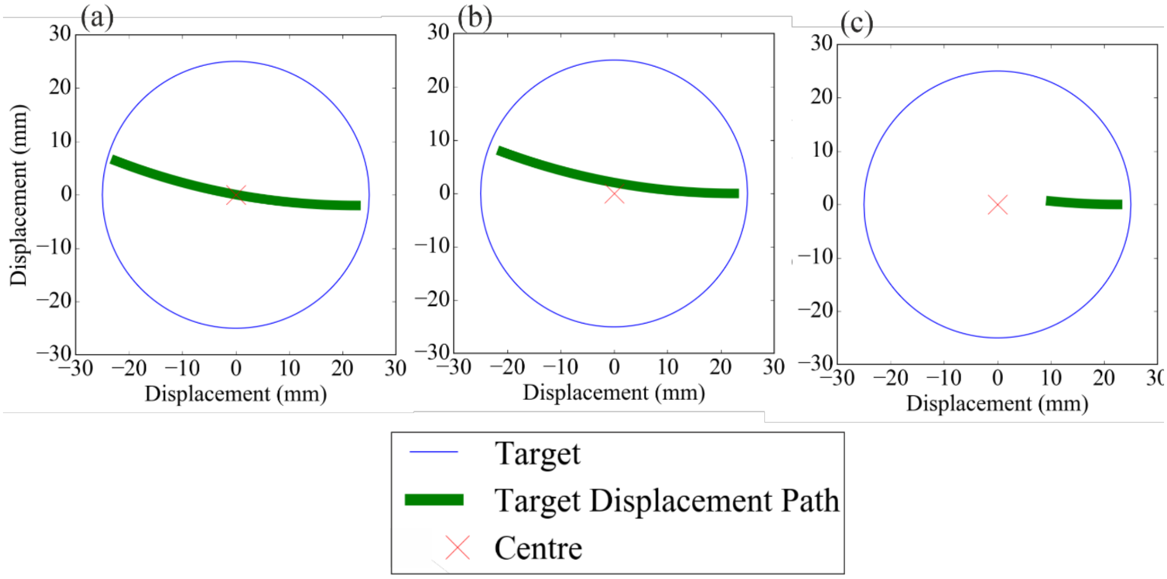

Figure 5.20. Modelled ablation path for BDA (a) through the centre (and axis of target rotation), (b) 2 mm above the centre and (c) for UDA.

Figure 5.20 (a) shows the heat map and stylus measurement of a target subject to UDA. These were created by extending the model described in Figure 5.13 that was created in MATLAB. The inner part of the ablation ring is still receiving 1 in 10 of the shots but, as before, these shots are spread between a larger area. This means that the discrepancies in the height, as shown by the stylus measurement, are less pronounced.

Figure 5.20 (b) shows a heat map of where the ablation beam is hitting the target, after 72,000 shots, when the beam travels across the targets centre. In this case, 1 in 10 pulses are hitting the central 3 mm x 3mm square, or 9 mm^2. The stylus measurement shows that the central region of the targets face has ~ 5x more material removed than the other regions. It also shows that 2x more material has been removed on the edge of the ablation ring than the intermediate areas which agrees with the heat map simulation.

Figure 5.20 (c) shows the heat map if the beam is moved 2 mm above the axis of rotation (the centre of the target). Here, there are no pulses in the central 3 x 3 mm of the target’s face. Now 1 in 10 pulses are hitting the area around this, which is 27 mm^2. This spreads the load and means the hole in the centre of the face will not be as deep, as is confirmed by the stylus measurement.

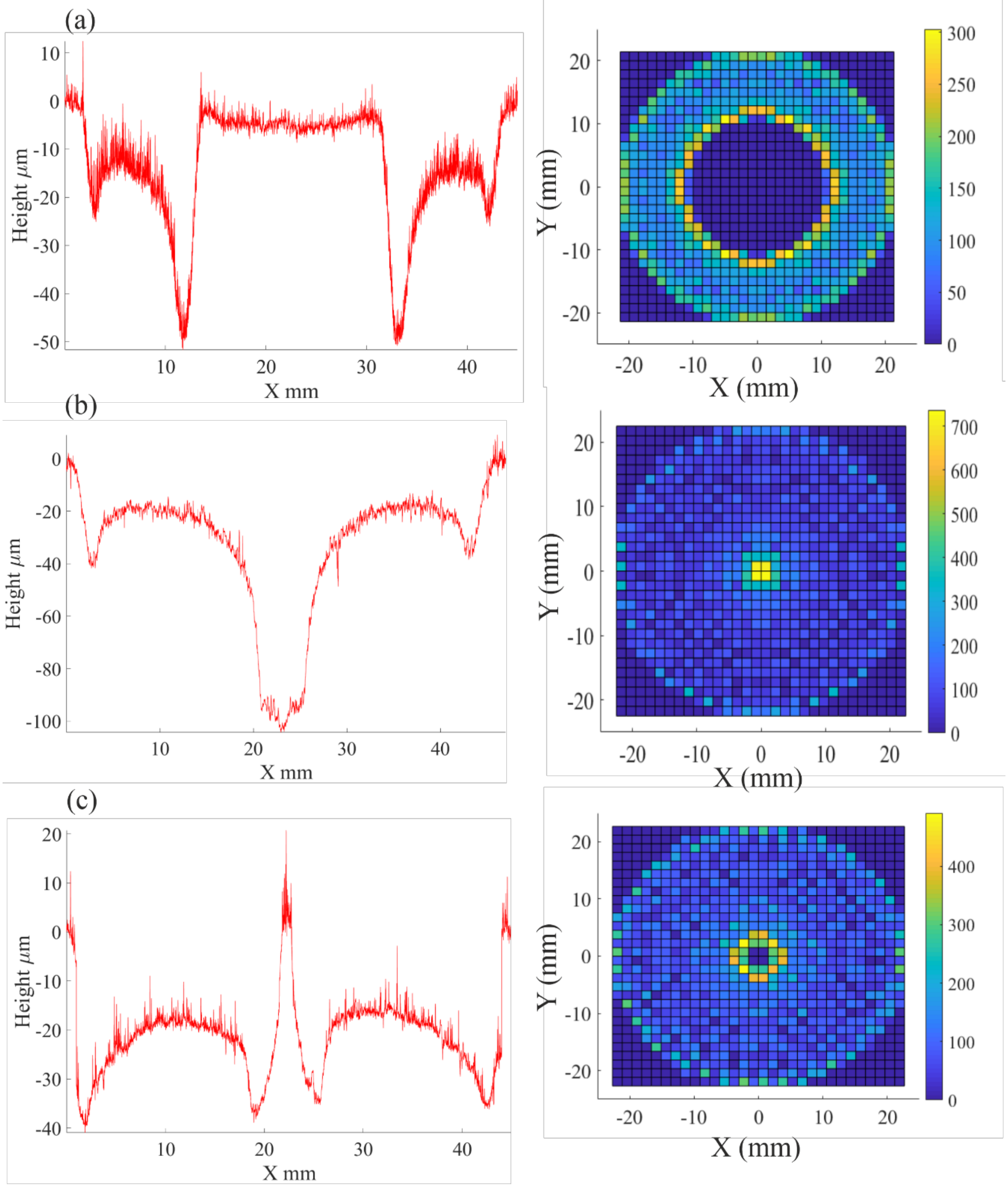

Figure 5.21. Simulation produced heatmaps of the number of shots per area on the targets surface after 72,000 shots and stylus measurements of targets after 72,000 shots, for: (a) UDA (b) BDA through the origin of the target and (c) BDA moving the displacement track 2 mm above the rotational axis.

This simulation does not account for the spot size of the ablation laser, but only takes into account where the centre of each pulse hits, giving an apparent discrepency between the stylus measurements and the heatmap. The stylus indicates that a ~ 5mm diameter region at the centre of the target’s face has a greater amount of material removed, whereas the heatmap is only ~ 3 mm diameter. Taking into account the spot size of 2.5 mm width at the target, then the model and measurements are in excellent agreement.

I have shown that with our BDA setup, by changing the vertical position of the ablation beam by 2 mm, the pulses are spread over a larger area and therefore remove 2x more material than other areas compared to 5x more than if the abaltion pulse hits the centre of the target. Changing the vertical position of the beam by differing amounts would produce the same effect if the centre region is not ablated, however, 2 mm ensures the centre is missed, and the maximum amount of target is utilised.

5.5.5 Summary of the bi-directional technique

In this section, I have presented BDA as a technique to reduce LIPSS and reduce the density of particulates in thin films, while increasing target utilisation by 50% compared to UDA. It has been shown that the directional cone-like structure formed on targets that have undergone UDA is prevented when BDA is used. The particulate density of films grown by BDA is reduced 5-fold and the surface roughness (Sa) reduced by a factor of 2. I have also demonstrated that films grown using BDA have a propagation loss of as low as 0.1 dB/cm, a record result for comparable films grown via PLD.

5.6 Conclusions

Particulates embedded into crystal films cause scattering of light, which increases the linear-propagation loss of crystal films. In this chapter, three methods have been presented for reducing the particulate density in PLD-grown films, shadow masks, segmented targets, and bi-directional ablation.

Through understanding of the fundamental theory of plume dynamics in PLD, particulates can be blocked with a SM, the plume will expand around the obstruction and still grow a crystalline film. Using this method, the particulate density in the grown film was reduced by 78x. In achieving this major improvement however, growth rate is reduced by 70% and for the growth of ternary materials the films stoichiometry is altered compared to the target composition. There is still promise in this technique for simple oxides in which the dopant is a similar mass to the host ions, such as Yb:Lu_2O_3. Other techniques such as a velocity selective gas jet to push the heavier ions into the substrate path should also be explored.

With segmented targets, a 250x decrease in particulate density was realised with a growth closer to stoichiometric YGG. There was evidence of binary-layer growth within the ternary crystal, when too many pulses hit one material sequentially, which caused broadening of the YGG (400) XRD peak. Improvements could be made through control of the timing of the ablation pulse and rotation speed of the segmented target. This could mean the interfaces between the segments could be avoided and provide control over the number of sequential pulses on each segment.

Using BDA, target utilisation is increased by ~50% compared to the standard approach used in our group prior to this work. It also doubled the longevity of the target, reduced the particulate density by ~90% compared to UDA, and reduced the post-ablated target roughness by ~50 %. Employing BDA demonstrated that low-loss waveguides are possible with the PLD technique, realising losses as low as ~0.1 dB/cm.

Each of these techniques reduce the particulate density, however, bi-directional ablation is a passive technique with a host of advantages, and it is now the default ablation technique used in our system. A revamped multi-target system that incorporates two bi-directional setups for two binary targets should also provide an effective solution to reduce particulate density and increase the versatility for materials development.

5.7 References

Ashfold, M. N., Claeyssens, F., Fuge, G. M. and Henley, S. J. (2004) 'Pulsed laser ablation and deposition of thin films', *Chem Soc Rev,* 33(1), pp. 23-31.

Barrington, S. J., Bhutta, T., Shepherd, D. P. and Eason, R. W. (2000) 'The effect of particulate density on performance of Nd:$Gd_3Ga_5O_{12}$ waveguide lasers grown by pulsed laser deposition', *Optics Communications,* 185(1-3), pp. 145-152.

Beecher, S. J., Parsonage, T. L., Mackenzie, J. I., Sloyan, K. A., Grant-Jacob, J. A. and Eason, R. W. (2014) '1.2 W Yb:Y_2O_3 Planar Waveguide Laser', *Advanced Solid State Lasers,* 22(18), pp. 22056-22061.

Grant-Jacob, J. A., Beecher, S. J., Riris, H., Anthony, W. Y., Shepherd, D. P., Eason, R. W. and Mackenzie, J. I. (2017) 'Dynamic control of refractive index during pulsed-laser-deposited waveguide growth', *Optical Materials Express,* 7(11), pp. 4073-4081.

Grant-Jacob, J. A., Prentice, J. J., Beecher, S. J., Shepherd, D. P., Eason, R. W. and Mackenzie, J. I. (2018) 'Particulate reduction in ternary-compound film growth via pulsed laser deposition from segmented binary-targets', *Materials Research Express,* 5(3).

Mackenzie, J. I., Grant-Jacob, J. A., Beecher, S., Riris, H., Yu, A. W., Shepherd, D. P. and Eason, R. W. 'Er:YGG planar waveguides grown by pulsed laser deposition for LIDAR applications', *Solid State Lasers XXVI: Technology and Devices*.

Ojeda, G. P. A., Schneider, C. W., Döbeli, M., Lippert, T. and Wokaun, A. (2015) 'The flip-over effect in pulsed laser deposition: Is it relevant at high background gas pressures?', *Applied Surface Science,* 357, pp. 2055-2062.

Parsonage, T. L., Beecher, S. J., Choudhary, A., Grant-Jacob, J. A., Hua, P., Mackenzie, J. I., Shepherd, D. P. and Eason, R. W. (2015) 'Pulsed laser deposited diode-pumped 7.4 W Yb:Lu_2O_3 planar waveguide laser', *Opt Express,* 23(25), pp. 31691-31697.

Sloyan, K. A., May-Smith, T. C., Eason, R. W. and Lunney, J. G. (2009) 'The effect of relative plasma plume delay on the properties of complex oxide films grown by multi-laser, multi-target combinatorial pulsed laser deposition', *Applied Surface Science,* 255(22), pp. 9066-9070.

Sloyan, K. A., May-Smith, T. C., Zervas, M., Eason, R. W., Huband, S., Walker, D. and Thomas, P. A. (2010) 'Growth of crystalline garnet mixed films, superlattices and multilayers for optical applications via shuttered Combinatorial Pulsed Laser Deposition ', *Optics Express,* 18(24), pp. 24679-24687.

Sloyan, K. A., May-Smith, T. C., Zervas, M. N. and Eason, R. W. (2012) 'Crystalline garnet Bragg reflectors for high power, high temperature, and integrated applications fabricated by multi-beam pulsed laser deposition', *Applied Physics Letters,* 101(8).

Chapter 6 Garnets

6.1 Introduction

As discussed in section 2.3, garnets have numerous advantages as a laser host material, leading to them being widely used for industrial lasers. In PLD, there has been a significant amount of research into the growth of RE-doped garnets for lasing applications. In particular, a PLD-grown Yb:YAG planar waveguide laser has been demonstrated with >21 W (CW) output power and 70% slope efficiency, furthermore a small-signal gain of >20dB was realised in a planar waveguide configuration (Kurilchik *et al.*, 2018). Waveguide lasers made with Yb:GGG and Yb:YGG films have been demonstrated with output powers of 1.8 W and 1.2 W and slope efficiencies of 11% and 15%, respectively (Beecher *et al.*, 2017).

These planar waveguide lasers and amplifiers show the promise of the PLD technique to grow high-power, low-loss, active waveguides. Despite their record performance, the aforementioned waveguides had propagation losses in excess of 1dB/cm. While gain was still achieved, this loss increases the lasing threshold and reduces efficiency, hence decreasing the maximum achievable output power. As shown in the previous chapter, propagation loss correlates with particulate density. These defects also degrade the beam quality by scattering light, and affect the physical parameters of the grown film, such as thermal conductivity.

In this chapter, advances in the quality of PLD-grown RE-doped YGG, YAG and LuAG on <100> YAG substrates are presented. Here, the steps taken to optimise and characterise the growths, and the optical experiments that followed are presented. By utilising the bi-directional ablation technique presented in chapter 3, I demonstrate losses less than 0.3 dB/cm in YGG and show lasing with the first PLD-grown double-clad (where the outer layers are formed by the substrate and air) Yb:LuAG waveguide laser.

6.2 Yttrium Aluminium Garnet

YAG the primary crystalline host material used for RE-dopants in lasers used in both research and industry. Recently in PLD, examples of lasing in Yb:YAG films have been demonstrated with 70% slope efficiency and >20 W output power (Kurilchik *et al.*, 2018).

The film used to create this laser was grown using the UDA method. This indicates that by using BDA, the particulate density and hence the propagation loss, could be reduced compared to this example. The reduction of defects and loss would result in higher efficiencies and output powers, which would enable PLD to be a viable alternative growth mechanism for planar waveguide lasers.

In the following sections, efforts to improve the stoichiometry, crystallinity and particulate density of Yb:YAG films are presented. The stoichiometry is improved by compensating for poor aluminium transfer from target to substrate via increasing the amount of aluminium in the target relative to yttrium. The particulate density and crystallinity are improved by optimising the ablation fluence and substrate temperature respectively. The optimisation of growth parameters to provide films with low particulate density and a single-crystal structure is presented.

6.2.1 Aluminium compensation in YAG films

The growth of ternary oxides using a one target system in PLD requires targets made from two binary oxide powders. The transfer of material from target to substrate is not necessarily stoichiometric and this needs to be considered when choosing the ratio of materials in a target. In general, when the target is ablated, lighter elements will form a larger plume in comparison to the heavier elements (discussed in section 2.2.2.2 (Droubay *et al.*, 2010)). This will mean that the lighter elements are spread out over a larger area, and so there will be a relative loss of lighter elements, leading to films with different stoichiometry than expected. In most cases, the changes to these parameters would be detrimental to the intended use. Consequently, the relative loss of lighter elements will need to be compensated for in the design of targets.

When attempting to grow YAG with a ternary target, which is fabricated using alumina and yttria powders, stoichiometric transfer of the molecular ratio of yttria to alumina requires the target to simply be a 3:5 mix ($Y_3Al_5O_{12}$). However, when ablated, the resultant yttrium will form a more directional plume than the aluminium. Therefore, a greater concentration of aluminium is needed in the target to compensate for its relative loss compared to yttrium in the transfer to the substrate. The peak position in the XRD spectrum of a YAG film with a ratio of yttrium and aluminium that is larger than it is for 3:5. Implying a relative decrease in aluminium would increase the lattice constant and therefore decrease the 2θ peak position. This can be used to observe the difference between a stoichiometric YAG film and an aluminium-deficient film.

Films were grown from targets with different aluminium compensations. Six films were grown with a target that was pre-compensated with an extra 2.5% alumina (molecular percentage) compared to ytrria, and eleven from a target with 8.5% extra aluminium. XRD measurements were performed and the <400> peak position noted and plotted in Figure 6.1. 2.5% compensated targets grew films with XRD peak positions on average 29.43° ± 0.01° using the standard error, in comparison to films grown with target compensation of 8.5% a 29.68 ± 0.01° XRD peak position was found. This peak position is 0.08° away from the expected peak position of 29.76° (Emiraliev *et al.*, 1976), 4 times closer than that of 2.5% compensated films and nearly perfectly stoichiometric YAG.

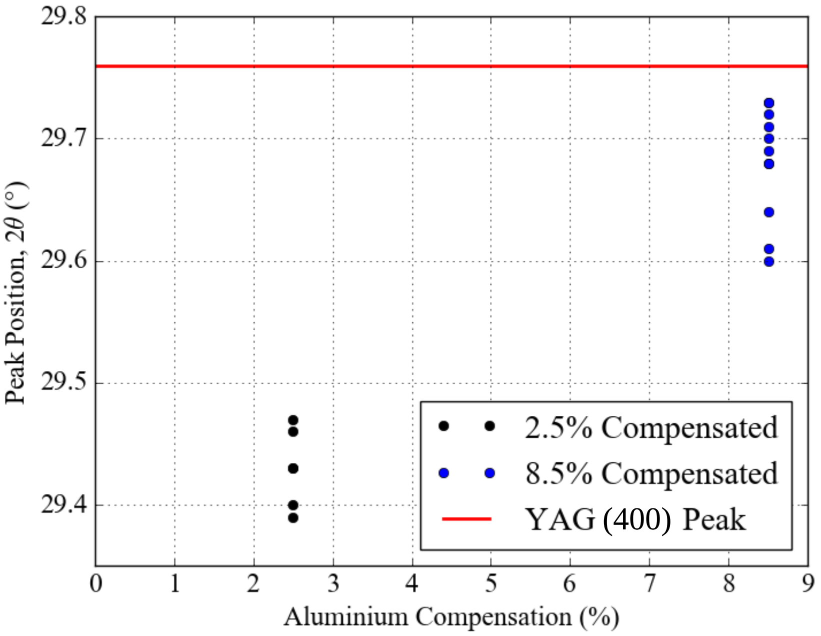

Figure 6.1. Peak positions of (400) peak for YAG films grown with 2.5% (black) and 8.5% (blue) aluminium compensated targets. The red line indicates the position of the peak position expected for perfectly stoichiometric YAG (Emiraliev *et al.*, 1976).

Figure 6.1 shows a variation of XRD peak position between different growths. This is because the stoichiometry between growths is affected by the growth conditions themselves, for example a smaller ablation spot size will increase the size of the plume (the flip-over effect, see section 2.2.2.2) with lighter elements expanding to a greater degree than heavier elements (Ojeda *et al.*, 2015).

In this section, it has been demonstrated that by changing the composition of targets nearly stoichiometric YAG can be grown. The growth conditions effect on the particulate density, crystallinity and the stoichiometry of YAG films is outlined in the following sections.

6.2.2 YAG fluence optimisation

The fluence used to grow samples will have an effect not only on the particulate density, but also the stoichiometry and temperature of the substrate. As discussed earlier in this chapter, PLD-grown Yb:YAG has demonstrated promising waveguide laser results with the UDA protocol. The development of BDA has created the real possibility of improving upon these results, with decreased propagation loss in the waveguide with anticipated improvements in laser power. The optimal fluence for minimising particulate density may not be the same for BDA as it is for UDA. In this section, I present 5-films grown with different ablation fluences. The samples growth conditions and particulate density can be seen in Table 6.1.

Table 6.1. Growth conditions and characteristics of YAG samples grown with 36,000 shots, 8.5% aluminium compensation and a repetition rate of 100 Hz.

Sample Number	Yb (%)	Substrate Heating (W)	Fluence (Jcm^{-2})	Scattering Point Density (%)	Thickness (µm)
JP195	3	19.0	1.65	6.97	1.85
JP196	3	19.0	1.45	4.34	1.75
JP197	3	19.0	1.85	8.34	2
JP198	3	19.0	1.20	2.05	1.5
JP199	3	19.0	1.00	1.22	1.35

The thickness of the films seen in Table 6.1 varies by 0.65 µm, hence, the change in particulates could be explained by varience in film thickness. To correct for this, the scattering point density can be divided by the thickness of the film. Figure 6.2 shows the thickness-corrected scattering density in Yb:YAG films as a function of ablation fluence. A trend can be seen that lower fluence values decrease the percentage value of scattering points in the films. This could be due to high-fluence values increasing the probability of exfoliation of particules from the target. While this is a good indicator of the optimal fluence for this target, different targets with different characteristics may require different ablation fluence values for low particulate growth.

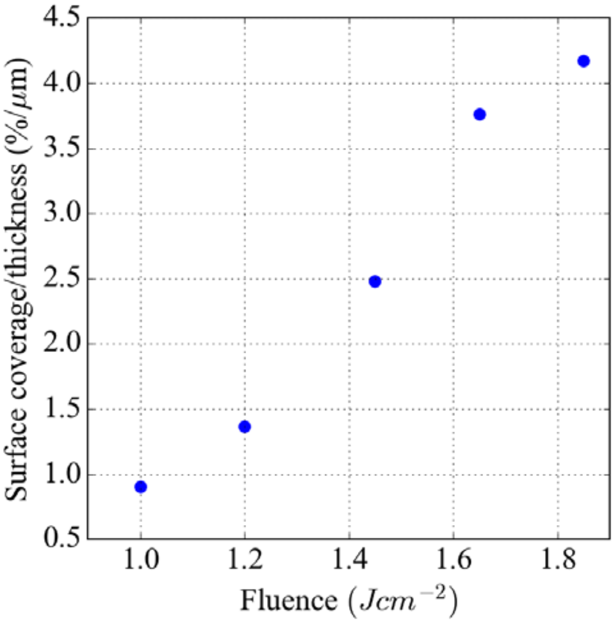

Figure 6.2. Scattering point density of Yb:YAG films grown with ablation fluence values from 1.0 - 1.85 Jcm^{-2}.

6.2.3 YAG temperature optimisation

The temperature at which a thin-film is grown is of crucial importance for the resultant crystallinity and the orientation of the growth. The technique used to analyse the crystallinity of films, XRD measurement, is challenging for homoepitaxial growth as it is hard to distinguish between peaks of the substrate and the film. An amorphous film for example, would not generate peaks in an θ/2θ XRD scan, and the X-rays can penetrate ~30 µm (depending on the incidence angle) into the samples, leaving only the substrate visible to the incident x-ray beam. To counter this, methods such as grazing incidence XRD (GIXRD discussed in chapter 2) and measuring the fluorescence of an active film can confirm its crystallinity.

The thickness of a growth will also influence the crystallinity of the films, with thick films not necessarily maintaining the crystal orientation of thin films grown with the same conditions (Burmester *et al.*, 2003) (DeLoach, 1998). For this reason, it is important to optimise the crystallinity at thicknesses that are usable for laser applications (>10 µm). To optimise the temperature of YAG films, four undoped films were grown to ~ 10 µm thickness under different substrate heating CO_2 laser powers. The growth conditions can be seen in Table 6.2. These films were measured using θ/2θ monochromatic XRD and GIXRD to analyse the crystallinity.

Table 6.2. Growth conditions of undoped YAG films grown with 180,000 pulses onto YAG substrates.

Sample Number	Substrate Heating (W)	Fluence (Jcm^{-2})
JP158	11.5	1.85
JP159	23	1.85
JP160	9	1.85
JP161	15	1.85

Initial observations of the θ/2θ XRD spectrum revealed peaks at the location of the YAG (400) XRD peak (~29.76°). The FWHM of an XRD peak is a good measure of crystallinity since a single crystal will have a FWHM of around 0.02° but defects and stress will cause broadening of the peaks. Figure 6.3 shows the FWHM of the peaks of the thick YAG samples. 11.5 W and 9 W have the lowest FWHM of around 0.02°, so this evidence alone would suggest that 11.5 W of substrate heating power is the optimum. However, to test that the 9 W and 11.5 W films were not amorphous, GIXRD (grazing incidence) XRD was performed since the x-rays would not penetrate to the substrate (see section 4.4.4.2).

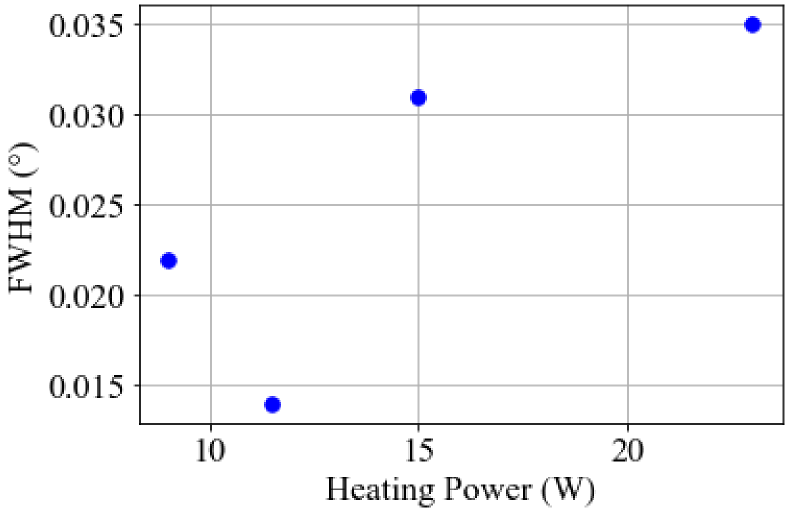

Figure 6.3. FWHM of 10 µm-thick YAG films as a function of substrate heating power.

GIXRD has different selection rules for which peaks will be observable in the spectrum. In the case of YAG (100), the (100) peak (where the (100) planes are perpendicular to the surface) cannot be measured using GIXRD with a 1° incidence angle. Therefore, when measuring a film that is YAG (100) the optimal spectrum would have no peaks visible. The GIXRD spectra for JP159 -JP161 are shown in Figure 6.4. Figure 6.4 (a) shows the GIXRD spectrum for JP160, where the substrate heating power was 9 W. The broad (~10° FWHM) peak around 30° indicates a film with a low degree of crystallinity (amorphous). JP158 which was grown at 11.5 W had an almost identical GIXRD spectrum and as such isn't shown here.

Figure 6.4 (b) shows the GIXRD spectrum for JP161 and displays three peaks. These peaks can be attributed to different orientations of YAG, seen in Figure 6.4 and the peak intensities are not much higher than the noise floor. This indicates that the signal from these orientations is weak (since the expected peak heights for single crystal material is ~10^5), and hence the volume of material with these orientations is small.

Figure 6.4 (c) shows the GI-XRD spectrum from JP159, and there are numerous peaks. These peaks can also be well attributed to standard YAG peaks, indicating that this film is slightly polycrystalline. However, like JP161, the peak intensities are small, indicating only small amounts of polycrystalline material.

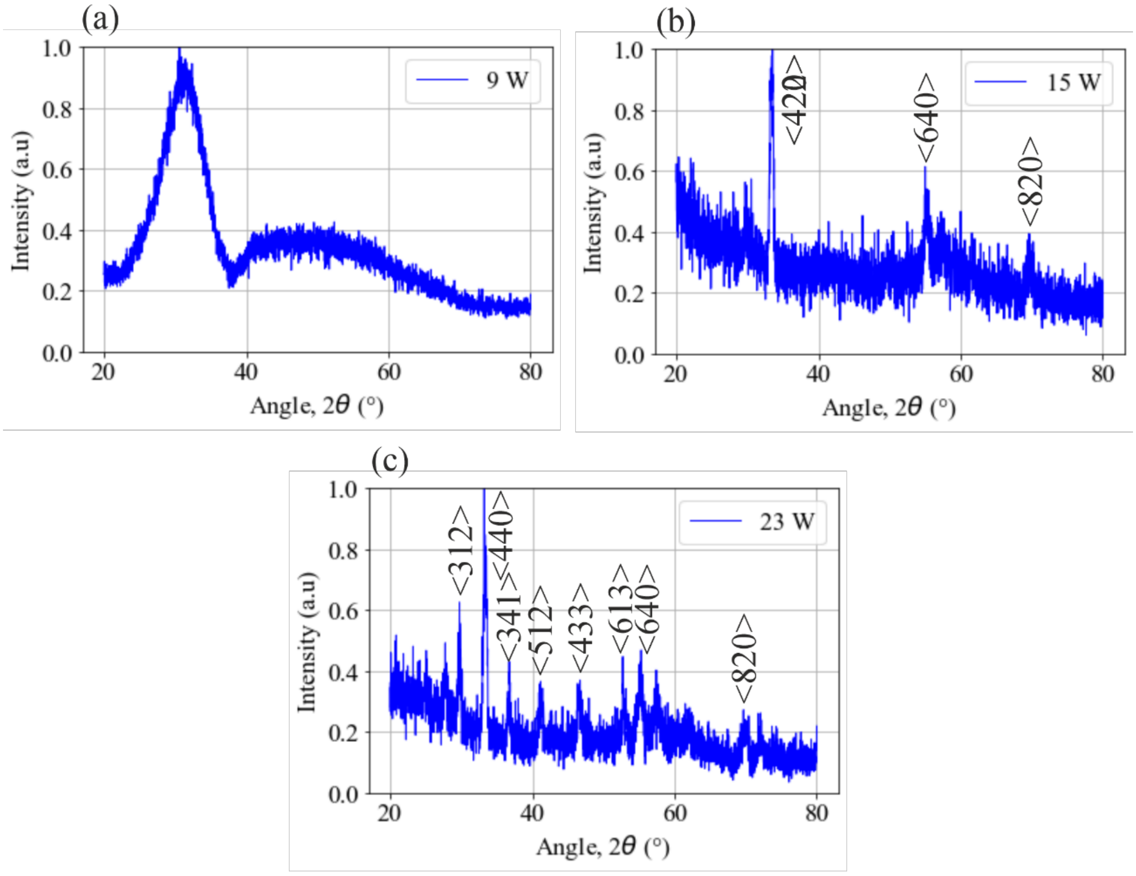

Figure 6.4. GIXRD spectrum from 20-80° for films grown with substrate heating temperature of (a) 9W, (b) 15 W and (c) 23 W. The corresponding YAG peaks are labelled (Emiraliev *et al.*, 1976).

Here, the difficulties in the characterisation of YAG films grown onto a YAG substrate have been shown. It has also been demonstrated that the optimum substrate heating power is ~15 W for an ablation fluence of 1.85 Jcm^{-2}. Further optimisation growths would be required to narrow down the optimal temperature.

6.3 Lutetium Aluminium Garnet

LuAG is an alternative to YAG as a RE-dopant host material. As discussed in section 3.2.2.2, both have similar physical and spectroscopic properties, but, due to the similar size of lutetium and RE-ions, the doping of LuAG with RE-elements does not cause a significant degradation of physical parameters, such as thermal conductivity. When fabricating high-power devices, the thermal conductivity is crucial for power scaling. Having a higher thermal conductivity allows heat to be removed from the device more quickly, therefore efficiency degrading thermal effects can be avoided when pumping with higher power densities.

LuAG has a higher melting point than YAG, 2060 ^{o}C compared to 1940 ^{o}C, respectively (Beil *et al.*, 2010). This small but significant difference adds to the complexity of the growth of LuAG via melting methods, since the melting temperature of LuAG is approaching the applicability limit of iridium crucibles. However, rhenium-crucibles, while more expensive, have a melting point of 3186 ^{o}C, making them more suitable for LuAG growth. RE-doped LuAG is now commercially available, however, RE-doped YAG still dominates as the choice for many applications that don’t require extreme power handling, primarily driven by cost/performance reasoning.

When growing LuAG, like YAG, there will not be stoichiometric transfer of the material from target to substrate and therefore the targets were aluminium compensated. All of the samples in this section are grown from 9% aluminium compensated targets unless otherwise stated.

In this section, I look at growth of a clad ytterbium doped LuAG and the lasing properties of a double-clad LuAG film grown on a YAG substrate.

6.3.1 Growth of double-clad LuAG film

As discussed in section 2.3, the numerical aperture (NA) of a single-layer planar waveguide limits the efficiency of pump coupling. The efficiency of pump coupling can be increased by growing thicker films, but the consequence of this is multi-mode operation, when fundamental mode operation is more desirable. Cladding layers are routinely used with optical fibres for power-scaling where, generally, a relatively small active core is surrounded by a larger non-active material. This increases the effective absorption length, requiring longer samples but this is not as much of a problem for optical fibres, as they can be several metres in length, as it is for planar waveguides as described in this thesis, which, in this case, are limited to ~1 cm.

The same technique as used in optical fibres can be used in planar waveguides. However, an increased absorption length is not as simple to overcome in planar waveguides. A method to overcome this is to increase the core's doping concentration, but this could increase the chances of detrimental thermal effects. Increasing the size of the core with respect to the cladding layers could also decrease the absorption length.

By using cladding layers, you can also choose a ratio of cladding and core thicknesses (Figure 6.5) that has higher order modes extending into the cladding, while confining the fundamental mode in the core. The fundamental mode would then be selected due to the limited gain region (Bhutta *et al.*, 2002; Mackenzie, 2007). A correctly chosen geometry should allow for beam qualities that are near diffraction-limited in the guided direction.

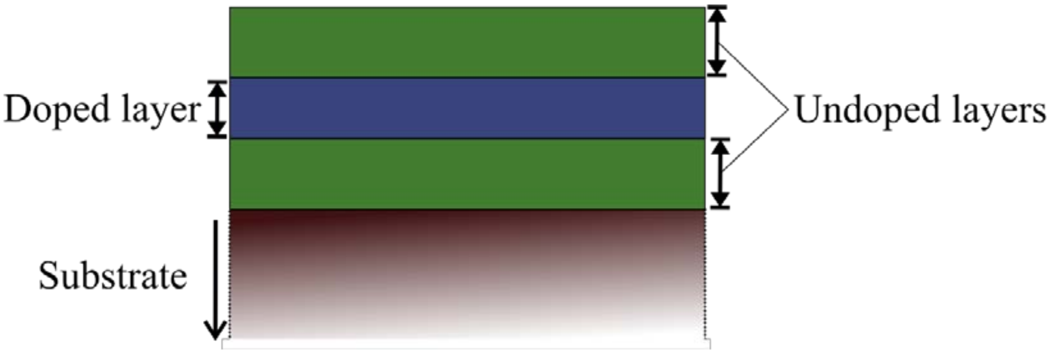

Figure 6.5. Diagram of active planar waveguide with undoped cladding layers surrounding a doped central layer.

In this section, I discuss the growth of a double-clad LuAG waveguide with layers of YAG/LuAG/Yb:LuAG/LuAG (Figure 6.5) with the UDA protocol. The process of the growth can be seen in Table 6.3. It is important to note that the sample needed to be cooled and taken to atmosphere to change the target between each step, which increases the chance of contamination of the surface between each layer.

Table 6.3. Process of growing a cladded Yb:LuAG film (JP67).

Step Number	Target	Heating Power (W)	Pulses	Fluence (Jcm^{-2})
1	LuAG	13	144000	1.1
2	Yb (4%) LuAG	13	288000	1.1
3	LuAG	13	144000	1.1

The thickness of JP67 was measured by a stylus profiler and found to be 8 µm. Dark-field microscope images were taken, seen in Figure 6.6 (a), and the scattering point density was found to be 11.12 % (with 10% threshold on a 50x microscope image). θ/2θ XRD and GIXRD measurements (Figure 6.6 (b) and (c) respectively) show that the crystal grown was highly textured with multiple peaks observed.

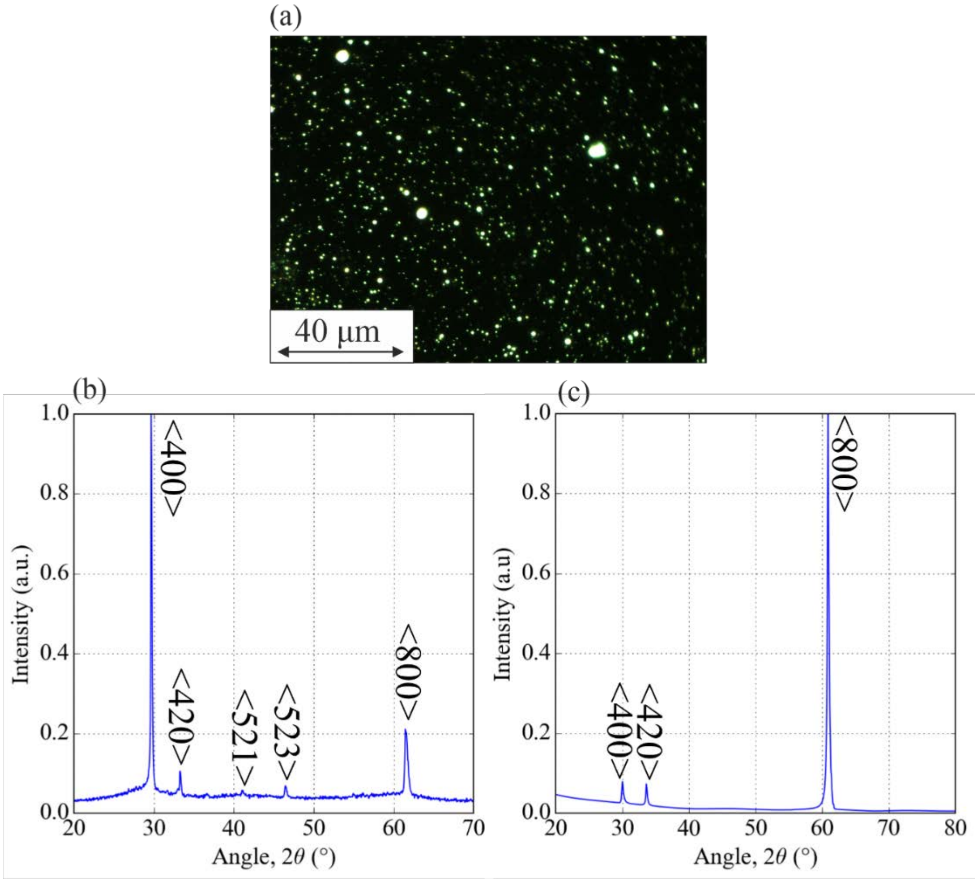

Figure 6.6. Characterisation measurements of JP67 with (a) dark-field image with 50x magnification and (b) θ/2θ and (c) GIXRD spectrum.

The high particulate density and the presence of the multiple peaks in the XRD spectrum indicate that the JP67 waveguide is not comprised of perfectly single-crystalline layers. Nevertheless, the sample was facet polished in-house on opposite sides to prepare for lasing experiments using the method described in section 4.3.2. Figure 6.7 shows an BSE image of the facet of JP67. The layers of the double-clad waveguide can be seen clearly (note: the contrast of Figure 6.7 has been adjusted to display the layers clearly).

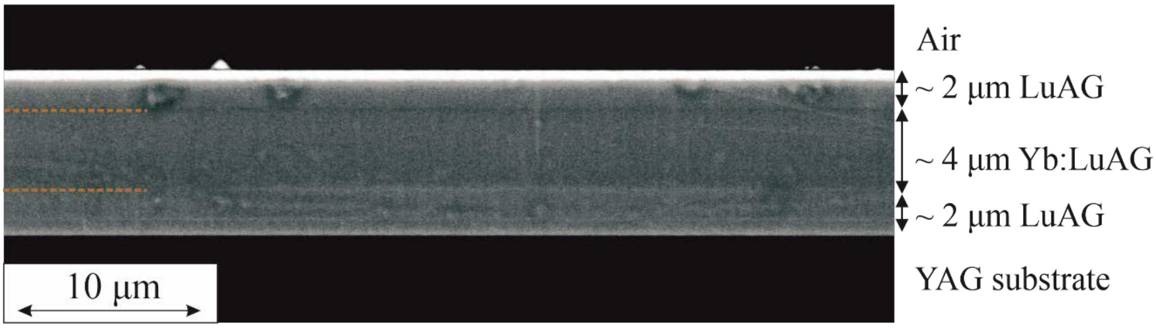

Figure 6.7. EBSD image of the facet of a cladded Yb:LuAG waveguide showing layers of undoped LuAG and doped LuAG at 6220x magnification. The dashed lines indicate the boundary between the doped and undoped layers.

In this section, the details of the growth process and characterisation of a cladded LuAG film were presented. The defect density and crystallinity of the layers are not ideal, but that the respective layers are clearly visible from BSE imaging, showing a doped core in a clad waveguide with a good refractive index profile. This PLD-grown LuAG structure is the first of its kind. In the following sections I will describe the optical characterisation and laser experiments with a double-clad LuAG waveguide (JP67).

6.3.2 Spectroscopic investigation of LuAG waveguide

Having explored the physical characteristics of JP67, to determine whether making a lasing device using this sample was feasible, the fluorescence and lifetime were measured. Comparing these measurements with those found in literature (Beil *et al.*, 2010), an assessment of whether the ytterbium ions are in the correct position in the lattice could be made.

An initial investigation of the polished waveguide was carried out by coupling the light from a HeNe (helium-neon, 633 nm) laser into the facet and observing any scattering that occured during propagation. In an ideal waveguide, with no defects, no scattered light should be observed at a normal to the samples surface, whereas in this case, large amounts of scattered light was observed.

Fluorescence from the doped core was measured via facet-pumping with a fibre-coupled 974 nm diode laser and capturing the Yb^{3+} emission by proximity coupling a graded index optical fibre (0.22 NA, 62.5 µm core-diameter) at the face of the waveguide. The other end of the fibre was attached to an OSA (ANDO AQ6317B), which was set to a resolution of 0.2 nm.

This setup was also used to measure the fluorescence lifetime, albeit with a pulsed pump-laser. Here, the emission was captured with a lens and focussed onto an InGaAs photodiode, as detailed in section 4.5.2. Fluorescence that was captured by the waveguide and propagated to the opposite end, with respect to the incident pump beam, was imaged with a Spiricon SP620U beam-profiling camera. A 20 × microscope objective was attached to a lens tube, fixed to the camera body, and the unit positioned with a precision 3-axis stage to measure the mode profiles of the waveguide excited by the fluorescence. The sample was pumped from the opposite facet by a 974-nm single-mode fibre-coupled diode laser. A HR (high-reflectivity) @915–980 nm, HT (high-transmissivity) @1030 nm dichroic mirror was used to reject the pump light and pass the fluorescence signal.

Figure 6.8 shows a photograph of a 633 nm laser beam being coupled into JP67. From this image looking down on top of the waveguide, there is visible scattering, with the beam easily visible, and spots of light indicating defect locations.

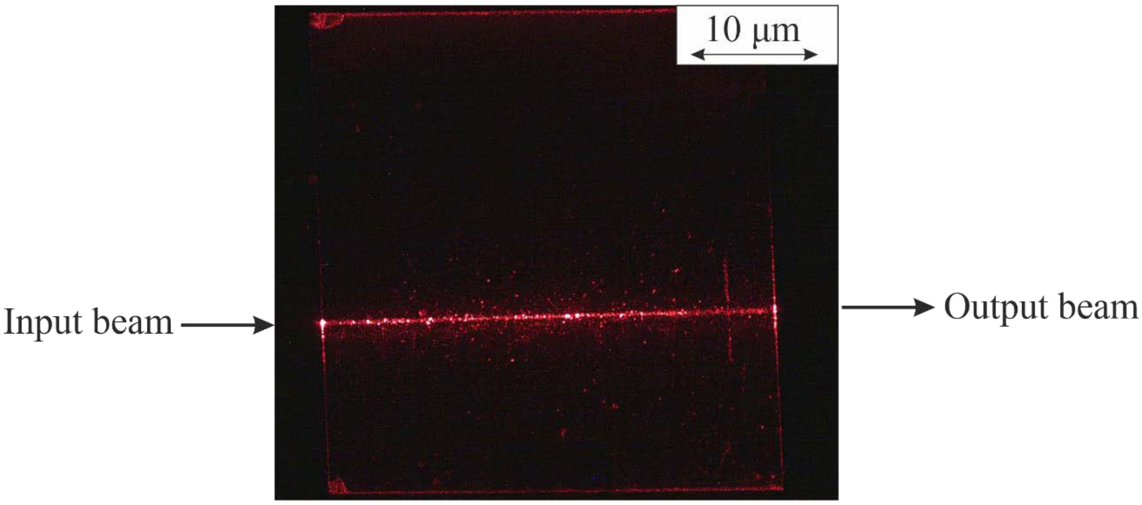

Figure 6.8. Top-view photograph of 633 nm light launched into the clad LuAG waveguide (JP67).

Figure 6.9 (a) shows the fluorescence spectrum of JP67 when pumped with a 974 nm diode laser. Peaks can be seen at 968 and 1030 nm, with the peak at 974 nm associated with the pump laser. This spectrum is similar to those found in literature (Beil *et al.*, 2010) which indicates that the ytterbium ions are in the correct position in the LuAG lattice. Figure 6.9 (b) shows the lifetime measurement and fit using equation 2.2. The lifetime was found to be 953 ± 5 μs which is similar to that found in bulk LuAG (965 and 985 μs for 10% and 15% ytterbium doped LuAG respectively (Beil *et al.*, 2010)). The lifetime of JP67 is likely shorter due to detrimental thermal effects caused by a high defect density.

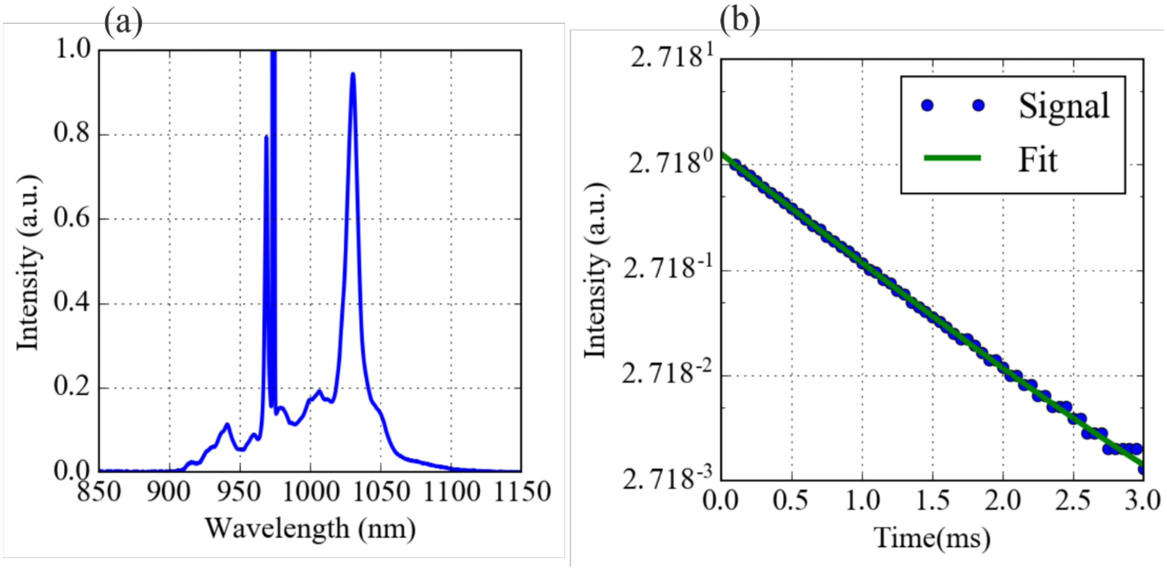

Figure 6.9. (a) Fluorescence spectrum of JP67 from 850 to 1150 nm pumped with 974 nm laser diode. (b) lifetime measurement and fit for calculation of the fluorescence lifetime.

The fluorescence mode profile can be seen in Figure 6.10. This demonstrates that waveguiding of light is occurring in JP67. The intensity is higher near the substrate since this is not a symmetrical waveguide and the refractive index contrast is lower between the film and the substrate. Slight disturbances can be seen on the interface between film and substrate likely caused by defects in the facet finish.

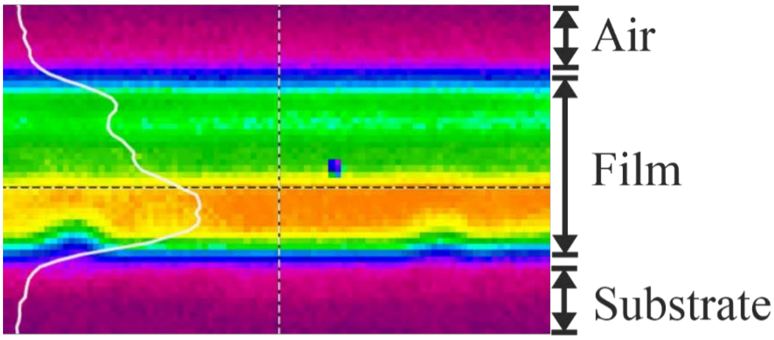

Figure 6.10. Fluorescence mode profile measured from the output facet of JP67

The propagation loss was determined via transmission measurements of an end-coupled 1064-nm wavelength Nd:YAG laser. 1064 nm does not fall within the Yb:LuAG absorption band so absorption can be assumed to be negligible. Accounting for Fresnel reflections from the facets totalling 0.77 dB and that coupling losses are zero, a maximum propagation loss per pass of 1.16 dB was obtained, equal to 1.22 dB/cm for this 9.5-mm-long sample.

As previously discussed, JP67 has the fluorescence spectrum and lifetime values that are similar to those reported for bulk Yb:LuAG (Beil *et al.*, 2010) Waveguiding has been shown by imaging the guided fluorescence at the output facet and the propagation loss was found to be 1.22 dB/cm. While the loss is not as low as seen with the YGG waveguides previously, it represented a good starting point to demonstrate the first PLD-grown cladded LuAG laser.

6.3.3 Lasing of Yb:LuAG waveguide

As discussed in section 3.2.2.1, ytterbium doped LuAG should be capable of higher average powers than ytterbium doped YAG. Theoretically, two identically sized, doped and quality samples consisting of Yb:YAG and Yb:LuAG, would result in the Yb:LuAG sample being capable of greater output powers. Unfortunately, exactly the same quality and doped Yb:YAG and Yb:LuAG waveguides are not attainable, however, using JP67, I can show that PLD is capable of growing laser grade Yb:LuAG.

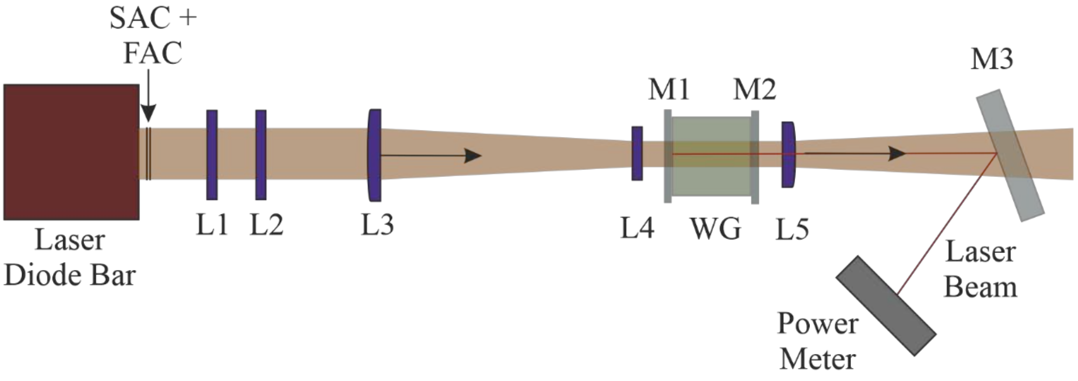

Figure 6.11. Setup for Yb:LuAG waveguide laser characterisation. L1 and L2 - fast-axis cylindrical-lens (5 × telescope); L3 - slow-axis focusing cylindrical lens (f = 50 mm); L4 - fast-axis focusing acylindrical lens (f = 10 mm); M1—input mirror (HR@1020–1100 nm, AR@910-990 nm); WG - planar waveguide; M2 - output coupler (PR@1030 nm); L5 - aspheric lens (f = 15 mm); M3 - dichroic mirror (HR@1030 nm, AR@940 nm). Arrows indicate the direction of travel of the laser beams.

A setup was built to pump JP67 with a 40 W, 940 nm diode-laser bar. The setup can be seen in Figure 6.11. In the unguided plane, the output beam from the diode-laser was focused (L3) to a D4σ width of 1.5 mm. The fast axis output was expanded using a 5.0 × cylindrical telescope (L1 and L2), then focused on the waveguide facet by an acylindrical lens (L4) to a beam height of 6.0 μm (D4σ, distance between the 4σ values, or four times the standard deviation). An aspheric lens (L5) was used to collect the laser output which was reflected by a dichroic mirror (M3) onto a power meter while allowing residual pump light to be transmitted.

An input mirror was placed close to the waveguide’s input facet (M1) and feedback was provided at the output facet by either Fresnel reflection (~8.5% reflection) or an output coupling mirror (M2). Characterisation of the lasing was performed with Fresnel reflection, or an output coupling mirror with reflectance values of 30% and 50% as presented in Figure 6.12 (a). Lasing by using Fresnel reflection feedback produced the highest maximum output powers of 3.3 W with a 20% efficiency, with 30% and 50% producing maximum output powers of 3.1 and 2.2 W and efficiencies of 17.1 and 12.5% respectively. The laser spectrum was collected by a 62.5-µm fibre attached and measured using an OSA (ANDO AQ6317B), the peak was found to be at 1030.7 nm and can be seen in Figure 6.12 (b). The bandwidth at half maximum was found to be 0.22 nm. There is also noticeable rollover above 20 W of input power which is assumed to be thermally induced. A more efficient heat sinking arrangement or a reduction of the density of particulates in the film (particulates would degrade the thermal conductivity of the sample) will delay the thermally induced rollover and therefore improve the performance of the device.

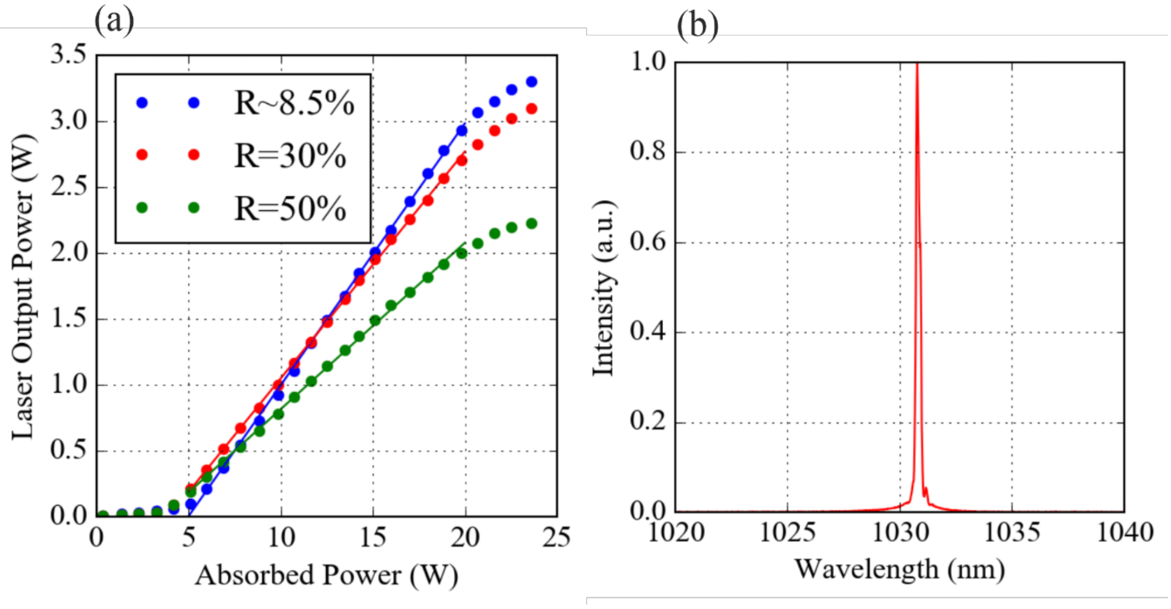

Figure 6.12. (a) Laser performance of Yb:LuAG clad waveguide with output mirror reflectance values of 8.5%, 30% and 50%. Lines of best fit are also shown, used for calculation of the laser efficiency. (b) laser output spectrum, peak wavelength 1030.7 nm, FWHM of 0.22 nm.

Here, the first PLD-grown double clad Yb:LuAG planar waveguide laser was presented. An output power of 3.3 W with an efficiency of 20% was realised. With further optimisation to create a single crystal LuAG structure with minimal defects, in particular by utilising the BDA regime which was created after this growth, the output powers could match and even exceed the powers achievable with Yb:YAG waveguides.

6.4 Yttrium Gallium Garnet

6.4.1 YGG fluence optimisation

Previous attempts to grow high-quality YGG films via uni-directional PLD have resulted in a high-density of particulates. Using bi-directional ablation, as seen in Figure 5.17, the particulate density was reduced significantly. By optimising the growth conditions, particularly the fluence, when using the bi-directional ablation setup, the particulate density could be further decreased.

To optimise the fluence and its effect on the particulate density, four films were grown at arbitrary fluences between 1.6-2.2 Jcm^{-2} with 36,000 shots at heating power of 11.5 W. The particulate density was calculated via the scattering point density method. The XRD spectrum and refractive index were measured; the parameters and characterisation results are shown in Table 6.4.

Table 6.4. Samples of Er (0.5%) YGG grown with 36000 shots with 11.5 W heating power

Sample Number	Fluence (Jcm^{-2})	Particulate Density (%)	XRD (100) Peak Position	XRD (100) Peak FWHM
JP143	1.6	0.31	28.86	0.05
JP144	1.75	0.16	28.84	0.04
JP145	1.9	0.12	28.83	0.04
JP146	2.2	0.17	28.83	0.03

Figure 6.13 (a) shows the scattering point density in Er (0.5%): YGG films grown with different ablation fluences, 36000 shots and 11.5 W of heating power. This indicates that an ablation fluence of 1.9 Jcm^{-2} is close to the optimal for minimisation of particulate density in the films further growths at fluences of >2.2 Jcm^{-2} would need to be explored to add weight to this conclusion. Figure 6.13 (b) demonstrates that the refractive index of the films decreases when the ablation fluence is increased. This can be explained by the change in the films stoichiometry resulting from different ratios of Y/Ga being ablated and the change in substrate temperature by the additional energy from the plume. The accepted value of the YGG refractive index is 1.91 at 633 nm (Mackenzie *et al.*, 2017), which is ~0.04 less than

the refractive index value for these films. The shift in peak position can be explained either by stress in the film or by the amount of Ga being transferred from the target to the film, being less than Y.

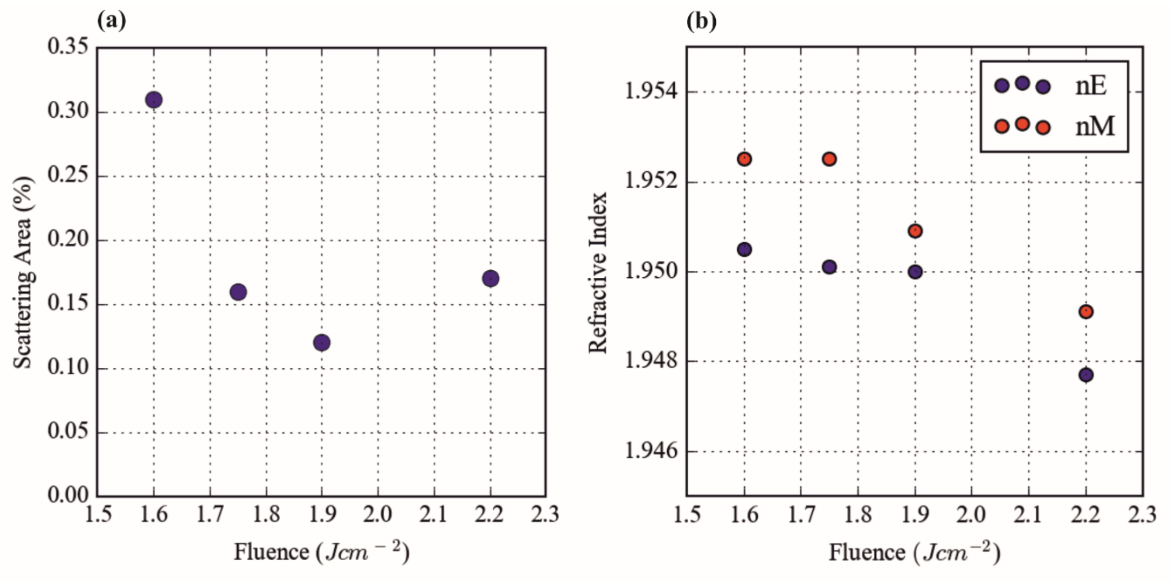

Figure 6.13. (a) Percentage area of coverage by scattering points in dark-field images for Er:YGG films grown with different ablation fluences and grown with 36,000 pulses, and, (b) the respective refractive index measurement at 633 nm.

6.4.2 YGG temperature optimisation

The temperature of the substrate during the growth is critical to the orientation in which the film will grow. However, as the film grows thicker the properties of the film itself can change as discussed in section 2.2.6. Thin films of 2 µm were observed to grow in a single crystal phase, but as they became thicker, e.g. to 20 µm, mixed orientations (depending on growth temperature) start to appear. In this section, I present the optimisation of the substrate heating power, and hence the temperature for single-crystal YGG growth for thick films.

Four YGG films were grown with process parameters as detailed in Table 6.5, with 1.6 Jcm^{-2} ablation fluence chosen to grow the most stoichiometric YGG despite the relatively small increase in particulate density. Despite being doped with different RE-ions, the vast difference in substrate heating power makes the relative differences in crystal growth useful for process optimisation. The XRD spectra of each film was measured and compared. Two of the films have identical growing parameters apart from growth time, to observe the difference in physical parameters when films are grown thicker. Three of the films were grown with the same ablation fluence, number of pulses and consequently thickness but different substrate temperature. These were grown to optimise the substrate temperature for growing single-crystal films.

Figure 6.14 shows the measured XRD spectrum of JP110 (blue line) and JP87 (black line). The XRD spectrum shows the thinner film is single crystal, <100> orientated YGG, whereas when grown thicker, shows the growth of domains, i.e. polycrystalline. This means that crystal orientation cannot necessarily be optimised with thinner films since it could change if grown to thicker, more useful, dimensions.

Table 6.5. Samples of YGG grown at different temperatures

Sample Number	Heating Power (W)	Number of Pulses	Fluence (Jcm^{-2})	Film Thickness (µm)	Dopant
JP110	15	360000	1.6	25	Yb (4%)
JP111	12	360000	1.6	25	Yb (4%)
JP125	9	360000	1.6	25	Er (1%)
JP87	15	36000	1.6	2.5	Er (.5%)

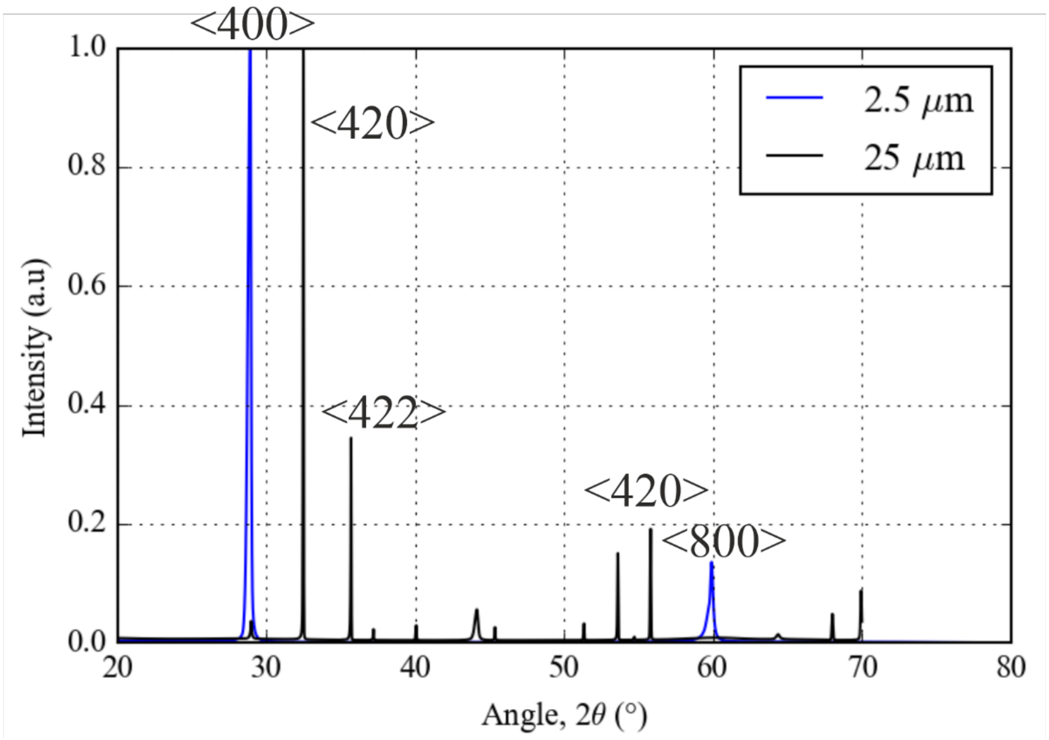

Figure 6.14. XRD spectrum of Er-doped YGG growths grown with 1.6 Jcm^{-2} ablation fluence and 15 W of heating power for 36000 and 360000 counts, resulting in 2.5-µm and 25-µm thick growths, demonstrating texture changes with thickness. The main peaks are labelled with the corresponding YGG orientations (Euler and Bruce, 1965).

Three, 25 µm thick YGG films were grown at 9, 12 and 15 W of heating power. The normalised XRD spectrum of these films can be seen in Figure 6.15. At 9 W of heating power, the film is predominately amorphous evidenced by the broad spectral features, at 12 W the film is single-crystal <100> YGG, and as we've previously seen in Figure 6.14, 15 W produced a polycrystalline film.

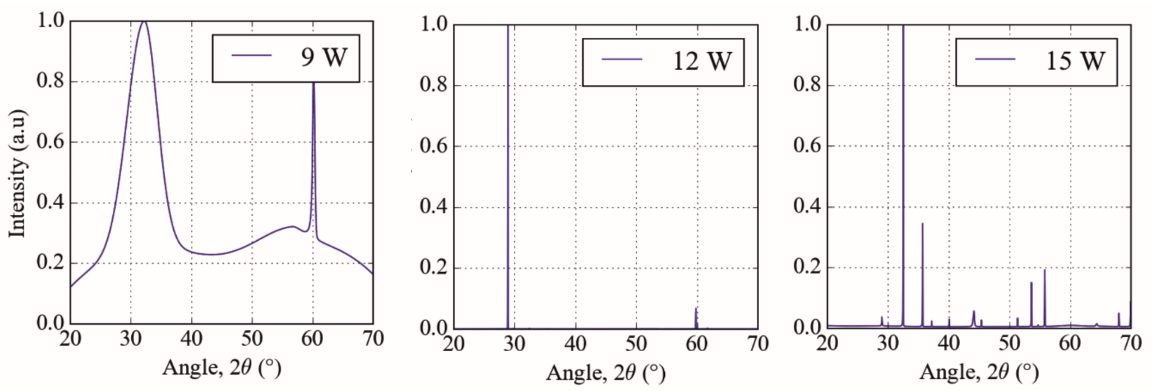

Figure 6.15. XRD spectrum from 25-μm thick YGG films grown with 9, 12 and 15 W heating power.

In this section, I have shown that films properties change when they are grown with a greater number of ablation pulses. In this case, two films grown to thicknesses of 2.5 μm and 25 μm with exactly the same growth conditions will be single-crystalline and poly-crystalline respectively as seen in Figure 6.14. I have also demonstrated that the optimum substrate heating power for YGG is around 12 W. Further experiments will be required to find what range of substrate heating powers around 12 W would also produce single crystal films.

6.4.3 Er-doped YGG

As discussed in section 3.2.1.2, Er-doped active material has emission bands in the 1.6 μm regime. In particular, Er:YGG has emission bands that make it suitable as a source for characterising greenhouse gases (CO_2 and methane) as discussed in section 3.2.2.2. In order to achieve useful gain for high power applications, the loss in the waveguides needs to be small. Using a combination of BDA and optimised growth parameters there is some promise of achieving this.

With this application in mind, thick films (up to 25 μm) were grown with dopant concentrations of 1, 2 and 4 %. The growth conditions of these samples can be seen in Table 6.6. These films were facet polished on two parallel sides and end-pumped with a fibre-coupled 974-nm wavelength laser diode. A multimode-fibre patch cable (0.275 NA, 62.5 μm core fibre) was placed in close proximity to the top surface of the film to measure the fluorescence using an OSA (Ando AQ6317B). The excitation lifetime was measured using the pump laser in a pulsed regime and a transimpedance amplified InGaAs photodiode (Thorlabs PDA10CS-EC). A longpass filter with a cut on wavelength of 1000 nm was used between the photodiode and the fibre to cut out the residue pump light.

Figure 6.16 (a) shows the fluorescence measured from a 2% Er doped sample. The other samples grown with different doping concentrations had an almost identical fluorescence spectrum. This demonstrates that the growths are repeatable and doping levels of up to 4% do not cause any significant degradation of the film’s emission properties. Figure 6.16 (b) shows the lifetime measurement for a 2% Er-doped sample. The lifetime was measured to be 5.39 ms which is close to that found by (Stange *et al.*, 1989) at 5.71 ms.

Table 6.6. Growth conditions of Er:YGG samples

Sample Number	**Ablation Regime**	**Er (%)**	**Substrate Heating (W)**	**Fluence (Jcm^{-2})**	**Thickness (µm)**
JP108	BDA	4	15	1.6	20
JP112	BDA	2	12	1.6	12.5
JP148	BDA	1	11.5	1.9	25
J109	UDA	2	10.5	1.9	6

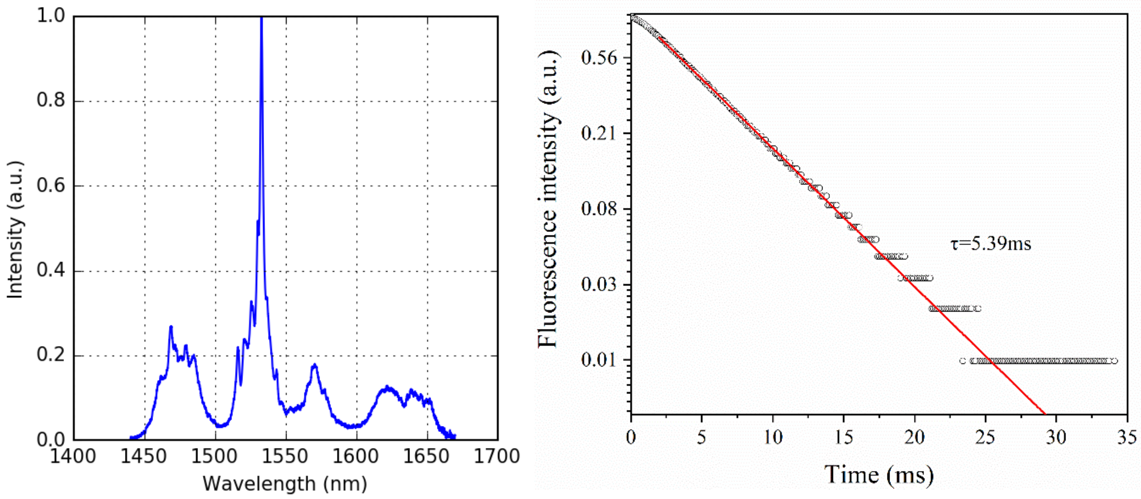

Figure 6.16. Fluorescence spectrum (a) and (b) lifetime measurement (b) of a 2% Er-doped YGG film

6.4.4 Fabrication of channel waveguides

It has been shown that by using ultra-precision dicing, ridge waveguides with sides of optical quality, comparable to that obtained via lapping and polishing can be achieved. This allows for rapid processing of samples and optical confinement in two dimensions rather than in the one-dimensional geometry of a planar waveguide, making it compatible with coupling of fibre pump sources.

Ridge waveguides were fabricated on the samples seen in Table 6.6 by Lewis Carpenter in the ORC. This was achieved with ultra-precision dicing, utilizing ductile mode machining. Using a similar process to that used in (Carpenter *et al.*, 2017) the dicing machining parameters were optimised to enable fabrications of ridge walls with as low roughness as possible. For these samples, a Disco DAD3430 dicing saw and a nickel bonded blade (Z09, Disco) with a small grit size (SD5000) were used. At a feed rate of 20 nm/rev, a 40-µm depth of cut was used to remove the material in a single pass. Throughout, reverse osmosis water was used as the coolant maintained at 21 ºC to reduce temperature differentials whilst processing. The facets were cut using the same process parameters. The surface topology of the facets was measured by a white light interferometer and the roughness parameters calculated, following form error correction through removal of long-range shape and tilt.

Nine ridge waveguides were fabricated on each sample. Microscope images of three of these can be seen in Figure 6.17 (a). The widths of the ridges were set to be in the range from ~13-28 µm with average surface roughness S_a and S_q of 3.8 ± 1.9 nm and 5.1 ± 2.5 nm respectively. The pump laser would be coupled into the edge of the facet seen in Figure 6.17.

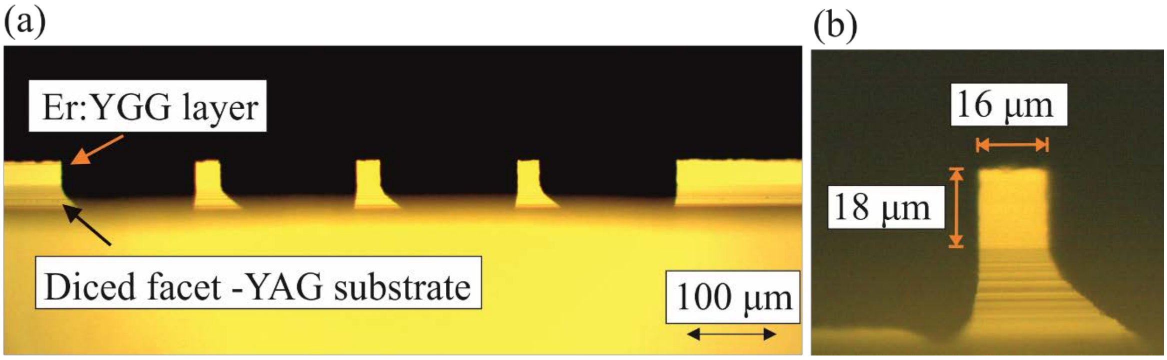

Figure 6.17. (a) Microscope image of the end facets of three adjacent Er:YGG ridge channel waveguides on JP108 (b) 100x magnification image of one ridge on JP108.

6.4.5 Er:YGG channel waveguide characterisation

Quantifying the waveguide mode properties is important to determine the optimum launch conditions for the waveguide to achieve the best possible coupling efficiency. Using a germanium scanning slit photodetector (NanoScan 2S Ge – Ophir), the intensity profile of the propagating mode(s) of the channel waveguides was measured at the exit facet. This was compared with the incident beam profile, measured at the location of the in-coupling facet of the channel.

The beam profile of the input beam (1480 nm laser diode) is shown in Figure 6.18 (a). The beam was launched into one facet, the exit beam measured, the waveguide was then rotated 180^{o} to launch from the other direction. This gives an indication in the difference in mode profiles at each end and highlights any irregularity in the channel shape. The exit beam from the two sides of an exemplar channel on JP112 is shown in Figure 6.18 (b) and (c). These show a slight asymmetry in the guide. Microscope images, which were calibrated using gratings of known size, found that the thickness of the film was not uniform across the guide, deviating ~ 1 μm over the length of the sample. Also, one of the sides of the ridge waveguide has a small inclination (<1^{o} from microscope images), meaning it is not perfectly perpendicular to the YGG film. Other channels did not provide a symmetric beam profile. This could be due to defects in the channel's surface, or particulates grown in the film itself.

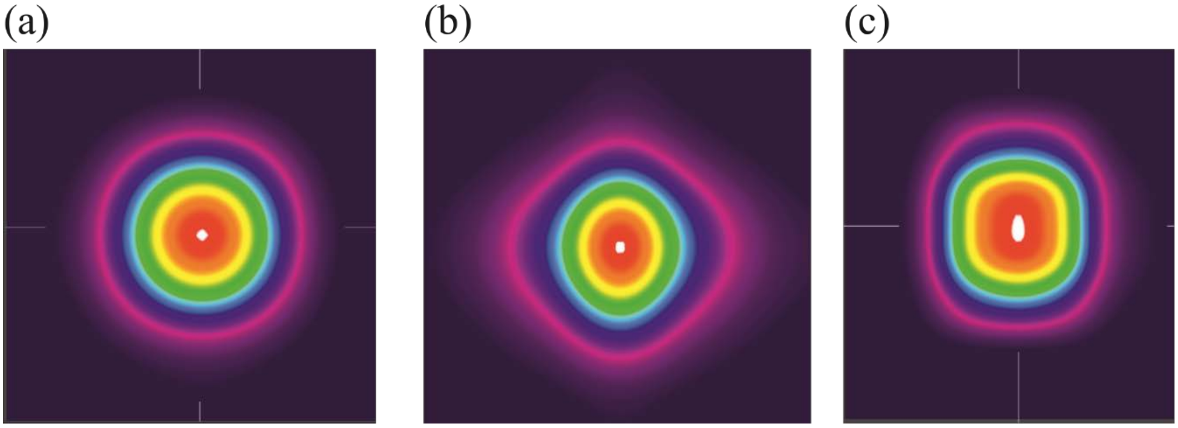

Figure 6.18. Beam profile images produced via line scans of each axis of (a) input beam ($\phi_{D4\sigma}$=10.4 μm), (b) mode profile at one end facet of the Er:YGG ridge channel waveguide on JP112 ($D4\sigma_X$=10.6 μm, $D4\sigma_Y$=10.4 μm), and (c) at the other end ($D4\sigma_X$=10.8 μm, $D4\sigma_Y$=12.4 μm)

6.4.6 Er:YGG amplifier performance

With knowledge of the mode dimensions, the channel waveguide facets were pumped, and gain measurements taken. These measurements give an indication of the quality and efficiency of the device. The channel with the shape most resembling the pump beam profile was chosen on each sample, to ensure good spatial overlap between the pump beam and laser mode, so that the coupling efficiency is as high as possible.

The gain measurements were taken using a modulated pump, with 20 ms pulses at 10 Hz, and a CW probe technique. In the setup (Figure 6.19), a fibre-Bragg-grating locked diode-laser pump operating at a wavelength of 1480 nm, was combined with a seed source via a wavelength division multiplexer. The seed source was a tuneable diode-laser in the C- or the L-band (1530-1565 nm and 1565-1625 nm respectively), or a 1651 nm distributed-feedback diode-laser. The pump and seed lasers were coupled into a single-mode fibre, and, using an adjustable magnification telescope to optimise the launch, free-space coupled into the waveguide. The light exiting the waveguide was collimated then reflected off a diffraction grating. Separating the pump and seed beams spatially after the focussing lens and the power of the seed was monitored as a function of pump power.

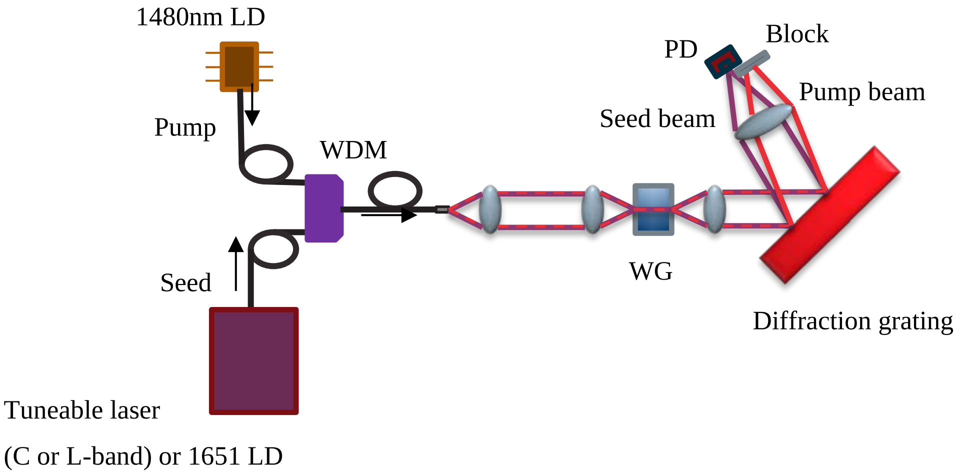

Figure 6.19. The setup for Er:YGG gain measurements. This includes a wavelength division multiplexer (WDM) to combine the pump and seed lasers which are launched into the waveguide. The amplification is measured at the photodiode (PD).

Using this setup, with the seed source in CW mode and the pump in pulsed mode, measurements were taken of the amplification of the seed wavelength. Measurements were performed with the seed set at three key wavelengths; 1533 nm is the peak in the emission cross section. 1572 nm is optimal for CO_2, and 1651 nm is for methane. The measured power of the seed after the waveguide in a function of the peak pump power, can be seen in Figure 6.20 (a). This shows the response of the transmitted seed power to a 20 ms pulse. The input seed power was 4.3 mW, without pump ~0.75 mW was measured after the waveguide. This is a combination of absorption, coupling efficiency, and propagation loss due to surface roughness in the channel side walls and particulates/defects. Figure 6.20 (a) shows an increase in seed output power from 0.7 to 7.5 mW with 353 mW of pump power. The gain with pump power can be seen in Figure 6.20 (b), which shows the gain increasing with pump power, up to 3.46 dB, and starting to saturate at ~200 mW of pump power.

Table 6.7 shows loss and gain measurements with samples JP108, JP112, JP148 and J109. JP112 has the highest internal gains for all seed wavelengths, which is attributed to the relatively low propagation losses and moderately high doping level. This is in comparison to J109, which was grown via UDA, and has the highest loss and lowest internal gains. This further demonstrates the significant effect of lowering the particulate density, as achieved with BDA. JP148 has the lowest loss at 1651 nm but does not have as high a gain as JP112, due to a lower 1% Er doping concentration. JP108 has a 4% Er concentration, but has a loss >1dB, furthermore, at this relatively high doping level excited-state parasitic energy transfer effects begin to play a major role, both of which significantly degrade its performance.

Table 6.7. Loss and maximum internal gain measurements for Er:YGG samples. Loss excludes -0.85 dB Fresnel reflection losses

Sample Number	**Er Doping (%)**	**Coupling, absorption and propagation loss (dB @ 1651 nm)**	**Internal gain, dB**		
			1533 nm	1572 nm	1651 nm
JP148	1	-0.27	1.57	0.45	0.35
JP112	2	-0.9	3.46	0.54	0.53
JP108	4	-1.2	-3.31	0.41	0.44
J109	2	-4.0	1.1	-1.95	-1.24

Figure 6.20 (a) shows that the seed output power is subject to parasitic effects such as excited state energy transfer and thermal effects, reducing the achievable gain. The parasitic effects were more significant in waveguides with a higher doping concentration, due to the increased energy transfer coefficients and heat loading density. The parasitic effects could be reduced by reducing the Er concentration and growing larger samples to increase the available gain. The current PLD setup is limited to the growth on 10x10 mm substrates, so an upgrade of this system would be required to optimise for the samples gain length product. Further optimisation of the dicing for this material could provide a more symmetrical channel and a decreased sidewall roughness, improving the coupling efficiency and consequently decreasing the associated loss.

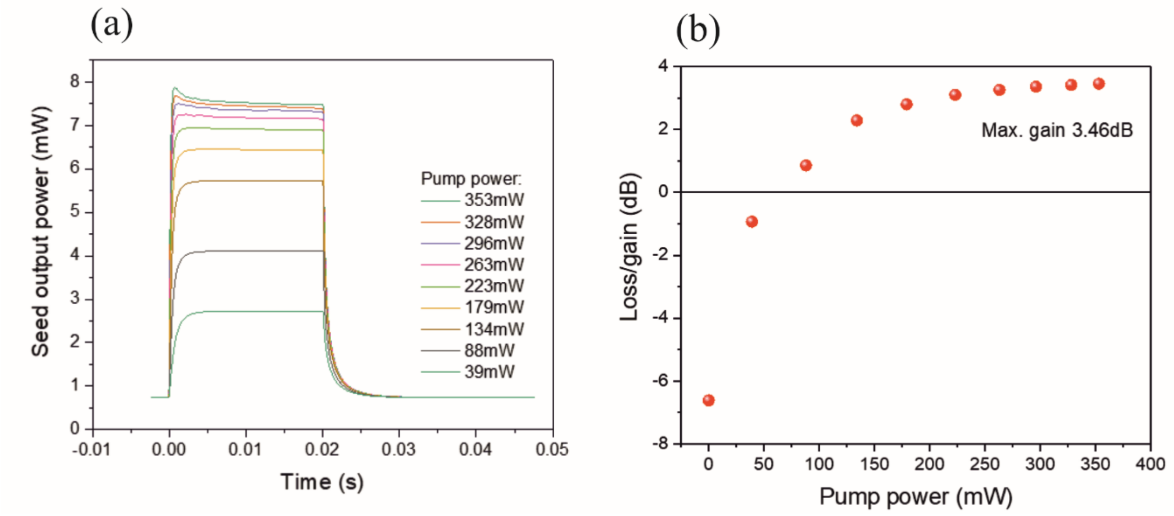

Figure 6.20. Gain measurements of the channel waveguides on JP112 (2 at.% Er-doping). (a) Measured seed power at 1533 nm when the channel was pumped with a pulse of peak power ranging from 39- 353 mW, the pulse is switched on at 0 seconds and (b) the associated loss/gain of seed power.

I have demonstrated Er:YGG waveguides with some of the lowest propagation losses recorded for a PLD-grown film. Moreover, these record low losses are inclusive of non-negligible losses associated with the channel fabrication. The spectroscopic parameters are comparable to those grown via the Czochralski method and record gain-levels have been measured for this material. With further optimisation of the growth and dicing parameters, along with growths on larger substrates, further improvements in the gain could be achieved. This would make PLD-grown Er:YGG a viable candidate for amplifiers that cover the absorption bands of CO_2 and CH_4.

6.5 Summary

In this chapter, I have explored the growth and functionality of garnet films grown via PLD. Initially, I looked at the growth and optimisation of YAG films, then demonstrated lasing in a PLD-grown Yb:LuAG cladded waveguide. Finally, I demonstrated gain in Er:YGG planar and channel waveguide amplifiers.

With the YAG films, attempts were made to reduce the particulate density and improve the crystalline properties compared to previous results, where 22 W of output power was achieved. The optimum substrate heating power for single-crystal growth was found to be 15 W, with lower temperatures growing amorphous and higher temperature polycrystalline.

I also found an optimum growth fluence for low scattering point density of 1.0 Jcm^{-2}. This low optimum fluence is likely caused by the difference in the powder size of the respective constituent oxides used to fabricate the target, along with the annealing processes that may have favoured clustering, and the final density of the targets. This means when high fluence values are used, exfoliation is more likely. However, single-crystal, thick-films with low particulate density have been grown and now require polishing to enable laser experiments.

3.3 W of output power and 22% efficiency were demonstrated with a Yb:LuAG cladded waveguide. This is the first time a PLD-grown clad LuAG waveguide laser has been demonstrated. The loss was found to be 1.22 dB/cm, which didn’t prevent gain being realised, however it did have a detrimental impact on the efficiency, laser threshold, and therefore maximum output power achieved. By using bi-directional ablation, the particulate density will be decreased and the output powers achievable should increase.

Finally, the optimisation of the growth of YGG films was presented. It showed the optimum substrate heating power was around 11.5 W, producing single-crystal films of up to 25-µm thick. It was observed that the optimum ablation fluence for low particulate density (down to ~0.1%) was 2.05 Jcm^{-2}. Gain was subsequently realised in Er:YGG channel waveguides, grown via PLD and then diced to fabricate the channels and facets, achieving 3.46 dB of internal gain at 1533 nm. A measurement of the loss found a minimum value of 0.27 dB including coupling and absorption losses @1651 nm. Howerver, in order to proceed with Er:YGG and produce desired levels of gain (>10dB), larger samples sizes are needed to increase the interaction length.

In this chapter the potential of PLD to produce high-quality RE-doped garnets for laser applications has been demonstrated. Using the knowledge gained here, especially regarding controlling the properties when grown thicker, it should be possible to produce garnet crystal-films, potentially scalable up to dimensions compatible with thin-disk dimensions laser requirements (on order of 100 microns), with properties approaching bulk equivalents grown via the Czochralski method.

6.6 References

Beecher, S. J., Grant-Jacob, J. A., Hua, P., Prentice, J. J., Eason, R. W., Shepherd, D. P. and Mackenzie, J. I. (2017) 'Ytterbium-doped-garnet crystal waveguide lasers grown by pulsed laser deposition', *Optical Materials Express,* 7(5), pp. 1628.

Beil, K., Fredrich-Thornton, S. T., Tellkamp, F., Peters, R., Kränkel, C., Petermann, K. and Huber, G. (2010) 'Thermal and laser properties of Yb:LuAG for kW thin disk lasers', *Optics express*, 18(20), pp. 20712-20722.

Bhutta, T., Mackenzie, J. I., Shepherd, D. P. and Beach, R. J. (2002) 'Spatial dopant profiles for transverse-mode selection in multimode waveguides', *JOSA B,* 19(7), pp. 1539-1543.

Burmester, P. B. W., Ishii, T., Huber, G., Kurfiss, M. and Schilling, M. (2003) 'Characterization of crystalline europium doped α-Y2O3 PLD-films grown on α-Al2O3', *Materials Science and Engineering: B,* 105(1-3), pp. 25-29.

Carpenter, L. G., Berry, S. A. and Gawith, C. B. E. (2017) 'Ductile dicing of $LiNbO_3$ ridge waveguide facets to achieve 0.29 nm surface roughness in single process step', *Electronics Letters,* 53(25), pp. 1672-1674.

DeLoach, J. D., and Aita, C. (1998) 'Thickness-dependent crystallinity of sputter-deposited titania', *Journal of Vacuum Science & Technology A: Vacuum, Surfaces, and Films,* 16(3), pp. 1963-1968.

Droubay, T. C., Qiao, L., Kaspar, T. C., Engelhard, M. H., Shutthanandan, V. and Chambers, S. A. (2010) 'Nonstoichiometric material transfer in the pulsed laser deposition of $LaAlO_3$', *Applied Physics Letters,* 97(12).

Emiraliev, A., Kocharov, A. G., Bakradze, R. V., Karimov, U. and Ahmetzhanov, Z. I. (1976) 'The neutron diffraction redefinition of the coordinates of the atoms of oxygen in yttrio-aluminium garnet.', *Kristallografiya,* 21, pp. 211-213.

Euler, F. and Bruce, J. A. (1965) 'Oxygen coordinates of compounds with garnet structure. ', *Acta Crystallographica,* 19(6), pp. 971-978.

Kurilchik, S. V., Grant-Jacob, J. A., Prentice, J. J., Hua, P., Eason, R. W. and Mackenzie, J. I. 'Pulsed-laser-deposited Yb:YAG planar-waveguide amplifier', *8th EPS-QEOD Europhoton,* Barcelona, Spain, 02-07 September.

Mackenzie, J. I. (2007) 'Dielectric Solid-State Planar Waveguide Lasers: A Review', *IEEE Journal of Selected Topics in Quantum Electronics,* 13(3), pp. 626-637.

Mackenzie, J. I., Grant-Jacob, J. A., Beecher, S., Riris, H., Yu, A. W., Shepherd, D. P. and Eason, R. W. 'Er:YGG planar waveguides grown by pulsed laser deposition for LIDAR applications', *Solid State Lasers XXVI: Technology and Devices.*

Ojeda, G. P. A., Schneider, C. W., Döbeli, M., Lippert, T. and Wokaun, A. (2015) 'The flip-over effect in pulsed laser deposition: Is it relevant at high background gas pressures?', *Applied Surface Science,* 357, pp. 2055-2062.

Stange, H., Petermann, K., Huber, G. and Duczynski, E. W. (1989) 'Continuous wave 1.6 µm laser action in Er doped garnets at room temperature', *Applied Physics B,* 49(3), pp. 269-273.

Chapter 7 Sesquioxides

7.1 Motivations

Sesquioxides have been widely researched as a laser host due to their advantageous properties as described in Chapter 2. However, difficulties remain in the growth of large scale, single-crystal sesquioxides due to their high melting points (Lu_2O_3 melting point is ~2500 ^oC). As such, the growth of sesquioxides via a melting process is an energetically and physically demanding process as the crucible must also be a refractory material (Peters *et al.*, 2009). During the past few years, transparent ceramics have been used as an alternative to single crystal (Beil *et al.*, 2013) since the fabrication of ceramics requires a lower temperature than the melting processes. Yb-doped Lu_2O_3 has attracted particular interest, with ceramic lasers demonstrating high-efficiencies (74%, (Sanghera *et al.*, 2011)) and high CW output-powers (174 W) (Kitajima, 2017).

When using PLD, the melting point of a material, while important to consider, is not a limiting factor (discussed further in section 2.2). Therefore, materials such as sesquioxides with high melting points (>2400 ^oC (Krankel, 2015)) can be grown with relative ease compared to for example Czochralski growth. High quality, low defect density material growth is crucial for lasing applications, and this is possible with PLD as shown with previous research where lasing was demonstrated in Yb:Lu_2O_3 (7.4 W output power), Yb:Y_2O_3 (1.7 W output power) and Tm:Y_2O_3 (35 mW output power) (Parsonage *et al.*, 2015; Beecher *et al.*, 2014; Szela *et al.*, 2013). These results show the potential of PLD as a growth technique for sesquioxides, however, these results were limited by the propagation losses in the films. With further optimisation of the growth conditions, and the implementation of bi-directional ablation, the quality of the resultant sesquioxide films could be improved. A higher quality crystal with fewer defects would lead to lower loss and consequently higher output power lasers.

A further advantage for using PLD is the ability to actively control the stoichiometry of the crystal layer when growing a mixture of sesquioxides. Mixing sesquioxides changes the lattice constant of the resultant film, which can be optimised to match that of the substrate. Lattice mismatch becomes important for thicker growths which are needed for compatibility when pumping waveguides with high-power diode arrays, or for films suitable as the gain element in a thin-disk laser (Giesen *et al.*, 1994). Good film lattice matching in films with less stress, so therefore thicker films with fewer defects are possible, as previously described in section 2.2.3.3. Optimising the stoichiometry using PLD can be realised by changing the ratio of constituents in the target material.

In this chapter, the focus of the research was lutetia (Lu_2O_3) and scandia (Sc_2O_3), with sapphire (α-Al_2O_3) being discussed in the next chapter. The optimisation of the PLD process binary and mixed sesquioxides and the influence of texture, affecting the propagation of light through the resultant waveguides is detailed.

7.2 Binary Sesquioxides - Lutetia

Binary sesquioxides have been grown with success using the PLD method as detailed in section 3.2.2.4. Key results report the growth of lutetia, scandia and yttria demonstrated and lasing realised in $Yb:Y_2O_3$ and $Yb:Lu_2O_3$. The lasing samples were grown on (100)-YAG substrates whereas in this work, the films were grown on c-cut sapphire substrates. This exploits the superior thermal properties of sapphire (30 $Wm^{-1}K^{-1}$ (Dobrovinskaya *et al.*, 2009) compared to 13 $Wm^{-1}K^{-1}$ for YAG (Kuwano *et al.*, 2004)), that ideally will allow for more efficient cooling and power scaling. Furthermore, optimisation of the ablation fluence should decrease the density of defects in the resultant films, minimising the propagation losses during waveguiding.

In the following sections, the growths of $Yb:Lu_2O_3$ on sapphire substrates are detailed and demonstrate the parameter optimisation for low particulate density and single-crystal growths. The presence of regions in the growths is observed and a potential solution to mitigate domain formation is presented.

7.2.1 Lutetia crystallinity study

As lutetia was grown onto sapphire, i.e. a cubic lattice onto a hexagonal lattice, the optimal orientation of growth is not necessarily obvious. As shown in section 5.1, the growth of <111> orientated lutetia, scandia or yttria seems to be optimal however the main goal should be for single-crystal growth. Polycrystalline growth increases the chances of local defects/stresses at the interfaces of the crystal domains.

Two 5% Yb-doped Lu_2O_3 films were grown with 360,000 pulses to thicknesses of ~15 µm with an ablation fluence of 1.4 Jcm^{-2}. Based on previous work performed by (Parsonage *et* *al.*, 2015), a substrate heating power of 20 W was used for one sample (JP130), 25 W for the other (JP129). These were measured using θ/2θ XRD and then GI-XRD for comparison.

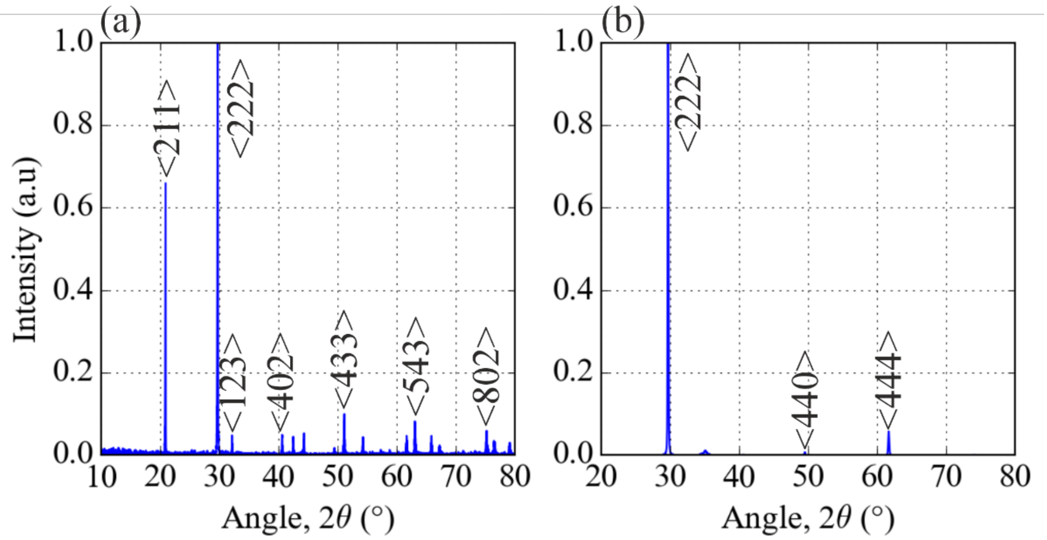

Figure 7.1. XRD spectrum of Yb:Lu_2O_3 films grown with 360,000 pulses with substrate heating powers of (a) 20 W and (b) 25 W. The main peaks are labelled and correspond to different orientations of Lu_2O_3, the smaller unlabelled peaks also correspond to orientations of Lu_2O_3 (Guzik *et al.*, 2014).

Figure 7.1 (a) shows θ/2θ XRD measurement of JP130 and has multiple orientations of Lu_2O_3 labelled on the figure. This demonstrates a highly polycrystalline growth. Figure 7.1 (b) however, shows the θ/2θ XRD spectrum from JP129. The main peak observed here is the <222> orientation and a couple of other, smaller peaks. While not perfectly single-crystal, it is less poly-crystalline than JP130. While this indicates that 25 W produces a higher-quality crystal film,

Figure 7.2 shows the GI-XRD spectrum of JP129, where multiple Lu_2O_3 peaks are observed. This implies that the top layers of JP129 have a greater number of orientations than the bottom layers, since the θ/2θ XRD scan did not register these orientations. In order to prevent these orientations, the substrate heating power needs to be optimised for thick-film growths. However, JP129 appeared to be mainly single crystal so could be polished and optically tested.

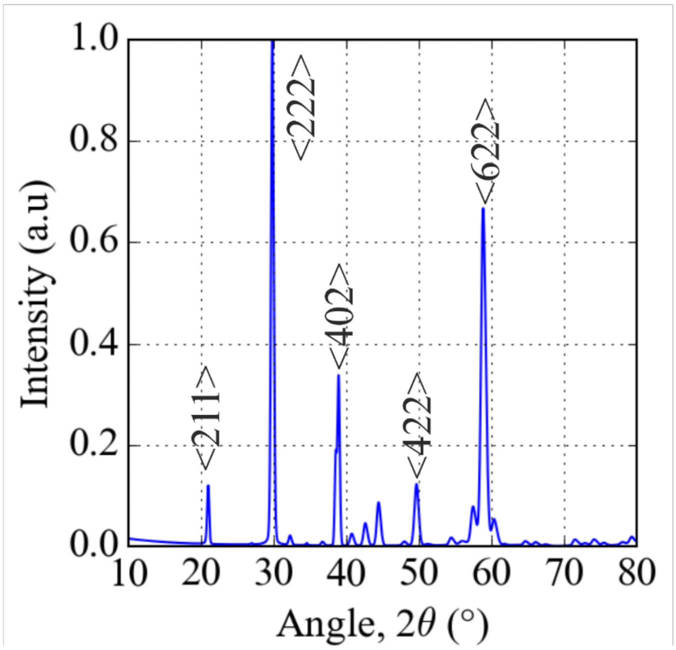

Figure 7.2. GI-XRD of Lu_2O_3 film grown with 25 W substrate heating power, 360,000 pulses and 1.4 Jcm^{-2} ablation fluence

7.2.2 Optical investigation of $Yb:Lu_2O_3$ films

The lifetime and fluorescence spectrum of an active material can indicate the quality of the film since defects in the film can reduce the lifetime of the dopant ion. JP129 and JP130 were tested to measure their lifetime and fluorescence spectra. This was compared with literature values (Guzik *et al.*, 2014).

In the experimental setup, the face of the samples was directly pumped with a 974 nm diode laser and the fluorescence captured by a Thorlabs M31L03 optical fibre that was proximity coupled at an angle to the back of the sample. This can be seen in Figure 7.3 along with green fluorescence observed on the sample, likely from Er contamination in the target due to the difficultly in separating RE elements from their naturally formed ores. Since erbium has a relatively small absorption cross section at ~980 nm, the ytterbium ions still absorb most of the pump at this wavelength. However, the energy absorbed by the ytterbium could be transferred to the erbium decreasing the efficiency of the device. This effect should be negligible due to the expected insignificant contamination evidenced through EDX measurements of the target, which could not find any erbium atoms. The optical fibre was attached to an OSA or an InGaAs photodetector.

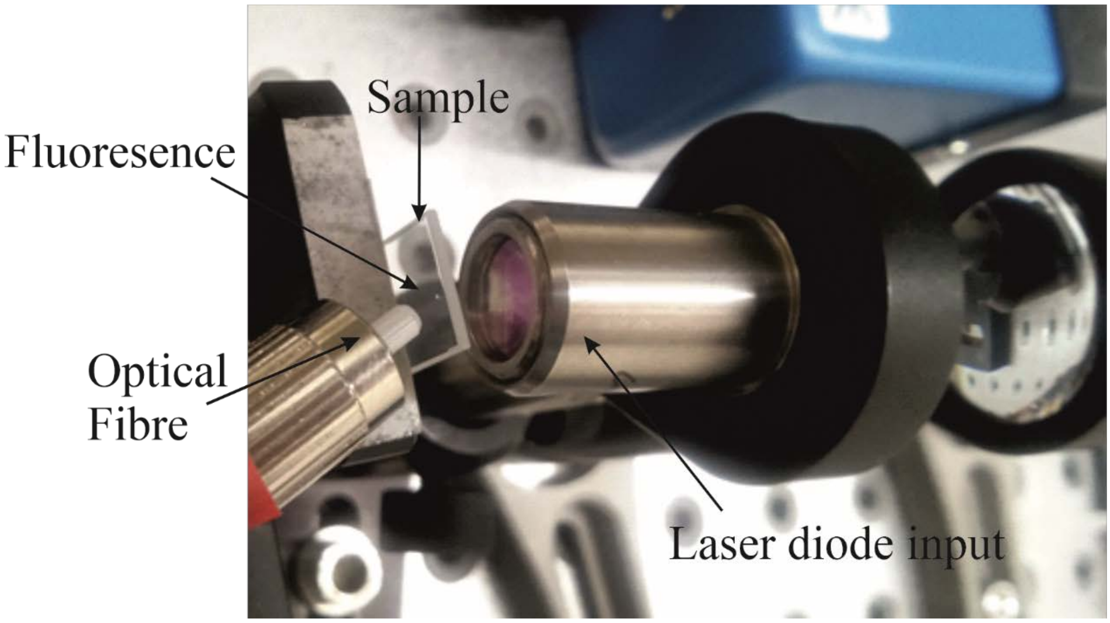

Figure 7.3. Setup for measuring the lifetime and fluorescence; fluorescence can be seen on the sample as a small green dot.

Figure 7.4 (a) shows the fluorescence spectrum and Figure 7.4 (b) the fluorescence lifetime for JP130. The dual-peak at ~976 nm can be attributed to the zero-phonon line of Yb:Lu_2O_3 and scattered 976 nm pump light. The spectrum is comparable to that of Yb:Lu_2O_3 found in literature and the lifetime found to be 808 µs, only 12 µs shorter than the low concentration limit seen in (Peters *et al.*, 2007) of 820 µs. This lifetime demonstrates an improvement on the PLD-grown Yb:Lu_2O_3 presented in (Parsonage *et al.*, 2015) which found a lifetime of 785 µs, with the shortened lifetime being attributed to quenching effects. Further crystal quality improvement could further increase the lifetime measured here.

The results of the fluorescence spectrum and lifetime were promising and hence facet polishing was undertaken. A photograph of JP130 is seen in Figure 7.5, where a 974 nm laser beam has been coupled to the active film of JP130. A 400-840 nm bandpass filter was placed between the sample and camera, so the green light that is likely emitted from erbium contamination, which is to be expected in an Yb-doped sample as previously discussed. While this photograph shows particulates scattering light by the passing pump light, only a few defect centres can be observed as bright points in the waveguide.

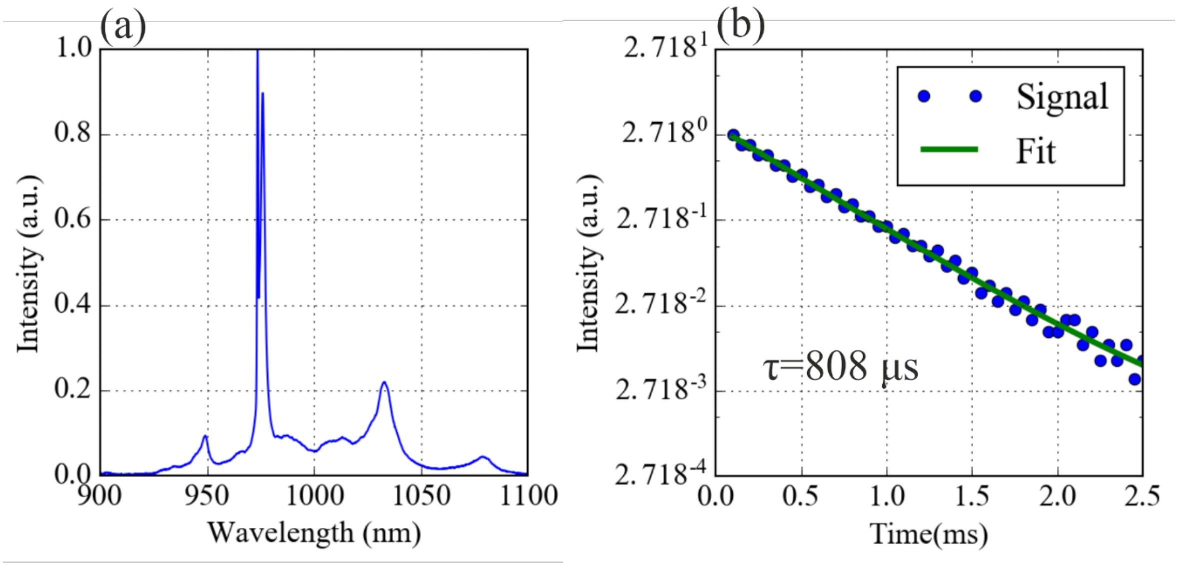

Figure 7.4. (a) Fluorescence spectrum and (b) lifetime measurement of emission from Yb:Lu_2O_3 film.

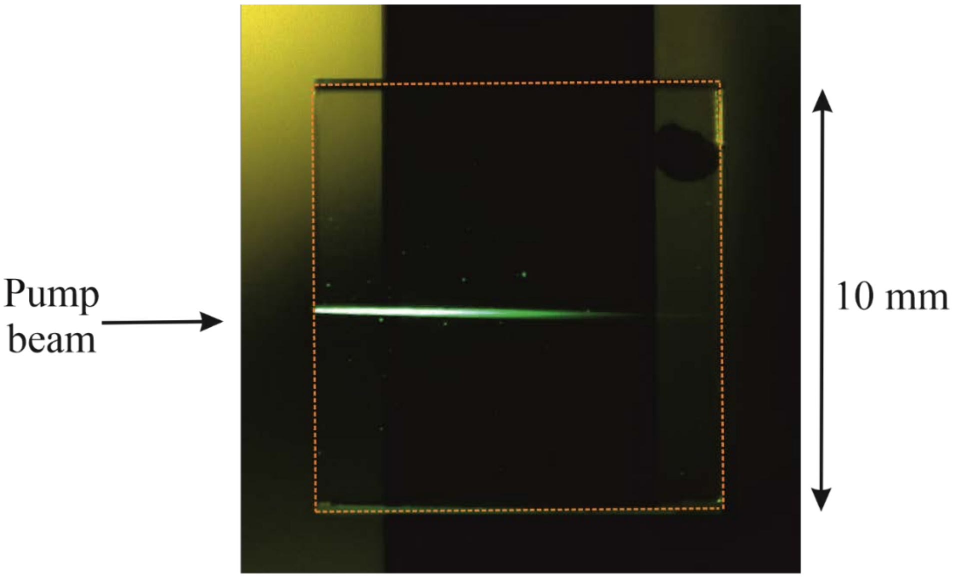

Figure 7.5. Photograph of 974 nm laser diode beam coupled into Yb:Lu2O3 film with a 400-840 nm band-pass filter placed between the sample and the camera. The edge of the sample is shown by the orange dashed line.

By coupling in a 1550 nm laser beam, a wavelength that isn't absorbed by the ytterbium dopant (however Er contamination could absorb at this wavelength, though the Er concentration isn't enough to cause significant loss), the propagation loss can be estimated. The incident and transmitted power was measured and used to calculate the propagation loss, after the combined Fresnel reflection loss from both facets was removed (calculated from equation 3.8). JP130 was found to have an average propagation loss of ~ -1.05 dB/cm (calculated from three measurements in three different locations). This is higher than optimal, but is again an improvement from that demonstrated in (Parsonage *et al.*, 2015), in which they demonstrated a -1.35 dB propagation loss in a Yb:Lu_2O_3 active waveguide.

I have shown that Yb:Lu_2O_3 has good optical characteristics, with the fluorescence emission and lifetime values comparable to bulk values (Guzik *et al.*, 2014). The lifetime and loss values are improved from previous PLD-grown Yb:Lu_2O_3 films. Lasing of these samples was not attempted, since the facets were not perpendicular. Re-polishing of the sample is required for further investigation.

7.2.3 Regions in Lu_2O_3 films

As demonstrated in Figure 7.5, JP130 has a low density of visible scattering points but the loss is ~1.05 dB/cm. As discussed in chapter 4, YGG films had losses approaching 0.1 dB/cm, and the reason for the higher loss values in Yb:Lu_2O_3 films is attributed to domains in the film. Regions will form interfaces that the light will need to travel through, which could cause scattering and hence increase the propagation loss. These domains can be observed by using BSE images of the polished facets.

Figure 7.6 shows a contrast adjusted, BSE image of the facet of JP130. Vertical regions of different grey-scale intensities can be seen on the polished facet, which indicates growth of a material with different physical characteristics. From the GIXRD spectrum, seen in Figure 7.2, the dominant growth is <111> Lu_2O_3 but there are multiple other orientations present in this film. These regions therefore could be different orientations of Lu_2O_3. The other possibility is that, since this is the growth of a <111> cubic lattice onto a <0001> hexagonal lattice, there are incompatible film seed positions for <111> growth as illustrated in Figure 7.7.

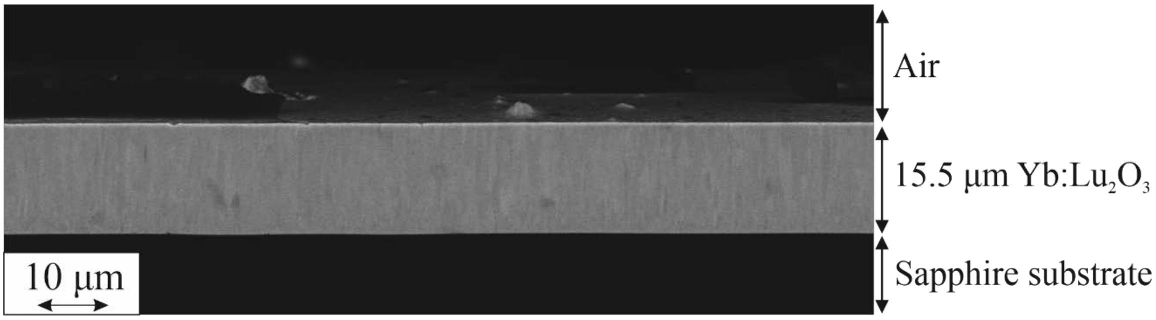

Figure 7.6. Contrast adjusted BSE image of Yb:Lu_2O_3 film.

The diagram shown in Figure 7.7 (a) shows two different seed positions for <111> growth onto a hexagonal lattice (the solid-purple and the dashed-green lines). If growth was seeded from these two positions, there would be a defect in the form of a vacancy between the two growths. This would form an interface between the two islands of growth and could be observed in an BSE as seen in Figure 7.6. The interface would also likely cause scattering of light propagating through, increasing the propagation loss of the waveguide.

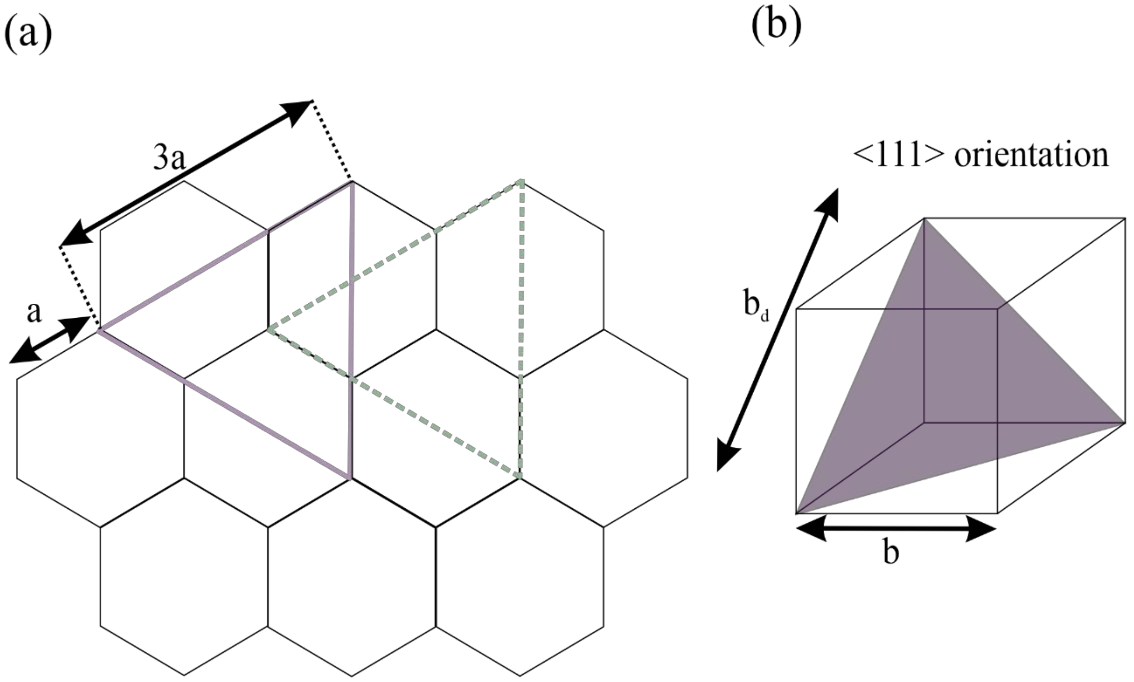

Figure 7.7. (a) Illustration of the incompatible potential seed positions for a <111> cubic lattice on a <0001> hexagonal lattice. The purple solid and green dashed lines demonstrate potential positions. (b) Diagram showing the <111> orientation on a cubic lattice

Preventing such domain formation observed in these Yb:Lu_2O_3 films could be the key for low loss waveguides and will be discussed in section 7.3.3. The fluorescence lifetime was measured to be 808 µs with losses of ~ 1.0 dB/cm, both improvements over published values reported in PLD-grown Yb:Lu_2O_3 waveguides (Parsonage *et al.*, 2015), likely due to a lower density of defects. Initial polishing of the facets was not of sufficient quality to use the Fresnel reflection as a mirror in a laser cavity. As such, further polishing of the thick Yb:Lu_2O_3 films presented here, to produce parallel, optical quality facets is needed to allow laser experiments and is expected to produce guides with higher output powers than previously seen with Yb:Lu_2O_3 PLD-grown waveguides.

7.3 Mixed Sesquioxides

As previously described, sesquioxides have the potential to be an exceptional active laser crystal host. When doped with ytterbium, their emission bandwidths have a relatively large FWHM, meaning, shorter pulse-widths can be supported, compared with Yb:YAG. It has also been shown that if sesquioxides are mixed to create a crystalline ternary compound, the emission bandwidth is wider still (discussed in section 3.2.2.3), providing further scope for ultra-short pulses (Beil *et al.*, 2013). However, growing mixed sesquioxides has proven difficult, with the achievable crystal quality hampering efforts in generating ultra-short pulses (Krankel, 2015). The difficultly lies with the high melting points of the primary sesquioxides of interest, i.e. scandia, lutetia and yttria, all being at ~2500ºC.

Growing sesquioxides onto sapphire substrates using PLD is possible, as demonstrated with the lutetia growths in section 7.2. Furthermore there is a reasonable match between a (0001) substrate and a <111> orientated sesquioxide, which provides a -2.5%, 2.8%, 4.8% lattice mismatch for scandia, lutetia, and ytterbia respectively (Bär *et al.*, 2003). These sesquioxides also have similar thermal expansion coefficients to sapphire, which reduces the thermal strain on the sample during growth and post-growth cooling. The lattice matching is particularly important when growing a 10 μm thick film, since any lattice mismatch will cause stress in the film, changing the physical and optical properties and can cause cracking of the samples (May-Smith *et al.*, 2011). Consequently, creating a film with a lattice constant equal to that of the substrate at room temperature is desirable, while also considering the thermal expansion coefficients during the growth and cooling of the sample during the PLD process. This can be achieved with a mix of scandia and lutetia, the optimum ratio being 51% scandia to 49% lutetia, assuming Vegards' law (Denton and Ashcroft, 1991). Calculations in the rest of this section involving estimation of lattice constants from the crystals constituents uses Vegards' law unless otherwise indicated. Vegards law assumes a linear relation of the lattice constant when materials are mixed.

In this section, the optimisation of the growth of ytterbium-doped lutetium scandium oxide is presented. As is the effect of changing the ratio of scandium and lutetium in the films, achieved by changing the constituents of the target. Process optimisation is reported, and the optical and physical characteristics of thick films presented.

7.3.1 Mixed sesquioxide growth optimisation

Starting with the fluence used for the growth of lutetia, as detailed in section 7.2, as a starting point, growths of lutetium-scandium oxide films were made. This ablation fluence resulted in the growth of high-quality films with a scattering point density as low as 0.37% and this meant I could focus on the crystallinity of the films rather than particulate density.

Four ytterbium-doped, scandium lutetium oxide films were grown with substrate heating powers ranging from 17-54 W. These films were grown with 1.05 Jcm^{-2} ablation fluence with 36,000 ablation pulses. Films were characterised using monochromatic XRD and the intensity and FWHM of the <222> peak of the XRD spectrum recorded. These measurements were compared across growths with different substrate heating powers with a higher peak intensity and lower peak FWHM indicating a higher quality growth.

Figure 7.8 displays a graph of the FWHM and intensity of the <222> peak of these mixed sesquioxide films, the intensity has been normalised to the thickness to account for this differentiation. It is clear from this graph that the heating power used for the highest peak intensity and the lowest FWHM is around 25 W. The rocking curve measurements of these films also indicated that ~25 W substrate heating power produced the highest quality films. However, the rocking curve peak FWHM was 0.5^{o} for 25 W of substrate heating power indicating a high degree of texture in the film. This could be caused by regions, similar to those seen in Figure 7.6 and will be discussed further in later sections.

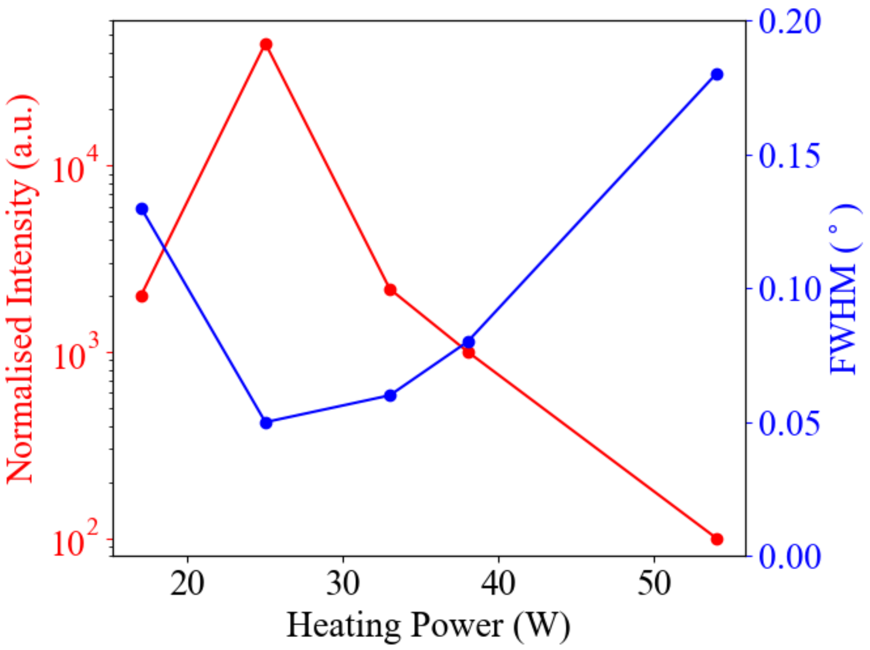

Figure 7.8. Plot of thickness-normalised intensity and FWHM of <222> peak measured from mixed-sesquioxide films grown at substrate heating powers ranging from 17 to 54 W. The red dots and lines indicate the intensity of the XRD peak normalised to the thickness of the film. The blue dots and lines indicate the FWHM.

7.3.2 Mixed sesquioxide optimal lattice constant

A key advantage of mixing lutetia and scandia is being able to control the lattice constant. So that when growing onto a c-cut sapphire substrate the lattice constant of the mixed sesquioxide can be altered to quasi-lattice match to the hexagonal lattice. A near perfect lattice matched film and substrate provides little stress in the film, which would alter the physical and optical characteristics, such as changing the refractive index or altering the fluorescence lifetime of the active impurity. It would also increase the chance of stress related dislocations, a contributor to the propagation loss.

I discussed in section 7.3 that the optimal ratio of scandia and lutetia is 51 % to 49 %, respectively. However, to produce an active film some doping needs to be introduced. In this case, I chose 5at.% doping of ytterbia. Therefore, a lattice constant that matches b_d and 3a seen in Figure 7.7 is needed. The value of 3a for sapphire is 14.27 Å. This means, through a simple Pythagoras calculation shown in equation 7.1 and 7.2, that the optimum value of "b_d" or the optimum lattice constant for the mixed sesquioxide is 10.09 Å. This corresponds to an optimum Yb-doped, mixed-sesquioxide formula of $(Yb_{0.05}Lu_{0.43}Sc_{0.52})_2O_3$.

$$(3a)^2 = 2(b_d)^2 \tag{7.1}$$

$$b_d = \frac{3a}{\sqrt{2}} \tag{7.2}$$

Three targets consisting of lutetia, ytterbia and scandia were purchased with different constituent ratios of lutetia/scandia and 5at.% doping of ytterbia. These targets have expected lattice constants as shown in Table 7.1. The resulting film's lattice constant, determined with XRD, is compared to the simple Vegard's Law estimation.

Table 7.1. Target compositions used to grow mixed-sesquioxide films and the expected lattice constant and lattice mismatch to a sapphire lattice assuming a perfectly stoichiometric transfer of materials

Target Number	**Target Composition**	**Expected Lattice Constant (Å)**	**% Lattice Mismatch**
1	$(Yb_{0.05}Lu_{0.5}Sc_{0.45})_2O_3$	10.12	0.35
2	$(Yb_{0.05}Lu_{0.4}Sc_{0.55})_2O_3$	10.07	-0.16
3	$(Yb_{0.05}Lu_{0.3}Sc_{0.65})_2O_3$	10.02	-0.67

A selection of samples were grown from these targets and XRD measurements performed. The (222) XRD peaks were compared with the (222) peaks of a Lu_2O_3 and a Sc_2O_3 film. SEM EDX measurements of the films were also performed to measure the constituents of the films.

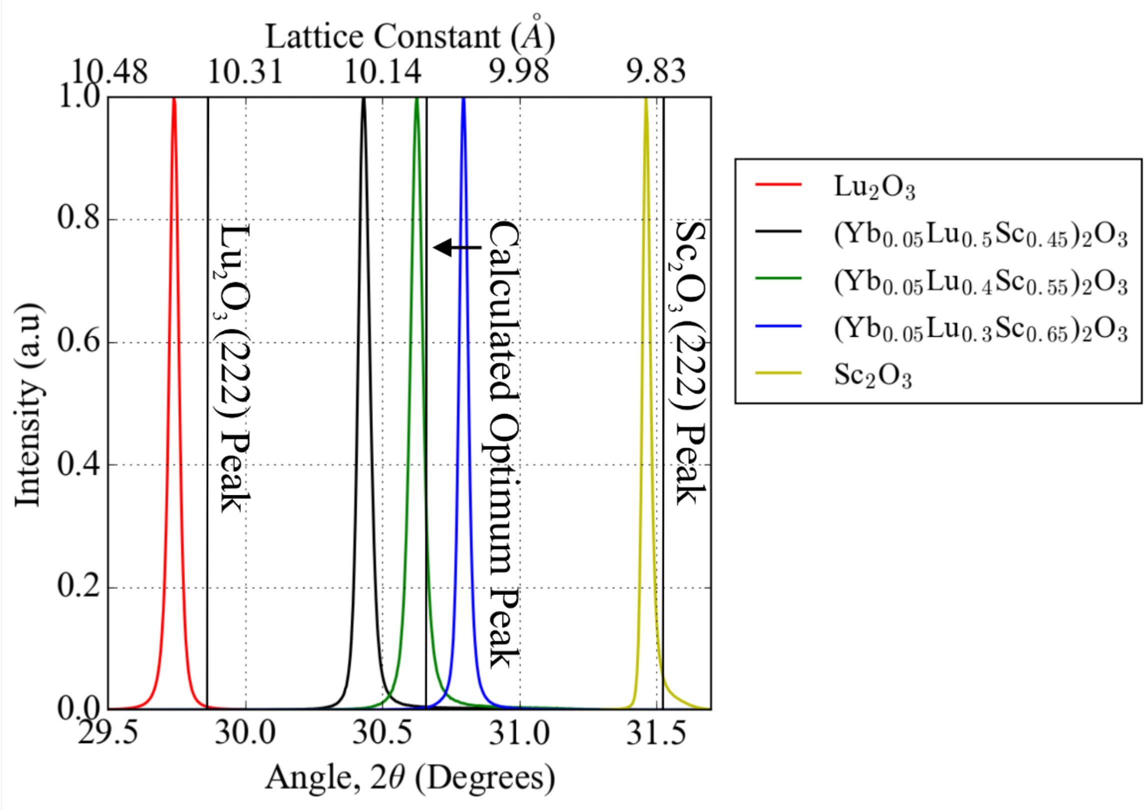

Figure 7.9. XRD spectra of five films grown on c-cut sapphire from Targets 1, 2 and 3 (Table 7.1), a Sc_2O_3 target and a Lu_2O_3 target. The calculated optimum lattice constant for quasi lattice matching with sapphire is indicated as well as the expected lattice constants for lutetia (222) and scandia (222) (Bär *et al.*, 2003).

Figure 7.9 shows the XRD spectra of five films, one Lu_2O_3 film, one Sc_2O_3 film and three mixed sesquioxide films. The expected peak positions for the binary sesquioxides are labelled, as is the optimum peak position for quasi-lattice matching with sapphire. The results clearly show that the lattice constant of the grown film correlate with the target composition, with “Target 2” providing a near perfect match with the sapphire lattice (Table 7.2). The Lu_2O_3 and Sc_2O_3 film peaks are not perfectly symmetrical and have a “shoulder”, which is generally associated with stress in the film, due to the lattice mismatch between the binary sesquioxides and sapphire (Ungar 2000). The mixed-sesquioxides have symmetrical peaks indicating they are not stressed.

EDX measurements determined that the 5at.% ytterbia doping was not fully transferred as expected, with only a 3at.% doping measured (Table 7.2). However, this could be subject to an error due to the difficulty distinguishing between the lutetium and ytterbium signal. Nevertheless, the EDX measurements agree with the XRD peak positions in terms of calculated lattice constant. The film grown from target 2 has the best lattice mismatch of 0.03%.

Table 7.2. The film composition compared to the target's compositions with the resultant lattice constant. The lattice mismatch is calculated with the optimum lattice constant of 10.09 Å.

Target Number	Target Composition	Film Composition	Film Lattice Constant (Å)	% Lattice Mismatch
1	$(Yb_{0.05}Lu_{0.5}Sc_{0.45})_2O_3$	$(Yb_{0.03}Lu_{0.56}Sc_{0.41})_2O_3$	10.14	0.5
2	$(Yb_{0.05}Lu_{0.4}Sc_{0.55})_2O_3$	$(Yb_{0.03}Lu_{0.45}Sc_{0.52})_2O_3$	10.087	-0.03
3	$(Yb_{0.05}Lu_{0.3}Sc_{0.65})_2O_3$	$(Yb_{0.03}Lu_{0.34}Sc_{0.63})_2O_3$	10.03	-0.6

This has reaffirmed that PLD can tune the stoichiometry of grown films, which can be useful for lattice matching to the substrate. I have demonstrated a near-perfect lattice match (<0.1 %) by growing a specific composition of ytterbium-doped lutetium scandium oxide onto a sapphire substrate. As discussed previously, any lattice mismatch would create stress in the film which can alter the physical characteristics and create detrimental lattice defects.

7.3.3 Thick-film mixed-sesquioxide films

Cross referencing with exemplar reports for similarly doped mixed sesquioxides, the crystalline quality can be ascertained. In addition, the fluorescence spectra provide insight into the RE-ion coordination in the material. A thicker film with the same dopant concentration as a thinner film would enable the fluorescence and lifetime to be measured more accurately since a higher proportion of pump light would be absorbed and hence a more intense fluorescence signal can be measured.

Two thick-film mixed-sesquioxide films were grown to thicknesses of ~ 10 µm from Target 1 and 2. Films grown from "Target 3" had average particulate densities of ~40% and consequently were considered too poor in quality to continue with. This is likely due to it being a poor-quality target, with a density of only 57.6 % of the theoretical single-crystal density, significantly less than Target 1 and 2 (65 % and 62 % respectively), which both produced films with < 1% particulate density. The two films were characterised via SEM, BSE and XRD measurements.

The thick films were grown with 25 W heating power and 1.05 Jcm^{-2} ablation fluence, as optimised in the previous sections. 576,000 pulses were used on each film to produce 10 µm thickness at a growth rate of 6.25 µm/hr. Such a low growth rate compared to that obtained for YGG, as shown in chapter 4, which had a growth rate of up to 25 µm/hr. The comparatively low growth rate can be attributed to the target composition with different ablation conditions and a significantly lower ablation fluence that ejects less material per pulse.

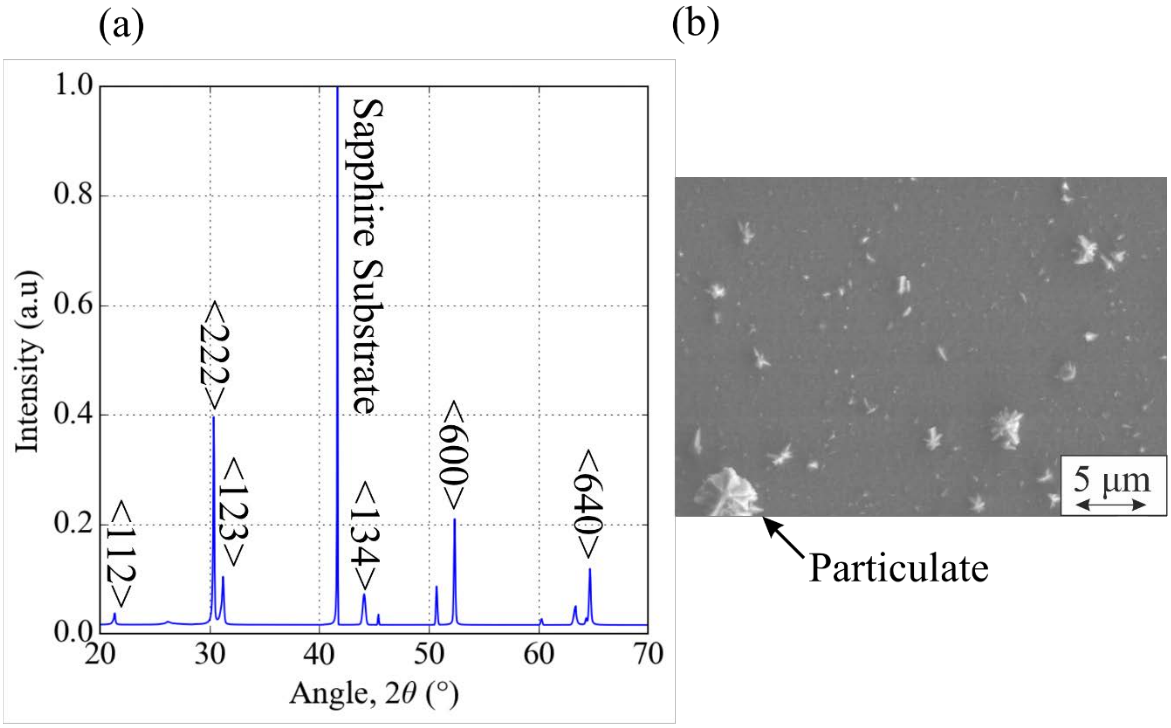

Figure 7.10. (a) Typical XRD spectrum from 10-µm thick mixed sesquioxide film with peaks labelled with their corresponding orientations. (b) SEM image of the film's surface.

The XRD spectrum of each film shows a polycrystalline growth with multiple orientations associated with lutetium scandium oxide (Figure 7.10 (a)). An SEM image (Figure 7.10 (b)) also showed a significant number of particulates (white regions) on each films surface, which is confirmed by dark-field microscopy measurements. If there are numerous particulates on the surface, the likelihood is that there are particulates embedded in the film itself. Interfaces between the orientations and the embedded particulates will cause scattering of propagating light and hence increase the waveguide loss.

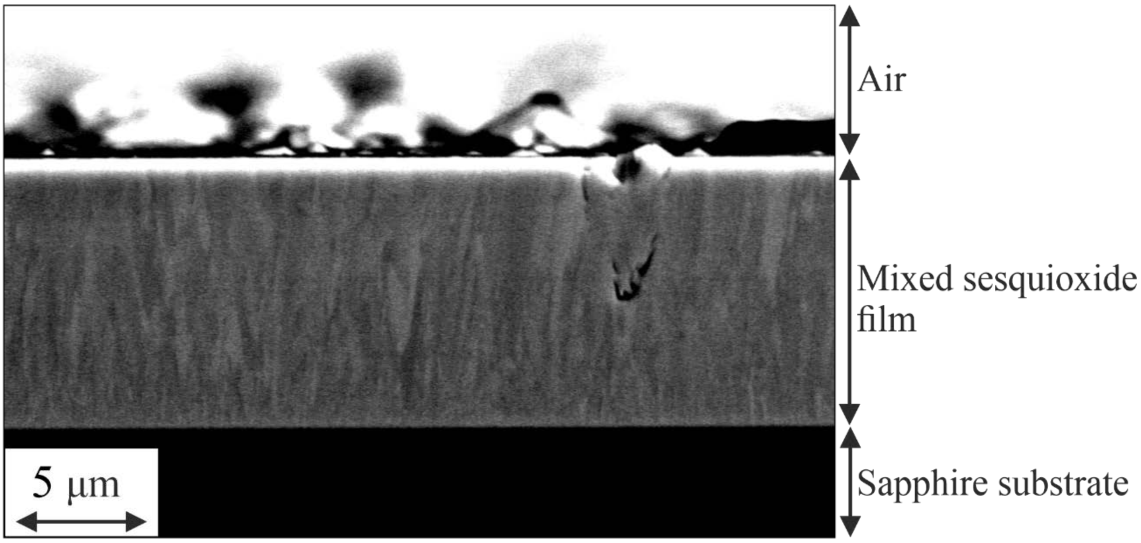

Figure 7.11. BSE image of the polished facet of a 10-µm thick mixed-sesquioxide film with a significant defect.

A BSE image of a mixed-sesquioxide films facet, Figure 7.11, shows regions similar to that seen in Figure 7.6. This could either be the incompatible seeding of growth discussed in section 7.2.3 or different orientations of growth due to this film being polycrystalline. Consequently, the regions seen in Figure 7.11 could be prevented by optimising the growth further, so that the growth is single-crystal or by stopping the incompatible seeding of growth by annealing the film or surface pre-treatment (Tiejun *et al.*, 2002; Lu *et al.*, 2000).

These two measurements show the change in properties that can occur when films are grown thicker; the film has grown polycrystalline and the target has degraded significantly producing more particulates. These films were grown with the UDA protocol and therefore as seen in chapter 5, will grow films with a higher scattering point density. To improve on these results the substrate heating power needs to be optimised for thicker growths and BDA should be used to decrease the particulate density. Higher density targets would also likely reduce the particulates generated by the target during ablation. Nevertheless, thick film ytterbium doped lutetium scandium oxide films have been grown and were subsequentially optically characterised.

7.3.4 Fluorescence measurements of mixed-sesquioxide films

The thick films characterised in the previous section were facet polished to allow excitation with a pump laser coupled to the waveguide. The films were pumped with a laser diode operating at a wavelength of 933 nm and the fluorescence spectrum and lifetime of each film measured and compared to literature values (method shown in Figure 7.3). The fluorescence spectrum was also compared to the spectra of Yb:Lu_2O_3, Yb:Sc_2O_3 and Yb:YAG and the FWHM of the ~1040 nm peak measured. A larger FWHM will have the potential for shorter laser pulses and is one of the key advantages of mixed sesquioxides as host media.

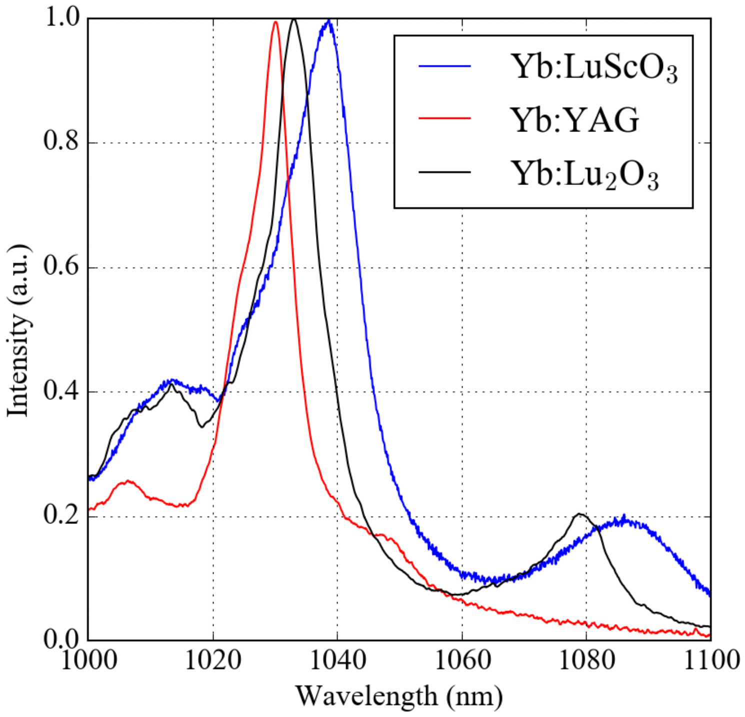

Figure 7.12. Fluorescence spectrum of ytterbium-doped mixed sesquioxide and YAG from 1000 nm to 1100 nm.

From Figure 7.12, the peak position is shifted 8 nm to 1038 nm for the mixed sesquioxide film compared to the YAG film (Table 7.3). It can be noted that the FWHM of the PLD-grown Yb:$LuScO_3$ is 19 nm compared to literature values of 22 nm. This could be due to a different stoichiometry of mixed sesquioxide compared to that used in literature, with this material having equal parts lutetia and scandia. Nevertheless, the FWHM is a factor of two larger than that of Yb-doped YAG and one and a half times than that of lutetia, demonstrating the potential for ultra-short pulse widths as shown in Table 7.3. The minimum pulse duration for each material was calculated with the time-bandwidth product limit for transform limited sech^2-pulses and dividing by the FWHM in the frequency domain (Beil *et al.*, 2013). It is possible to utilise non-linear effects such as self-broadening to demonstrate pulse durations shorter than this limit (Shen and Yang, 2006).

The lifetime of the mixed-sesquioxide grown from Target 2 was measured to be 719 µs, 131 µs smaller than that found in literature (Beil *et al.*, 2013). This is a function of crystal quality, with lattice defects and abnormalities causing rapid non-radiative decay paths for excited dopant ions, implying our film is not as high quality.

Table 7.3. Measured emission bandwidth and peak positions for PLD grown, ytterbium-doped films. The theoretical minimum of pulse durations and expected bandwidths are taken from (Beil *et al.*, 2013) and (Lacovara, 1991). The expected lifetimes were taken from (Parsonage *et al.*, 2015) and (Peters *et al.*, 2009).

	Yb:$LuScO_3$	**Yb:YAG**	**Yb:Lu_2O_3**
Emission Bandwidth (FWHM) (nm)	19	10	13
Expected Bandwidth (FWHM) (nm)	22	9	13
Emission Peak Position (nm)	1038	1030	1033
Minimum Pulse duration (fs)	51	120	86
Measured Lifetime (µs)	719	937	808
Expected Lifetime (µs)	850	950	820

Coupling of light into the waveguide showed that there was too much scattering of the pump light to realise gain. As has been detailed, there are problems with growing thick-film $LuScO_3$, such as a large particulate density, domains, and having a polycrystalline structure. These are likely to be improved with the BDA protocol and further substrate temperature optimisation. Nevertheless, the work has demonstrated control of the lattice constant of PLD-grown films, having lattice matched Yb:$LuScO_3$ grown on a c-cut sapphire substrate with a mismatch of <0.1 %. If the propagation losses can be mitigated, this mixed sesquioxide would be an excellent gain medium for ultrashort-pulse lasers with enhanced spectroscopic parameters compared to binary sesquioxides and YAG.

7.4 Summary

In this chapter, the experimental work in the growth of high-quality binary sesquioxide via PLD along with the first realisation of a PLD-grown, RE-doped mixed-sesquioxide film.

Initial optimisation of the growth of lutetia on a sapphire substrate was presented, to demonstrate a film with a scattering point density of 0.06% and showed that 25 W of substrate heating power produced a largely single-crystal film in the <111> orientation. However, it was concluded that the upper layers of the film were beginning to grow polycrystalline. Also presented was the fluorescence spectrum and lifetime of a Yb:Lu_2O_3 film, with the lifetime measured as 808 µs, 98.5% of that found in literature. SEM images of a polished 10 µm thick Yb:Lu_2O_3 film showed evidence of crystal domains, which could either be different orientations of Lu_2O_3 or defects associated with incompatible seed positions on the sapphire substrate. In order to allow further scaling of PLD-grown Yb:Lu_2O_3 the domains created during the growth will need to be prevented from forming.

The growth of single-crystal lutetium scandium oxide has been presented along with demonstration of control of the lattice constant through tailoring the composition of the target, growing onto c-cut sapphire with a mismatch between film and substrate of only 0.03 %. Lattice matching will decrease the stress in the growing film which, if not dealt with, would increase the likelihood of lattice defects and detrimentally affect physical parameters such as thermal conductivity. Thick-film mixed sesquioxide films and SEM images of domains in the lattice, very similar to those previously reported in Lu_2O_3 have been observed. The promise of Yb:$LuScO_3$ for ultra-fast pulse laser was demonstrated with a wide emission bandwidth of 19 nm. This is greater than obtained with Yb:YAG or Yb:Lu_2O_3 and would allow pulses down to 51 fs in principle with low-loss laser configurations. Laser experiments were not tenable due to the high scattering losses in the waveguides, but with further optimisation combined with the use of BDA the losses are expected to decrease dramatically.

Two key outcomes from the work presented in this chapter include: PLD as a growth technique for RE-doped sesquioxides and the presentation of the first Yb:$LuScO_3$ PLD-grown film and which has been lattice matched to a sapphire substrate.

7.5 References

Bär, S., Huber, G., Gonzalo, J., Perea, A., Climent, A. and Paszti, F. (2003) 'Europium-doped sesquioxide thin films grown on sapphire by PLD', *Materials Science and Engineering: B,* 105(1-3), pp. 30-33.

Beecher, S. J., Parsonage, T. L., Mackenzie, J. I., Sloyan, K. A., Grant-Jacob, J. A. and Eason, R. W. (2014) '1.2 W Yb:Y_2O_3 Planar Waveguide Laser', *Advanced Solid State Lasers,* 22(18), pp. 22056-22061.

Beil, K., Saraceno, C. J., Schriber, C., Emaury, F., Heckl, O. H., Baer, C. R. E., Golling, M., Südmeyer, T., Keller, U., Kränkel, C. and Huber, G. (2013) 'Yb-doped mixed sesquioxides for ultrashort pulse generation in the thin disk laser setup', *Applied Physics B,* 113(1), pp. 13-18.

Denton, A. R. and Ashcroft, N. W. (1991) 'Vegard's law', *Phys Rev A,* 43(6), pp. 3161-3164.

Dobrovinskaya, E. R., Lytvynov, L. A. and Pishchik, V. (2009) *Sapphire: material, manufacturing, applications.*: Springer Science & Business Media.

Giesen, A., Hügel, H., Voss, A., Wittig, K., Brauch, U. and Opower, H. (1994) 'Scalable concept for diode-pumped high-power solid-state lasers.', *Applied Physics B,* 58(5), pp. 365-372.

Guzik, M., Pejchal, J., Yoshikawa, A., Ito, A., Goto, T., Siczek, M., Lis, T. and Boulon, G. (2014) 'Structural Investigations of Lu2O3 as Single Crystal and Polycrystalline Transparent Ceramic', *Crystal Growth & Design,* 14(7), pp. 3327-3334.

Kitajima, S., Nakao, H., Shirakawa, A., Yagi, H. and Yanagitani, T., 2017, October. CW performance and temperature observation of Yb: Lu2O3 ceramic thin-disk laser. In Advanced Solid State Lasers (pp. JM5A-32). Optical Society of America. 'CW performance and temperature observation of Yb: Lu_2O_3 ceramic thin-disk laser', *Advanced Solid State Lasers*, Nagoya, Aichi Japan: Optical Society of America.

Krankel, C. (2015) 'Rare-Earth-Doped Sesquioxides for Diode-Pumped High-Power Lasers in the 1-, 2-, and 3-μm Spectral Range', *IEEE Journal of Selected Topics in Quantum Electronics,* 21(1), pp. 250-262.

Kuwano, Y., Suda, K., Ishizawa, N. and Yamada, T. (2004) 'Crystal growth and properties of $(Lu,Y)_3Al_5O_{12}$', *Journal of Crystal Growth,* 260(1-2), pp. 159-165.

Lacovara, P., Choi, H.K., Wang, C.A., Aggarwal, R.L. and Fan, T.Y. (1991) 'Room-temperature diode-pumped Yb: YAG laser.', *Optics Letters,* 16(14), pp. 1089-1091.

Lu, Y. F., Ni, H. Q., Mai, Z. H. and Ren, Z. M. (2000) 'The effects of thermal annealing on ZnO thin films grown by pulsed laser deposition', *Journal of Applied Physics,* 88(1), pp. 498-502.

May-Smith, T. C., Sloyan, K. A., Gazia, R. and Eason, R. W. (2011) 'Stress Engineering and Optimization of Thick Garnet Crystal Films Grown by Pulsed Laser Deposition', *Crystal Growth & Design,* 11(4), pp. 1098-1108.

Parsonage, T. L., Beecher, S. J., Choudhary, A., Grant-Jacob, J. A., Hua, P., Mackenzie, J. I., Shepherd, D. P. and Eason, R. W. (2015) 'Pulsed laser deposited diode-pumped 7.4 W Yb:Lu_2O_3 planar waveguide laser', *Opt Express,* 23(25), pp. 31691-31697.

Peters, R., Kränkel, C., Petermann, K. and Huber, G. (2007) 'Broadly tunable high-power Yb: Lu_2O_3 thin disk laser with 80% slope efficiency ', *Optics Express,* 15(11), pp. 7075-7082.

Peters, R., Petermann, K. and Huber, G. 'A new mixed sesquioxide Yb: $LuScO_3$: spectroscopic properties and highly efficient thin-disk laser operation.', *Advanced Solid-State Photonics*, Denver, Colorado, United States: Optical Society of America.

Sanghera, J., Frantz, J., Kim, W., Villalobos, G., Baker, C., Shaw, B., Sadowski, B., Hunt, M., Miklos, F., Lutz, A. and Aggarwal, I. (2011) '10% Yb^{3+}-Lu_2O_3 ceramic laser with 74% efficiency', *Optics Letters,* 36(4), pp. 576-578.

Shen, Y. and Yang, G. (2006) 'Theory of Self-Phase Modulation and Spectral Broadening', *Alfano R.R. (eds) The Supercontinuum Laser Source.* New York: Springer.

Szela, J. W., Sloyan, K. A., Parsonage, T. L., Mackenzie, J. I. and Eason, R. W. (2013) 'Laser operation of a Tm:Y2O3 planar waveguide', *Opt Express,* 21(10), pp. 12460-8.

Tiejun, L., Qihong, L., Jingxing, D., Yunrong, W., Jun, Z., Jingru, L., Zhiming, Z. and Fanghong, S. (2002) 'Improved adhesion of diamond coating on cobalt-cemented tungsten carbide hardmetal by using pulsed-UV-laser substrate surface pretreatment.', *Applied Surface Science,* 193(1), pp. 102-119.

Ungar , T. (2000) 'Warren-Averbach Applications', in Chung, F.H. and Smith, D.K. (eds.) *Industrial Applications of X-ray Diffraction*. New York, pp. 847.

Chapter 8 Sapphire

8.1 Motivations

Sapphire, or α-Al_2O_3, is an important and widely used laser material when doped with transitions metals. The first laser demonstrated was based on Cr-doped sapphire, more commonly known as ruby (Maiman, 1960). Furthermore, Ti-doped sapphire with its broad gain bandwidth, is consequently commonly used in tuneable and ultrashort-pulse laser systems (Moulton, 1986). A major part in the success of sapphire as a host material can be attributed to the desirable thermo-mechanical properties of sapphire, i.e. a high thermal conductivity (30 $Wm^{-1}K^{-1}$ (Dobrovinskaya *et al.*, 2009) compared to 11 $Wm^{-1}K^{-1}$ for YAG (Kumaran *et al.*, 2009)) and an excellent chemical stability under harsh conditions.

With the commercial success of RE-based lasers, such as Yb:YAG, it is of interest to find a host material with superior thermo-mechanical properties such as sapphire. However, incorporating RE materials into the sapphire lattice is challenging due to the large difference in ionic radii of the host cations. The radius of Al^{3+} is 0.53 Å and of Yb^{3+} 0.99 Å (Dobrovinskaya *et al.*, 2009; Waeselmann *et al.*, 2016), making the ytterbium ion almost eight times the volume. This size difference makes the incorporation of ytterbium into the sapphire lattice extremely low when grown from melt. Nevertheless, it has been proven that a RE ion can form a stable compound in the Al_2O_3 lattice. To achieve a higher doping concentration, a method of growth that does not rely on thermal equilibrium is needed, such as PLD.

Growth of RE-doped sapphire was first demonstrated by (Kumaran *et al.*, 2009) using MBE to grow Nd:sapphire with some success. A PLD-grown Nd:sapphire film was the first to demonstrate lasing (Waeselmann *et al.*, 2016) with output powers of 130 mW and efficiencies of up to 7.5%. This low efficiency was caused by the large scattering losses in the Nd:sapphire film, so reducing the scattering would drastically increase the efficiency and achievable output powers.

To the best of our knowledge, no demonstration of lasing in Yb:sapphire has yet been achieved. Yb-doped sapphire would allow a large amount of power scaling due to both the small quantum defect in ytterbium, decreasing detrimental thermal effects, and the relatively high conductivity of sapphire allowing more efficient cooling. In this chapter, I discuss progress toward the growth of RE-doped sapphire with ytterbium and neodymium as dopants. I also present single-crystal thick-films of sapphire (up to 35 µm) and the optical properties of Yb:sapphire along with evidence of waveguiding.

8.2 Yb-doped sapphire

8.2.1 Incorporation of ytterbium into the sapphire lattice

One of the main reasons for using PLD as a growth mechanism for RE-doped sapphire is its ability to incorporate useful amounts (>0.5% Yb-doping) of RE ions into the sapphire lattice. PLD is not a thermodynamic equilibrium technique and as such should be able to incorporate a usable amount of ytterbium. Since this is a doped binary oxide (Al_2O_3), a doping of just 1% would be the equivalent of 2.7% doping for YAG ($Y_3Al_5O_{12}$) in terms of the doping concentration.

To ensure the ytterbium is incorporated into the sapphire lattice, a film of Yb:sapphire was grown and surface imaged via EDX. The growth conditions for this film are shown in Table 8.1 as “JP79”. Initially, an abnormally high substrate heating power of 55 W was chosen to be certain that the 1100 ^{o}C threshold for the growth of alpha-alumina (sapphire) was reached (Łodziana and Parliński, 2003). This does not, however, mean that alpha-alumina cannot be grown at lower temperatures, simply that above this threshold, only the alpha-phase can be grown. The SEM EDX images mapped the surface of the film for its atomic constituents, so that any segregation of atoms could be observed. If the ytterbium ions appeared to be evenly distributed, the fluorescence spectrum would add further evidence that the ytterbium ions were in the correct position in the lattice.

Table 8.1. Growth parameters of sapphire films grown onto c-cut sapphire

Sample Number	Substrate Heating Power (W)	Ablation Fluence (Jcm^{-2})	Ytterbium doping (%)	Number of pulses
JP53	33	1.05	1	36,000
JP76	40	1.08	0	36,000
JP79	55	1.4	1	180,000
JP133	33	1.6	1	36,000
JP225	33	2.7	3	360,000

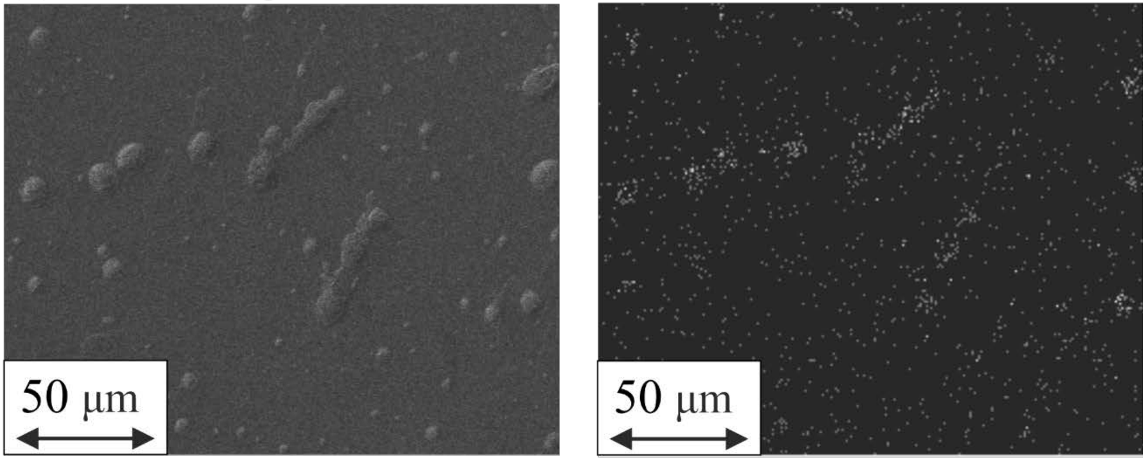

(a) SEM image

(b) Ytterbium Map

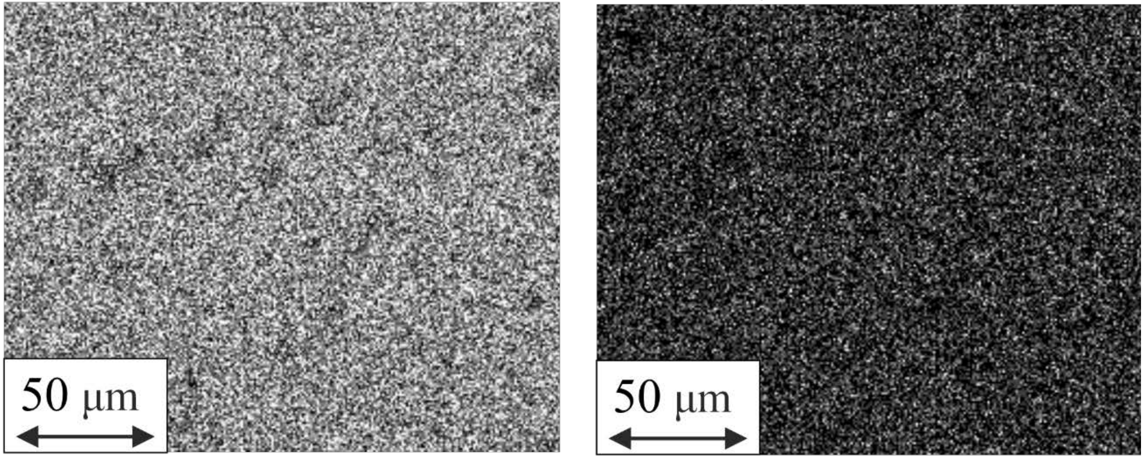

(c) Aluminium Map

(d) Oxygen Map

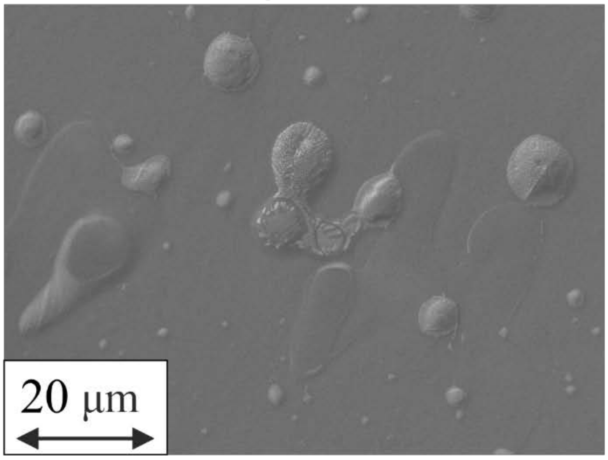

(e) SEM image

Figure 8.1. SEM EDX map of the surface of JP79 with (a) SEM image of the area of interest, (b) the map of detected ytterbium in the area of interest, (c) map of detected aluminium and (d) map of detected oxygen. (e) showing a high-resolution SEM image of the samples surface.

The SEM images (Figure 8.1 (a) and (e)) show that there are globules of material that appear to have melted onto the surface. The EDX map of ytterbium (Figure 8.1 (b)) appears to show that there is a concentration of ytterbium at these sites, with the EDX map of aluminium (Figure 8.1 (c)) showing a deficiency at these sites.

This result suggests that in JP79 the ytterbium ions are seperate from the sapphire lattice. This could be due to the high substrate heating power, which was high enough to permanently distort the sapphire substrate, or the fluence was too low. A higher fluence provide the deposited atoms with more energy to overcome the thermodynamic equilibrium barrier to incorporate the ytterbium ions. To enable higher fluences to be used, the excimer laser beam path to the PLD chamber needed to be shortened. A shorter beam path would reduce the energy loss through free space, which, through observations, was found to be ~20% per metre, and hence the beam path was shortened by ~2 m. This allowed fluence vales of 3 Jcm^{-2} with a spot size of ~3x2 mm to be achieved.

A growth with a higher fluence was attempted with JP133, which had a lower substrate heating power and a higher ablation fluence. JP133 was measured via SEM EDX and no segregation of ytterbium was found. This was confirmed with measurements of the XRD spectrum of several films with different doping concentrations with an θ/2θ scan. The peak position of the (0001) sapphire will be decreased through the incorporation of ytterbium as it will increase the lattice constant. Films grown with fluences above 1.6 Jcm^{-2} displayed a significant shift in 2θ peak position when doped with ytterbium, however sapphire films grown below a fluence value of 1.6 Jcm^{-2} did not shift significantly. This is displayed in Figure 8.2 along with the errors calculated with the standard error.

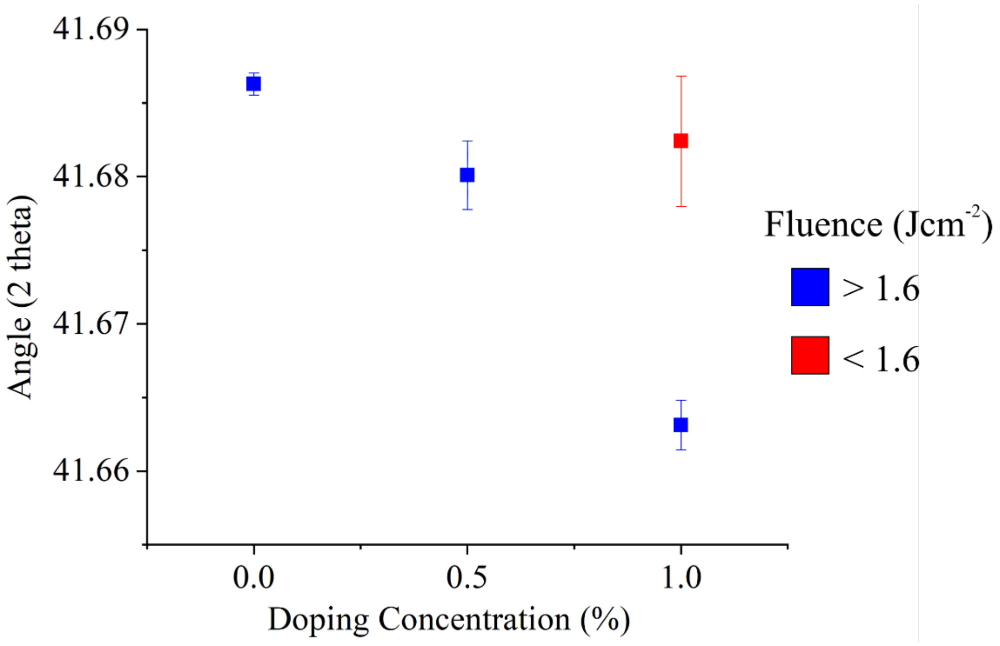

Figure 8.2. Average peak position of 0, 0.5 and 1% Yb-doped (0001) sapphire for films grown with an ablation fluence above 1.6 Jcm^{-2} (blue) and below 1.6 Jcm^{-2} (red). The errors were calculated via the standard error.

The fluorescence was measured with the same method described in chapter 7 (Figure 7.3). When measured, JP53 and JP79 did not emit any fluorescence, whereas JP133 and JP225, did emit measurable fluorescence. This is consistent with the EDX observations and 2θ peak position measurements that a high fluence (>1.6 Jcm^{-2}) allows the incorporation of ytterbium ions whereas the temperature has less of an influence. The fluorescence spectrum will be discussed later in this chapter.

I have demonstrated that PLD can incorporate ytterbium ions into a sapphire lattice at dopant levels not possible via traditional techniques. I have shown that to do this, the ablation fluence must be above 1.6 Jcm^{-2}, and lower fluence levels cause segregation of ytterbium into clumps of ytterbium oxide.

8.2.2 Hexagonal island growth on sapphire films

The growth of structured thin films has been frequently observed in various thin-film growth techniques (Liu *et al.*, 1993), including PLD (Shen *et al.*, 2013). It is especially common during the growth of ZnO nanorods onto c-cut sapphire substrates where hexagonal islands are grown rather than a monolayer of material (Doherty *et al.*, 2007). Previous experiments with the growth of Ti:sapphire onto sapphire substrate observed the growth of hexagonal islands and therefore this could be expected during the growth of RE-doped sapphire.

For our application of planar waveguides, Frank–van der Merwe monolayer growth is ideal, which would leave a flat, uniform film. Purely Volmer–Weber-type island growth with gaps between each island would not produce a useable waveguide due to the many scattering sites at these discontinuities. However, Stranski-Krastanov growth (islands and layers) could produce useable waveguides if the islands grown on the face of the film are polished off, leaving a flat film. These films could still be prone to scattering defects at the junctions between the joined islands.

Initial thin-film growths (36,000 pulses) of Yb:sapphire provided evidence of hexagonal scattering points (Figure 8.3) through dark-field microscopy. Although in these images the hexagonal shape is partially obscured due to poor microscope camera resolution, the images do clearly demonstrate surface structure. However, the islands were not visible in a stylus microscope measurement, implying their size is insignificant compared to the films thickness (1.5 μm). To observe whether this surface structure becomes significant and then to see whether they could simply be polished back, thick films of undoped, and Yb-doped sapphire were grown.

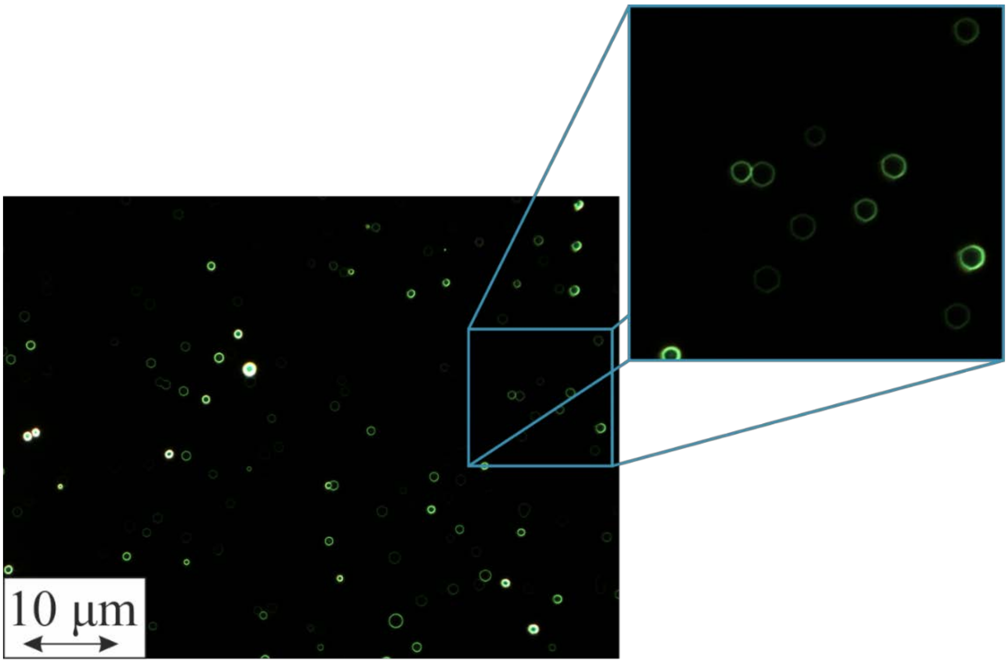

Figure 8.3. Dark-field microscopy at 50x magnification of a typical Yb:sapphire film grown (JP76, Table 8.1) with 36,000 pulses and a magnified portion of the image is also shown.

Table 8.2 shows the growth conditions of two thick sapphire films. JP226 is 5x thicker than JP190, which will give a good idea of the progression of island growth. Dark field images of JP190 and JP226 (Figure 8.4 (a) and (b) respectively) show clear evidence of hexagonal island growth, with the quantity of islands larger on the thicker growth. JP226, the thickest film at 35 µm has hexagonal islands of ~2.5 µm in height (Figure 8.4 (d)). Surface roughness measurements found an Sa of ~700 nm for JP226 which is extremely large compared with typical Sa values of PLD-grown films of 1-2 nm (seen in Section 5.5.2).

Table 8.2. Growth conditions of thick-film sapphire

Sample Number	Substrate Heating Power (W)	Ablation Fluence (Jcm^{-2})	Ytterbium doping (%)	Number of pulses	Thickness (µm)
JP190	33	2.8	0.5	180,000	7
JP222	34	2.7	1	360,000	14
JP226	34	2.6	0	1,000,000	35

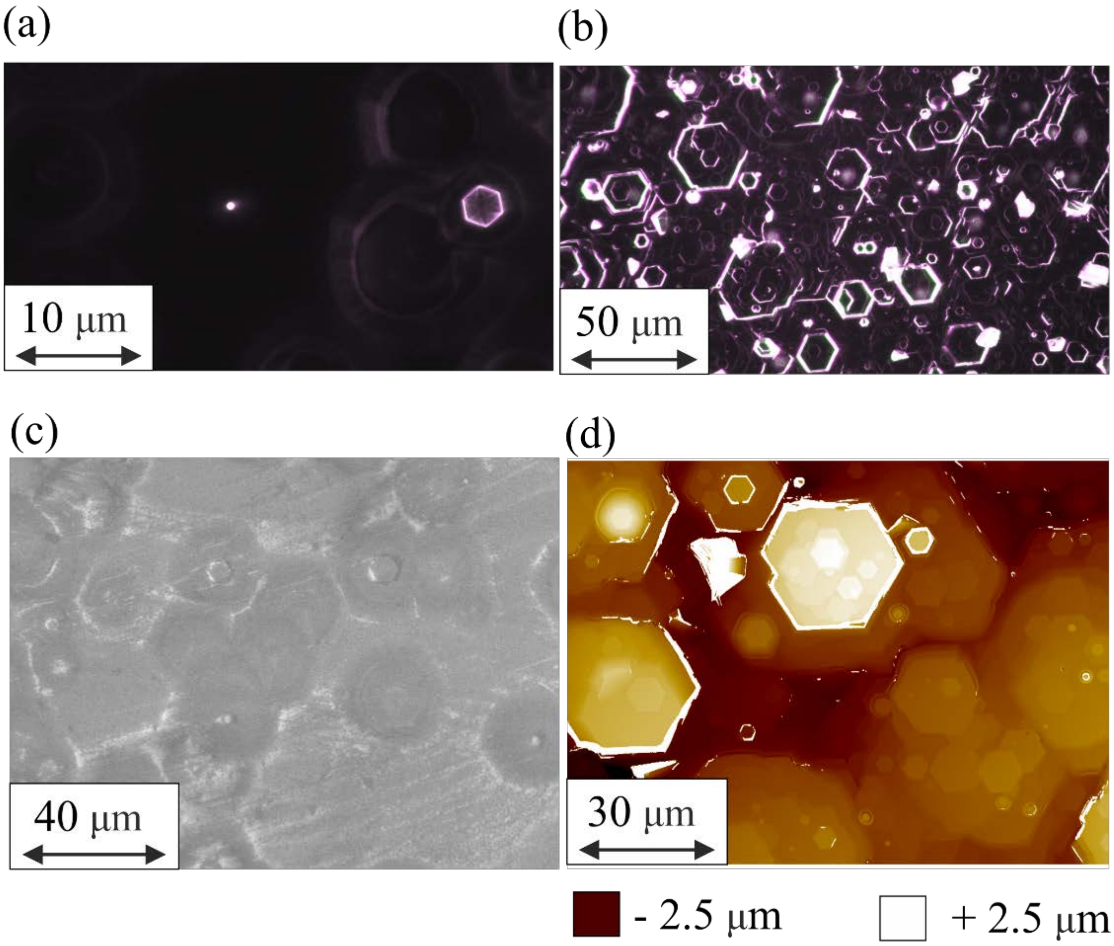

Figure 8.4. Hexagonal island growth observed on (a) JP190 via dark field microscopy at 100x magnification, (b) JP226 via dark-field microscopy at 20x magnification, (c) SEM image of JP190 and (d) optical profiler image of JP226 at 50x magnification.

The surface roughness of these films would cause significant scattering of guided light, increasing the propagation loss of these films. The face surface of these films could be polished back to a flat surface, however, if there are interfaces between the islands, there could still be significant scattering effects.

8.2.3 Face polishing of sapphire films

Sapphire is particularly hard and wear resistant (the second material in the Moh’s hardness scale), which means it takes a long time to polish. This does mean however, that nm scale thicknesses of material can be removed without fear of removing too much material. Consequently, to remove the island growth on the sapphire films, the face can be polished.

JP190 and JP222 were face polished in preparation for facet polishing and optical experiments. They were lapped for 10 minutes at 30 rpm with 1 μm alumina powder and then polished with syton for 10 minutes. This removed 2 μm from both JP190 and JP222. This was enough to remove hexagonal features from JP190 but did not remove all the features from JP222. Consequently, JP222 was lapped for a further 20 minutes and polished for another 10 minutes to remove 6 μm in total.

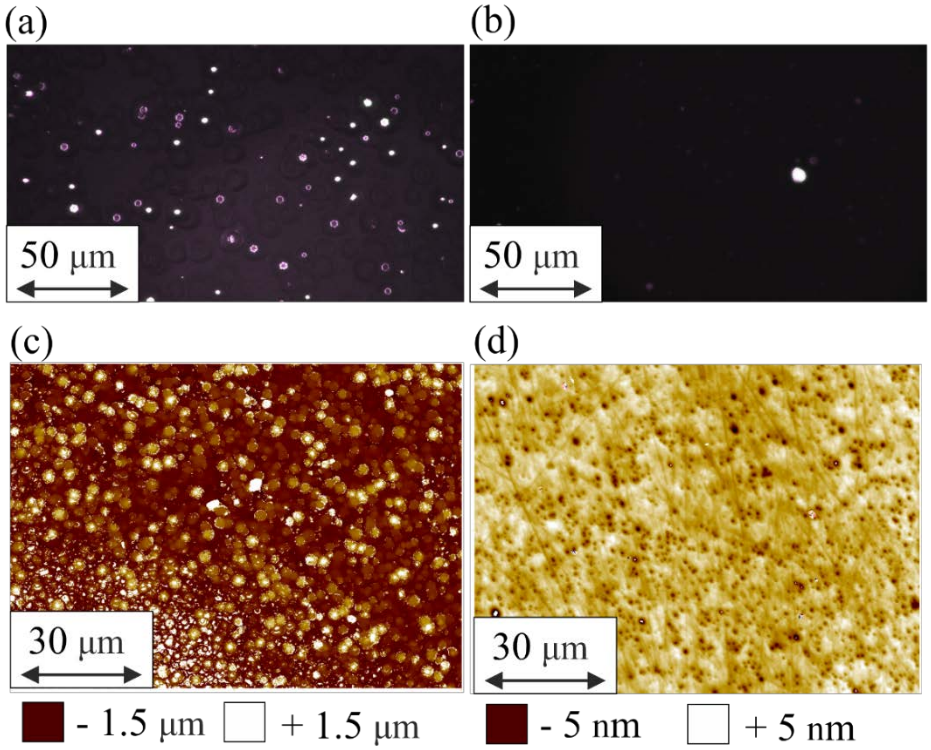

Figure 8.5. Dark-field images of JP190 (a) before and (b) after face lapping and polishing and optical profilometry images of JP222 (c) before and (d) after face lapping and polishing.

The hexagonal features were removed as seen from Figure 8.5 (a) and (b) which show dark-field images of JP190 before and after face polishing. This was also observed on JP222 with the roughness (Sa) was reduced from 350 nm to 8 nm. Figure 8.5 (d) shows an optical profiler map of the post-polished surface of JP222 and displays a slightly porous structure. The pores are likely due to particles being removed as a whole rather than polished. However, these pores are <5 nm in depth and therefore will not cause significant scattering of propagating light in the waveguide.

The 40x reduction of surface roughness in these films will reduce the scattering loss during light propagating in these films. The promise of this technique led to polishing of the surface becoming standard practice for sapphire films so subsequent films were grown deliberately thicker than required to account for the loss in thickness after face polishing.

8.2.4 Substrate heating power optimisation of sapphire

As seen when growing YAG onto YAG substrates, measuring a grown film that is similar to the substrate can prove challenging. For sapphire, unlike with YAG, I found that when measuring the film with θ/2θ XRD, there was no significant shift in XRD peak position. This is to be expected with epitaxial growth with binary oxides, since if the growth is the correct phase and orientation, the stoichiometry can only be that of the film. However, with thicker films (>30 µm) the substrate signal will not be significant and the results of θ/2θ XRD are reliable. With thinner films, an amorphous film would attenuate the substrate signal, meaning the peak intensity will be lower, indicating the presence of an amorphous film. When using GI-XRD, the (006) peak (found at 41.68^{o}) is not visible in this setup, but other peaks will be visible allowing us to determine whether a film is poly-crystalline. Using a combination of θ/2θ XRD and GI-XRD, it can be found whether a film is amorphous, poly-crystalline or single crystal.

Initially four thin films (~3 µm) were grown at substrate heating powers of 30-50 W to determine the optimum heating power. After this, a thick film (~15 µm) was grown at heating powers of 34 W to analyse the progression of growth for thicker films. Fluences of above 1.6 Jcm^{-2}, as seen in Table 8.3, were chosen to ensure incorporation of the ytterbium.

Table 8.3. Growth conditions of 1% Yb-doped alumina films

Sample Number	**Substrate Heating Power (W)**	**Ablation Fluence (Jcm^{-2})**	**Number of pulses**
JP213	35	2.2	72,000
JP217	30	2.8	72,000
JP220	50	2.6	72,000
JP221	40	3.0	72,000
JP222	34	2.7	360,000

The GIXRD shows that JP217 (Figure 8.6 (a)) grew as κ-phase alumina (Ollivier *et al.*, 1997) showing that this growth was below the threshold temperature of 1100^{o}C for the growth of α-alumina (sapphire) (Dobrovinskaya *et al.*, 2009). JP213 (Figure 8.6 (b)) does not present any peaks suggesting that JP213 is either single-crystal sapphire or amorphous. JP221 (Figure 8.6 (c)) has a small peak but is similar to JP213 and JP220 (Figure 8.6 (d)) is polycrystalline with numerous sapphire peaks. Further tests found that substrate heating powers down to 32 W produced similar GIXRD patterns to JP213, indicating an optimum range of 32-40 W.

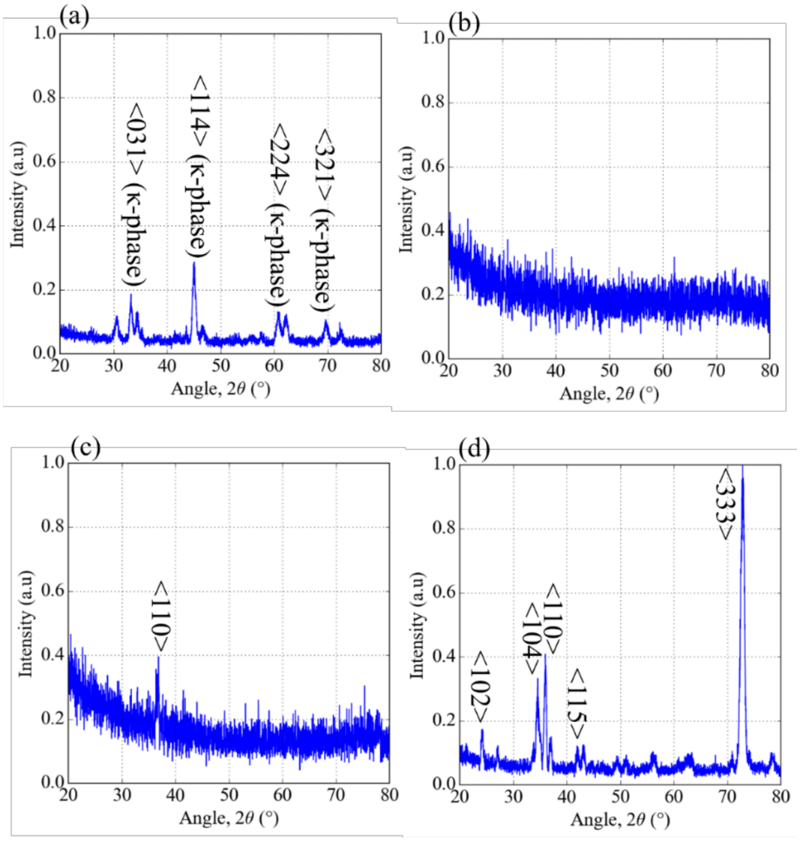

Figure 8.6. GIXRD spectra of (a) JP217, (b) JP213, (c) JP221 and (d) JP220 grown at different substrate heating powers (30 W, 35 W, 40 W and 50 W, respectively). The orientations shown are for orientations of α-alumina (sapphire) unless otherwise stated.

These results have narrowed down the optimum growth parameters for sapphire, however as it has been seen previously, as films are grown thicker, the range of optimum growth temperature narrows. As such a thick film was grown (JP222) and the GI-XRD spectrum was compared to the θ/2θ XRD spectrum. The GI-XRD spectrum of JP222 demonstrated that the top layers of JP222 were polycrystalline (Figure 8.7 (b)) whereas the bulk appeared to be single crystalline (Figure 8.7 (a)).

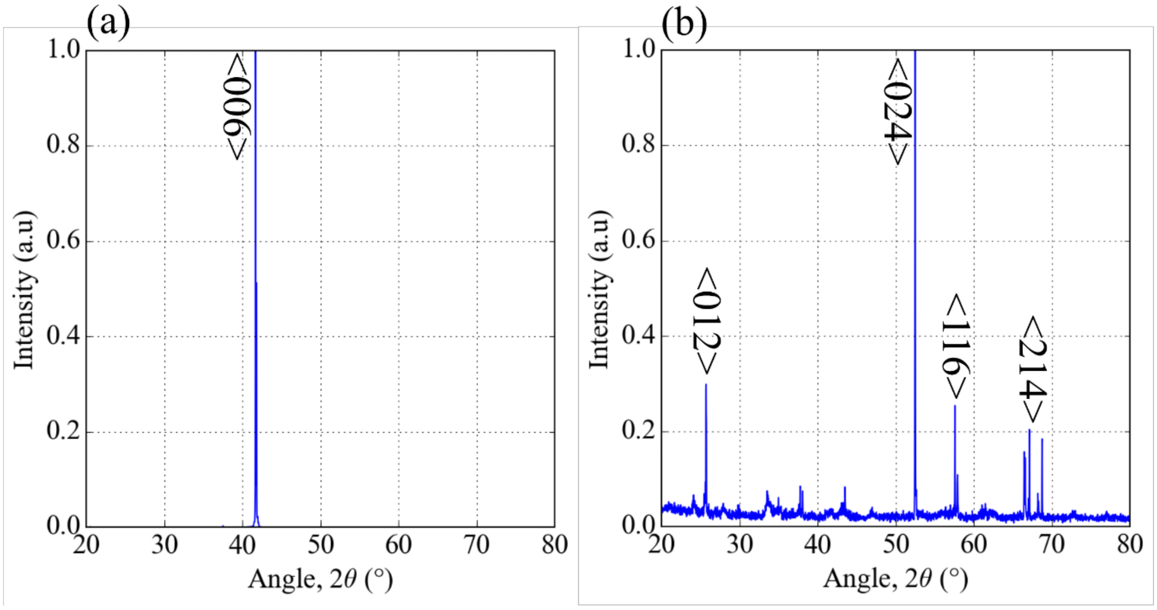

Figure 8.7. a) θ/2θ XRD spectrum and (b) GI-XRD spectrum of JP222 with the α-phase sapphire orientations labelled.

Face-polishing was performed on JP222, as described in section 8.2.3, and the GI-XRD spectra before polishing and post polishing were compared. This can be seen in Figure 8.8, where the post-polished sample has fewer orientations. The <024> and <214> orientation has been completely removed whereas there are still indications of the <012> and <116> orientation. These remaining orientations have been significantly reduced in terms of peak intensity, approaching the noise floor of the instrument.

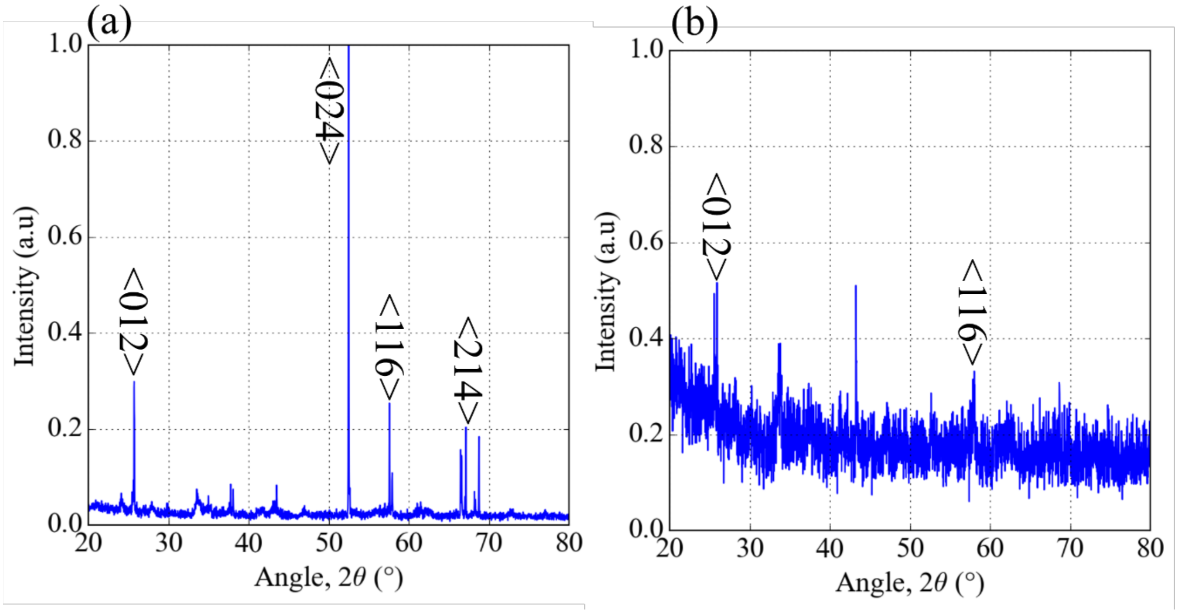

Figure 8.8. GI-XRD spectra of JP222 (a) before and (b) after face polishing.

From these results it can be ascertained that a film grown with 30 W of substrate heating power grows as κ-phase alumina rather than α-phase alumina (sapphire) and that growths with 50 W substrate heating power grow polycrystalline sapphire. Furthermore, it is demonstrated that 2-µm thick sapphire films are single-crystal at substrate heating powers between 33-40 W however, when grown thicker, different orientations begin to evolve. With face-polishing, a significant portion of the polycrystalline layers could be removed.

8.2.5 Optical properties of Yb-doped sapphire

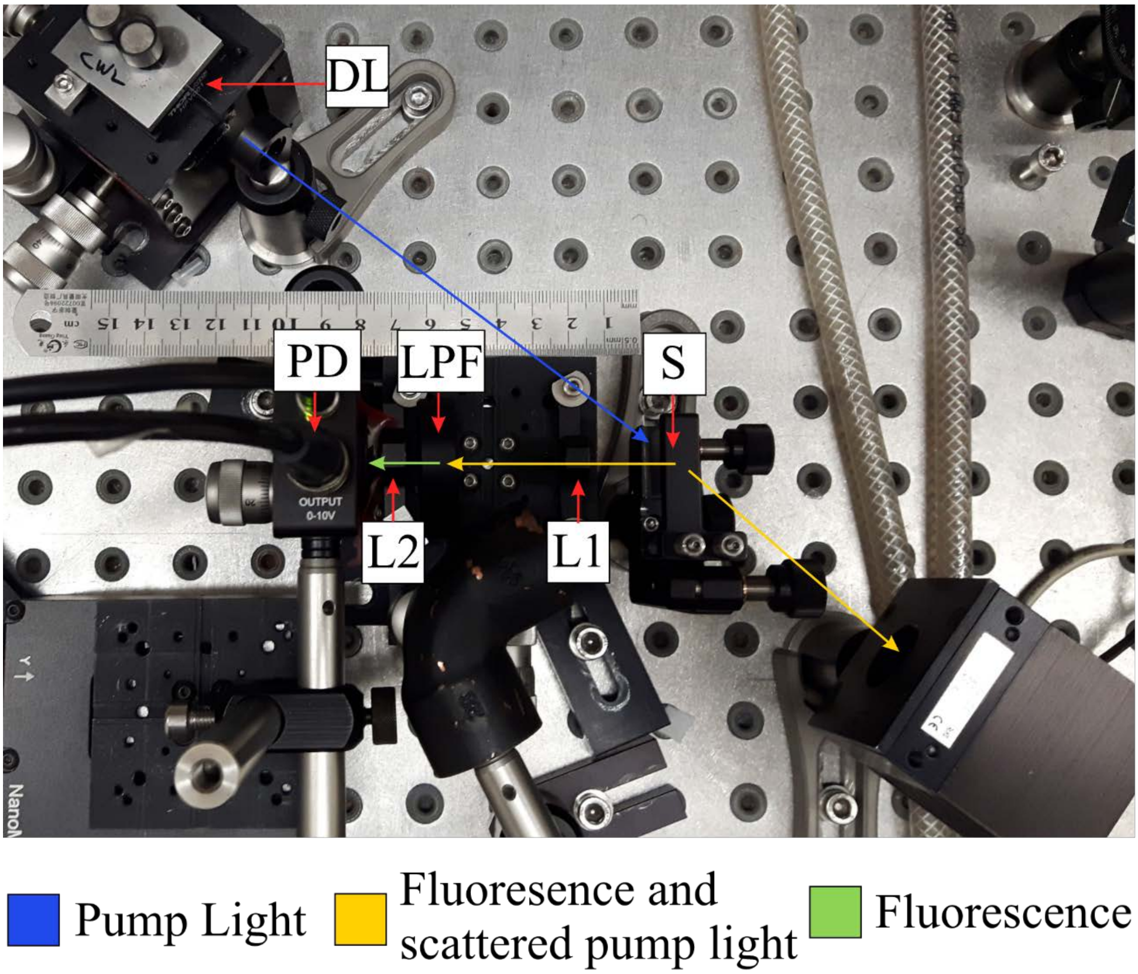

Figure 8.9. Photograph of the setup to measure the fluorescence spectrum and fluorescence lifetime. DL is a fibre-coupled single-mode diode laser: 974 nm. S is the sample, L1 is lens with f=18.4 mm and L2 f=8 mm. LPF is a long pass filter with a cut on wavelength of 1000 nm to attenuate the pump light. PD is a transimpedance amplified InGaAs photodiode (Thorlabs PDA10CS-EC). To measure the fluorescence spectrum, the photodiode was replaced by a fibre attached to an OSA.

An experimental setup, detailed in Figure 8.9, consisting of face pumping the doped films enabling the Yb^{3+} fluorescence to be characterised. Both lifetime and spectral signatures were compared to what was available in literature reports. Here, the sample (S) is pumped with a laser diode with an output wavelength of 974 nm and the scattered fluorescence and pump light is collected by the lens L1. The pump light is filtered out using a long pass filter (LPF) and the fluorescence is focussed onto either a photodiode (PD) to measure the fluorescence lifetime, or a fibre connected to an OSA to measure the spectrum.

The fluorescence spectra and lifetime of Yb:sapphire films were measured with films that were grown with different substrate heating powers. By comparing with literature values, a level of confidence of the Yb^{3+} site position can be achieved. The growth conditions of the Yb:sapphire films can be seen in Table 8.4.

The fluorescence spectra for JP213, JP217 and JP220 can be seen in Figure 8.10. The films grown at substrate heating powers of 30 and 35 W present peaks at 1008, 1030 and 1082 nm, which is in good agreement with (Heinrich *et al.*, 2012). However, the signal for JP217 (grown at 30 W) was weak, implying poor crystallinity. JP220 (grown at 50 W) did not display these peaks and instead presented a peak at 1002 nm. This implies that the ytterbium may not be in the correct position in the alumina lattice for this film.

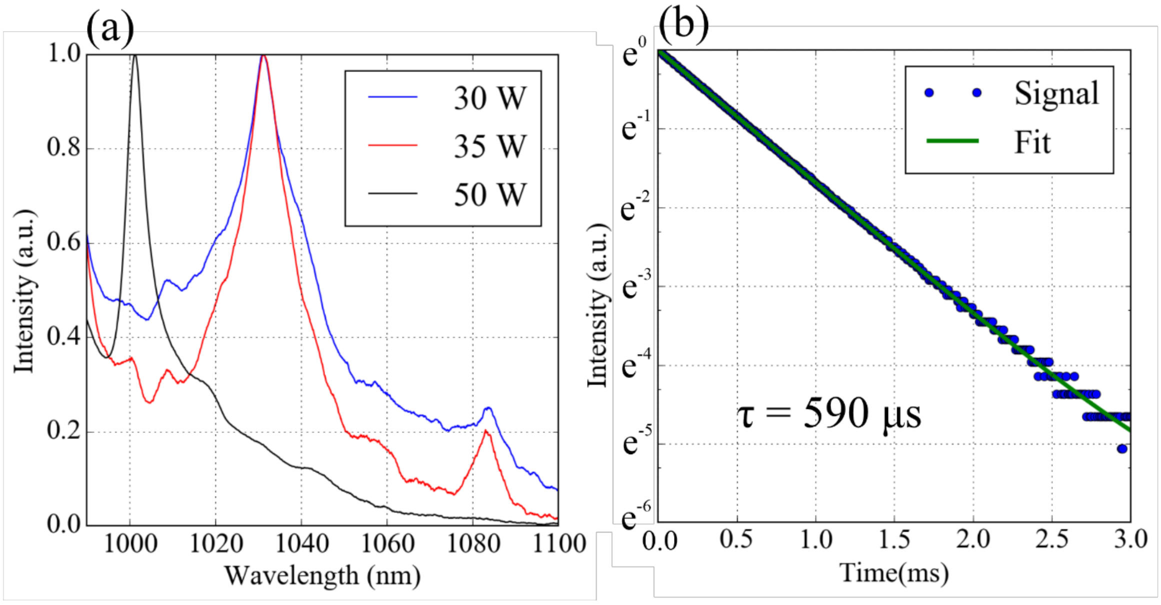

Figure 8.10. (a) Fluorescence spectrum of Yb:sapphire films grown at 30 W (JP217), 35 W (JP213) and 50 W (JP220) of substrate heating power and (b) lifetime measurement of JP225 (33 W).

The lifetime of the samples was measured using the setup seen in Figure 8.9 with samples that emit suitable fluorescence intensities. Generally, thin-film samples (<2 µm thick) were not sufficient to provide the required intensities. The lifetime of JP225 was found to be 590 µs, which is between the low dopant density (1% doping) lifetime found in (Heinrich *et al.*, 2012) of 617 µs and the high dopant density lifetime (10% doping) of 500 µs. JP225 was 3% Yb-doped, hence it would be expected to be between these two values.

Table 8.4. Growth conditions of Yb:sapphire films and their measured fluorescence lifetimes

Sample Number	Substrate Heating Power (W)	Ablation Fluence (Jcm^{-2})	Ablation Pulses	Expected Yb-doping (%)	Lifetime (μs)
JP133	33	1.6	36,000	1	639
JP137	30	3.0	36,000	1	632
JP189	33	2.8	36,000	0.5	638
JP190	33	2.8	180,000	0.5	618
JP194	32	1.8	180,000	0.5	606
JP225	33	2.7	360,000	3	590
JP227	34	2.2	720,000	1	594
JP228	34	2.8	720,000	1	599

Numerous fluorescence spectra and lifetimes of Yb:sapphire films were measured. Those films grown at ablation fluence values less than 1.6 Jcm^{-2} did not emit any measurable fluorescence, however Table 8.4 shows the films grown at 1.6 Jcm^{-2} and above and their measured lifetimes. The lifetime values show that when a film is grown thicker, the lifetime decreases, which suggests the film quality decreases as the thickness increases. This is likely due to the greater density of crystal orientations. The lifetime measured for thin films of up to 639 μs is 22 μs longer than that reported by (Heinrich *et al.*, 2012) implying less non-radiative processes and hence a higher crystal quality. The doping concentration also appears to affect the lifetime, with 3% Yb-doped JP225 measured lifetime being 590 μs, smaller than the thicker, 1%-doped JP227 and JP228.

8.2.6 Waveguiding in a thick Yb:sapphire film

The growth of Yb:sapphire has been demonstrated with confidence that the ytterbium is incorporated throughout the lattice in the correct position. The next step is check that there is a significant refractive index difference between the substrate and film. If there is no refractive index difference, the film will not guide light and therefore is will not be possible to create a Yb:sapphire laser with these samples.

Tests on face polished samples on an m-line prism coupler yielded inconclusive results, due to poor prism quality or the refractive index difference being too small. Therefore, six thick-film Yb:sapphire films were face-polished and then subsequently facet polished. In this section, the focus is on JP225 (growth conditions in Table 8.4). This sample was chosen due to its relatively high Yb-doping concentration of 3%, increasing the likely refractive index difference. The facets of JP225 were imaged with a microscope and SEM backscatter (Figure 8.11), subsequently the output of a fibre-coupled diode-laser, operating with a wavelength of 974 nm was coupled into the facet. The output signal from the opposite end of the waveguide with the pump light filtered via a longpass filter, therefore could only be the fluorescence signal. Imaging the exit facetwith a CCD camera (Spiricon SP503U) allows the measurement of the mode size, for the light propagating along the waveguide.

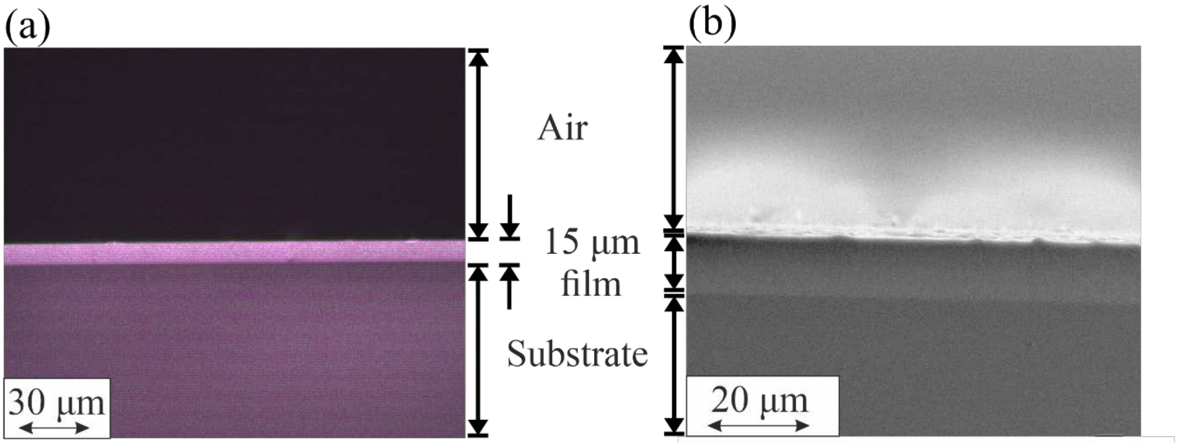

Figure 8.11. (a) Dark-field microscopy image of the facet of JP225 and (b) SEM backscatter image of the same facet.

The facet of JP225 is seen with dark-field microscopy (Figure 8.11 (a)) and SEM backscatter (Figure 8.11 (b)), but films with a lower dopant concentration could not be distinguished from the substrate. An SEM backscatter image detect differences in the physical properties of the film, and so this indicates a negligible material difference between film and substrate, which also suggests a small refractive index contrast between the film and substrate.

The filtered output from JP225 was imaged and calibrated against an optical fibre of known size in the same setup to determine the magnification of the setup. This allowed us to calculate the beam waist $\left(\frac{1}{e^2}\right)$ of the mode which was 14.3 µm.

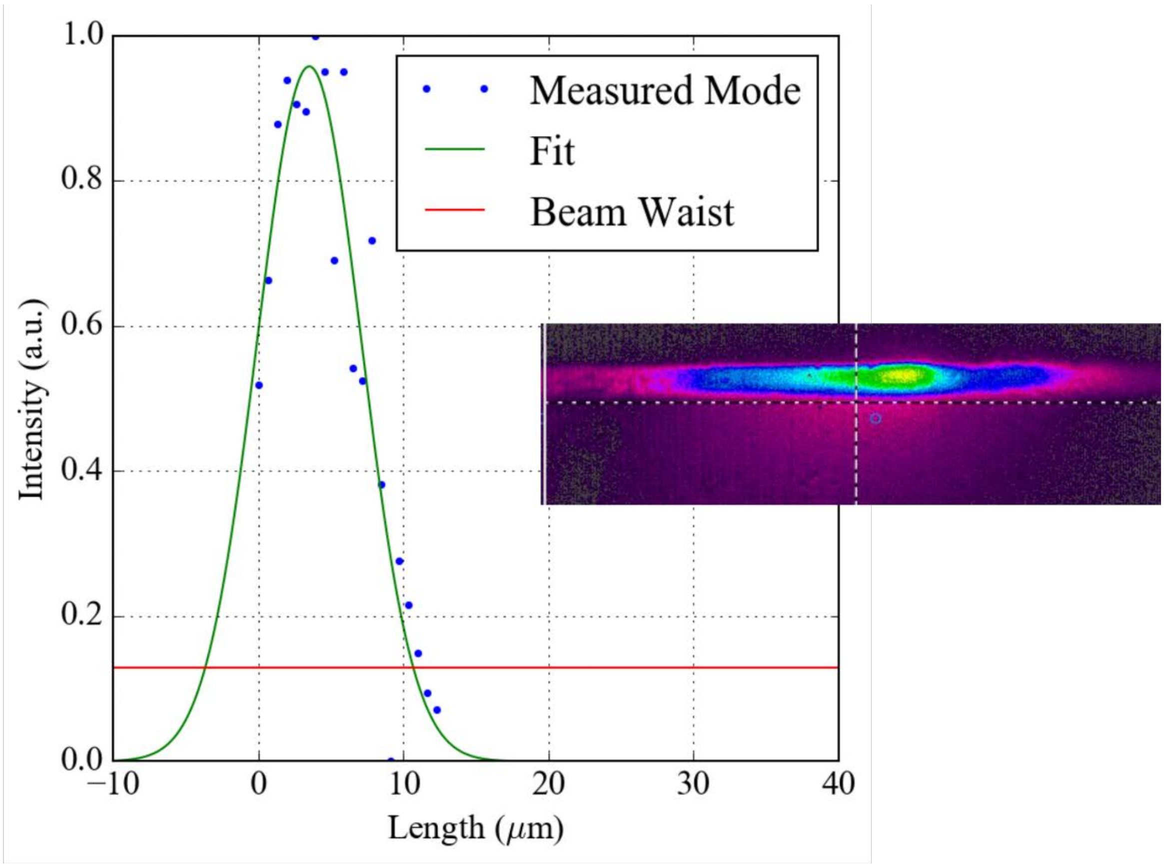

Figure 8.12. Measurement of the mode in JP225 with a Gaussian fit and the beam waist indicated via the red line. The inset displays the raw image from the CCD camera.

This demonstrates that JP225 guides light, since the fluorescence generated at one side of the film will need to propagate to the output facet. However, observations during preliminary tests indicated a high propagation loss. This could be due to interfaces between the island growths, or a high particulate density. If the growth of Yb:sapphire could be optimised to grow as monolayers the propagation loss could be reduced.

8.3 Nd-doped sapphire

Trivalent neodynium (Nd^{3+}) is a commonly used dopant ion for high-power lasers, in particular Nd:YAG (Q-switched) lasers. Like Yb:YAG, if the host material could be replaced with sapphire, the superior thermodynamic properties of sapphire would allow increased power scaling. The concept of a Nd:sapphire waveguide laser has already been proven by (Waeselmann *et al.*, 2016) who demonstrated 137 mW of output power at 7.5% slope efficiency with PLD-grown films. This was then improved by the same group with channel waveguides, increasing the output power to 322 mW with a slope efficiency of 12%

(Waeselmann *et al.*, 2017). While these results show the proof of concept, there is scope for improvements in output powers.

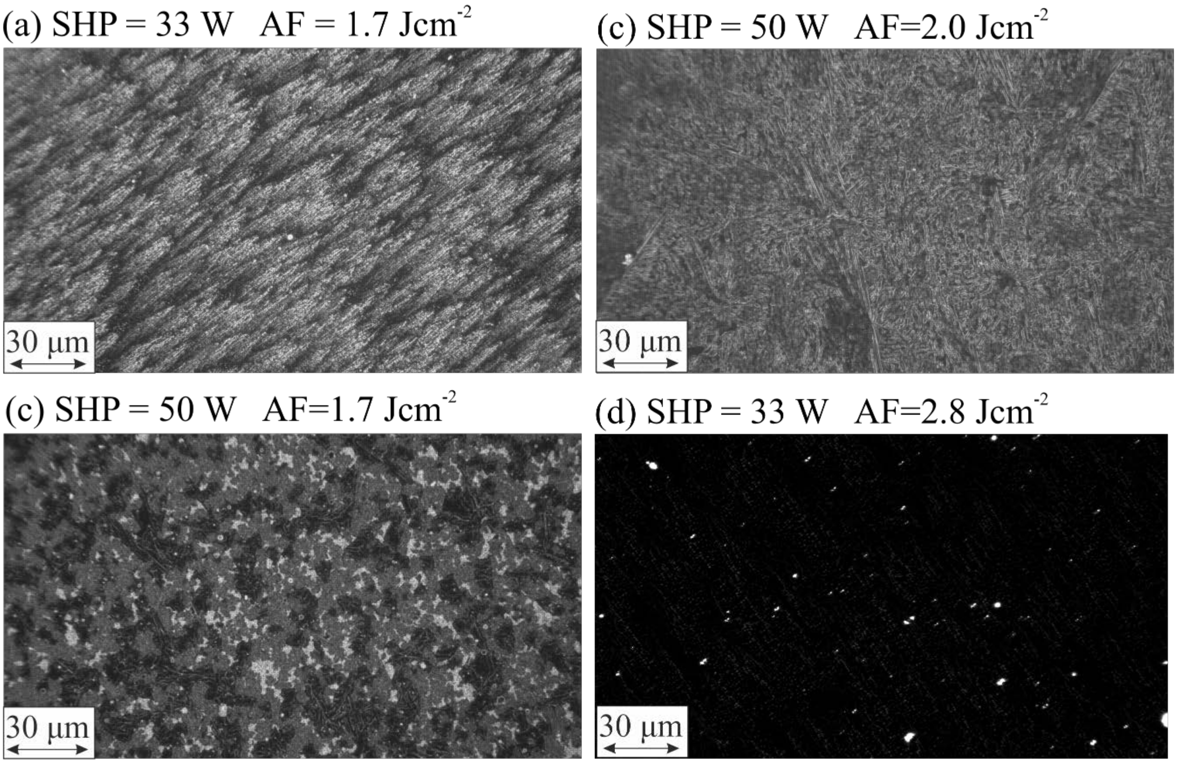

Figure 8.13. Dark-field images of Nd (0.5%): sapphire films with the substrate heating power (SHP) and ablation fluence (AF) labelled for each image.

Ten preliminary growths of Nd:sapphire have been attempted so far and, like Yb:sapphire, the growths display significant amounts of surface structure. Figure 8.13 shows four dark-field images of Nd (0.5%): sapphire films grown with a range of parameters, displayed in the figure. There appears to be significant segregation of materials in Figure 8.13 (c), with Figure 8.13 (a) and Figure 8.13 (b) showing less segregation, but still with significant surface structure. This could be explained by the size of Nd^{3+} ions, having a ~7% larger radius than ytterbium, despite being 24% less massive. Figure 8.13 (d) has significantly less surface structure. These process parameters appear to be nearer the optimum for Nd:sapphire, but more optimisation needs to be performed.

$\theta/2\theta$ XRD measurements do not show any orientations other than (0001), but it is unclear whether this is merely the substrate. GI-XRD measurements and attempts to take the fluorescence spectrum of the Nd:sapphire films are required to ensure that these films are growing as a single-crystal.

8.4 Summary

In this chapter, the optimisation of growth for Yb:sapphire and Nd:sapphire and the optical characterisation of Yb:sapphire films has been presented.

I have shown that growing Yb:sapphire below an ablation fluence of 1.6 Jcm^{-2} causes the segregation of the ytterbium from the sapphire lattice, but at or above this value, the ytterbium is incorporated into the lattice. I have also described the formation of hexagonal islands during sapphire growth and shown that the surface of the sample can subsequently be polished from a surface roughness of ~350 nm to 8 nm, an over forty times improvement.

I have measured the fluorescence spectrum and lifetime of Yb:sapphire and shown it is in good agreement with literature values. The lifetime values were found to vary with the thickness and doping concentration of the films, with thin-film Yb:sapphire displaying lifetime values longer than those found in previous research (639 µs compared to 617 µs). I also presented the first evidence of waveguiding in a Yb:sapphire planar waveguide. Laser experiments are ongoing with these waveguides.

The growths of Nd:sapphire show a significant amount of surface structure, but preliminary optimisation of the growth parameters have shown a reduction of surface structure at high ablation fluence values (2.8 Jcm^{-2}). Further experiments are needed to test the crystallinity and the incorporation of neodymium into the sapphire lattice.

8.5 References

Dobrovinskaya, E. R., Lytvynov, L. A. and Pishchik, V. (2009) *Sapphire: material, manufacturing, applications.*: Springer Science & Business Media.

Doherty, R. P., Sun, Y., Sun, Y., Warren, J. L., Fox, N. A., Cherns, D. and Ashfold, M. N. R. (2007) 'Growth of nanostructured ZnO thin films on sapphire', *Applied Physics A,* 89(1), pp. 49-55.

Heinrich, S., Gün, T. and Huber, G. 'Neodymium and ytterbium doped sapphire films grown by pulsed laser deposition.', *In Advances in Optical Materials,* San Diego, California United States: Optical Society of America, IF2A-5.

Kumaran, R., Webster, S. E., Penson, S., Li, W., Tiedje, T., Wei, P. and Schiettekatte, F. (2009) 'Epitaxial neodymium-doped sapphire films, a new active medium for waveguide lasers', *Optics Letters,* 34(21), pp. 3358-3360.

Liu, S., Zhang, Z., Comsa, G. and Metiu, H. (1993) 'Kinetic mechanism for island shape variations caused by changes in the growth temperature', *Phys Rev Lett,* 71(18), pp. 2967-2970.

Łodziana, Z. and Parliński, K. (2003) 'Dynamical stability of the α and θ phases of alumina', *Physical Review B,* 67(17).

Maiman, T. H. (1960) 'Stimulated optical radiation in ruby', *Nature,* 187(4736), pp. 493-494.

Moulton, P. F. (1986) 'Spectroscopic and laser characteristics of Ti: Al_2O_3', *JOSA B,* 3(1), pp. 125-133.

Ollivier, B., Retoux, R., Lacorre, P., Massiot, D. and Férey, G. (1997) 'Crystal structure of κ-alumina: an X-ray powder diffraction, TEM and NMR study.', *Journal of Materials Chemistry,* 7(6), pp. 1049-1056.

Shen, K. C., Jiang, M. C., Liu, H. R., Hsueh, H. H., Kao, Y. C., Horng, R. H. and Wuu, D. S. (2013) 'Pulsed laser deposition of hexagonal GaN-on-Si(100) template for MOCVD applications', *Opt Express,* 21(22), pp. 26468-74.

Waeselmann, S. H., Heinrich, S., Kränkel, C. and Huber, G. (2016) 'Lasing of Nd^{3+}in sapphire', *Laser & Photonics Reviews,* 10(3), pp. 510-516.

Waeselmann, S. H., Rüter, C. E., Kip, D., Kränkel, C. and Huber, G. (2017) 'Nd:sapphire channel waveguide laser', *Optical Materials Express,* 7(7).

Chapter 9 Conclusions and future work

9.1 Conclusions Summary

9.1.1 Summary of introductory chapters

Chapters 1-4 described the state-of-the-art for the PLD process and presented details of the characterisation tools utilised during the project and the theory behind them. Previous milestones with the growth of active crystals were presented and other deposition techniques compared to PLD. It was found that, compared to the other techniques, PLD may not always provide the film quality, however the versatility, growth rates and relative ease of the PLD technique has great potential for producing novel crystalline layers.

Previous techniques for the reduction in particulates were covered in some detail as this was a broad theme across the results chapters. The advantages and disadvantages of each particulate reduction technique were covered, and it was concluded that the complexity and reliability issues most of the active techniques (such as a velocity filter) have was a major drawback. While the novel and simple approach of BDA lead to substantial improvements in crystal quality.

9.1.2 Summary of results chapters

In chapter 5, various techniques for particulate reduction were discussed. I showed how a shadow mask placed in front of the substrate, blocked the particulates while atoms and ions wrapped around the mask, depositing onto the substrate. Reduced particulate density in $LuScO_3$ films from 38.5% to 0.49%, a nearly 80-fold reduction was demonstrated. However, the shadow mask also influenced the stoichiometry of the films, losing a substantial amount of the heavier element in the transfer from target to substrate. This could be compensated for by modifying the target composition, however the growth rate was also reduced by over three times. The stoichiometry changes and the reduction of growth rate was concluded to be too much of a drawback for this technique.

Segmented targets were then presented for the growth of ternary oxides using only binary targets. This technique reduced the particulate density by ~250 times and produced a more stoichiometric film compared to a film grown from an equivalent ternary target. This technique is extremely effective; however, binary sublayers were observed in the film. This could be prevented by reducing the number of sequential pulses on each segment.

Finally, in chapter 5, I presented a novel ablation protocol, namely bi-directional ablation of which I presented a thorough analysis. This technique altered the way the target was moved in the PLD system to effectively ablate the target from two different directions. Compared to the method used at the start of this project, BDA increased target face utilisation by ~50% and reduced the targets post-ablated surface roughness by 50%. The average film particulate density grown via BDA was 80% lower than the average film grown by UDA. With BDA it was demonstrated that a YGG film with propagation losses of 0.12 dB/cm, 2.8 dB/cm less than those grown with UDA.

In chapter 6, I discussed the growth of various types of garnets throughout this project. In different sections I presented the growth optimisation of YGG, YAG and LuAG. It was seen how when a film is grown thicker, the optimum growth parameters narrow, putting an emphasis on thick-film optimisation. I also discussed the relative loss of aluminium in YAG and LuAG growths, and the loss of gallium in YGG growths, and how this could be compensated for by putting more aluminium/gallium in the targets.

I presented the first PLD-grown Yb:LuAG double-clad waveguide and its performance when operated as a laser, with output powers of up to 3.3 W and a slope efficiency of 20%. Er:YGG channel waveguides were also demonstrated for the first time, which had been grown via PLD and channels fabricated via precision dicing. These channel waveguides demonstrated up to 3.46 dB internal gain and propagation losses down to 0.12 dB/cm, some of the lowest losses seen in PLD-grown waveguides.

Chapter 7 described work with sesquioxides and mixed sesquioxides. I demonstrated the optimisation of the growth conditions for lutetia grown onto sapphire. However, the presence of domains in the crystal films frustrated further progress with these films. I also presented research into mixed sesquioxides, showing it is possible with PLD to tune the stoichiometry of the crystal film to lattice match with the substrate. In this case, a near perfect match between the mixed sesquioxide film and the sapphire substrate was achieved, with only a 0.04% lattice mismatch. Domains in the mixed sesquioxide films were observed and, when doped with Yb^{3+}, confirmed the large emission bandwidth of Yb:$LuScO_3$ (19 nm) compared to Yb:Lu_2O_3 (13 nm) and Yb:YAG (10 nm).

Finally, in chapter 8, I discussed the progress in growing RE-doped sapphire films via PLD. I presented the growth conditions needed for incorporation of Yb ions into the sapphire lattice and optimisation of the growth parameters. I then presented the fluorescence spectrum and lifetimes of various Yb:sapphire films, finding that thickness and doping concentration affect the lifetime values. Evidence of waveguiding in a Yb:sapphire film for the first time to my knowledge was presented .

9.2 Future directions

This work has focussed a lot of attention on what is considered the main drawback of PLD, namely particulates. Although substantial progress has been made in reducing the density of particulates in the film, there is still more that needs to be done before the commercial applications of PLD for active crystal films can be fully realised. BDA is a simple yet effective countermeasure against particulates, yet it does only ablate from two different directions. A multi-directional ablation (MDA) setup would ablate from many different directions, reducing the surface structure on a post-ablated target further and consequently reducing the particulates embedded into the film during growth. This could be achieved through raster scanning the target across the beam and then rotation. By having a suitable MDA system, the targets should last longer allowing even thicker growths, however, as I discussed earlier this setup would be even more complex.

Through increasing the utilisation of the target in the new BDA system, thicker growths have become the norm in this project, with single-crystal films up to 35 µm grown. By simply doubling the diameter of the targets used from 50 mm to 100 mm, the useable target area would multiply by 4. This would allow growths of high-quality, single crystal, 100 µm thick films. This combined with high-dopant concentrations that are achievable with PLD, could open the door for PLD-grown films to be exploited in a thin-disc laser architecture.

This work has shown a lot of promise with increasing the film quality of YAG and lutetia. The knowledge of how to grow these materials as single-crystal and with low particulate densities should be utilised to create laser devices with higher output powers and higher slope efficiencies than previously realised. An Yb-doped sapphire film has been shown to waveguide and needs to be tested as a laser. Further optimisation of RE-doped sapphire is needed to produce high-quality films, in particular, optimisation for “Frank-Van der Werve” growth is needed to prevent the formation of hexagonal islands.

Using the novel ablation protocol of BDA, pulsed laser deposition can be seen as a reliable crystal growth technique for low-loss active films. Exceptionally low losses have been demonstrated with YGG, and other materials can now be grown with low defect densities and hence, be explored to their full potential with PLD.